

Drug-Membrane and Protein Interactions in tethered Bilayer Lipid Membranes Studied by Surface Analytical Methods

A thesis submitted for the degree of Doctor of Philosophy

By Julius Zieleniecki

Bachelor of Science (Honours) (Nanotechnology)



Flinders
UNIVERSITY

Faculty of Science and Engineering

School of Chemical and Physical Sciences

Start Date: Tuesday, January the 31st, 2012

Submission Date: Friday, February the 17th, 2017

Completion Date: Friday, June the 30th, 2017

Declaration

I certify that this thesis does not incorporate, without acknowledgment, any material previously submitted for a degree or diploma in any university; and that to the best of my knowledge and belief it does not contain any material previously published or written by another person except where due reference is made in the text.

Mr. Julius Leo Zieleniecki

Signed: _____

Date: _____

Acknowledgments

The last five years of my life have been a journey filled with every emotion possible. I have met and worked with many wonderful people without whom this project would never have eventuated and developed. Science truly is an eye-opening collaborative effort with incredible talents and minds. The lessons I have learned will stay with me forever, ready to be passed on with only the greatest respect and admiration.

To my supervisors, Doctor Ingo Köper and Professor Joe Shapter, thank you so much for your kind supervision, seemingly endless spare time, constant effort, careful guidance, understanding patience, and repeated words of advice and wisdom. You have both been role models to me since my second year at university and will forever continue to be. Over time I have grown understood your ideas; sometimes a person just simply needs to be left to experience their own ideas to understand his or her own mistakes.

As part of my ongoing research, certain individuals deserve considerable mentions. From Flinders University, I would like to thank Renee Goreham, Jackie Knobloch, Jakob Andersson, Josie Nunn, and Yuya Samura, as your ideas, support, laughter, and shared experiences have been incredible. Equally, Jenny Brand and Colin Raston, your kind words and wisdom is incredible and heart-warming. From the Australian Centre for Plant Function Genomics, I thank Maria Hrmova, Yagnesh Nagarajan, Jay Rongala, and Shane Waters for their excitement, repeated guidance, support, care, and patience. As part of my time spent in the National Institute of Materials Science in Japan, I would like to thank Kohei Uosaki, Mikio Ito, Hidenori Noguchi, Kyoko Okada, and Kayoko Hartori, as you all made me feel incredibly welcome and taught me so much. At the Australian Nuclear Science and Technology Organisation, I would like to thank and show appreciation to Stephen Holt, Andrew Nelson,

and Anton LeBrun, for all your help, jaw-dropping experience, and collective guidance. For my time spent in America, I would like to thank Joseph Robertson and Jacob Forstarter for your wealth of ideas, advancements toward my project, and continuous guidance.

A special thank you goes to John Kasianowicz; you helped me when I needed it most and have since been a calm but exciting, collected and inspiring, and insightful as well as wise role-model both within as well as outside of the field of science. I hope I can be a light for someone the way you have been for me.

To all my friends, especially Steve, Rowan, Daniel, and Rob, you have stood firmly by my side since I started this project in my Honours year, and whether I have been able to show it or not, your patience, help, and support has always been appreciated beyond belief.

Dear Belinda, my fiancé to be, I started this work many years before you came into my life and am closing it now, in front of you; my appreciation and excitement to and for you knows no bounds. The care, patience, support, and love you give every day is greater than any person could hope for. I appreciate every gesture, big or small, you send my way and I thank you for everything you have done since I met you. You have been a guide and a teacher to me more than you know.

And finally, to my parents Iwona and Leo, or better known as Miś and Z, you are two incredible people without whom I could never have started or finished this journey. I can only imagine that in 1989 when you first set eyes on me, you did not see me spending five years of my teens and tweens trying to unravel how alcohol interacts with cells, or at least not behind the desk of a lab! Your never-ending love and unquestioning support is something I hope I can carry into the future with as much brightness, warmth, and patience as that which shines in your hearts; my admiration and appreciation to you knows no bounds.

Abstract:

Approximately 60–70% of all drugs released in 2006-2008 were designed specifically to target membrane bound proteins [1-3]. Although these drugs are targeted, they also interact non-specifically; which is suggested to be one cause of their side-effects. Even though lipid membranes are one of the major building blocks of a cell as well as the organelles within them, they are currently significantly understudied. To improve how drugs interact with the body, the properties of membranes as well as molecules interacting with them should be studied further. In this case, focusing on the simple anaesthetic ethanol, a literature search indicates that few studies have set out to understand how ethanol interacts with a simple, protein or peptide-tested, and realistic, model membrane both electrically as well as physically.

Equally understudied as membranes and non-specific drug interactions, are cellular-membrane proteins. These proteins are difficult to crystallise and generally embedded deep within a cell, unreachable to study. Although computational methods and speeds are improving, being able to reconstitute these proteins without the need for bacteria, directly from RNA into an *in vitro* membrane which can be studied both electrically as well as physical, affords unprecedented improvements in supporting computational studies as well as learning about these proteins.

This thesis is a summary of experiments undertaken regarding: 1) the interactions of ethanol with a tethered Bilayer Lipid Membrane (tBLM) and 2) the use of a tBLM as a matrix for embedding and testing the protein HvBot1 translated *in vitro* by cell-free synthesis.

In the first series of experiments, tBLMs were tested using Electrochemical Impedance Spectroscopy (EIS), Femto-Second Vibrational Sum Frequency Generation (fs-vSFG), and

Neutron Reflectometry (NR) to interpret: the electronic and physical effect of ethanol on a tBLM; the position of ethanol within a tBLM; and the indirect effect of ethanol on the peptide Valinomycin within the membrane at various ethanol concentrations.

In the second series of experiments the same type of tBLM system was used, in conjunction with cell-free synthesis, to observe and test the expression and embedding of HvBot1 formed from RNA *in vitro* in the tBLM system.

Overall this research develops the knowledge of membrane-drug interactions and extends the understanding of the viability of cell-free synthesis of large proteins such as HvBot1 with tBLMs.

Publications:

Published work originating from work completed within this thesis:

Zieleniecki, J.L., Nagarajan, Y., Waters, S., Rongala, J., Thompson, V., Hrmova, M. and Köper, I.,

Cell-Free Synthesis of a Functional Membrane Transporter into a Tethered Bilayer Lipid Membrane.

Langmuir, Vol. 32(10), pp.2445-2449. (2016)

Additional publications originating from work which is related to this thesis:

Vogel, N., Zieleniecki, J. and Köper, I.,

As flat as it gets: Ultrasmooth surfaces from template-stripping procedures.

Nanoscale, Vol. 4(13), pp.3820-3832. (2012)

Knobloch, J., Suhendro, D.K., Zieleniecki, J.L., Shapter, J.G. and Köper, I

Membrane–drug interactions studied using model membrane systems.

Saudi Journal of Biological Sciences. Vol. 22(6), pp.714-718. (2015)

This thesis is dedicated to my parents and wife-to-be,

Iwona and Leo Zieleniecki and Belinda Zanello;

the unbelievable patience, effort, and love you

all show is incredible.

Table of Contents

1. Introduction.....	1
1.1. Chapter Overview.....	2
1.2. Lipid Bilayer Membranes.....	4
1.2.1. Why membranes exist.....	4
1.2.2. Lipids and cellular membranes.....	4
1.2.3. Lipid types.....	6
1.2.4. Common lipids.....	7
1.3. Model membranes.....	9
1.3.1. Requirements of a model membrane.....	9
1.3.2. Supported BLMs.....	9
1.4. Proteins.....	17
1.4.1. Peptide, Proteins, and Pore Stabilisation.....	18
1.4.2. Valinomycin.....	19
1.4.3. HvBot1.....	21
1.5. Drugs.....	23
1.5.1. Drug-membrane research historically.....	23
1.5.2. Common drug interactions.....	24
1.5.3. Ethanol-membrane interactions.....	25
1.6. EIS and membranes.....	31
1.6.1. EIS theory.....	31
1.6.2. Applying EIS to tBLMs.....	35
1.6.3. Common electrical elements in EECs.....	36
1.6.4. Charge pathways applicable to EIS.....	37
1.6.5. EEC interpretations.....	39
1.6.6. Plotting EIS Data.....	42
1.7. Alternative techniques.....	44
1.7.1. Fourier Transform Infrared Red Spectroscopy.....	44
1.7.2. Cyclic Voltammetry and Reductive Desorption.....	48
1.7.3. Femtosecond-VSFG.....	51
1.7.4. Neutron Reflectometry (NR).....	54
1.8. Study Scope:.....	56
1.8.1. Ethanol.....	56
1.8.2. HvBot1.....	56
2. Methods.....	57
2.1. Chapter Overview.....	58
2.2. General Experimental.....	59
2.2.1. Chemicals and consumables.....	59
2.2.2. Column Chromatography.....	61
2.2.3. Thin Layer Chromatography.....	63

2.2.4. FTIR	64
2.2.5. NMR.....	66
2.2.6. Cyclic Voltammetry	67
2.2.7. Electrochemical Impedance Spectroscopy	72
2.2.8. Femto-Second Vibrational Sum Frequency Generation (fs-vSFG).....	79
2.2.9. Neutron Reflectometry	82
3. Data Interpretation and Modelling Processes.....	84
3.1. Chapter Overview	85
3.2. EIS Data Collection and Modelling Process.....	86
3.2.1. Basics of data interpretation	86
3.2.2. Applying an EEC of choice.....	87
3.3. CV and Reductive Desorption	94
3.3.1. Au(111) surface area calculation.....	94
3.3.2. Reductive desorption coverage calculation	96
3.3.3. Issues with CV and reductive desorption curve integration	97
3.4. fs-vSFG.....	101
3.5. Neutron Reflectometry	104
4. Results: Ethanol and tethered membranes	108
4.1. Chapter Overview	109
4.2. Introduction	110
4.3. Ethanol's Effects on a tBLM	112
4.3.1. EIS Analysis.....	112
4.3.2. FTIR, NMR, and CV analyses.....	115
4.3.3. fs-vSFG	122
4.3.4. Neutron Reflectometry	129
4.4. Ethanol's Effect on Valinomycin through the tBLM.....	134
4.4.1. Qualitative observations of Bode plots during Valinomycin condition.....	138
4.5. Conclusions	146
4.5.1. Ethanol	146
4.5.2. Valinomycin.....	148
4.5.3. In Summary	149
4.6. Importance of Current Outcomes and Future Suggestions	150
4.6.1. Importance of this work.....	150
4.6.2. Improvements.....	150
5. Results: Borate transport using the barley Bot1 anion efflux transporter, HvBot1.....	152
5.1. Chapter Overview	153
5.2. Introduction	154
5.3. EIS study of HvBot1 in tBLM membranes.....	156
5.3.1. Prior to HvBot1 incorporation.....	156
5.3.2. HvBot1 Testing and Discussion	158
5.4. Comparisons between previous and updated EIS EECs results.....	168
5.5. Conclusions	171

5.6. Importance of Current Outcomes and Future Suggestions	172
5.6.1. Importance of this work.....	172
5.6.2. Future Work	172
6. Appendices.....	174
6.1. EIS EECs without CPEs	175
6.1.1. Single RC-Meshes: (R(RC)C) and (R(RC)).....	175
6.1.2. Double RC-Meshes (R(RC)(RC)), (R(RC)(RC)C)	180
6.1.3. Triple-RC meshes or greater.....	182
6.1.4. Overall.....	183
6.2. EECs with CPEs	184
6.3. Types of EIS plots	187
6.4. Concerns regarding Cyclic Voltammetry	189
6.5. VSFG.....	192
6.5.1. Theory	192
6.5.2. Molecular orientation and interaction.....	193
6.5.3. Types of polarisations.....	194
6.5.4. Effect of solvent	195
6.6. Ethanol Data	196
6.7. Assigned NMR Spectrum of DPhyTL.....	197
6.8. HvBot1 Information.....	198
6.9. HvBot1 Structure	201
7. References.....	203

List of Figures:

Figure 1:	Example of a simplified: cellular; 3D; and 2D membrane model.	5
Figure 2:	2D representation of various types of lipid membrane arrangements.....	6
Figure 3:	The phosphocholine group structure.	7
Figure 4:	Composition of lipids in various areas of a mammalian cell.....	8
Figure 5:	A schematic of a DPhyTL-DPhyPC bilayer formed on Template Stripped Gold.	11
Figure 6:	A DPhyTL-DPhyPC bilayers with an incorporated Valinomycin peptide and HvBot1 protein.....	17
Figure 7:	Structural formula of Valinomycin.....	19
Figure 8:	Bilayer resistance as a function of salt concentration.	20
Figure 9:	Example structures of borate anions.....	22
Figure 10:	Interactions of penetration-enhancing drugs with intercellular lipid membrane domains.....	25
Figure 11:	Example sine wave of applied potential and the response of current.	32
Figure 12:	Various areas of a bilayer with different electrical properties.	38
Figure 13:	Schematic of a transmission line	39
Figure 14:	An example of the EEC used to interpret membrane properties.....	41
Figure 15:	Example Bode plot	43
Figure 16:	Bulk-DPhyTL FTIR spectrum of the C-H stretching region.	45
Figure 17:	FTIR spectra of DMPC in two forms.	47
Figure 18:	The EEC circuit used to interpret the tBLM with defects.....	88
Figure 19:	Bode plot representing the effect of lowering f_{\min} on auto-fitting.	89
Figure 20:	A diagram explaining where EIS f_{\min} cut-offs were locked during data fitting.	92
Figure 21:	A diagram representing the structure of Au(111).....	94
Figure 22:	Example CV gold reductive peak of Au(111) in H_2SO_4	97
Figure 23:	Integration curve of Figure 22 using Origin.	98
Figure 24:	A standard fs-vSFG spectrum of a polystyrene film in air.	101
Figure 25:	fs-vSFG spectra of DPhyTL with polystyrene on Au and a bare gold surface.....	102
Figure 26:	fs-vSFG spectrum of DPhyTL on Au with polystyrene after normalisation.	103
Figure 27:	Example NR reflectivity curves of three different solvent ratios as a function of Q of a tBLM.	105
Figure 28:	Example NR nSLD profile of each contrast solution while testing a tBLM.....	107
Figure 29:	FTIR CO region spectrum of bulk DPhyTL.....	116
Figure 30:	FTIR CH region spectrum of bulk DPhyTL.....	117
Figure 31:	NMR (400MHz) spectrum of DPhyTL solution in chloroform-D.....	118
Figure 32:	Cyclic Voltammogram of Au(111).....	119
Figure 33:	Cyclic Voltammogram of DPhyTL attached to Au(111).	120
Figure 34:	fs-vSFG spectrum of DPhyTL signal post normalisation in Argon.....	123
Figure 35:	fs-vSFG spectrum of DPhyTL signal post normalisation in Milli-Q water.....	124
Figure 36:	fs-vSFG spectrum of DPhyTL-DPhyPC Bilayer in Buffer Solution.	125
Figure 37:	fs-vSFG spectrum of DPhyTL-DPhyPC Bilayer in 25% _{v/v} ethanol solution.....	127
Figure 38:	fs-vSFG spectrum of DPhyTL monolayer in Argon.....	128
Figure 39:	nSLD profile of a DPhyTL-DPhyPC tBLM before, during, and after 10% _{v/v} d-EtOD in D_2O	130
Figure 40:	nSLD profile of a DPhyTL-DPhyPC tBLM before, during, and after 25% _{v/v} d-EtOD in D_2O	131
Figure 41:	nSLD profile of a DPhyTL-DPhyPC tBLM before, during, and after 50% _{v/v} d-EtOD in D_2O	132
Figure 42:	Bode plot, pre-ethanol, indicating the effect of Valinomycin in NaCl and KCl solution.	139
Figure 43:	Bode plot indicating the effect of 1% _{v/v} ethanol on Valinomycin function.	140
Figure 44:	Bode plot indicating the effect of 5% _{v/v} ethanol on Valinomycin function.	141
Figure 45:	Bode plot indicating the effect of 10% _{v/v} ethanol on Valinomycin function.	142
Figure 46:	Bode plot indicating the effect of 25% _{v/v} ethanol on Valinomycin function.	143
Figure 47:	Bode plot indicating the effect increasing ethanol on Valinomycin function.....	144
Figure 48:	Bode plot presenting the effect of increasing ethanol concentrations on Valinomycin action.	145
Figure 49:	Bode plot of tBLM pre HvBot1 reconstitution, testing the bilayer matrix using Valinomycin.....	162
Figure 50:	Bode plot of a tBLM testing borate anion conduction pre-HvBot1 reconstitution.....	163
Figure 51:	Bode plot of a tBLM pre HvBot1 reconstitution, prior to NaCl inclusion at pH 6.....	164

Figure 52: Bode plot of a tBLM pre HvBot1 reconstitution, including NaCl at pH 6.	165
Figure 53: Bode plot of a tBLM pre HvBot1 reconstitution, including NaCl at pH 7.5.	166
Figure 54: Bode plot of a tBLM pre HvBot1 reconstitution, including NaCl at pH 9.	167
Figure 55: Common types of R-RC and R-RC-C meshes.....	176
Figure 56: Schematic of a lipid bilayer membrane with a defect and the circuit applied to it.	179
Figure 57: A type of R-RC-RC EEC.....	182
Figure 58: A type of triple RC mesh EEC.	182
Figure 59: SAM of EG ₃ -OMe on gold. Reproduced from Zolk et al. [2000]	194
Figure 60: SFG spectrum of EG ₃ -OMe on gold in ambient atmosphere in CCl ₄ , D ₂ O, and air.....	195
Figure 61: Assigned 400 MHz NMR Chloroform-D spectrum of DPhyTL	197
Figure 62: SDS-Page gel electrophoresis of HvBot1 into various types of liposomes.....	200
Figure 63: Modelled structure of HvBot1.....	201
Figure 64: Various spatial arrangements of the multimeric forms of HvBot1.....	202

List of Tables:

Table 1:	Chemical and consumable list for all experiments.	59
Table 2:	Effect on EEC values by extending the f_{\min} value during fitting.	89
Table 3:	Surface area of a flat and circular electrode of various diameters.	100
Table 4:	Blood Alcohol Concentration (BAC) in terms of concentration and %v/v.	111
Table 5:	Effects of ethanol on fitted EEC values of a DPhyTL-DPhyPC bilayer.....	112
Table 6:	EEC R_{def} resistance at various concentrations of ethanol normalised to initial bilayer resistance...	113
Table 7:	Coverage results of DPhyTL on Au(111) as per method 3.3.1 and 3.3.	121
Table 8:	Fitted ethanol-valinomycin data using a R_s - $[C_{\text{mH}}/R_{\text{def}}-Z_{\text{sub}}]$ EEC.	136
Table 9:	Effect of f_{\min} on Z_{sub} of an R_s - $[C_{\text{mH}}/R_{\text{def}}-Z_{\text{sub}}]$ EEC.....	137
Table 10:	EEC values during HvBot1 experiments in a DPhyTL-DPhyPC membrane.	161

List of Equations:

Equation 1: Output Voltage as a function of time.	32
Equation 2: Output current as a function of time.	32
Equation 3: Capacitive output current as a function of time.	33
Equation 4: Fourier transform of capacitive output current as a function of angular frequency.	33
Equation 5: Complex impedance as a function of frequency.	33
Equation 6: Rectangular and polar coordinates of impedance.	34
Equation 7: Modulus of complex impedance.	34
Equation 8: The real component of impedance as a rectangular coordinate.	34
Equation 9: The imaginary component of impedance as a rectangular coordinate.	34
Equation 10: The phase difference between the real and imaginary components.	34
Equation 11: Impedance due to a resistor.	36
Equation 12: Impedance due to a capacitor.	36
Equation 13: Impedance due to a CPE.	36
Equation 14: Description of the oxidation of an Au(111) surface.	95
Equation 15: Description of the reduction of a di-thiol (such as DPhyTL) from an Au(111) surface.	96
Equation 16: The ‘momentum transfer vector’ or ‘scattering vector’ equation.	104
Equation 17: The ‘momentum transfer vector’.	105
Equation 18: Fricke’s application of dielectric values to membrane capacitance.	114
Equation 19: Common forms of a CPE equations.	185

List of Acronyms:

BAC	Blood Alcohol Level
BLM	Bilayer Lipid Membrane
CV	Cyclic Voltammetry
EEC	Electronically Equivalent Circuit
EIS	Electrochemical Impedance Spectroscopy
FTIR	Fourier Transform Infrared Spectroscopy
MC	Monte Carlo [simulations]
MD	Molecular Dynamics [simulations]
NMR	Nuclear Magnetic Resonance
NR	Neutron Spectroscopy
nSLD	Neutron Scattering Length Density
PMF	Potential of Mean Force
SLB	Supported Lipid Bilayer
tBLM	Tethered Bilayer Lipid Membrane
TLC	Thin Layer Chromatography
TSG	Template Stripped Gold

1. Introduction

1.1. Chapter Overview

A drug is a chemical substance which affects the function of a living organism. Tens of thousands of drugs are currently in use on the market, many of which target membrane-proteins, however, non-specific interactions of drugs with cellular membranes are rarely studied and are postulated to be one of the causes of drug-related side effects. Studying the interactions of drugs with lipids and membrane proteins in complex environments is difficult due to the vast number of molecules and redundancy pathways that cells include and exhibit. To study this, a simplified system mimicking a cellular environment, which can be studied using several techniques, is used in this thesis.

The first results chapter of this thesis uses a simplified tethered bilayer lipid membrane system to test the effects of ethanol on the structure of a membrane. To extend this work further, the transporter peptide Valinomycin is embedded in the membrane. By embedding the peptide, the membrane is able to be electrically tested for physical relevance as a realistic membrane and also allows indirect effects of ethanol to be studied on the peptide. Overall, this work will: 1) examine the effect of ethanol on a model lipid bilayer membrane to confirm limited physical and computational studies; 2) develop a greater understanding of how the simple drug, ethanol, interacts with the model membrane; and 3) elucidate the indirect effects of ethanol on the transporter peptide Valinomycin.

The second results chapter in this thesis concerns itself with using a DPhyTL-DPhyPC tBLM as a membrane for testing the reconstitution of a large transmembrane borate anion transporter protein. In conjunction with the Australian Centre for Plant Function Genomics, the process of reconstituting the large protein HvBot1 into the tBLM was tested. Cell-free synthesis allows a protein to be reconstituted directly from mRNA *in vitro*. Successfully embedding

transmembrane proteins is a difficult process and is sometimes only partly successful as it requires exact conditions to occur. Overall, it was observed that the protein reconstituted into the membrane and retained function.

1.2. Lipid Bilayer Membranes

1.2.1. Why membranes exist

Cells require membranes to help contain reactants and products of small volumes and help shuttle those compounds and molecules to their respective organelles using various types of compartments known as organelles, vesicles, or liposomes [4]. To achieve this, lipids are used widely and equate for almost half of the mass of a mammalian cell, with a cellular membrane alone containing approximately 5×10^6 molecules within a $1 \mu\text{m}^2$ space; the remainder of a cell's mass is mostly protein, highlighting the structural complexity of the cellular membrane [5-8]. To date, over 40,000 different lipids have been found in nature [9].

1.2.2. Lipids and cellular membranes

A lipid generally consists of a head-group and non-polar acyl chains [10]. The non-polar acyl chains self-associate due to an entropic drive by water while the hydrophilic moieties interact with each other as well as the environment; these properties create the physical basis for spontaneous structure lipid bilayer formation (Figure 1) [4]. A lipid bilayer is externally hydrophilic and internally hydrophobic and therefore acts as a barrier between different aqueous solutions. It is commonly used as a supporting matrix (for pores, peptides, proteins, and saccharides), filter membrane, and messenger (during signal transduction) [6]. A membrane is tailored with various lipids which either are or are not miscible in water, creating controllable phase-related properties (such as domains) [6]. The different modalities of a membrane's use determine the ratios of various lipids and other molecules, which in turn determine a membrane's structure, rigidity, viscosity, charge, and thickness, amongst many other properties. This type of control is highly effective when paired with a membrane's semi-permeability, controlling the passage of small polar molecules or ions [7, 11, 12].

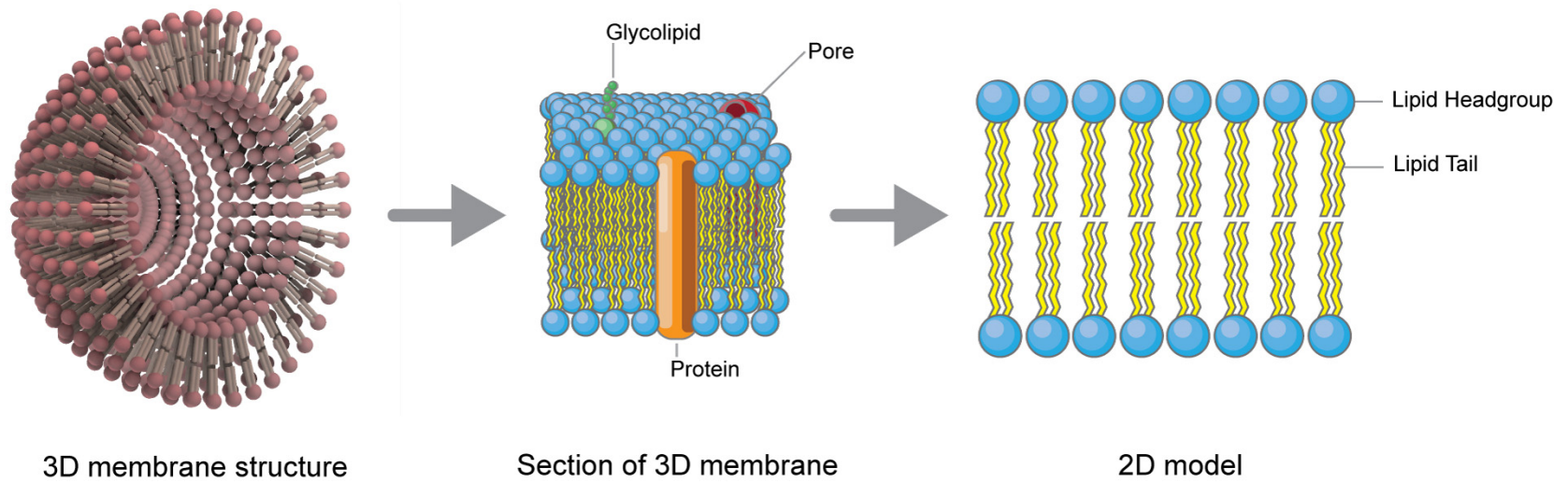


Figure 1: Example of a simplified: cellular; 3D; and 2D membrane model.

From left to right: A sliced-open structure of a simplified vesicle (representing a simplified cellular membrane); a 3D representation of simplified membrane in model form; and a simplified 2D structure representing the 3D form to its left.

1.2.3. Lipid types

Each lipid has its own melting regime, however, as mixtures, lipids are able to organise into mixtures with defined phase boundaries with each mixture having its own characteristic properties [6]. Lipids can take the shape of single- or multi-layered vesicles or micelles (Figure 2). Other structures, such as cubic and hexagonal phases, have been witnessed but generally relate to transient bio-membranes such as during fusion, fission, and pore-formation.

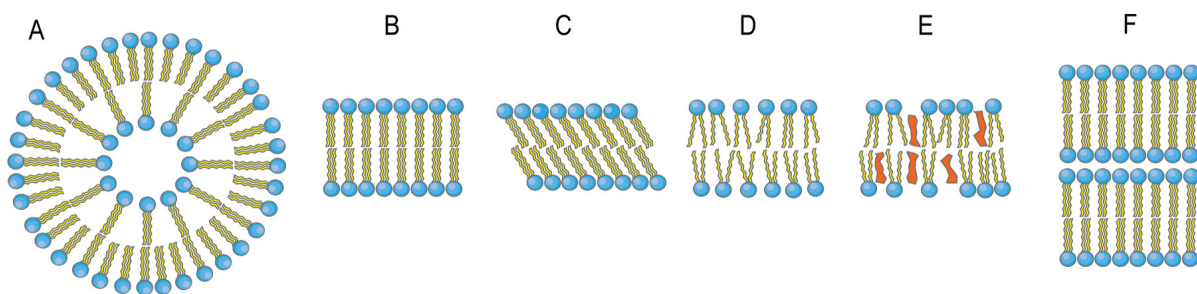


Figure 2: 2D representation of various types of lipid membrane arrangements.

In order, types of lamellar phases: A) vesicle; B and C) two different gel phases; D) liquid-disordered phase (liquid crystalline); E) liquid-ordered phase (and if the red areas represent cholesterol or glycosphingolipids than this called a raft structure); and F) multi-lamellar structure. The three structures in the middle represent lamellar phases [13-15].

The varying lamellar layers include differing mixtures of solid and liquid phases and are generally defined as solid-gel structures, liquid-disordered, or liquid-ordered phases (Figure 2); the two gel phases differ from the liquid-disordered phase due to the effects of temperature whereas the liquid ordered phase is an example of an extra component being added, such as cholesterol [6, 14]. A bilayer's adopted phase depends on each lipid's structure, head-group, and tail saturation, as well as the surrounding solution's pH, ionic strength, temperature, and concentration [6, 16].

1.2.4. Common lipids

Mammalian lipids can be separated into three major categories, sterols, sphingolipids, and phospholipids; classified further depending on their headgroup hydrophobicity or hydrophilicity, tail length, and saturation [4]. Glycero-phospholipids equate for approximately 40-60% of the total lipid content of bilayer membranes, while cholesterol and sphingolipids equate for approximately 35% and 10-20% respectively [17, 18].

The most common lipid headgroup in nature, also used in the model membrane of this thesis, is choline. In the case of a glycerophospholipid, the headgroup is attached to two fatty acid chains through a phosphate and then glycerol group; glycerophospholipids are typically named by ‘*phospho*’ followed by the headgroup, such as ‘*choline*’; phosphocholine (PC) can be observed in Figure 4 detached from the glycerol and fatty acid chains [6].

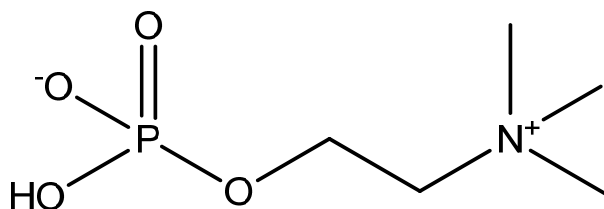


Figure 3: The phosphocholine group structure.

Phospholipids can either be zwitterionic due to the phosphate being negatively charged and the positive charge coming from their nitrogens, like a phosphatidylcholine or phosphatidylethanolamine.

Other predominant glycerophospholipids headgroups include phosphatidic acid (PA), phosphatidylglycerol (PG), phosphatidylethanolamine (PE), phosphatidylserine (PS), phosphatidylinositol (PI); PC, PE, PS, and PI [19]. When considering the lipids for this study, the choice of lipid was limited based on predominance (Figure 4).

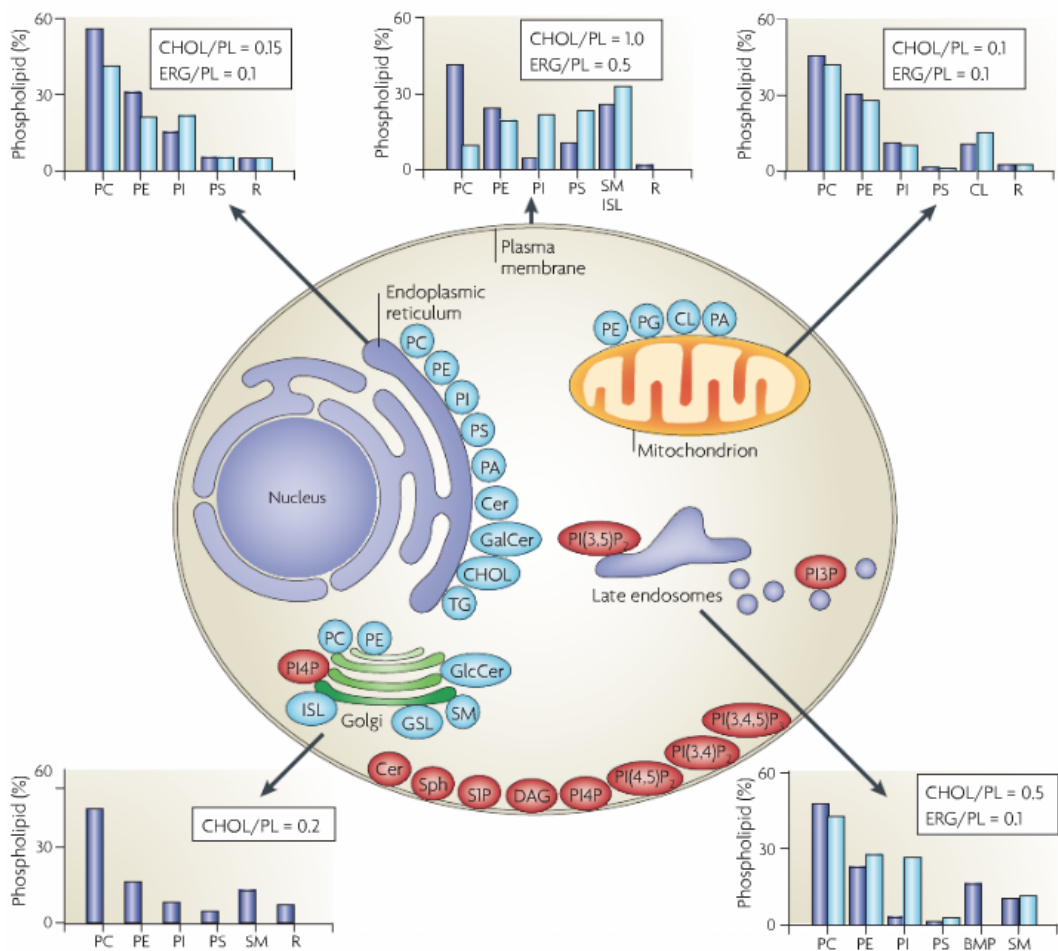


Figure 4: Composition of lipids in various areas of a mammalian cell.

This diagram indicates the various types of lipids which are found in cellular or organelle membranes. Graphs representing the frequency of particular lipid head-groups in various organelle membranes are presented, in order from top left to bottom right, as follows: endoplasmic reticulum; plasma membrane; mitochondrion; Golgi Apparatus; and endosomes. The acronyms of the various lipids are found in 1.2.4, however, those not stated in 1.2.4 are 'R', 'SM', 'ISL', 'CL' and 'BMP', which stand for sphingomyelin, inositol sphingolipid, cardiolipin, and bis(monoacylglycero)phosphate respectively. Reproduced from van Meer, Voelker, and Feigenson [2008],

Reprinted by permission from Macmillan Publishers Ltd: Nature Reviews Molecular Cell Biology (van Meer, G., D.R. Voelker & G.W. Feigenson, Membrane lipids: where they are and how they behave. 9(2): p. 112-24), copyright (2008).

1.3. Model membranes

1.3.1. Requirements of a model membrane

In 1972 the fluid mosaic model was first proposed by Singer and Nicholson, describing the membrane structure, however, studies contrasting lipid properties and introducing bilayers began with Gorter and Grendel as early as 1925 [19-23]. Model membranes are used to systematically represent natural biological membranes while limiting the composition and specific components included within the membrane [24-27]. Furthermore, by using model membranes, proteins located in intracellular membranes can potentially be accessed and the number of proteins in any given membrane can be controlled [28]. A key requirement of a model system architecture when electrically studying membrane pore, peptide, or protein transport properties, is that it should possess the ability to be a barrier. By preventing the leakage of an analyte between the inner and outer environment, protein function can govern the transport processes using a controlled route [29]. By selecting particular lipids, the fluidity, thickness, lipid packing, density, and surface charge can be controlled, which is important in nature to not distort protein structures [4, 19]. Subsequently membranes should contain some lateral mobility and fluidity to allow for the incorporation and proper rearrangement of proteins and other molecules [19, 29, 30].

1.3.2. Supported BLMs

Supported lipid bilayer membranes were developed to improve upon the stability of membrane-based experiments while also enabling new modes of analysis [30-32]. Fabrication and characterisation quickly began on surfaces which would allow membranes to self-assemble, be able to withstand varying physical and chemical conditions, enable electrical testing, and allow protein and peptide incorporation [32-34].

In general, the term Supported Lipid Bilayer (SLB) includes bilayer membranes which are directly in contact with smooth hydrophilic surfaces. These surfaces are known as solid supports and can be made from mercury, mica, silicon, and Template Stripped Gold (TSG) [21, 35]. After monolayer deposition, SLBs are completed by the deposition or fusion of lipids or vesicles onto one of the aforementioned substrates [35].

The space below an SLB is important as, apart from protecting the metal surface from the electrolyte solution, it controls the surface charge, which partly determines the reservoir's performance. The spacer below the membrane can be formed from a number of different moieties (such as esters and ethers) and has a defined length, all of which determines the stability as well as properties of the membrane [32, 34, 36]. The sub-membrane space is generally filled with a semi-ordered water layer and has a higher viscosity and lower di-electric constant than bulk water [33]. Depending on the density of the support, there may or may not be enough space below the membrane for a protein to express or operate correctly and laterally diffuse [33, 35].

1.3.2.1. General properties of tethered Bilayer Lipid Membranes

Tethered Bilayer Lipid Membranes (tBLMs) refer to a membrane architecture which is raised from a support-substrate using a mono-molecular tether (Figure 5).

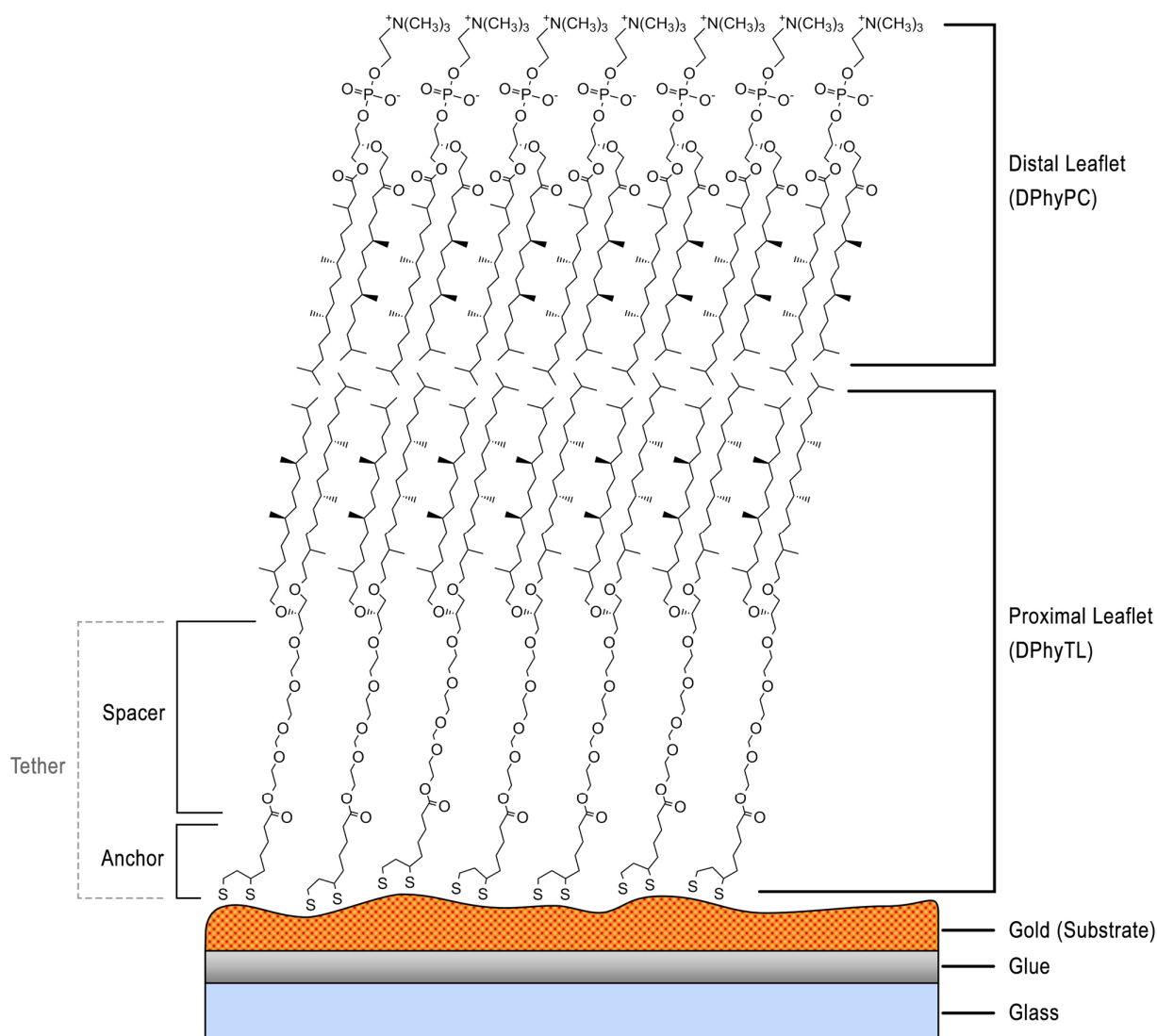


Figure 5: A schematic of a DPhyTL-DPhyPC bilayer formed on Template Stripped Gold.

In the case of the DPhyTL-DPhyPC bilayer, the general thickness the gold is 50nm, the proximal leaflet including the spacer is approximately 4.7 nm, the distal leaflet is approximately 3.5 nm, while the roughness of the gold is approximately 0.1-0.5 nm [37-39].

Generally, tBLMs have a defined composition, retain bio-mimetic properties, are utilisable in conductivity experiments, and have a crystalline or semi-crystalline arrangement; these are all properties that polymer-cushioned bilayer lipid membranes typically lack [29, 33, 40, 41]. tBLMs can be stable for months at a time, are robust during mechanical solvent mixing of solutions, and do not require elaborate stabilising or destabilising molecules to form; these are common in other systems and are unwanted impurities within the hydrophobic interior [29, 42, 43].

To achieve a stable tBLM with a strong resultant membrane-protein capacitive and resistive current during testing, the lipid bilayer must be sufficiently flexible and defect free to aid channel transport efficiency, with a lipid-liquid interface existing on either side [40, 41]. Attaching through an anchor which binds rigidly to surface metal atoms, the tether interposes the support and the lipid bilayer (Figure 5). The tether, which raises the membrane from the hydrophilic surface, is typically anchored to the support via sulfhydryl, di-sulphide, or silane groups, depending on whether the substrate is gold, mercury, silica, or glass [29, 33, 41]. The roughness of the metal support can cause issues with bilayer formation and rearrangement and as such should be atomically smooth [33, 40].

A tBLM monolayer is commonly completed to a bilayer using liposomes [33, 42, 44, 45]. For this, the density of tethers across the surface must be high [42]. In some cases the monolayer covering the surface requires a lesser density when spacer molecules are included in the mixture, generally in the form of short alkyl chains, which are not to be confused with the spacer of the tether, described in Chapter 1.3.2.4 [41, 46]. It is believed that a lower fraction of the tethered lipids or tethers improves mobility of the lower-leaflet, mimicking physiological conditions more accurately than a rigid tethered surface [40, 47]. A typical molecule tethered to a substrate surface which also accommodates two phytanyl chains is equal to approximately

65 Å² in area while DPhyPC, used to complete the upper leaflet, requires an area of approximately 50 Å² [48, 49].

1.3.2.2. tBLMs: The metal substrate and its preparation

Gold is typically used as it is a noble metal which is inert [50]. Depending on the method of preparation, the surface can be controlled when produced via one of three methods: sputtered TSG; evaporated TSG; or polished Au(111) [51].

Cleaning gold surfaces is important to decrease variation and errors in experiments. Ozone in some cases is used to clean the gold surface, however, in the case of TSG Electrochemical Impedance Spectroscopy (EIS) investigations, a basic-piranha wash (Chapter 2.2.7.1) of the silicon prior to gold deposition is generally sufficient and does not etch the surface, which is a common problem with gold ozone treatment [43, 50, 52-57]. When performing cyclic voltammetry on Au(111), another form of substrate cleaning, voltage cycling, is required [58]. Voltage cycling needs to be completed sparingly and with care, as it can damage the surface. Fischer et al. [2009] describes several cleaning processes in detail, however, no other processes described in that paper were used within the boundaries of this thesis.

Mercury-supported membranes are advantageous too, owing to their defect free properties, high mechanical stability, resistance to electric fields, and reproducibility, however, gold-based tBLMs are used in this thesis as gold is safer to work with and is equally capable of forming the required tBLMs [33].

1.3.2.3. tBLMs: Part 1 of the tether - The anchor

Tethers and anchors are parts of specifically synthesised lipids involved in anchoring a molecule to a substrate to form a densely packed organised surface (Figure 5) [29, 33, 42, 59]. The length of the anchor and the spacer together determine the length of the tether [42]. Various tethers include: sulfhydryl; disulphide (with lipoic acid); benzyl disulphide; chlorosilane, chlorodimethylsilane; trichlorosilane; and alkoxy silane groups [29, 33, 42]. From the list above, alkanethiol lipids are commonly used for mercury and gold substrates whereas the last four are specific to silicon dioxide substrates [59].

Depending on the source of information, the anchor is either covalently or semi-covalently linked to the rest of the lipid molecule [29, 40, 59]. Disulphides, unlike thiols, do not oxidise on storage or cause di- or poly-merisation [42]. Overall, the anchor directs the lipid molecule hydrocarbon tails to be pointed away from substrate and toward the buffer solution above the membrane [33].

1.3.2.4. tBLMs: Part 2 of the tether - The spacer

The spacer linkage is about 14 Å long and is a dynamic interfacial region which affords significant control over membrane properties [37]. The spacer region, in the case of DPhyTL-DPhyPC tBLMs, compensates for surface roughness effects and prevents proteins, peptides, or channels from touching the substrate surface [29]. Furthermore, the spacer region creates a gap below the membrane which becomes an aqueous space (Figure 5), therefore both the buffer and respective ions have an area in which they can be transported into [42]. In general, by controlling the structure of the spacer moiety, the aqueous region's suspension and properties can be changed significantly [29].

The length of the spacer is critical as the effects caused by steric repulsion define the bio-mimetic properties of the membrane [60]. Zolk et al. [2000] indicated that short (two)ethylene glycol chains exhibit protein resistance, as do tri-ethylene glycol moieties, however, the same study also found that conformation plays a significant role too, stating that alpha-helical membranes are more inert regarding protein adsorption than all-trans conformers [60]. A longer tether allows for more space for proteins with extra-membrane regions to overcome steric hindrances and embed correctly while also increasing the mobility of ions and relaxing packing restrictions [42].

tBLM spacer hydration is also important when considering tethered systems as the tether hydration determines the effect of the tether on membrane-embedding molecules and ion transport. The answer lies within the tether's chemical structure and its subsequent conformation [33, 40]. The chemical structure determines the interfacial electric field and its interaction with the metal support below; when extended the hydration is expected to be high whereas when coiled into an alpha helix the hydration is expected to be low [33]. With respect to this thesis, in the case of DPhyTL, the hydration is known to be lower under positive potentials, increasing with more negative potentials before the anchor desorbs [33]. In general, the hydration of polyethyleneoxy moieties of thiolipids anchored to substrates is low [33]. Extra-membrane domains typically require considerable space on the respective sides of the bilayer, and as such typically only smaller ionophores such as Valinomycin and gramicidin are used with tethered systems instead of larger peptides or proteins, however, it has also been shown that increasingly complex proton pumps can incorporate into gold-supported lipid bilayer membranes, these include Cytochrome-C Oxidase and F_0F_1 ATPase [33]. As such, it can be concluded that, electronically, the proportions of the spacer have a significant effect on the structure, bio-mimetic abilities, and overall resistance of the membrane.

1.3.2.5. Bilayer Formation

There are two common methods of forming DPhyTL-DPhyPC membranes: vesicle deposition and solvent exchange. Vesicle deposition is advantageous in that it commonly uses less material than solvent exchange to form a complete and dense monolayer, however, solvent exchange can be completed in a fraction of the time required for vesicle deposition. Vesicle deposition occurs by preparing lipid-based vesicles in a solution, commonly water with or without salt. The vesicles, once prepared to a specific size by utilising a combination of vortexing, sonication, heating, and extruding, are introduced to a system with a pre-prepared monolayer. After being left to incubate for a length of time (between eight and 18 hours), the newly formed bilayer is rinsed with salt or buffer solution and left ready to use [44, 61]. In solvent exchange, lipids are dissolved into a solution in which they are miscible, injected into a cell, and after one to two minutes a buffer solution is flushed through the cell, forming a bilayer membrane [42].

1.3.2.6. Why branch the lipid tails

tBLM membranes have previously used either saturated or unsaturated alkyl chains as tails [29]. The tail effects the temperature which the lipid transitions at; in the case of DPPC the transition temperature is 41.5 °C whereas for DPhyPC the transition temperature is -81.9 °C [62, 63]. Lipids with higher transition temperatures typically require increasingly complex experimental conditions during experiments. One commonly used example of a branched lipid is DPhyPC, which is found in extremophiles or archaea bacteria to stabilise fluid membranes in harsh environments [8, 29, 62]. The branching of the lipid's chains has been shown to be a strong determinant of resistance to thermally induced trans-bilayer migration within a liposome as well as improved thermal stability [64]. It is also suggested that the phytanyl residue strongly interacts with neighbouring lipids to prevent optimal chain packing and effect lipid flip-flop [64].

1.4. Proteins

Pores, channels, peptides, and proteins allow compartmentalised systems to interconnect using mediated and non-mediated leakage of ions and molecules, controlled by the bilayer membrane. Biological channels, peptides, and proteins commonly translocate H^+ , Na^+ , K^+ , Li^+ , Ca^{2+} , and Mg^{2+} [65, 66]. Bio-mimetic surfaces take advantage of translocation by employing either pores, channels, peptides, or proteins.

The following experiments within this thesis use the peptide Valinomycin as well as the protein HvBot1, where Valinomycin is a small non-specific cation transporter and HvBot1 is a large non-specific anion transporter (Figure 6 and Chapters 1.4.2 and 1.4.3).

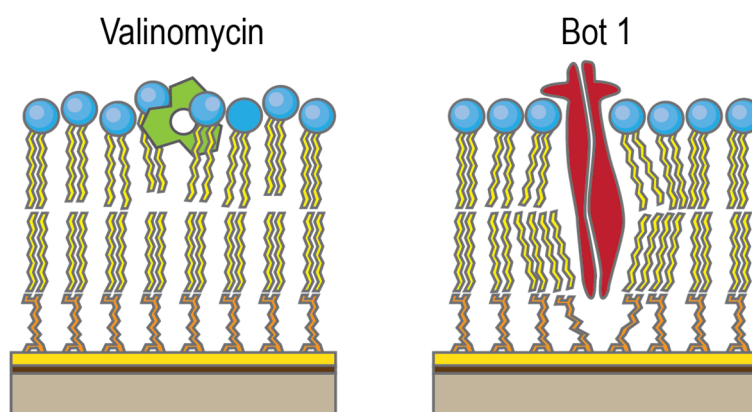


Figure 6: A DPhyTL-DPhyPC bilayers with an incorporated Valinomycin peptide and HvBot1 protein.

tBLMs are able to host proteins, making them responsive to molecules of interest. A number of peptides and proteins have been used previously; Valinomycin, Gramicidin [40], α -Hemolysin [67], M2 [68], BK or Maxi-K [40], M2delta [40], MscL [40], and Cytochrome-c Oxidase [69], with varied success. Typically peptides incorporated into tBLMs are known to have a conductance which is between a third and a tenth of that found within normal vesicles [40].

1.4.1. Peptide, Proteins, and Pore Stabilisation

Membrane proteins, being amphiphilic, anchor to and float within membranes and can be considered a source of internal surface tension [7, 41]. For a protein to embed, there is a dynamic process between nucleation defects and the energy needed to form the pore [70]. Protein's and peptide's inter and intra-electrostatic interactions alter the thermodynamic membrane properties making their abilities co-dependant on the properties of the lipids and phases contained within the membrane [41]. General considerations taken into account when pores are formed include: 1) membrane tension created when a peptide binds causing membrane thinning or thickening; 2) pore formation dependent on critical peptide concentration, peptide orientation, and lipid type; 3) the stress created by introducing a peptide to a membrane created by increasing membrane area, this is sometimes called the internal membrane tension because it does not exert a force at the membrane boundary; and 4) all peptides first bind to the head group region of the membrane before some, or all, peptides, depending on the binding free energy, relocate into the membrane, causing a change in free energy. The change in free energy during pore interactions can either be positive or negative, influencing the ratio of peptides that relocate. A negative binding energy thickens the membrane but also limits the ratio and local concentration of peptides able to interact to form a pore, whereas a positive free energy change does the opposite [70].

During pore formation and peptide or protein inclusion there is an associated energy cost which varies with hydrophobic mismatch between channel length, bilayer thickness, channel radius, and membrane properties such as thickness, curvature, and associated elastic compression and bending moduli [71]. As such, irrespective of the sequence, structure, or oligomerisation, pore-induced peptides increase the probability of pore-formation in membranes as well as stabilising pores which appear [7].

1.4.2. Valinomycin

Valinomycin is a common cyclic peptide which is part of a larger group of depsipeptides [72]. The structure of Valinomycin is shown in Figure 7. Valinomycin's lone pairs on the oxygens are found to point into the centre of the ring (Figure 7). Once included in a membrane and but still unpaired with a cation, the oxygens in the ring are tilted out to one side, allowing the lone pairs to interact with the ions in solution [73].

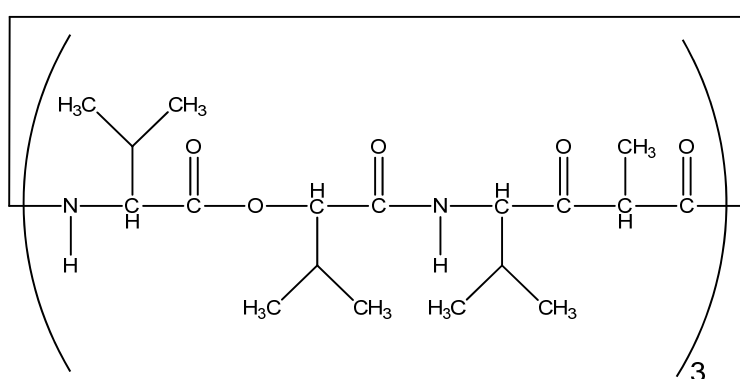


Figure 7: Structural formula of Valinomycin.

Valinomycin is a cyclic peptide made up of three identical series of L-valine, D-hydroxyisovaleric acid, D-valine, and L-lactic acid [30, 74].

Valinomycin's unique flexibility in conformation allows it to discriminate between K^+ and Na^+ before passively transporting the ion through a membrane along a concentration gradient [41, 62, 72, 74-82]. Valinomycin has been shown to have a preference for charged ions in the following order: $Rb^+ > K^+ > Cs^+ > Na^+ > Li^+$ in methanol; according to Eisenman, Krasne, and Ciani [1975], the preference for potassium ions over sodium ions is significant ($\frac{P_{Na^+}}{P_{K^+}} \sim 10^{-4} \text{ to } 10^{-5}$) while Kendall et al. [2010] suggests that Valinomycin has a 200-fold preference for K^+ over Na^+ . [72, 74]. Finally Valinomycin's transport has been suggested to occur through bilayer defects rather than by disorganising a lipid bilayer [76].

Valinomycin does not transport ions without a concentration gradient and as such if both side of a membrane are submerged in the same solution, there is no transport. Electrochemical Impedance Spectroscopy creates a potentiostatic gradient by applying a sinusoidal potential. In the presence of a potentiostatic gradient, also known as transmembrane potential, Valinomycin transports cations such as those mentioned above; it is also aided by a potentiostatic gradient formed during the transfer of ions [82]. Both the on and off states of the Valinomycin molecule are equal in time, suggesting that both phases are kinetically equivalent. Importantly, the action of Valinomycin within a standard DPhyTL-DPhyPC bilayer has been shown as a function of concentration (Figure 8), and this thesis will use 100 mM concentration salt solutions, allowing Valinomycin to transport optimally [72, 73].

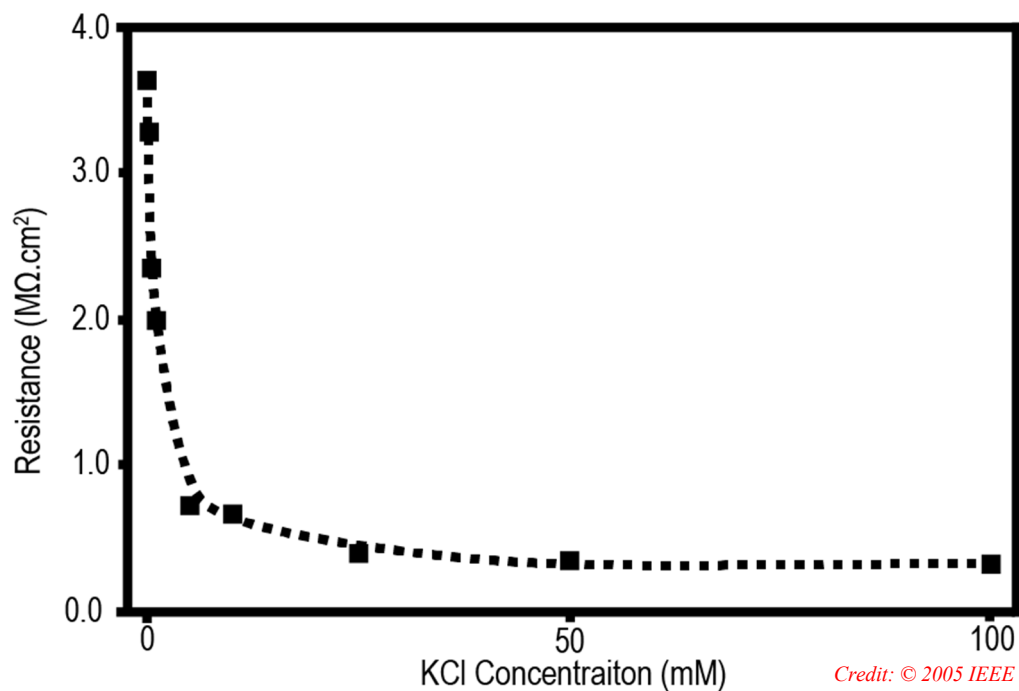


Figure 8: Bilayer resistance as a function of salt concentration.

The concentration of ions in a solution effects Valinomycin transport, however, the effect of ion limitation stabilises beyond 25 mM KCl concentrations. Reproduced from Vockenroth et al. [2005].

Membrane proteins and peptides are commonly introduced into bilayer membranes through one of three methods, from solvent, from doped vesicles, or through cell-free synthesis [84, 85]. The first of the three methods are used most commonly in this thesis. Valinomycin is solvated using ethanol at a controlled concentration before being put into the ionic solution to embed into the membrane [39]. The use of a solvent allows a peptide or protein to introduce directly into a model membrane without the need for vesicles of any kind.

1.4.3. HvBot1

In a separate series of experiments in this thesis, eukaryotic wheat germ-based cell-free synthesis was used to embed a form of the plant membrane transport protein, Bot1, *in vitro*, into a tBLM (Figure 6).

Cell-free synthesis is the process of translating m-RNA into proteins or peptides, directly in a vessel, and embedding the protein into the membrane where it is required. Cell-free synthesis allows for proteins to be produced on mass in the reaction vessel where a pre-formed membrane already exists and is ready for protein incorporation [84]. Originally developed to study transcription and translation processes, this method has been retrofitted to enable experiments of various types and scales [84].

Plant transporters facilitating the transfer of the tetrahydroxy borate anion $[B(OH)_4]^-$ are classified as the 2.A.31 anion exchanger family [86]. Plants typically found requiring this family are able to tolerate both high and low boron concentrations in soils [86]. Nagarajan et al. [2016] studied the barley boron efflux transporter Bot1 from *Hordeum vulgare* (thus named HvBot1), identifying its three-dimensional structure and the molecular basis of permeation. Bot1 is a pore-like plant-membrane anion transporter, which shares a high homology with other

anion transporters and is one of several proteins which control the transport of borate anions, $[B(OH)_4]^-$, across a membrane (Figure 9) in barley plants [84, 86].

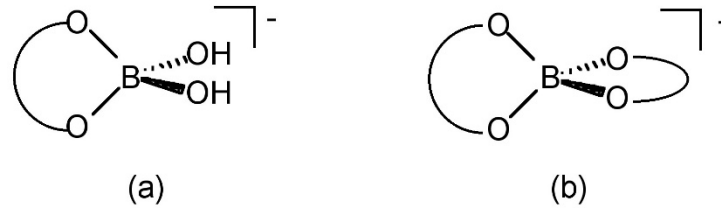


Figure 9: Example structures of borate anions.

Notably, even with successful translation and embedding from mRNA *in vitro* into the membrane using the cell-free synthesis method, the transport of borate may not be recorded as it is co-factor and pH dependent [84, 86]. HvBot1 requires low concentrations of sodium to be present for the protein to function, while for the borate anion to be present in high concentration in solution the pH of the solution needs to be high, 8.5 or above, due to a high pKa value of boric acid, which is 9.24 [60].

1.5. Drugs

Munos, a drug administration record, suggested that drug companies have produced drugs at a constant rate over the last 60 years, with the caveat being that ‘significant therapeutic gains’ have been consistently low [1, 2]. There is growing concern regarding the amount of side effects and adverse reactions that drugs cause; in 2003 it was evidenced that approximately 80 to 95% of all potential therapeutic agents in circulation had poor bio-availabilities and or pharmacokinetic properties, potentially adding to burgeoning healthcare costs [1].

As a part of drug manufacture, approximately 60–70% of all drugs released in 2006-2008 were designed specifically to target membrane bound proteins [1-3]. And yet, few tests are being undertaken to understand how drugs targeting a membrane-protein or channel affect the membrane itself [87]. With the focus on proteins, genetics, and computer algorithms, lipid research is underrepresented, understudied, and little is known about drug-lipid and drug-lipid-protein interactions [88-90].

1.5.1. Drug-membrane research historically

Membrane-related drug research dates back to the early 1900s where Myer and Overton initially researched the effect of drugs and narcotics on membranes; since then, drugs have been found to act via a number of processes by which they can interact [71, 91, 92].

The main-stay topics of drug-interactions with membranes include: pore occlusion by binding to the binding site; alteration of function by binding to the membrane and changing the environment and therefore free-energy differences between protein conformities; the binding of drugs to selected sites at the protein-membrane interfaces, resulting in changes to both non-specific accumulation at the protein or bilayer interfaces, affecting lipid-packing; and

membrane-lipid partitioning at the membrane-liquid interface, not only altering the bilayer itself, but also the contribution of the bilayer to its conformational equilibrium [71]. Drug permeability experiments have been completed on many aspects of simplified membranes: looking at solvent effects on phospholipid liquid-crystalline surfaces [93-95]; molecular effects on hydration and order [71, 96-101]; and changes in bilayer bending [102-104] and compression moduli [105-107]. In many of those cases, the membranes were not tested for their viability as viable matrices with active proteins or peptides.

1.5.2. Common drug interactions

Drugs have three key pathways in which they can act on molecular target sites: as endogenous receptors (proteins which recognise a body's own chemicals); macromolecules (enzymes, transport molecules, or nucleic acids); and through lipid-membranes [108-111]. Many drugs are non-specific or multimodal in their action as they can interact in a detergent-like manner, self-associating and binding with the membrane causing disruption and solubilisation [16, 112]. Common drug-membrane interactions observed are shown in Figure 10. This thesis will focus on the detergent-like effect of drugs.

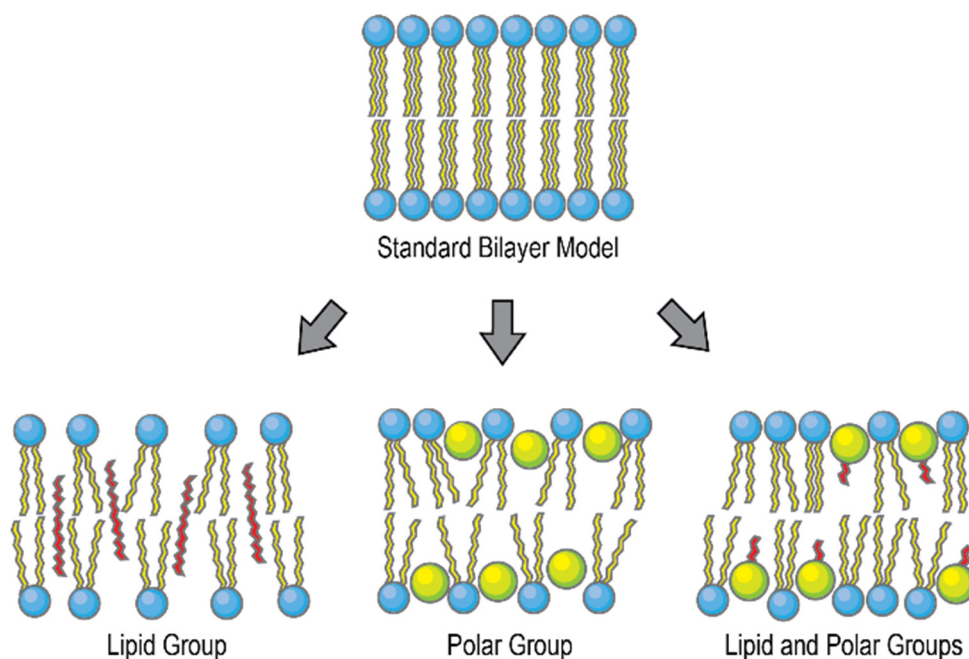


Figure 10: Interactions of penetration-enhancing drugs with intercellular lipid membrane domains.

From left to right: The drug is interacting with the lipid membrane only; the drug is interacting with the head-group region of the membrane; and the drug is interacting with both the lipid and head-group region of the lipid bilayer. Adapted from Williams, and Barry [2012].

1.5.3. Ethanol-membrane interactions

Ethanol, which traditionally was used as an anaesthetic, is commonly used to improve transdermal interactions of creams, medicines, and other chemicals [113-116]. Many reports state the physiological and biochemical effects of ethanol though to date few papers detail the pathways of interaction with natural membranes [117]. Techniques which have already been applied to simple ethanol membrane research, amongst others, include forms of scattering, calorimetry, spectroscopy, resonance, and reflectometry [118]. Finer details have been investigated using model systems such as bacteria, model membranes, and MD simulations [113-116].

1.5.3.1. General information

Ethanol is a small-amphiphilic molecule which has a profound effect on biological systems [119]. In the 1990s it was indicated that effect of alcohol on a membrane increases as the alkyl chain-length of the alcohol increases, however, the system used in this case used bacteria, which are not representative of a mammalian membranes [120].

A number of drugs exhibit bi-phasic behaviour, including local anaesthetics, tranquilizers, antihistamines, anti-inflammatories, sedatives, narcotics, steroids, peptides, and certain vitamins [16, 100]. An alcohol molecule can position itself in one of five different sites in a membrane: water phase; upper leaflet hydrogen-bonded; upper leaflet; lower leaflet; and lower leaflet hydrogen-bonded. A theoretical study indicated that short and even medium chain length alcohols have been found to permeate the membrane, aligning parallel to the lipid tails, and mostly hydrogen bonding with the phosphocholine group while also interacting with the lipid tails to a lesser extent. As such ethanol is the most widely employed drug for enhancing the permeability of other drugs [114].

1.5.3.2. Headgroup interaction

Short chain alcohols are known to interact with the head-group regions of lipid bilayers, forming hydrogen bonds between the phosphate and carbonyl groups; it is suggested that this effect is the direct cause of a membrane's increase in elasticity, fluidity, and permeability generally observed with alcohols [117]. These changes are typically referred to as changes in bilayer mechanics, as they concern changes in shape and stability of cells as well as liposomes; potentially effecting membrane function [117].

Based on a number of model and bacteria membranes studied using atomic force microscopy, micro-pipetting, and electron paramagnetic resonance experiments, ethanol's

biological effects have been suggested to be caused by the disruption of the aqueous phase at polar sites or through a disordering of the acyl chains; overall the effects of ethanol lead to a fluidising of the membrane [8, 118, 119, 121]. Ethanol PC-lipid phase diagrams indicate that domain formation of bilayers should occur at approximately 3.2 – 5% and that full bilayer interdigitation should occur by 10 – 12%. These results are further complicated by AFM studies which indicate that overnight ethanol incubation creates domains of a similar height which co-exist with the bilayer [118].

1.5.3.3. Induction of various gel-phases

A model system, with increasing temperatures, will go through a number of phases: the highly ordered sub-gel phase; the planar gel phase; the rippled gel phase; and the fluid-like liquid crystalline phase [122].

An AFM study found that the inclusion of an amphipathic molecule can induce the interdigitated planar gel phase and replace the rippled gel phase transition; at the same time the opposing monolayer can interdigitate, decreasing the bilayer thickness [122]. The longer the chain, between 1-4 carbons, the greater the tendency to induce the alternative phase-change pathway [122]. It was also suggested that the difference between 1 and 2-propanol's branches causes greater steric hindrance which leads to poorer induction of the integrated planar gel phase [122].

As a side note, during the induction of molecules such as tetradecanol, the molecules insert asymmetrically causing local thinning by drawing both leaflets together to allow the tetradecanol to span the whole hydrophobic core of the membrane [116]. As such, one indirect effect of ethanol is the change in the possible gel-phase change of the distal monolayer. A pure bilayer has previously been shown to have a thickness of approximately 1.8 nm in each

direction from its centre and ethanol shifts the thickness to as low as 1.6 nm, suggesting an increase in area per lipid [115].

In the case of MD simulations on PC and PE model membranes, at 12%_{mol} ethanol, the bilayer underwent expansion, the thickness decreased, and there was an enhancement in the interdigitation of the acyl chains [114]. This effect was stated to be similar to that of DMSO, which decreases the rigidity of the membrane [114]. The same study concluded that at higher concentrations of ethanol, the bilayer's lipids tended toward an irregular inverse-micelle structure in the interior of the membrane with water or ions being trapped in small pockets, depending on the experiment; DMSO did not have this tendency [114]. In the same vein, DPPC bilayers increased their area per lipid by 7% for ethanol [115].

A key interest in ethanol-membrane studies is whether an alcohol forms hydrogen bonds with the leaflets [115]. Theoretical studies indicate that the interaction of a drug with the membrane is, in part, determined by its polarity and how energetically favourable the bond with the surrounding solution is in comparison to the bilayer. For example, because ethanol is less polar than methanol and it has an ethyl group, it can interact with both the headgroup as well as tails of a phosphocholine lipid. On the other hand, methanol does not form hydrogen bonds with lipids as it is energetically favourable to bind with water and, due to its polarity, methanol rarely interacts with the lipid tails as it would do so in small clusters with water [115]. Therefore, ethanol is able to cross from one leaflet to another, however, the exact position of ethanol, and its retention, is yet to be experimentally clarified [115]. Notably, if ethanol was to hydrogen bond with the membrane's surface, the membrane potential would change due to a rearrangement of the P-N angle of the head groups of a membrane which would result in a net change in dipole moment at the surface; this kind of rearrangement and change is not typically observed theoretically and as such gel-phase interactions require further study[115].

It has also been suggested that ethanol decreases the bending modulus of the bilayer, whereas longer chain 1-alkanol alcohols have been shown to stiffen bilayers [116]. Other molecules stated to have a similar relationship are ketones and other amphipathic molecules, demonstrated through biological activity and organisms [120]. The amphiphilic character of alcohols has been shown to change the interaction within a membrane, with each new CH₂ unit added to an alcohol molecule leading to a further decrease in surface tension, known as Traube's Rule; having a significant effect on the membrane [115].

An ethanol molecule's permeability coefficient in bacteria, yeast, and rabbit cells can be as high as 10⁻⁴ cm.s⁻¹, whereas water's permeability in the same systems is approximately 10⁻³ cm.s⁻¹ [8, 119]. On a similar note, one should consider the dehydration due to ethanol, which effects the waters' dipole orientation and the electrostatic potential across the membrane; it has been show that both are only slightly affected. Simulations suggest that the effect of ethanol is greatest specifically through concentration and hydration. This balance effects the regime of the lipid molecules and therefore the order parameter, however, the effects are only gentle, supporting the suggestion of non-specific binding of ethanol [115].

1.5.3.4. Alcohol-membrane interactions with bacteria

Yeast cells often need to survive and function in solutions where ethanol concentrations reach 10%_{v/v} or more [117]. Live bacteria left in ethanol environments were shown to have a higher number of saturated lipids, sterols, and transmembrane lipids, as compared to their glycerophospholipid counterparts. Bacteria which were still able to grow in environments with 25 g.L⁻¹ of ethanol had increased membrane fluidity, however, the representative study stated that this outcome did not show a correlation between fluidity and composition directly [8]. It is suggested that bacteria which are able to survive in these environments must have other mechanisms to deal with the increased ethanol [8]. In fact, using transcriptomic analysis, the

reaction to ethanol of bacteria indicate that bacteria focus on fluidity changes by increasing biogenesis, osmoregulation, expression of heat shock proteins, carbohydrate transport, glycolytic enzymes, protein turnover, and sometimes sporulation; again leading back to focusing on membrane changes [8].

1.6. EIS and membranes

Within SLB research, EIS research has become increasingly popular for interpreting *in vivo* lipid bilayer membrane changes under *in vitro* conditions. EIS is able to monitor membrane properties with spatial variation and is commonly used in conjunction with neutron diffraction, capacitance measurements, fluorescence, as well as a number of electrochemical techniques [123, 124].

1.6.1. EIS theory

At its core, EIS studies focus on the relationship between electrical responses and system properties. The data collected is interpreted using Electrically Equivalent Circuits (EECs) that model the collected responses which, in conjunction with other data, allows EIS data to be translated into physical changes. The EEC defines the membrane as discrete electrical components which respond to the applied sinusoidal potential. The details collected from the changes can be detailed either quantitatively or qualitatively, though more often qualitatively, into molecular layers, defects, packing densities, distances, and molecular motilities.

By comparing periodic Voltage waveforms with the resultant steady-state current, in the time domain (Figure 11), the immittance, or overall output of a system, is studied.

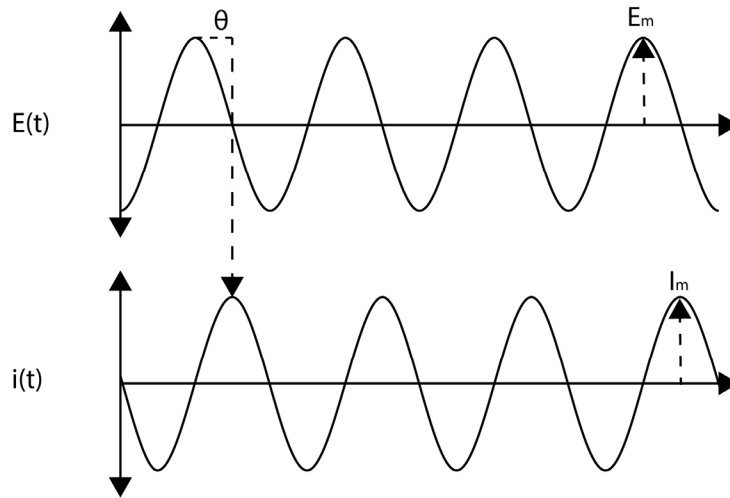


Figure 11: Example sine wave of applied potential and the response of current.

The equations supporting $E(t)$ and $i(t)$ are found under Equation 1 and Equation 2.

Equation 1: Output Voltage as a function of time.

Note: ω is angular frequency, θ is the phase difference between the input voltage and output current, and the subscript 'm' the maximum values of the respective monochromatic signals (Figure 11) [125].

$$E(t) = E_m \sin(\omega t)$$

Equation 2: Output current as a function of time.

$$i(t) = I_m \sin(\omega t + \theta)$$

Studying Equation 1 and Equation 2, it can be observed that a purely resistive component, which has a θ of 0, is not affected by angular frequency, whereas capacitors have a θ between 0 and $-\pi/2$, requiring further investigation.

The impedance of a capacitor can be observed in Equation 3.

Equation 3: Capacitive output current as a function of time.

Note: C is the capacitance.

$$i(t) = \left[\frac{dE(t)}{dt} \right] C$$

This differential equation (Equation 3), and its respective voltage equivalent which is not shown as it relates to inductance, can be simplified using Fourier transform (Equation 4).

Equation 4: Fourier transform of capacitive output current as a function of angular frequency.

Note: $j = \sqrt{-1} \equiv e^{j\pi/2}$.

$$i(j\omega) = C\omega jE(j\omega)$$

With rearrangement, Equation 4 can be represented as Equation 5, where the impedance of a capacitive system is observed.

Equation 5: Complex impedance as a function of frequency.

Where $Z(j\omega) = 1/C\omega j$

$$Z(j\omega) \equiv Z(\omega) = \frac{E(\omega)}{i(\omega)}$$

This impedance can be represented as a planar vector on the argand plane (Equation 6).

Equation 6: Rectangular and polar coordinates of impedance.

Note: Z' is real and Z'' is imaginary as you rotate around the unit circle [125].

$$Z(\omega) = Z' + jZ''$$

Therefore, the vector magnitude can be expressed as a root of the sum of the squares:

Equation 7: Modulus of complex impedance.

$$|Z|(\omega) = \sqrt{([Z'(\omega)])^2 + ([Z''(\omega)])^2}$$

The angle of the planar vector on the argand plans is shown in Equation 10, by replacing the coordinates in Equation 6 with the rectangular coordinates: Equation 8 and Equation 9.

Equation 8: The real component of impedance as a rectangular coordinate.

$$Z' = |Z| \cos \theta, \text{ and}$$

Equation 9: The imaginary component of impedance as a rectangular coordinate.

$$Z'' = |Z| \sin \theta$$

Equation 10: The phase difference between the real and imaginary components.

$$\theta(\omega) = \tan^{-1} \left(\frac{[Z'(\omega)]}{[Z''(\omega)]} \right)$$

As such, using EIS experiments, the alternating current waveform is varied in frequency to explore sequential time domains which are collected as respective impedance points and used later to model the immittance of the system.

1.6.2. Applying EIS to tBLMs

Electronically, a bilayer is an insulating surface isolating charges like a parallel plate capacitor; this capacitive property is further reinforced by the capacitive effects of the tether and substrate [42]. When membrane testing with EIS, during a charging cycle charge is transferred to the bilayer while during discharge, over milliseconds, seconds, or minutes, the charge transfer, due to decreasing voltage, simultaneously discharges the membrane and charges the tether-gold region [42]. These relationships reflect the phase-difference between Voltage and current of tBLMs, where the current lags behind the voltage by up to 90 degrees [42]. As such, a bilayer can be viewed electrically as both electrically resistive and reactive [126]. An appropriate EEC should realistically mimic cellular membrane resistance and capacitance values [47]. A standard bilayer membrane has the following properties: a resistance of between 0.01-1 $\text{G}\Omega\cdot\text{cm}^2$ and a capacitance of approximately 0.1-1 $\mu\text{F}\cdot\text{cm}^2$ [35, 47]. Such electrical properties are applicable to EIS testing frequency ranges, as the time domains of interest are microseconds or greater and electric fields can interact with a surface in two principal ways: 1) the reorientation of dipole electrical moment within defects and 2) translational motion of charge carriers [125].

In a non-exhaustive literature search, tBLM studies applied EECs to membrane formation [29, 39, 46, 62, 69, 76, 77, 127-130], during patterning [131-134], when testing ion carriers such as: Valinomycin; H^+ -ATP-synthase; M2; cytochrome-C oxidase; and α -haemolysin [30, 68, 69, 73, 77, 130, 132, 135-137]; and when comparing the effects of bias potentials on membranes [137]. Where most circuits involve a few RC meshes, some more elaborate RC-mesh circuits are also used and are in some cases hard to relate physically (Appendix Chapters 6.1 and 6.2 include further details).

1.6.3. Common electrical elements in EECs

The application of EIS is neatly explained by Becucci, and Guidelli [2014]. When applying an AC potential of amplitude E and frequency f , to a resistor with resistance R , a current is found to be equal in frequency and amplitude and proportional to V with respect to R ; as such the impedance of a resistor can be defined as Equation 11.

Equation 11: Impedance due to a resistor.

$$R \equiv Z_R \equiv |Z|, \text{ where } \theta = 0$$

When applying the same current to a capacitor with capacitance C , the current emitted, i , will continue to have a frequency of f , an amplitude of $2\pi fC$, and a phase shift of $\frac{-\pi}{2}$ with respect to the voltage, shown by Equation 12.

Equation 12: Impedance due to a capacitor.

$$Z_C = \frac{1}{j\omega C}, \omega = 2\pi f$$

During EIS experiments in some cases the response of the surface is not quite capacitive, in which case a CPE element is required; further details are explained in Appendix Chapter 6.2. A Constant Phase Element's (CPE) impedance can be described using multiple forms, where one common one is described with Equation 13.

Equation 13: Impedance due to a CPE.

Note: Later in this thesis n is referred to as alpha, due to convention.

$$Z_{CPE} = \frac{1}{Z e^{-\frac{\pi}{2}nj}}, 0 < n < 1$$

A virtual circuit can be combined in several different configurations. Equation 11, Equation 12, and Equation 13 represent the perfect response of physical elements used in EECs. An equivalent EEC can be infinitely complicated to best represent a body of data or surface being tested, however, this is hard to physically define. EECs are often chosen by balancing the emittance and physical representation [125, 138]. When modelling a real system, a system's: equilibrium or steady-state; presence and selection of mobile and immobile charged species; material homogeneity between the electrodes; electrode choice; charge pathways; and electronic components are critically evaluated [125].

1.6.4. Charge pathways applicable to EIS

A surface can be defined through three key parameters: polarizability; blocking or non-blocking character; and reversibility [125]. The first defines the electrical behaviour of the electrode-electrolyte interface whereas the last two define the electro-chemical character of the interface [125]. An electrode-electrolyte interface is non-polarisable if the potential drop across the interface is independent of the current passing through the interface. The current is partially polarisable if it is dependent on the electrode-electrolyte interface potential difference. It is completely polarisable if the current, which is faradaic, is completely prohibited from flowing [125]. A polarisability of a species is either the result of a slow electrode reaction or slow transport action; generally caused by a limiting factor [125]. This thesis will concern itself with slow transport.

For completeness, an example of a slow electrode reaction is a non-blocking but kinetically non-reversible reaction, whereas an example of slow or non-existent transport reaction is diffusion (or chemical reactivity) control [125]. Transport can either be controlled by semi-blocking the charged species passing through the membrane or by a complete halting of any charge exchange across the membrane [125].

Channels, proteins, and peptides within membranes provide a parallel low-impedance pathway for ion conduction, however, unless a sufficient number of channels or transporters exist within a membrane, the membrane-resistance as measured by EIS, is unaffected [47]. Enough pathways per unit area will cause a sufficiently noticeable flux, and due to this flux the membrane resistance decreases [47].

A tBLM is generally represented, with an EEC, as a collection of sections with different dielectric properties (Figure 12) [123].

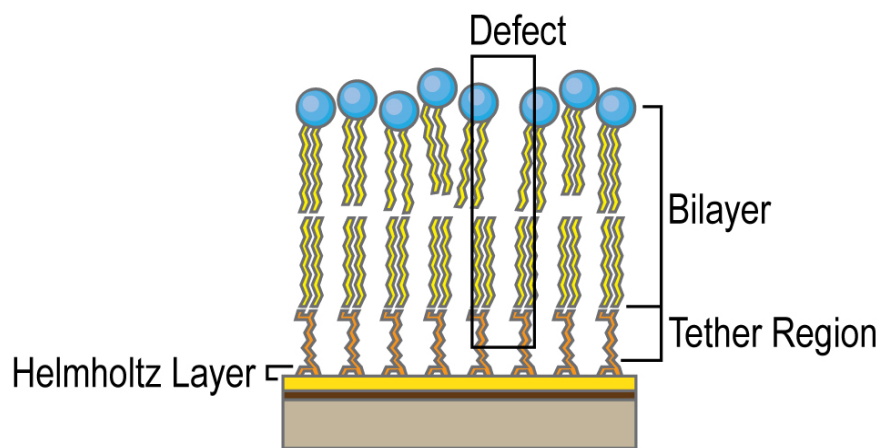


Figure 12: Various areas of a bilayer with different electrical properties.

Each area shown in the diagram above indicates a different set of electrical properties which are, or have been previously, accounted for when applying an EEC to tBLM membranes.

In some cases, as with tBLMs, ions accumulate at the boundaries of adjacent sections, causing a ‘discontinuity’ in the electric displacement vector equal to the product of the electric field E and dielectric constant ϵ . This accumulation effect gives rise to a capacitive current, i_c , which as described earlier, has a maximum displacement of $\frac{-\pi}{2}$ [123]. The total current is therefore the sum of the ionic and capacitive currents. As such, each dielectric section can be emulated with a resistance and capacitance, accounting for both the ionic and capacitive currents. This combination of elements is defined as the RC mesh, where tBLMs can, and have

been, defined through a number of these RC meshes placed either in series or other more complex variations [123].

1.6.5. EEC interpretations

1.6.5.1. The tether

Traditionally, the anchor is represented through either a single RC mesh or an infinite mesh of resistors and capacitors attached in series and parallel; the second example is known as a transmission line (Figure 13). As is discussed in Chapter 6.1, there is a real struggle to determine a model which can undergo strict mathematical analysis, be relatable to the surface it is being applied to, and be statistically as well as physically relevant [138]. A single RC mesh ignores the complexity of defects interacting with the Helmholtz-tether region and combines it into two elements and theoretically should not be used (see 1.6.5.2) [138]. The transmission line, though considered more appropriate, is difficult to model and generally cannot be used. An RC mesh is therefore applied across the board and typically represents the Helmholtz double layer using a capacitor as well as the limited ion transport through the tether's surroundings using a resistor.

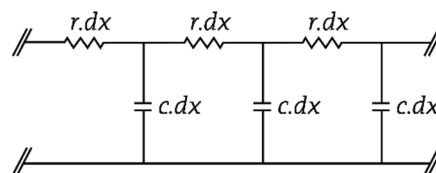


Figure 13: Schematic of a transmission line

This circuit is commonly used to represent the area of the tether in close contact with the substrate, i.e. the metal-water interface and the Helmholtz layer.

The first attempt by Krishna et al. [2003], stated that the sub-membrane space had a significant effect on the measured signal. To account for a change in conductance, Krishna et al. [2003] used a series of ten RC meshes, forming a non-uniform distributed-parameter

network. Questions have arisen whether this distribution is: statistically or physically relevant; adequately describes the electrical impedance features; and is able to predict changes in spectra through controllable defect and geometry parameters [139]. Valincius, Meškauskas, and Ivanauskas [2012] exemplified Krishna et al. [2003]'s paper using bilayer measurements in a two-stage analysis. By first only testing tethered monolayers, the sub-membrane space was measured; once complete, the bilayers were formed on identical tethers and attributed values were compared. Valincius, Meškauskas, and Ivanauskas [2012] note that the monolayer properties could not be resolved from the bilayer spectra to allow separate properties to be directly contrasted [138]. As such, between these two studies it can be assumed that studying the sub-membrane space is difficult. Alternative methods have been proposed and will be discussed in chapter 1.6.5.2.

1.6.5.2. EEC used throughout this thesis

A significant number of studies exist applying EIS to model membranes and defining appropriate EECs which are representative of the membranes they are being applied to. Because the historical nuances are not vital to understanding the data interpreted in this thesis, the detailed analysis of this is shown in Appendix 6.1 and 6.2. This chapter as such, will concern itself with the specific model of choice, shown in Figure 14.

A defect-free tethered bilayer bathed in a salt-buffer solution is theoretically homogenous and thus identical in response across its entire interface, and can be represented by the series EEC, $R_{\text{mem}}-C_{\text{mem}}$ [140]. More accurately, however, membranes tethered to a surface can be represented by the direct series EEC, $R_{\text{solution}}-C_{\text{membrane}}-R_{\text{submembrane}}-C_{\text{Helmholtz}}$, where R_{sol} represents the resistance of the solution between the reference electrode and the membrane, C_{membrane} refers to the capacitance of the membrane, $R_{\text{submembrane}}$ represents the volume between the bilayer and the metallic substrate which the tethers attach to, and $C_{\text{Helmholtz}}$

represents the interface between the metal and buffer solution, although, as soon as a defect is introduced, the perfect series RC response changes [141]. Both examples are missing the effects due to a defect or transporter.

In principle, depending on the size of a defect, a defect reaches across a membrane through to the metal substrate and leaves the area polarisable. This causes the EEC to become a combination of elements represented by multiple RC meshes strung together. Theoretically, a defect, R_{def} , interacts directly with the transmission line as well as resistive solution in the submembrane-tether region, which is non-polarizable. The defect, by definition, is a series combination of R_{def} and Z_{sub} , because the defect likely does not reach through the tethered monolayer as well and the tether is acting like a partial capacitor too. The sealing of the membrane are accounted for with a series combination of the capacitances of the membrane, C_{mem} , as well as Helmholtz layer, C_{H} , as follows: $C_{\text{mH}} = (1/C_{\text{mem}} + 1/C_{\text{H}})^{-1}$.

All told, a series circuit is formed where R_{sol} is in series with a combination of the series R_{sub} and $Z_{\text{submembrane}}$ in parallel with as C_{mH} (Figure 14 - similar to Figure 56).

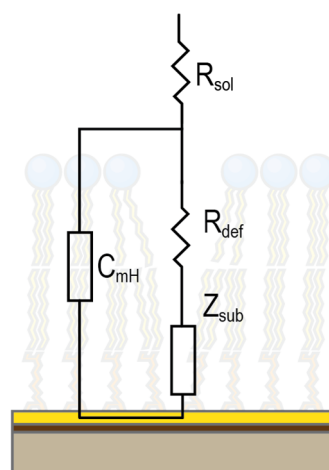


Figure 14: An example of the EEC used to interpret membrane properties.

Based on Valincius, Meškauskas, and Ivanauskas [2012]; this EEC is a specific interpretation of specific elements used when modelling membranes in this thesis.

1.6.6. Plotting EIS Data

Three major key types of plots are used in EIS spectroscopy analysis and presentation: the Bode; Cole-Cole; and Nyquist plots. To a lesser extent, the M^* plot is also used. In this thesis, only the Bode plot will be used; the other three are explained in the Appendix for reference (Chapter 6.3).

The Bode plot displays both $\log |Z|$ and phase angle ($^\circ$) as a function of $\log f$, where $|Z|$ is the magnitude of the impedance (Figure 15) [123]. Depending on the frequency range selected and surface being tested, a Bode plot can show a single-mode, bi-modal, or multi-modal frequency-dependent impedance response. A phase shift of -90 for phase vs $\log f$ plot and a slope of -1 on the $\log Z'$ vs $\log f$ plot indicates the response of an ideal capacitor [130]. Ideal resistors are represented by a low phase difference and horizontal slope [130].

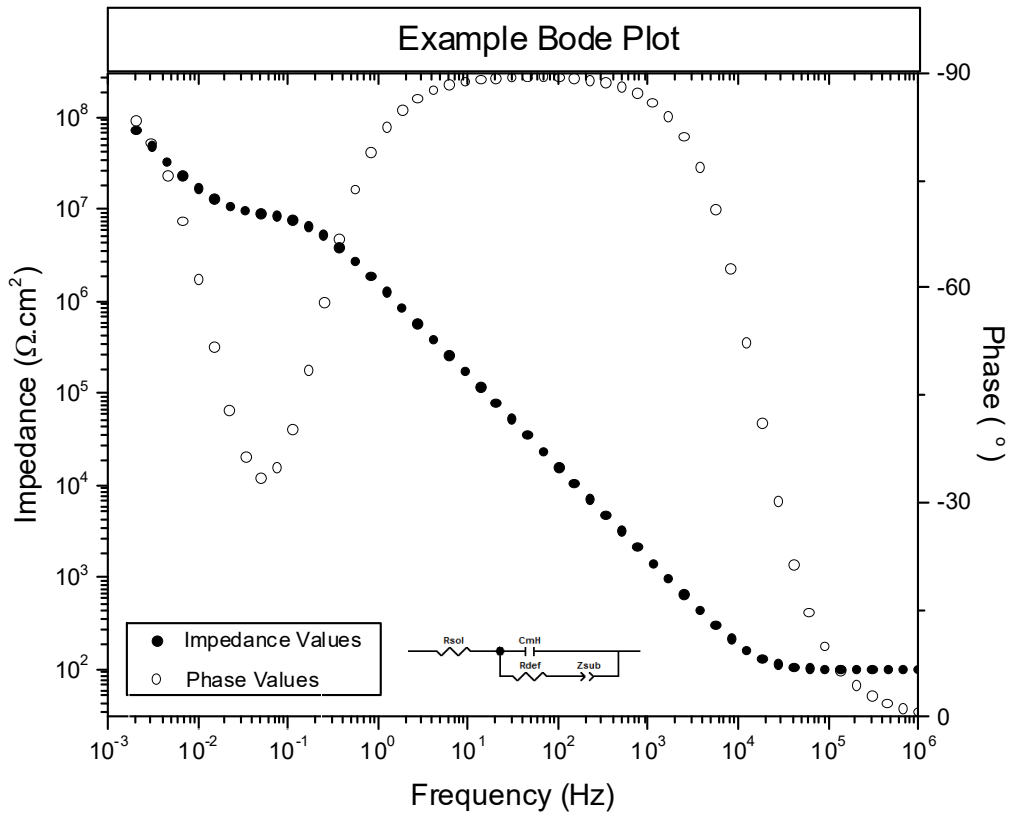
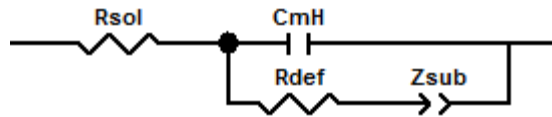


Figure 15: Example Bode plot

Note: This is an example which uses the following EEC (which is used throughout this thesis):



Values applied to the EEC for this example: $R_{sol} = 100 \Omega \cdot \text{cm}^2$; $C_{mH} = 1 \times 10^{-7} \mu\text{F} \cdot \text{cm}^2$; $R_{def} = 1 \times 10^7 \Omega \cdot \text{cm}^2$; $Z_{sub} = 1 \times 10^{-6} \Omega \cdot \text{s}^{-\alpha} \cdot \text{cm}^2$; and $Z_{sub-\alpha} = 1$. Modelling using ZView (version 3.3B Scribner Associates).

1.7. Alternative techniques

Here, EIS is the major analytical tool to probe the properties of tBLMs, however, other techniques are used to elucidate the function and regulation of proteins within lipid structures. Thin layer and column chromatography, Fourier Transform Infrared Spectroscopy (FTIR), Cyclic Voltammetry (CV), Nuclear Magnetic Resonance (NMR), femtosecond Vibrational Sum Frequency Generation (fs-vSFG), and small angle neutron reflectometry are used. In this thesis, apart from neutron reflectometry, the interactions of molecules or molecular positions as well as structures are not directly observed [142].

1.7.1. Fourier Transform Infrared Red Spectroscopy

FTIR is a relatively inexpensive spectroscopic technique, which can be used to detect changes in molecular vibrations of various molecules [143-145]. A key advantage of FTIR is its lack of need for any extra molecular probes or the use of detergents to extract information. FTIR is sensitive to a number of moieties, including choline, due to its sensitivity to νOH and νCH vibrations [145]. Furthermore, due to its similarity to fs-vSFG, FTIR is a fast way to determine which peaks of a molecule may be vSFG active. As stated in Chapter 1.5, drugs interact with and effect head-group region of membranes, and as such, because in FTIR the phosphocholine head group is apparent, FTIR can be considered a powerful diagnostic tool for pre-probing the lipid bilayer membrane [145]. It should be noted that FTIR is able to yield semi-high resolution structural information about the packing of a lamellar crystalline or gel phase surface, however, it will not be used in this way in this thesis [143-145].

1.7.1.1. DPhyTL and DPhyPC spectra

Two major regions are tested using FTIR, the C-O and C-H spectra; the same regions which are used for fs-vSFG. The first key interest is the DPhyTL tails and the second is the choline headgroup of DPhyPC.

1.7.1.2. Lipid Tails

Leitch et al. [2009] specifically details the various vibrations and stretches for DPhyTL. By collecting spectra of benzyl lipoate, tetraethyleneglycol, and DPhyTL, Leitch et al. [2009] deconvoluted the IR spectra (Figure 16) for both the C-O and C-H spectra. During FTIR and SFG analysis, the assignments of the various vibrations are based on the paper mentioned.

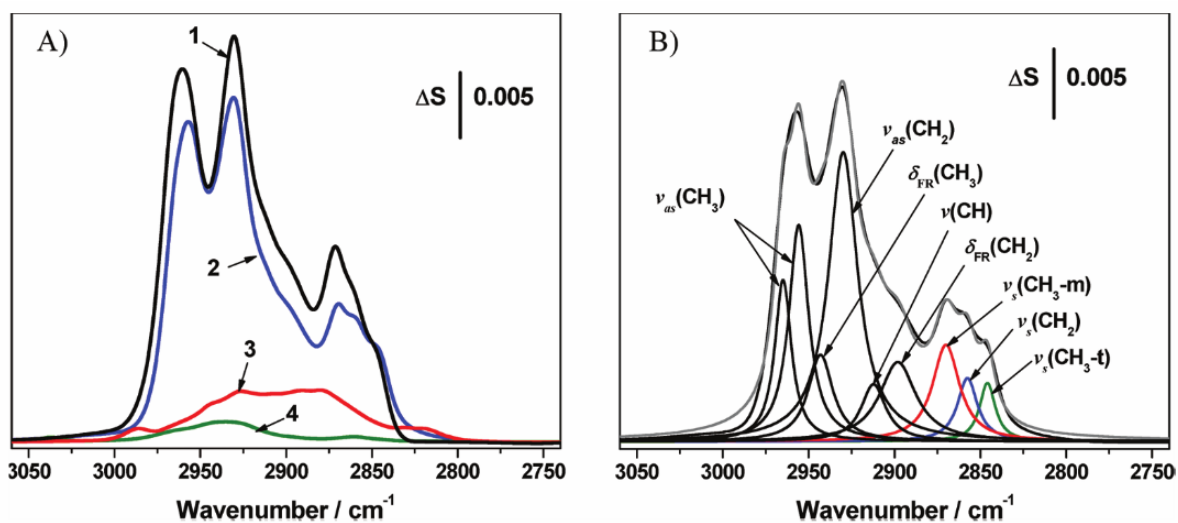


Figure 16: Bulk-DPhyTL FTIR spectrum of the C-H stretching region.

(left) DPhyTL (curve 1, black line), DPhyTL_{d16} (curve 2, blue line), TEG (curve 3, red line), and BLA (curve 4, green line); (right) deconvoluted DPhyTL. All spectra were calculated using optical constants determined from transmission spectra of these compounds dissolved in CCl₄. Spectra reproduced from Leitch et al. [2009].

Reprinted (adapted) with permission from Leitch, J., J. Kunze, J.D. Goddard, A.L. Schwan, R.J. Faragher, R. Naumann, W. Knoll, J.R. Dutcher & J. Lipkowski, *In Situ PM-IRRAS Studies of an Archaea Analogue Thiolipid Assembled on a Au(111) Electrode Surface*. *Langmuir*, 2009, 25(17): p. 10354-10363. Copyright 2009 American Chemical Society.

1.7.1.3. Choline Headgroups

According to Pohle et al. [2001] the choline peak is witnessed as the large peak at 3270 cm^{-1} and is attributed to the OH stretching vibration (Figure 17). The same paper states that any peak higher than that is attributed to the water, which is known to place itself among the phosphocholine head groups, as is seen with the small peaks in the 3370 cm^{-1} region of the DMPC spectrum (Figure 17). In the C-H spectrum, Pohle et al. [2001] states that only one main feature is retained between different choline-based compounds, and that is the ν_{CH} of the nitrogen-bound methyl groups at 3030 cm^{-1} [145]. A number of bands are expected between $2850 - 2950\text{ cm}^{-1}$ regarding ν_{CH} , however, these are strongly influenced by other groups, making it difficult to discern their exact origin [145]. It is suggested that 2852 cm^{-1} is the expected position of $\nu_{\text{s}}(\text{CH}_2)$ and 2921 cm^{-1} is the expected position of $\nu_{\text{as}}(\text{CH}_2)$ [146]. Pohle et al. [2001] also detail $\nu_{\text{PO}_2^-}$ in the 1230 cm^{-1} region, however, this thesis will not detail this.

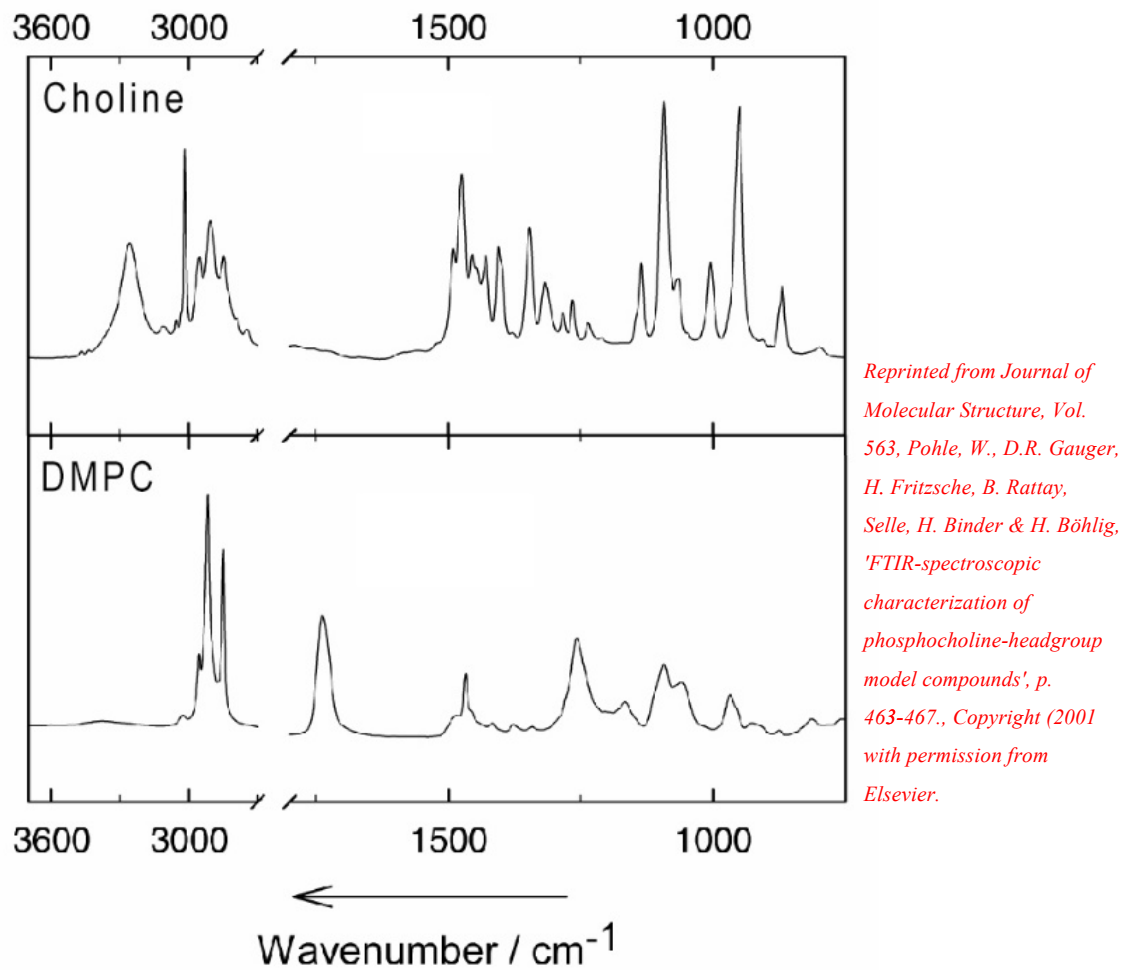


Figure 17: FTIR spectra of DMPC in two forms.

the C-O and C-H vibrations of Choline and DMPC in ZnSe windows either as liquid (choline) or in chloroform (DMPC) at 0% relative humidity. Reproduced from Pohle et al. [2001].

1.7.2. Cyclic Voltammetry and Reductive Desorption

Cyclic voltammetry scans a surface by applying a potential at a constant rate, from initial to final potential, and then inverting the scan again until the initial potential is reached [123]. The process can be cycled in order to determine if reversible and non-reversible changes are occurring at the surface [123]. The result is typically plotted as a trace of current versus applied potential [123, 147].

A significant amount of conversation exists regarding the use of cyclic voltammetry and reductive desorption in regards to calculating surface coverage, as such, this is discussed in the Appendix (Chapter 6.4).

1.7.2.1. Hanging meniscus method

The hanging meniscus method places the electrode above the solution and by dipping the co-planar surface into the solution a meniscus is formed between the electrode (or active surface) and solution below. This method is known to have a few key issues regarding contact area and scan rate, however, the shape of the peak can still be used to determine whether the molecule is bound to a surface.

In terms of contact area, the real contact area is based on the area of the electrode in contact with the solution, which is rarely accurately repeatable; further, the surface area, on a nano-scale, will significantly differ to the visual surface area calculated for each electrode [148]. As such, it is difficult to calculate the exact area of the electrode.

In terms of scan rate, García-Raya et al. [2010] found that as the scan rate decreases the charge density of the reductive peak increases, and that their results did not reach the ‘saturated’ current density expected of another author, even with a scan rate as low as $10 \text{ mV}\cdot\text{sec}^{-1}$. As

such, comparing the current density of a collected spectrum to a theoretical value, for example to calculate coverage, contains significant error.

1.7.2.2. Pre-desorption and gold surface checking

The gold surface needs to be checked for its surface quality before a thiol is organised on it such as to determine if it is the desired surface plane [52]. During this process, contaminants may be removed by repeated CV cleans, however, without careful consideration, damage can be accrued [52, 147].

During reductive desorption of the gold, the specific peak of interest is the AuO reductive peak found between 750 mV and 1100 mV (using an Ag/AgCl reference electrode) [149-152].

1.7.2.3. Peaks observed during thiol desorption

Calculating the area of adsorption is attributed to the redox reaction seen in Chapter 3.3.1 below. The process of introducing an electron to the system above a certain potential enables the molecules to be desorbed. The charge number used introduced by Schneider and Buttry in this discussion, and has provoked a number of theories since [49]. The reductive desorption process is a substrate-solution reaction, where solvent molecules replace the bond of the substrate to the presently desorbed molecule(s) [49]. As such, reductive desorption employs cyclic voltammetry to probe surfaces and reductive desorption and oxidative adsorption can be used to observe the surface coverage of a monolayer [46, 153].

While under alkaline conditions, by running a linear potentiometric sweep in the negative direction, the molecule may desorb from the surface. The alkaline conditions prevent the desorbed molecules from being protonated. Amongst the general process of desorption, it

can be seen that, at very negative potentials, the trace mimics that of a SAM free surface, which is a general indicator of complete desorption [154].

When desorbing thiols from Au(111), typically two major anodic peaks are observed and are attributed to different surface energies. Reduction of atoms at gold edges or steps which can also take the form of valleys occurs at ≤ 1.10 V [51] and the gold surface's flat terraces occurs at $(\sqrt{3}\times\sqrt{3})R30^\circ \approx -0.9 - 0.80$ V [51, 62, 147, 148, 155]. The process of stripping the lattice of thiols however requires the nucleation and growth of holes, which is an explanation for the high Q value for the peak [5, 51]. A large dip can be noticed at increasingly negative potentials; if witnessed, it is caused by oxygen in the solution.

Importantly, the pH of the solution determines whether the desorbed molecules are protonated.

1.7.2.4. Common charge densities of thiols on Au(111)

The charge density of hexagonally packed octane thiol monolayers is approximately $83 \pm 5 \mu\text{C}\cdot\text{cm}^{-2}$ [156]. Other reports value the charge density at 109, 130, and 150 $\mu\text{C}\cdot\text{cm}^{-2}$ [51, 156]. Notably, a single thiol has a charge density of $38-40 \pm 5 \mu\text{C}\cdot\text{cm}^{-2}$ (for Bis(3-sulfopropyl)disulfide (SPS) and 3-mercapto-1-propane-sulfonic acid respectively) [157].

The area consumed by each DPhyTL molecule is approximately 58 \AA^2 and is stated to be unrealistic [49]. Molecular modelling suggests that a lipoic acid moiety requires $51-65 \text{ \AA}^2$ [62]. Practical results pairing LB films in conjunction with potential stepping result in surface areas of $85\pm 9 \text{ \AA}^2$ [49]. This is supported by the fact that, based on van der Waals model, two phytanyl chains require 65 \AA^2 [49].

1.7.3. Femtosecond-VSFG

vSFG is a coherent second-order nonlinear optical technique that exploits the selection rules of both Raman and IR spectroscopy [158, 159]. Since being first reported in 1990, it has grown to become a technique able to probe molecules at surfaces where symmetry is broken; of which lipid bilayers are an example. By focusing a pulsed IR laser as well as a phase matched pulsed visible laser onto a sample, the instrument can excite atomic bonds. The bonds require both IR and Raman activity to be visible by vSFG [158]. Because the signal is recovered from a second-order non-linear process, the SFG signal only appears in media without inversion symmetry [160]. SFG is therefore surface or interface sensitive, as inversion symmetry is broken at surfaces unlike in bulk media which have inversion symmetry; this specific property makes vSFG unique as depth penetration is not relied upon unlike in most other surface-sensitive techniques [160]. The theory underpinning vSFG is discussed in Appendix 6.5.

1.7.3.1. Peaks observed in VSFG

Due to gold's non-resonant background, all peaks are negative in the spectrum [161]. C-H and O-H, C=O, amide I, SO₃, and N-H are all commonly studied bonds [160]. A list of most commonly studied bonds is as follows:

- An unsaturated C-H stretch (symmetric and asymmetric) of maleimide is at 3066 and 3130cm⁻¹ [161];
- C=O stretch of the $\alpha - \beta$ unsaturated maleimide group is at 1728cm⁻¹ [161];
- Symmetric and asymmetric CH₂ stretches of the alkane chain at 2862 and 2937cm⁻¹;
- Methyl symmetric stretching (2875cm⁻¹) [160];
- Fermi resonance and methyl asymmetric stretching (2940cm⁻¹ and 2965cm⁻¹) [160];
- Broad peaks between 3000 and 3600cm⁻¹ are O-H stretching modes found at the bilayer surface [160];
- Peak at 3200cm⁻¹ is from ice-like water [160];
- Peak at 3400cm⁻¹ from liquid-like water [160]; and,

- Peaks at 2860 and 2920 cm^{-1} due to CH_3 fermi resonance and CH_3 symmetric stretching modes in xylene [162].

1.7.3.2. Factors affecting spectra

Intensity of spectra can change significantly; it has been shown that methylene group signals can be enhanced by an increase in gauche conformations while methyl groups are typically affected by variations to their second-order susceptibility, as mentioned below. This is a function of the tilt angle of the methyl principal axis versus the surface normal [160]. Furthermore, the signal not only contains intensity information, but also phase information, also referred to as the direction of the functional group [160, 161]. By studying the methyl vibration mode, constructive and destructive addition of the peaks can be seen against the background signal and the inference can be used to analyse the orientation of moieties [160].

SFG intensity is also affected by the Fresnel factor, which is why the peak intensities change with different polarizations. Fresnel factors can be calculated from the Fresnel equation. Furthermore, by polarising the laser pulses in either SSP, PPP, or SPS configurations (in order of sum frequency beam, polarizable visible beam, and IR beam), one can determine orientation for azimuthally symmetric and non-azimuthally symmetric surfaces [160]. If ATR-FTIR is used in combination with vSFG, by determining the order parameter from ATR-FTIR, SFG can determine average orientation as well as orientation distribution [160].

The effect of metals when studying molecules organised on surfaces is significant. Metals, such as gold, absorb a significant number of photons due to the screen of the electric field parallel to the metallic surface (s-polarised component) in the infrared spectrum, thus requiring a fixed p-polarised IR beam. If this factor is not corrected for, metals create a large background reading which is large and broad, and in some cases, such as with gold, cannot be corrected. As such relative intensities are compared rather than applied from direct non-linear

susceptibility component multi-polarisation studies [163]. Polarisation dependent studies on metals are rare [163]. In some cases, the signal is small in comparison to the background reading, making it difficult to collect required data.

Bilayers themselves have specific issues; although SFG can be used to determine the heterogeneity (position and orientation) of molecules at a surface (see Appendix 6.5.2), lipid monolayers have a low vSFG absorptivity. Probing the exact properties of a bilayer can be difficult, especially when gold and water is used due to the aforementioned reasons [159].

1.7.3.3. Studying Alcohol

Based on IR, Raman, and theoretical studies, the assignment of the C-H containing structures is difficult even for simple molecules [164]. In the last decade, the assignment of ethanol peaks to the various modes and orientations has still been considered troublesome [164].

SFG was used in various polarisation modes in conjunction with different deuterated ethanol molecules to distinguish the various modes which the molecule contains. It was found that the major peaks represent the symmetric stretching CH_3 and CH_2 modes, Fermi resonance of the symmetric stretch CH_3 mode, and the overlapping anti-symmetric CH_3 and the symmetric stretching CH_2 Fermi resonance modes, at approximately 2875-2880, 2930-2940, and 2970-2975 cm^{-1} , with a peak width of 9.8, 6.8, and 7 cm^{-1} respectively [162, 164, 165].

1.7.4. Neutron Reflectometry (NR)

NR is commonly used to study the properties of bilayers, states of proteins, and the effects of various antigens in given situations [26, 166-169]. This technique can probe the structure and composition of surfaces such as films and membranes [170].

NR uses an incident beam of neutrons to analyse thin films and determine structural information by directing selected neutrons toward a surface at various angles using a time-of-flight reflectometer. NR is sensitive to light elements such as hydrogen, carbon, nitrogen, and oxygen; all of which are elements found in natural systems [168, 169]. Furthermore, because neutrons are sensitive to isotopes, these systems can be studied by replacing, for example, the hydrogen with deuterium, whilst having little effect on the chemistry; such contrast variation increases model accuracy [168, 169, 171]. As each atom has a particular neutron scattering length density and by extension molecule does too (such as H₂O having an nSLD of -0.8 and D₂O being 6.1), the solvent can be adjusted to have a similar or significantly different nSLD from the film or part of a structure of interest; this is called contrast matching.

Several issues exist within NR. The major restriction with NR is the source of the neutrons determining their wavelength and the length of time they need to be collected. The collection time directly influences the quality of the fit as long as the surface is homogenous and smooth, however, if the surface is rough and non-homogenous, extra collection time will not improve the quality of the data (explained further in Chapter 3.5) [172]. Furthermore, if the slabs are non-homogenous or defect-free, many parameters need to be simulated [171]. A membrane is occupied by two monolayers, with polar groups on either side, known as interfaces, which are highly hydrated [7, 173]. The specific positions of various molecules are significantly variable, as lipid, water, and embedded molecules will have a distribution of displacements with respect to their average structure over time, adding variability [7].

Furthermore, dynamic rearrangements are driven by thermal fluctuations, potentially leading to stochastic defects and pores at random times which are witnessed in the spectra as an average [7]. DPhyTL has been shown to have high packing densities with relatively low water incorporation, approximately 5% by volume, and furthermore because it is bound to the surface, the inhomogeneity of DPhyTL is limited, improving the ability to model the data accurately [171].

1.8. Study Scope:

1.8.1. Ethanol

The interaction of drugs with lipid bilayers are mostly studied on membranes without active peptides or using forms of computer simulations. These methods, though successful, limit collected details. In a bid to improve rigour and detail, the aim of Chapter 4 is to:

1. observe the effects of the simple anaesthetic ethanol on a DPhyTL-DPhyPC tBLM;
2. elucidate ethanol's position; and,
3. test the indirect effect of the drug on the peptide Valinomycin by ethanol's interaction with the membrane.

1.8.2. HvBot1

The expression of proteins directly into membranes using *in vitro* systems has many advantages in terms of control over purity and the ability to form surface sensors. This series of experiments seeks to:

1. observe the expression of HvBot1 into a DPhyTL-DPhyPC tBLM and,
2. study the effect of the co-factor Na^+ and concentration of the borate anion, by controlling pH, on HvBot1 transport.

2. Methods

2.1. Chapter Overview

Both the study of drug interactions as well as protein expression via cell-free synthesis with model membranes required countless substrates and model membranes to be formed.

During the experiments, various methods of substrate and membrane preparations were used as multiple sources of data from multiple instruments were needed. These variations were stringently controlled so that the surfaces and membrane-results were comparable.

This chapter will describe all chemicals, processes, and experimental setups required throughout all of the experiments.

2.2. General Experimental

2.2.1. Chemicals and consumables

All chemicals or consumables used in this study are detailed in Table 1, where any aqueous solutions or dilutions use 18.2 MΩ Milli-Q water (A10, Millipore, Australia or WRX10, Yamato, Japan).

Table 1: Chemical and consumable list for all experiments.

Note: In regards to the Wako chemicals, the grades are those stated by supplier.

Chemical	Supplier	Grade	Purity	Product Code
Acetone	Chem-Supply	AR Grade	-	A008-2.5L-P
Ammonia	Chem-Supply	AR Grade	-	AA005-2.5L
Calcium Chloride	Sigma Aldrich	-	>99.9%	429759 Aldrich
1-Decanethiol	Sigma Aldrich	-	99%	705233 Aldrich
Dichloromethane	Wako	“JIS-Special Grade”	99.50%	133-02447
DPhyPC (Hydrogenated)	Avanti Lipids	N/A	>99%	4ME 16:0 PC
DPhyTL	Synthesised	N/A	Purified	N/A
Epoxy (for Au111 preparation)	Maruto	N/A	N/A	Technovit 4004
Epoxy (for TSG)	Epo-tek	N/A	N/A	Epoxy Technology 353ND41LB Kit Part A Epoxy Technology 353ND41LB Kit Part B
Ethanol	Chem-Supply	Analytical	100%	EA043-2.5L-P
Ethanol	Scharlau	HPLC Grade	99.80%	ET00102500
Deuterated Ethanol	Sigma Aldrich	Anhydrous	>99.5	186414-1G
Ethanol	Wako	“JIS-Special Grade”	99.50%	057-00451
Ethyl Acetate	Wako	HPLC / “Super Special Grade”	>99%	057-03371

Iron(III)ferrocyanide	Chem-Supply	AR Grade	-	234125-25G
Gold Wire	Tanaka	N/A	>99.999%	N/A
Helmanex III	Sigma Aldrich	N/A	N/A	N/A
Hexane	Wako	“JIS-Special Grade”	96%	085-00411
Hydrogen Peroxide	Chem-Supply	AR Grade	-	HA154-2.5L-P
Hydrochloric Acid	Wako	“Super Special Grade”	35-57%	083-03435
Hydrogen Peroxide	Wako	“Super Special Grade”	30%	086-07445
Iodine	Wako	N/A	100.00%	45105-5g
Nitric Acid	Wako	“JIS-Special Grade”	69-70%	143-01326
Potassium carbonate	Wako	“JIS-Special Grade”	99.50%	162-03495
Potassium Chloride	Chem-Supply	LR Grade	-	PL054-500g
Potassium permanganate	Wako	“JIS-Special Grade”	99.30%	167-04182
Silica Beads (~50 nm)	Chemsupply	N/A	N/A	SL043
Silicon Wafer (TSG)	CrysTec (Berlin, Germany)	-	-	P-Type
Silicon Wafer (vSFG)	Shin-etsu	-	-	P-Type
Silicon Wafer (NR)	El Cat Inc., Waldwick, NJ	-	-	-
Sodium Chloride	ChemSupply	AR Grade	-	SA046-500g
Sodium Hydroxide	Wako	“JIS-Special Grade”	97%	198-13765
Sulfuric Acid	Wako	“Super Special Grade”	96-98%	190-04675
Valinomycin	Sigma Aldrich	-	>98%	V0627-10mg

2.2.2. Column Chromatography

2.2.2.1. Burette Preparation

A 100 ml burette was packed with 50 nm silica beads to form a column. To correctly pack the column, a gel-like state was prepared by adding solvent to dry silicon beads (ChemSupply, Australia) and then mixing them quickly until a homogenous suspension was created; the mixture was then poured, quickly but smoothly, into a burette. If the gel-like state, after settling, would include fissures or trapped air pockets, the process would either be restarted or the burette would be repeatedly flipped until the mixture became homogenous before being left to resettle. Once the column was loaded, the burette would be left to settle for about 30 minutes before being rinsed with extra solvent.

2.2.2.2. DPhyTL Purification

Before loading the sample of DPhyTL lipid onto the column, solvent was drained to gently expose the surface; subsequently 50 mg of DPhyTL was mixed with 2 mL of solvent (for solvent mixture ratio see ‘Purification 1’ below) and loaded onto a column by slowly pipetting it down the side of the burette onto the gently exposed silica-gel surface. If needed, further solvent was drained from the column to aid loading, however, the ‘load’ was kept as thin as possible to increase separation quality.

Once loaded, further solvent was drained to gently re-expose the surface of the column. To protect the gel from being disturbed when further solvent would be added, a piece of filter paper was cut to size and placed on top of the gel. Once the burette was filled, separation could commence. The separation typically required 30 separate, 5 mL, vials. To retain the purity of each fraction, the tip of the burette was rinsed with extra solvent prior to replacing the fraction’s vial with the next vial.

Thin Layer Chromatography (TLC) was performed for each fraction; DPhyTL typically extracted across four fractions (numbers 21-24 typically). After combining the fractions, solvent was removed using a rotating evaporator (Buchi Rotavapor R-3) under vacuum using a water bath set to 30 °C. This process was repeated twice to improve DPhyTL purity, however the second purification used the second solvent mixture ratio (see ‘Purification 2’ below). Once complete, a final purification would be completed using a ‘plug’, where the column would only be 5 cm long. Once all possible solvent was removed using the rotating evaporator, the pure DPhyTL was stored under nitrogen in a freezer at -20 °C and left until needed.

2.2.2.3. Chemicals Mixtures

Purification 1: 25%_{v/v} Ethyl Acetate (Wako) and 75%_{v/v} Hexane (Wako) was used for the first 15 fractions, then 50%_{v/v} Ethyl Acetate to 50%_{v/v} Hexane was used for the next 3 fractions, and finally 75%_{v/v} ethyl acetate to 25%_{v/v} Hexane was used for the last samples.

Purification 2: 90% Ethyl Acetate and 10% Hexane.

Note: In the first case, the yellow mark of the lipid did not pass through the column until a high concentration of Hexane was used. With the second column, the yellow mark passed through quickly.

2.2.3. Thin Layer Chromatography

2.2.3.1. The Process

TLC sheets with similar retention properties to the separating column were prepared into plates 6-7 cm long and 2 cm wide. To improve separation quality, repeated cuts were made gently with a Stanley knife to not disturb the silica until each side was cut. Each plate was marked with a start and end line, 5 cm apart. When loading the TLC plate, little DPhyTL was needed to overload a TLC plate, as such a pasture pipette was heated under a Bunsen flame and stretched when hot resulting in a capillary tube which was used to load each spot.

Once loaded, each plate was placed into a jar containing the representative solvent and allowed to run and finish. The plate was either air dried or dried using a hair-dryer to speed up the drying process. The plate was stained to reveal the chemical components effected by the solvents.

Staining Solution: Potassium permanganate (1 g), potassium carbonate (7 g), 10% sodium hydroxide (1.25 mL), and water (100 mL).

2.2.4. FTIR

2.2.4.1. Bulk liquid FTIR

Purified DPhyTL was pipetted between two CaF₂ windows, allowed to spread, placed into the FTIR test chamber, and left to purge with nitrogen for an hour (BioRad FTS-30/ESC).

All spectra were measured by integrating 256 interferograms to improve the signal to noise ratio. Each spectrum was collected with p-polarised light between 800 cm⁻¹ and 4400 cm⁻¹ at a resolution of 2 cm⁻¹. A background spectrum was subtracted from each set of spectra. Water was subtracted manually using WinIR, with a spectrum taken earlier (BioRad). A diode laser (13 mW.cm⁻²) was used as a light source and a mercury cadmium telluride (HgCdTe) detector was used, cooled with liquid nitrogen. A similar method was used by Arsov, and Quaroni [2007] and Naumann et al. [2003].

The data analysis was performed using MagicPlot Student Edition (Magic Plot Systems, Ver. 2.5.1) and Origin (Ver. 9, OriginLab, Northhampton, MA, USA). Further baseline correction was applied prior to deconvolution using Fityk (John Allspaw, Ver. 0.9.8).

2.2.4.2. Reflectance-mode FTIR

To form a monolayer for testing, a cleaned polycrystalline gold puck (2 cm in diameter) was placed into a pre-made 0.2 mg.ml⁻¹ DPhyTL solution in ethanol (Wako, >99%) for 18 hours. Once ready, the puck was removed from solution and cleaned repeatedly with ethanol (Wako, >99%). The puck was then placed in a reflectance-measurement holder and FTIR spectra were taken (FTS-30/ESC by BioRad, using WinIR by BioRad).

The deterioration of the lipid on the gold surface under nitrogen was tested over the period of two weeks, once daily. In all cases the chamber was continually purged with nitrogen.

Each spectrum was collected with p-polarised light between 800 cm^{-1} and 4400 cm^{-1} at a resolution of 2 cm^{-1} . All spectra were measured by integrating 1024 interferograms. A background spectrum was subtracted from each set of spectra. Water was subtracted manually using the WinIR (BioRad Software). A diode laser ($13\text{ mW}\cdot\text{cm}^{-2}$) was used as a light source. A mercury cadmium telluride (HgCdTe) detector was used, cooled with liquid nitrogen.

The data analysis was performed using MagicPlot Student Edition (Magic Plot Systems, Ver. 2.5.1) and Origin 8 SP1 (OriginLab Corporation, Ver. 9.1). Further base-line correction was applied prior to deconvolution using Fityk (John Allspaw, Corporation, Ver. 8 SP1).

2.2.5. NMR

NMR spectra were collected from 0.5 mg of DPhyTL in 5 ml of Chloroform-D (Jeol Resonance JNM-ECA 400). 16 scans of a proton 1D NMR spectra were taken at 400MHz and averaged. The chemical structure of DPhyTL was analysed using splitting diagrams based on the structure.

2.2.6. Cyclic Voltammetry

2.2.6.1. Au(111) crystal formation

An Au(111) single crystal was prepared from a 1 mm diameter pure gold wire (Tanaka, >99.999%) using the Clavilier method [175, 176]; this process is similar to that used by Darwish et al. [2010]

To form a crystal, a gold wire (Tanaka, Japan), 1 mm in diameter, was cut to a 10 cm length and one end was heated under an oxygen-butane flame; upon slow melting a drop would form. The size of the drop is dependent on the thickness of the wire and skill of the scientist. It was found that the best method of forming the bead was to place the gold wire in a clamp and slowly move a flame underneath it, reducing vibrations and movement. The type of Bunsen head used had two separate nozzle chambers, the first was a large single flame in the centre and the second was a series of smaller holes surrounding the central nozzle. The flame was set such that the central nozzle was mostly heating the gold and the outside nozzles were less powerful; large amounts of oxygen were being added to both, although the overall flame was weak, reducing errors throughout the gold bead's crystal lattices. Once the bead was formed, the butane pressure was decreased slowly, controlling cooling.

2.2.6.2. Facet selection

After gold crystal formation, the gold-crystal bead included two sets of visible facets, the 111 and 110 facets; the facet of interest was 111. Using tweezers, the wire was gripped about 1 cm below the bead and slowly formed into a coil that would act as a platform on which the bead could be placed and glued to a brass puck using super-glue. Once the glue was set, the puck was placed onto a home-made jig which projected a red laser beam onto the top of the puck to check whether the facet of interest was coplanar to the base it was glued to. Using the

jig, the facet was moved into place by twisting and bending the supporting wire of the crystal. To check whether the facet was 'true', the puck was rotated to all four cardinal points.

2.2.6.3. Au(111) surface formation

Once glued, the brass puck, along with the attached crystal, was placed in a tight-fitting Teflon holder that was 3-4 cm tall. A two-part epoxy (Technovit, Maruto, Japan), used for polishing, was prepared until the mixture reached the viscosity equivalent to thick honey. The epoxy was poured carefully onto the brass base and added until the gold crystal was covered, after which the epoxy was left to set; once set the Teflon container was removed.

The epoxy above the gold was cut away using a circular saw (Buehler IsoMet Low Speed Saw, Illinois, USA) and the remaining brass puck was glued onto a larger polishing base using beeswax. The flat-polisher (ML-150L, Maruto, Japan) was setup with a 500-grade abrasive paper attached. Using water as a lubricant, the epoxy was slowly polished until a reasonable area of gold crystal was exposed. The abrasive paper was then changed to 1000-grade and used until the circumference of the exposed gold surface was almost equivalent to that of the largest circumference of the gold crystal. The surface was analysed visually for marks using a 25x stereo-microscope (SZIII Stereo Zoom Microscope, Olympus, Tokyo, Japan) as a reference point for all further polishing; subsequently, 1500-grade paper was used to remove larger scratch marks on the gold surface before the gold was polished with 2500 grade paper.

Once the largest gold circumference was reached and most marks removed, the abrasive paper was replaced with polishing mats. Polishing liquids were used to smooth the surface further with 3, 1, and 0.5 μm beads (PC Suiyousei P12092, P11036, and P5082-A); separate mats were used for each bead size. Sonication (As One - Single Frequency Cleaner, Japan) in

Milli-Q water (Yamato, Japan) was used between each bead size to clean any larger particles away and decrease the chances of larger scratches being formed on the gold surface. Once satisfied with the polished surface under microscope viewing, the brass pucks were separated using a heating mantle to melt the beeswax.

The brass puck, with the gold crystal and epoxy surrounding it, was placed in dichloromethane (Wako) overnight or until the epoxy would swell and separate from the brass puck and gold crystal; the superglue holding the crystal to the brass puck dissolved as well. The gold crystal was then removed carefully, so as not to scratch its polished surface, and rinsed with sonicated in clean dichloromethane. Finally, the gold crystal was placed in a crucible, face-up, and left in a muffle furnace (Yamato KDM650, Japan) which was programmed to heat to 1050 °C over the period of one hour and hold that temperature for 18 hours before slowly cooling to room temperature over a further 6 hours. Once complete, the Au(111) surface was ready for use.

2.2.6.4. Gold Surface Characterisation

A 0.05 M H₂SO₄ (Wako) solution was deoxygenated by vigorous bubbling of nitrogen for at least 30 min before each experiment [153]. While the solution was bubbling, the Au (111) surface was flame-annealed for 15 minutes using a hydrogen flame. During annealing, the crystal was heated until it reached a dim-red-orange colour before being cooled slowly under an Argon (99.9995%) stream; this was repeated 5-10 times.

Electrochemical measurements used a three-compartment hanging-electrode electrochemical cell. Once annealed, the gold surface was attached, by its base, using an alligator clip, and placed in a hanging meniscus configuration, co-planar to the surface; and

after deoxygenation, the Au(111) surface was carefully dipped into the solution and pulled back until the thinnest meniscus was formed.

Data was collected using a potentiostat (HA-151, Hokuto Denko, Japan), function generator (HB-111, Hokuto Denko, Japan), recorded using an X-Y recorder (Graphtec, WX1200), and viewed using a custom-made data-logging program. The settings are as follows: rate of 25 mv.sec⁻¹; start Voltage of 0 mV; high Voltage of 950 mV; low Voltage of -200 mV; an Ag/AgCl reference electrode; and a platinum counter electrode. The scan would be repeated up to 10 times. If needed, the process of bubbling, annealing, dipping, creating a meniscus, and checking, would be repeated multiple times to improve spectra; in some cases, the quality of the CV result would improve markedly, however, the overall process would be repeated as little as possible to preserve the quality of the gold surface.

Once completed, the gold would be removed from the solution, rinsed with running Milli-Q (WRX10, Yamato, Japan), and re-annealed under a hydrogen flame, before being placed into Ethanol (Wako) and then into the DPhyTL solution (0.2 mg.ml⁻¹ ethanol) and left for 18 hours to form a monolayer.

2.2.6.5. DPhyTL Desorption:

Data was collected using a potentiostat (HA-151, Hokuto Denko, Japan), function generator (HB-111, Hokuto Denko, Japan), recorded using an X-Y recorder (Graphtec, WX1200), and viewed using a custom-made data-logging program. The solution used for reductive desorption was 0.1 M KOH (Wako), made-up as needed, deoxygenated with vigorous nitrogen bubbling for at least 30 min before each experiment [153].

Settings used: Hold-potential of -200 mV (this is vital or else the surface will be damaged instantly); rate of $25\text{mv}\cdot\text{sec}^{-1}$; start Voltage of -200mV; high Voltage of -195mV; low voltage of -1200mV; Ag/AgCl reference electrode; and platinum counter electrode.

2.2.6.6. Data Analysis

To integrate the area of each graph, the X-Y recorder data was converted into digital images, exported in high resolution from Origin (Ver. 9, OriginLab, Northhampton, MA, USA), and imported into Adobe Photoshop CC. The areas of each graph were 'cut out' using vector lines and the areas were 'weighed' using pixel data. This method was used because some data incurred poor signal to noise ratios causing far larger areas to be measured than would otherwise be expected. For more specific details see Chapter 3.3.

2.2.7. Electrochemical Impedance Spectroscopy

2.2.7.1. TSG Slide Preparation and formation

Many of the following preparation and testing methods are similar to those found in Naumann et al. [2003].

Silicon slides were first pre-cleaned by filling a staining jar with basic-piranha solution, 1:1:5 of Hydrogen Peroxide (Sigma Aldrich), Ammonia (Sigma Aldrich), and Milli-Q water (Millipore, Australia), and placing the jar in a hot-water bath at 70 °C for between three and five hours. The solution was then replaced with Milli-Q water (Millipore, Australia) and placed in a sonicator bath (Unisonics Australia, Ultrasonic Cleaner) for a further 10 minutes; this step was repeated a further four times. The Milli-Q water (Millipore, Australia) was then replaced with ethanol (Analytical Grade, Sigma Aldrich) and sonicated further; this step was repeated a further four times as well. Finally, the silicon was placed in a sonicator, cleaned one last time with ethanol (HPLC-Grade, Sigma Aldrich), drained, and left under low vacuum over night to remove any ethanol trapped in the oxide layer.

Once required, the silicon was removed from the desiccator and placed in an evaporator ready for gold deposition. Gold was deposited using electro-thermal evaporation in two steps, a slow and then quick rate. Initially the rate of deposition was 0.1 nm.min⁻¹ for the first 5 nm after which the rate was increased to 5 nm.min⁻¹ (Angstrom Engineering Covap and Infinicon SQC-310C); vacuum was approximately 2-5x10⁻⁶ mbar. Once complete, the gold-deposited silicon slides were stored in glass containers, sealed, and kept in the dark, until needed.

Prior to creating the silicon-gold-glue-glass sandwich, glass microscope slides (Livingstone, 7105-1) were split in two, placed in staining jars, and rinsed in a 10% Hellmanex III soap solution (Sigma Aldrich) while sonicating for 10 minutes. The slides were then rinsed

with a 1:1 mixture of Milli-Q (Millipore, Australia) and ethanol (Analytical-grade, Sigma Aldrich) before being rinsed with ethanol five times with a short burst of sonication (1-2 minutes each), and then Milli-Q five times with a short burst of sonication (1-2 minutes each). Finally, the slides were rinsed with pure ethanol (HPLC-grade, Sigma Aldrich) before being dried under a stream of nitrogen, until needed.

Meanwhile, the epoxy glue was mixed at a ratio designated by the manufacturer (Epotek), 1:10, warmed to 30 °C and mixed with a spatula until combined. After mixing, the solution was degassed at approximately 45×10^{-6} mbar to remove any trapped air-bubbles (Woosung Automa W2V20).

Once the glass slides were dry and the gold slides ready, the gold-deposited silicon slides were coated with the degassed epoxy glue (Epotek), glass slides were placed on top, and the combination was placed onto a hotplate to allow the glue to spread by becoming thin (instead of viscous), but not hardened; in some cases, pressure was applied to 'sandwich' the slides and remove further glue from in-between. Once sufficiently 'sandwiched', the slides were either removed from the press and rinsed with acetone (Chem-Supply) or simply rinsed with large amounts of acetone to remove any excess glue from all the outer edges and sides.

Finally, the slides were placed on a second hot plate and heated slowly to 150 °C until the glue colour changed (to a darker amber) signifying the epoxy had hardened. Once darkened, the slides were removed from the hot-plate and left to cool slowly before being stored in a separate staining jar until needed.

2.2.7.2. Monolayer Formation

Once ready, a slide-sandwich, like the one prepared above, would be separated and instantly rinsed with ethanol (HPLC-grade, Sigma Aldrich) before being dipped into and left in the lipid solution for 18 hours at 3 °C, forming a DPhyTL monolayer. Note: monolayer formation is a quick process initially but requires time to organise and fully complete [62, 178]. After monolayer formation, the slides were removed from solution and rinsed heavily under a constant stream of ethanol (HPLC-grade, Sigma Aldrich) for 15 seconds to remove any excess DPhyTL left over from the solution after removal from the vial, which is a vital step [179]. The slide was then dried under a stream of nitrogen and placed into the Teflon ‘reactor’ and quickly submerged in either 100 mM NaCl or KCl solution, depending on need.

- **Drug studies:** NaCl (100mM) solution.
- **HvBot1 studies:** KCl (100mM) solution.

Note: Typically, a new DPhyTL solution was generally prepared every two months unless contaminated earlier. Each time, 10 mL aliquots were prepared from purified DPhyTL and ethanol (HPLC-grade, Sigma Aldrich) at a concentration of 0.2 mg.ml⁻¹.

2.2.7.3. Reactor (Teflon-housing) Cleaning

During monolayer formation, the Reactor, or Teflon cell, was cleaned with 2% Hellmanex solution (Sigma Aldrich) in Milli-Q (Millipore, Australia) solution at room temperature with sonication (Unisonics Australia, Ultrasonic Cleaner) for 30 minutes, rinsed with ethanol (Analytical-Grade, Sigma Aldrich) with sonication for a further 30 minutes, gently rinsed with Ethanol (HPLC-Grade, Sigma Aldrich) followed by large volumes of Milli-Q water (Millipore, Australia), before being sonicated again. Finally, the cell was left submerged in

Milli-Q water (Millipore, Australia) until needed. In every case, the Teflon cell was fully cleaned within 24 hours of use.

2.2.7.4. Vesicle preparation

Vesicles were prepared by weighing 2 mg.mL⁻¹ of DPhyPC lipid (Avanti Lipids) into a microcentrifuge tube, which was then topped up with 1 M NaCl solution and vortex-mixed. This mixture was heated for at least 40 minutes in a water-bath and set to between 40 and 55 °C; during heating the mixture was typically vortexed twice to improve vesicle formation. The vesicle-solution was filtered through an Avestin extruder using a 50 nm pore-size membrane (Avestin 50x Polycarbonate 0.75" 50nm filters). The vesicle mixture was placed in the fridge until needed but always used the same day.

2.2.7.5. Electro chemical impedance spectroscopy settings

The impedance spectrometer (Autolab PGSTAT 30) was set to *potentiostatic frequency response analysis* mode. Perturbation frequencies ranged from 2 mHz to 0.1 MHz, which are commonly used [123]. A controlled DC bias potential of 0 V was applied and an AC amplitude of 10 mV; no other DC offset was used. A silver-silver chloride electrode was used (Microelectrodes MI-401F Micro Reference Electrode), and was generally pre-treated and checked using Cyclic Voltammetry once a month (see chapter 2.2.7.6).

2.2.7.6. Reference electrode pre-treatment process

The settings for Ag/AgCl reference electrode pre-treatment were: a scan rate of 0.025 V.sec⁻¹; step voltage of 0.01 V; start potential of 0.2 V; high potential: 0.8 V; and low potential: 0 V; the solution used was 250 mM Ferrocyanide (Chem-Supply), the counter electrode was a carbon-carbon glassy electrode or platinum electrode, and the working electrode was also

platinum. One peak in each direction was expected: Cathodic Peak at approximately 420 mV and Anodic Peak at approximately 380 mV.

2.2.7.7. Monolayer testing

After cleaning the reactor and forming the monolayer (chapters 2.2.7.2 and 2.2.7.3), the gold slide was placed into the Teflon housing and submerged with buffer solution. As soon as possible, the electrodes were connected and or submerged and the monolayer was tested, as per 2.2.7.5. Generally fewer frequencies were tested to limit test times and allow vesicles to be added as soon as possible.

2.2.7.8. Bilayer organisation and testing

Vesicle Deposition: Bilayer formation was completed by adding 25 μL of extruded 50 nm vesicles to a submerged, and checked, DPhyTL monolayer system in either in a 100 mM NaCl or KCl buffer solution at room temperature. The overall concentration of the vesicles in the 1 mL cell, being homogenously dispersed and prior to deposition was equivalent to 2.36 mM. To form a bilayer, the process typically required between 8 and 15 hours; once finished, the system was flushed with further buffer solution, tested once, and left until needed, though typically used straight after. Further EIS used the same settings as those outlined in chapter 2.2.7.5.

Solvent exchange: A dried monolayer was housed in the Teflon chamber and 25 μL of 2 $\text{mg}\cdot\text{mL}^{-1}$ DPhyPC lipid (Avanti Lipids) in ethanol (HPLC-Grade, Sigma Aldrich) solution was injected using a pipette into the 1 mL cell, submerging the monolayer; the final concentration of solution was 59 μM . After leaving the system for 20 minutes, the lipid-ethanol solution was replaced using a fast burst of 100 mM buffer solution (NaCl or KCl as needed).

It should be noted that the length of time for solvent exchange, i.e. 20 minutes, is only used to ensure that the solution has interacted with the surface as much as possible.

2.2.7.9. Valinomycin peptide addition

Valinomycin (Sigma Aldrich) was diluted to $10 \text{ mg}\cdot\text{mL}^{-1}$ in ethanol (HPLC-grade, Sigma Aldrich) upon arrival. When needed, a diluted solution ($2 \text{ mg}\cdot\text{mL}^{-1}$) was prepared from an aliquot of the stock solution, and $25 \mu\text{L}$ was injected into each reactor chamber (per bilayer); each reactor chamber was 1 mL in volume [77, 132].

2.2.7.10. Drug testing procedure

After monolayer and bilayer formation, the spectrometer used the same settings as observed in 2.2.7.5.

Before injecting ethanol (HPLC-Grade, Sigma Aldrich), the sequence of tests progressed as follows: bilayer in NaCl solution; bilayer in KCl solution; and bilayer in NaCl solution. After injecting the peptide Valinomycin, the process was repeated and if the resistance was significantly diminished in comparison to the results of KCl without the peptide, experiments progressed to drug testing.

Drug tests followed this final method (for each concentration of ethanol): bilayer in NaCl solution with ethanol, bilayer in KCl solution with ethanol, bilayer in NaCl solution with ethanol; and bilayer in NaCl without ethanol; this method was used for 1%_{v/v}, 5%_{v/v}, 10%_{v/v}, 25%_{v/v}, and 50%_{v/v} concentrations of ethanol.

Example solution (10%_{v/v} ethanol in NaCl): 1 mL ethanol (HPLC-grade, Sigma Aldrich) and 9 mL of 100 mM NaCl solution in Milli-Q (Millipore, Australia) mixed

thoroughly; higher concentration ethanol solutions did not equal the volumes of their separate parts.

Take note, the concentration of ethanol in solution would not affect the measurements as a decrease of NaCl or KCl concentration by 100 mM to 50 mM would render the resistance due to solution relatively unchanged as is shown in Figure 8 [73].

2.2.7.11.HvBot1 testing procedure

This method is shown in Zieleniecki et al. [2016].

After thoroughly cleaning the reactor housing and preparing a bilayer (as per 2.2.7.3, 2.2.7.7, and 2.2.7.8), a transcription reaction was set up and purified mRNA, along with the wheat germ extract, cofactors, and amino acids, was added to a pre-formed tBLM in a Teflon reactor. The reactor was left in a room at 22 °C and protein synthesis was left to complete over 24 hours without shaking or movement. Testing typically followed the following method after protein expression:

1. Bilayer in HEPES-BTP solution; Bilayer in HEPES-BTP solution with borate; and Bilayer in HEPES-BTP solution, at pH 6
2. Repeat of step 1, but with 5 mM NaCl in each solution.
3. Repeat of step 2, but at pH 7.5 and pH 9

Due to the sodium-dependence of the transporter, the buffer solution included either HEPES–BTP buffer (20 mM HEPES) or HEPES–BTP buffer with borate (20 mM HEPES, 50 mM boric acid), and either did or did not include 5 mM NaCl; each solution had a controlled pH of either 6, 7.5, or 9.

Note: All solutions were pH controlled using KOH. Testing was completed using a pH Balance Probe (Mettler Toledo, Five Easy FE20)

2.2.7.12. Data analysis:

All raw data was analysed using the ZView software package (version 3.3B Scribner Associates). Data was fitted using the EEC seen in 1.6.5.2. All values were normalised to an active electrode area of 0.28 cm².

2.2.8. Femto-Second Vibrational Sum Frequency Generation (fs-vSFG)

2.2.8.1. Silicon cleaning

A silicon wafer (Shin-etsu) was first cut to size then washed in a 3:1 H₂SO₄:HCl (Wako, Japan) followed by 3:1 H₂SO₄:H₂O₂ (Wako, Japan). Milli-Q water (Yamato, Japan) was used to wash the surfaces with sonication (As-One, Japan) before the surface was dried with ethanol (Wako, Japan).

2.2.8.2. SAM preparation

After cleaning a silicon surface using basic piranha solution (as per chapter 2.2.7.1), gold was sputtered at $1.2 \times 10 \text{ pA} = 0.2 \text{ \AA}\cdot\text{s}^{-1}$ (Sanyu Electron Quick Coater SC-701 MkII, Japan) until 60 nm was deposited. The surface was gently flame-annealed for approximately four seconds, cooled, and dipped into a solution of 0.2 mg.ml⁻¹ DPhyTL solution for 18 hours to organise a SAM (as per chapter 2.2.7.2). Once ready, the surface was placed into the fs-vSFG housing and purged with Argon and ready for scanning.

2.2.8.3. DPhyTL SAM characterisation and resistance to 8mW Femto-second laser pulses

The housing, along with the DPhyTL surface, was placed in position and the surface was aligned. Two one minute scans were taken every 15 minutes over the period of 1.5 hours. Between each scan, the laser was blocked from passing through to the sample as not to illuminate the surface. If the symmetric and asymmetric νCH_3 bonds of DPhyTL were observed in the collected spectra, and the signal was strong, final alignments were made and initial spectra were taken in duplicate (using 60 second scan lengths). Six different positions were sampled across the SAM surface. Afterward, a Polystyrene spectrum was taken for reference.

2.2.8.4. DPhyTL-DPhyPC Bilayer characterisation

50 nm of gold was sputtered onto glass and flame annealing was used (10 sec, low heat). The gold surface was checked by fs-vSFG for signal quality; a poor signal indicated extra annealing time necessary. If the spectrum was clean, a sample spectrum was measured and a second spectrum was taken with a Polystyrene slide in-line with the beam.

Next, a pre-prepared sample, with a DPhyTL SAM was placed inside a sealed chamber with a CaF_2 window, was checked in air and a spectrum was taken; a second spectra with the Polystyrene slide was also taken. 5ml of 18 M Ω Milli-Q water (Yamato, Japan) was mixed with 125 μl of 5 mM CaCl_2 (Sigma Aldrich), and 50 μl of 2 mg.ml⁻¹ DPhyPC 50nm extruded vesicles (Avanti Lipids); prepared using 50 nm extrusion. The cell was left to stand for 18 hours at 24 °C. After flushing, a spectrum was taken followed by a second Polystyrene spectrum.

2.2.8.5. Bilayer ethanol testing

A solution of 25%_{v/v} ethanol (Wako) in 100 mM NaCl or KCl solution was injected into the cell and a spectrum was taken. The bilayer was then rinsed before 100mM KCl buffer solution was pumped through and another spectrum was taken.

2.2.8.6. Instrument settings

Fs-vSFG experiments were carried out at NanoGreen, NIMS, Japan. In short, a Ti:sapphire femtosecond oscillator set to 0.6 Watts (Tsunami, Spectra-Physics) and a regenerative amplifier (Titan, Quantronix) laser system pumped by a Nd:YLF laser (Darwin, Quantronix) generated 2.1 mJ pulses at 800nm with a 100 fs duration at a repetition rate of 1 kHz. The output was split and one half was directed toward a home-made spectral shaper which generated narrow-band pico-second pulses at 800nm (30 μ J/pulse) to improve the spectral resolution. The other half was pumped into an optical parametric amplifier/difference frequency generator (OPA/DFG) (Light Conversion Inc., TOPAS) thus generating tuneable IR pulses (6 μ J/pulse @ 3 μ m) with a spectral width of 200 cm^{-1} . The two beams were then overlapped on the sample surface at 70° and 50° respectively.

Spectra were collected using a CCD detector (iDus DU420A, Andor) attached to a spectrograph (SR-500i, Andor) [180]; the system was cooled using a phase-change cooler. Scan times: 60 seconds, visible wavelength: 600nm, IR wavelength: 1176.11nm, visible power: 40mW, IR power: 8mW, polarisation: SSP; each scan was background corrected. The signal is presented as arbitrary absorbance as a function of wavenumber, as seen previously [160, 181].

2.2.8.7. Data analysis:

This analysis was performed using (Solis, Andor Technology) software and Origin 9 (Ver. 9, OriginLab, Northhampton, MA, USA).

2.2.9. Neutron Reflectometry

2.2.9.1. Silicon surface cleaning

Each 5” silicon disk (El Cat Inc., Waldwick, NJ) was prepared by pre-polishing and then cleaning the surface in a bath of basic Piranha solution (5:1:1 H₂O₂, NH₄⁺, H₂O) for two hours. Chromium was sputtered onto the surface (50 Å) followed by gold (50 nm).

2.2.9.2. DPhyTL monolayer formation

The cleaned silicon disk was submerged in 0.2 mg.ml⁻¹ DPhyTL solution for 24 hours and then washed with ethanol (HPLC-grade, Sigma Aldrich). The silicon disk was then sealed under nitrogen before use; all of this was typically completed the day before.

2.2.9.3. DPhyTL-DPhyPC bilayer formation

The silicon disk, along with the deposited DPhyTL monolayer, was sealed in the NR housing. The bilayer was completed using the solvent exchange method; the solvent exchange was performed by injecting a 10 mg.ml⁻¹ solution of DPhyPC in ethanol (HPLC-grade, Sigma Aldrich) into the chamber and leaving it for 20 minutes before injecting buffer solution (100 mM KCl) as quickly as possible. Note: Solvent-exchange was used to deposit the distal monolayer in place of vesicle deposition due to it typically forming bilayers more successfully over large surfaces.

2.2.9.4. Monolayer and bilayer testing

NR data was collected using a time-of-flight reflectometer (Platypus, Bragg Institute, Australian Nuclear Science and Technology Organisation, Australia). Three incident angles were tested: $\theta = 0.8$; 1.6; and 3.5°; allowing each surface to be tested over a wide range of incident angles. Furthermore, each sample was measured with three contrasts to improve the

confidence of the fits, H₂O, CM4, and D₂O, respectively; the respective nSLDs are $-0.8 \times 10^{-6} \text{ \AA}^{-2}$; approximately $3.5 \times 10^{-6} \text{ \AA}^{-2}$; and $6.1 \times 10^{-6} \text{ \AA}^{-2}$. The solvents of choice were D₂O, D₂O/H₂O, and H₂O, where the D₂O/H₂O neutron Scattering Length Density (nSLD) was approximately $4 \times 10^{-6} \text{ \AA}^{-2}$ (CM4). Both hydrogenated (DPhyTL-DPhyPC) and deuterated (dDPhyTL-dDPhyPC) bilayers were tested.

2.2.9.5. Ethanol tests

Ethanol concentrations were collected with three contrasts at concentrations of: 0%_{v/v}, 10%_{v/v}, 25%_{v/v}, and 50%_{v/v}; a process similar to Knobloch et al. [2015]. The nSLD of dEtOD is 6.1.

2.2.9.6. Data analysis

See Chapter 3.5.

3. Data Interpretation and Modelling Processes

3.1. Chapter Overview

Throughout the length of this work, careful steps were taken when analysing the various sources of data. The interpretation and comparison of the data was rigorous to improve data and interpretation quality. This chapter will explain the major steps taken during data interpretations processes for EIS, CV, fs-vSFG, and NR.

3.2. EIS Data Collection and Modelling Process

3.2.1. Basics of data interpretation

Data interpretation, using EIS, is commonly completed by representing the surface of interest with electrical elements (introduced in Chapter 1.6.3), known collectively as EECs. When focusing on membrane systems, chapter 1.6.2 outlines that the most common elements are resistors, capacitors, and constant phase elements, in various configurations. It is vital that the electrical circuit representing the surface is relatable physically as well as electrically; generally comparing the two, especially when peptides or proteins are involved, can become quite complicated. If the surface is imperfect or damaged, the response of the emittance may also create further difficulties when interpreting the surface.

To acquire quantitative data from the EECs, each element of the EEC is represented using a mathematical equation (Chapter 1.6.3) and, by using Kirchoff's laws, the separate elements can be combined into one complete mathematical equation. Although this can be completed manually, as is stated in Chapter 2.2.7.12, the ZView software package (version 3.3B Scribner Associates) can automatically form the equations, representing the results on the same graphs as the collected data, allowing models to be refined both visually or by using automatic fitting methods.

The data, upon collection, is not normalised to a certain surface area. After measuring the surface area, one of two methods can be used to normalise values from the fitting process, either: 1) the ZView software package (version 3.3B Scribner Associates) can be used to normalise the data or 2) after modelling the data using an EEC and acquiring values for each circuit element, each element is area-normalised.

The data collected used for modelling cannot be averaged between sets of data, as each system has its own unique response due to being a natural system. To average the results, several identical sets of experiments must be completed, only then can the values be averaged. A single set of data can take up to two weeks to collect depending on the steps taken making this a long and extensive process.

3.2.2. Applying an EEC of choice

Initially when employing the newer EEC, it was identified that it was unable to fit a common multimodal phase-response. On the other hand, this EEC's major advantage, as is explained in chapter 1.6.5.2, is that it is more appropriate to the physical model than the previously used R-RC-RC-C EEC. As such, to observe relevance, one major assumption and a few steps were taken to determine if the EEC should continue to be used. The major assumption in this case is that the lowest-frequency observable mode in a Bode typically represents sealing areas of the bilayer which also are not of interest in this case. To be able to ignore the lower-frequency mode using a cut off, first the lower frequency limit, or f_{\min} , would need to be studied, then the compromise between f_{\min} position and changing responses would be studied, and finally the error incurred by locking the f_{\min} modelling position between certain sets of data would be studied. Overall, the following steps (outlined below) determined that the updated EEC would be used for future modelling.

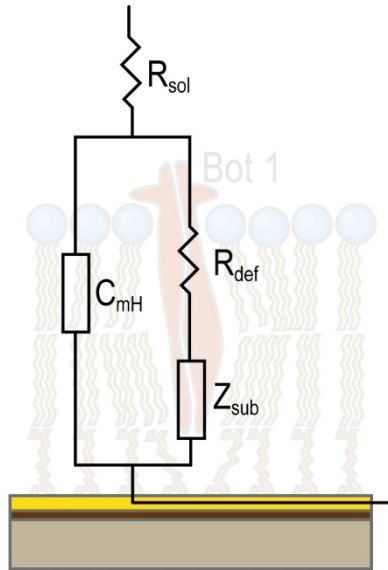


Figure 18: The EEC circuit used to interpret the tBLM with defects.

This EEC is represented in Chapter 1.6.5.2 as a simpler circuit.

3.2.2.1. EEC Error: Applicability and Frequency Range Selection

To be able to focus on the Bode plot phase's higher-frequency mode, it was important to understand: 1) the weighting that the lower frequency parameter, f_{\min} , had on the fitted values of the EEC and 2) if f_{\min} was extended to increasingly lower frequencies, how significantly the fitted values would be effected.

A specific tBLM response result was selected for testing this process, where the data was stable across all time domains between 100,000 Hz and 0.0005 Hz and had a clear bimodal phase response. The data was auto-fitted between an f_{\max} of 840Hz and increasingly lower frequency limits, shown in Figure 19 and Table 2 with f_{\min} decreasing from 0.25 Hz to 0.0005 Hz. Observing Figure 19, the EEC's fitting was unable to match the lower-frequency mode of the phase difference, and in fact visually seemed to worsen with an increasingly lower f_{\min} boundary, however, the impedance response matched in all cases.

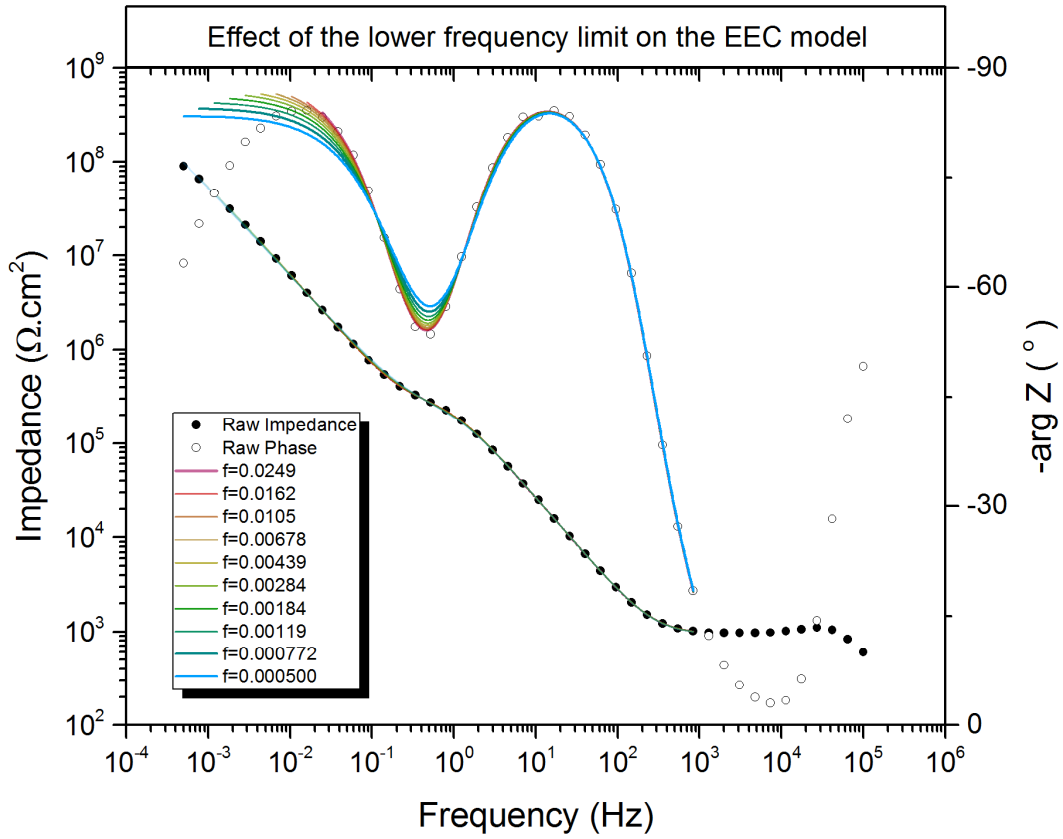


Figure 19: Bode plot representing the effect of lowering f_{\min} on auto-fitting.

Closed shapes refer to the impedance trace whereas the open symbols refer to the phase trace.

Table 2: Effect on EEC values by extending the f_{\min} value during fitting.

Fit	F_{LowerLim} (Hz)	R_{def} ($\text{M}\Omega\cdot\text{cm}^2$)		C_{mH} ($\mu\text{F}\cdot\text{cm}^2$)		Z_{sub} ($\Omega\cdot\text{s}^{-\alpha}\cdot\text{cm}^2$)		Alpha		χ^2
1	0.0249	0.38	± 0.0024	0.597	± 0.0012	1.79	± 0.0081	0.98	± 0.00272	0.000192
2	0.0162	0.38	± 0.0026	0.597	± 0.0013	1.79	± 0.0084	0.97	± 0.00253	0.000233
3	0.00461	0.37	± 0.0030	0.597	± 0.0016	1.78	± 0.0099	0.97	± 0.00270	0.000357
4	0.00679	0.37	± 0.0039	0.597	± 0.0020	1.77	± 0.013	0.96	± 0.00313	0.000631
5	0.00439	0.37	± 0.0053	0.596	± 0.0028	1.75	± 0.017	0.96	± 0.00392	0.00127
6	0.00284	0.37	± 0.0071	0.596	± 0.0038	1.73	± 0.023	0.95	± 0.00481	0.00238
7	0.00184	0.36	± 0.0098	0.596	± 0.0053	1.70	± 0.031	0.94	± 0.00608	0.00459
8	0.00119	0.35	± 0.013	0.595	± 0.0072	1.67	± 0.040	0.93	± 0.00757	0.00840
9	0.000772	0.35	± 0.017	0.596	± 0.0094	1.63	± 0.051	0.92	± 0.00915	0.0141
10	0.000500	0.34	± 0.022	0.596	± 0.012	1.58	± 0.062	0.91	± 0.0110	0.0227
%dif		-11.7%		-0.167%		-13.3%		- 7.70%		N/A

Note: %_{dif} = the percentage change to the final EEC value (10) from the first EEC value (1)

When modelling using EECs, an error of 1-5%, and as high as 10%, is observed in literature and considered acceptable [30, 130, 182]. However, this process will instead use the published accepted chi-squared cut-off value of 0.0015 for future discussion [183, 184]. The most appropriate boundary was determined to be between an f_{\max} of 840 Hz and an f_{\min} of 0.0249 Hz (Table 2, Fit 1), as the error of any single element was less than 1% and the overall chi-squared value was over an order of magnitude less than the maximum allowed. When the EEC was fitted 1.75 decades lower (using an f_{\min} of 0.500 mHz, Table 2, Fit 10), the deviations of R_{def} , Z_{sub} , and alpha were all below 10% (6.4%, 2.0%, 3.9% respectively), on the other hand, the chi-squared value was 0.0227, well over the 0.0015 cut off value.

Although all the fits were acceptable by percentage-error, only the first five were in fact useable based on their chi-squared value, with Fits 1 to 5 having chi-squared values either equal to or less than 0.00127. As such, it was concluded that the EEC model's semi-appropriate fit affected the chi-squared value undesirably, with the chi-squared value almost doubling with each successive decreasing f_{\min} data point. Therefore, to maintain an appropriate fit, the f_{\min} value would need to be controlled carefully such as to pass the chi-squared threshold and each element's value still have a reasonable error. This outcome, of course, is specific to this example, however, a) the fitting process itself was observed to be successful and b) could be adjusted for other cases.

3.2.2.2. EEC Error: Position of f_{\min} on EEC Output

The second question which remained was to quantify how much the EEC values changed with a changing f_{\min} . When fitting the data to increasingly lower frequencies, the EEC values decreased. The impedance of the sub-membrane space was most affected, followed by the resistance of the defect, the alpha value, and finally the capacitance of the membrane-Helmholtz layer. In the most extreme case, the values changed by -13.3, -11.7, -7.7, and -

0.167% respectively (Table 2, Fit 10 in comparison to Fit 1). On the other hand, the previously accepted Fit 4 indicated changes of 2% max, with the other values changing less (in comparison to Fit 1). As such, the effect of the position of f_{\min} on EEC values is minimal at first, however, it can be significant and as such its position should be selected carefully.

Two major conclusions can be drawn from these outcomes, first that the chi-squared value is a useful indicator of error and will be employed in further fitting, able to indicate too-low f_{\min} values, and secondly that changing the f_{\min} value can change the fitted EEC values significantly, potentially overwhelming or masking physical membrane changes.

3.2.2.3. EEC Error: Locking f_{\min} Values Between Sets

During EEC fitting processes, it was noticed that by only changing the fitting frequency ranges, the values representing each element of the EEC would change, sometimes significantly; part of this change is physical whereas part is nonphysical, that is, some of this is due to a change of information for auto-fitting from collected data and part is due to a difference in influence of the data on the auto-fitting process. Therefore, to not overwhelm the physical changes to the membrane with changes due to changing EEC frequency parameters, the f_{\min} value would be locked between specific sets of data; such as *bilayer before ethanol in both NaCl and KCl* (Figure 20) while being unlocked and changed if needed between two different ethanol concentrations.

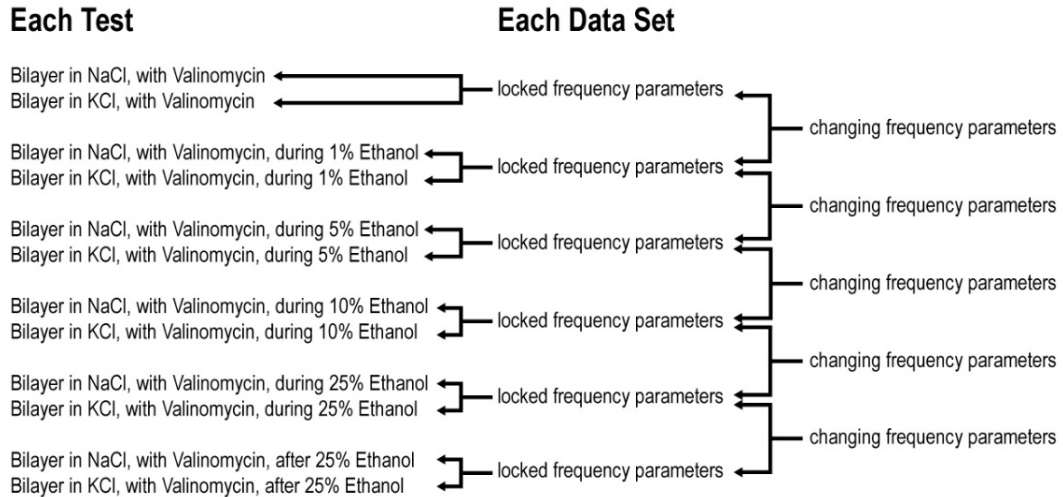


Figure 20: A diagram explaining where EIS f_{\min} cut-offs were locked during data fitting.

The parameters are changed or kept constant to minimise error between certain data comparisons.

This compromise (lock of f_{\min} value) is not without fault and requires investigation. For example, focusing on some ethanol data seen later, due to the fitting method Table 9 displayed significantly larger chi-squared error values during KCl conditions as compared to their NaCl counterparts. Furthermore, the data (Figure 42 to Figure 47) indicates that as the ethanol concentrations increased the frequencies at which the defect resistances appeared also changed and to accommodate for this change, fitting frequency parameters were also adjusted. Thus, changing the frequency parameters between sets of data introduced greater non-physical error when comparing fittings between data sets (such as *before 1% ethanol* and then *after 1% ethanol* – see Figure 20).

Thus, because the defect resistances are larger under NaCl conditions than under KCl conditions, the NaCl conditions need to be fitted using larger (generally lower) frequency ranges which are not needed to fit KCl conditions, forcing the EEC to fit extraneous data under

KCl conditions and adjusting certain EEC values non-physically but also increasing the chi-squared error.

Overall, it is important to note that locking f_{\min} for a set of data results in increased intrinsic error between data sets, therefore more error should be implied when comparing EEC values between sets of data. However, the higher chi-squared values for KCl solutions are offset by limiting the non-physical error within each data set and increasing the significance when comparing values.

In conjunction with using the chi-squared value, it was decided that, to limit error, the frequency parameters (f_{\min} and f_{\max}) could be changed between sets of data, i.e. for the HvBot1 data seen later, changed between pH 6, 7.5, 9, etc, however, within each set (eg. pH6 without conduction, pH6 with conduction, and again pH6 without conduction) the parameters would be kept constant, or locked.

3.3. CV and Reductive Desorption

Cyclic Voltammetry and reductive desorption were used together to calculate the coverage of a thiol bound to a surface. First the area of the gold was calculated followed by the charge needed to desorb the thiol.

3.3.1. Au(111) surface area calculation

Gold area was collected from a plot similar to Figure 32, and the specific peak of interest was the AuO reductive peak between 750 mV and 1100 mV.

Before calculating the gold area from Figure 33, the charge density of the gold surface was defined. Figure 21 represents a $(\sqrt{3}\times\sqrt{3})R30^\circ$ gold surface and the area of the equilateral triangle (black and blue combined) represents one half of a gold atom.

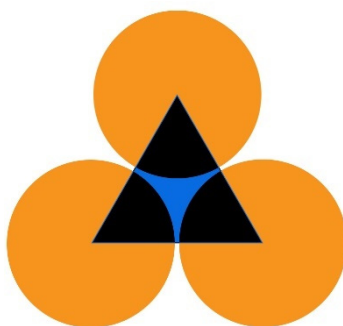


Figure 21: A diagram representing the structure of Au(111)

$(\sqrt{3}\times\sqrt{3})R30^\circ$ Au(111) architecture. Distance between each gold atom is 2.886 Å as per [185].

The first step was to calculate the number of gold atoms per square centimetre on a perfectly smooth surface. Knowing that the distance between each gold atom is 2.886 Å using Figure 21, the area of the portrayed triangle is as follows:

$$\text{Area of Triangle} = 0.5 \times 2.886 \times 10^{-8} \times \sqrt{3} \times 1.443 \times 10^{-8} = 3.6065 \times 10^{-16} \text{ cm}^2$$

Therefore, the number of gold atoms per 1 cm² is

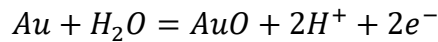
$$\frac{1}{2 \times 3.6065 \times 10^{-16}} = 1.386 \times 10^{15} \text{ atoms}$$

The charge density of a gold surface is therefore

$$1.386 \times 10^{15} \text{ cm}^{-2} \times 1.6 \times 10^{-19} \mu\text{C} = 222 \mu\text{C} \cdot \text{cm}^{-2}$$

Note, the standard model for gold oxidation and desorption indicates two electrons are lost for each gold atom, as per Equation 14, and as such, to account for each oxygen's desorption, the charge density of an Au(111) surface is doubled and equal to 444 $\mu\text{C} \cdot \text{cm}^{-2}$.

Equation 14: Description of the oxidation of an Au(111) surface.



Now that the theoretical charge density of the Au(111) surface has been determined, the charge required during the desorption of the oxygen could be compared. For example, the total integral may have been 0.162 mA.mV; at a rate of 25 mV.sec⁻¹, by dividing the integral by the rate, the overall charge was 0.00065 mV.sec, or 0.65 $\mu\text{Coulombs}$.

Therefore, comparing the charge collected from the gold to the theoretical charge, the area of the gold surface was:

$$\frac{6.5 \times 10^{-1} \mu\text{C}}{444 \mu\text{C} \cdot \text{cm}^{-2}} = 0.0015 \text{ cm}^2$$

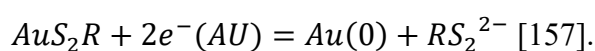
Note, this process, though straightforward, is discussed in more depth in chapters 3.3.2 and 3.3.3 - due to difficulties.

3.3.2. Reductive desorption coverage calculation

The second key step to determining thiol surface coverage is determining the charge required to reductively desorb the thiols from the same surface. By completing a cyclic Voltammetry scan of the thiol coated surface, the reductive desorption peak for DPhyTL is observed at -970 mV, as in Figure 33. To calculate the surface coverage, the area (or integral) of the reductive peak is divided by the rate before being divided by the charge density required to desorb thiols, i.e. $77 \mu\text{C}.\text{cm}^{-2}$.

Note: This process with DPhyTL requires two thiols to be removed per DPhyTL molecule (Equation 15) and as such, theoretically, the charge density can be doubled or the charge required for desorption halved.

Equation 15: Description of the reduction of a di-thiol (such as DPhyTL) from an Au(111) surface.



$$\frac{[\textit{Integrated Area}] \textit{mA}.\textit{cm}^2.\textit{mV} \times 1000}{[\textit{Rate}] \textit{mA}.\textit{sec}.\textit{cm}^{-2}} = x \textit{C}.\textit{cm}^2$$

$$\frac{x \textit{C}.\textit{cm}^{-2} \times 2}{77 \textit{C}.\textit{cm}^{-2}} \times 100 = \textit{Percentage Area of thiol on gold}$$

3.3.3. Issues with CV and reductive desorption curve integration

To calculate the coverage of DPhyTL on an Au(111) surface, two separate forms of area integration were tested due to a poor signal to noise ratio of some results; such as that seen in Figure 22. The comparison is shown as follows.

After importing the data into Origin (Ver. 9, OriginLab, Northhampton, MA, USA), the data was plotted on an X-Y plot (Figure 22). Integrating the data using Origin, an absolute area of 73.9 mV.mA was found (using the *Analysis -> Mathematics -> Integrate* command).

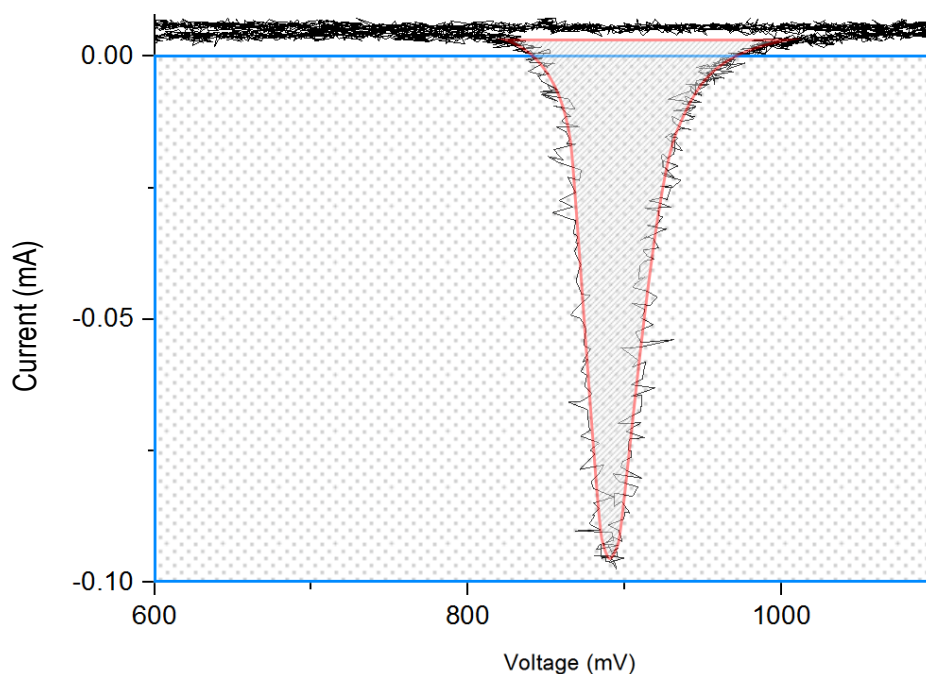


Figure 22: Example CV gold reductive peak of Au(111) in H₂SO₄.

An example of the integration method using Adobe Photoshop CC. The red (diagonal patterned) area is the integrated area of the desorption curve whereas the blue (dotted patterned) area is the integrated area used to represent each pixel's mV.mA⁻¹ in the graph - used to determine the overall area of the curve mA.mV.

The integrated area as a function of voltage is shown in Figure 23, and what becomes apparent is that the noise is considerable.

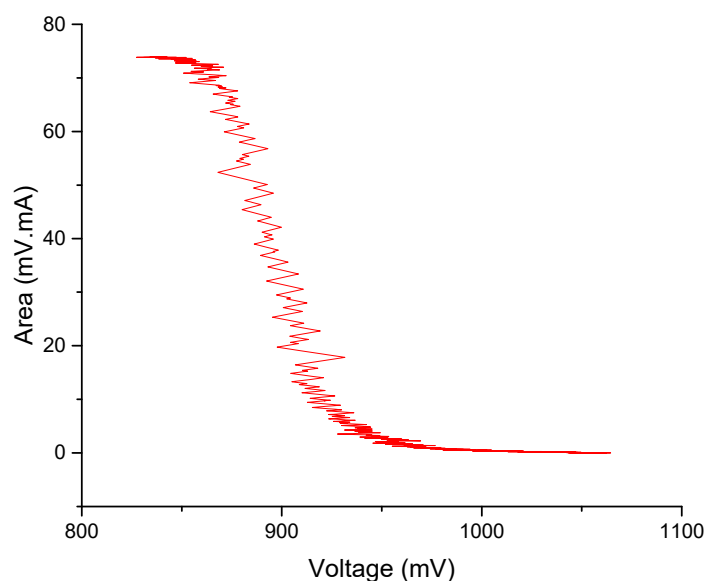


Figure 23: Integration curve of Figure 22 using Origin.

Example: Sample 7A (see Table 7). Parameters for integration: 1050 mV to 847 mV

On the other hand, Adobe Photoshop CC was used to calculate the area of the peaks, and using the same data in Adobe Photoshop CC, the area was found to be 4.86 mV.mA; less than a tenth the size, and therefore the Adobe Photoshop CC process was used due to the information outlined below.

The example piece of data collected of an Au(111) surface was imported into Origin and exported into Adobe Photoshop (see Figure 22).

Two key pieces of data were taken at this point: the equivalent area (mA.mV) which each pixel represents in the graph (using the blue dotted rectangle) and the number of pixels represented by the curve of the gold response (red diagonal-stripped shape). From here, several calculations were needed.

Calculating the area (mV.mA) defined by the curve was completed as follows:

$$\text{Area of rectangle: } 500 \text{ mV} \times 0.1 \text{ mA} = 50 \text{ mV.mA}$$

Using Adobe Photoshop CC's *Rectangular Marquee Tool*:

$$\text{Number of pixels in rectangle: } 461753$$

$$\text{Area per pixel in the graph: } \frac{50 \text{ mVmA}}{461753} \cong 0.000108283 \text{ mV.mA.pixel}^{-1}$$

Using Adobe Photoshop's *Pen Tool* to create vector outlines which were converted into shapes using the *Make Selection Tool*:

Area under the graph

$$\begin{aligned} &= [\text{Area per pixel}] \times [\text{pixels within the red (diagonal pattered) curve}] \\ &\cong 4.86 \text{ mV.mA} \end{aligned}$$

The integrated area interpreted by Photoshop, in this case, was 4.86 mV.mA, whereas Origin's equivalent was 73.8 mV.mA (in absolute-area mode, and baseline set to 'use end points as straight line'); this difference is greater than an order of magnitude, however, a further calculation of gold surface area is the defining feature of the difference between the two modes of area calculation.

Consider the surface area of the Au(111) surface, its diameter was typically between 0.2 and 0.5 cm. A quick calculation of area based on the various diameters in this range is shown in Table 3 below.

Table 3: Surface area of a flat and circular electrode of various diameters.

Note: All values only consider a 2D surface, which theoretically Au(111) is.

Diameter (cm)	Area (cm ²)
0.5	0.20
0.45	0.16
0.4	0.13
0.35	0.096
0.3	0.071
0.25	0.049
0.2	0.031

Now, consider the integrated result from Photoshop (4.86 mV.mA):

$$\frac{\text{Area (mA.mV)}}{\text{Rate of measurment (mV.sec}^{-1}\text{)}} = \frac{4.86 \text{ mA.mV}}{25 \text{ mV.sec}^{-1}} = 0.022 \text{ mA.sec} = 22 \text{ }\mu\text{Coulombs}$$

A standard Au(111) surface has a charge per square centimetre of 444 $\mu\text{C.cm}^2$ (Chapter 3.3.1 for more information), and as the charge calculated from the reductive desorption of the gold surface was 22 μC , the surface area of the electrode in contact with the solution is:

$$\frac{22 \text{ }\mu\text{Coulombs}}{444 \text{ }\mu\text{Coulombs.cm}^{-2}} \cong 0.050 \text{ cm}^2$$

This value is appropriate to the size of the electrode. Using the integrated area Origin suggests offers an electrode surface area approximately 6.64 cm^2 , or an electrode diameter of approximately 1.4 cm, which is unrealistic keeping in mind that the surface is meant to be planar. As such, Adobe Photoshop CC was used to complete any further integrations instead of Origin.

3.4. fs-vSFG

The process of analysing the fs-vSFG spectrum is rudimentary. Data for all samples was collected and during each sample, a polystyrene film was placed in the beam path to collect a polystyrene spectrum as well. The data's polystyrene spectra were used to adjust the graphs based on the polystyrene peaks exemplified in Figure 24 below.

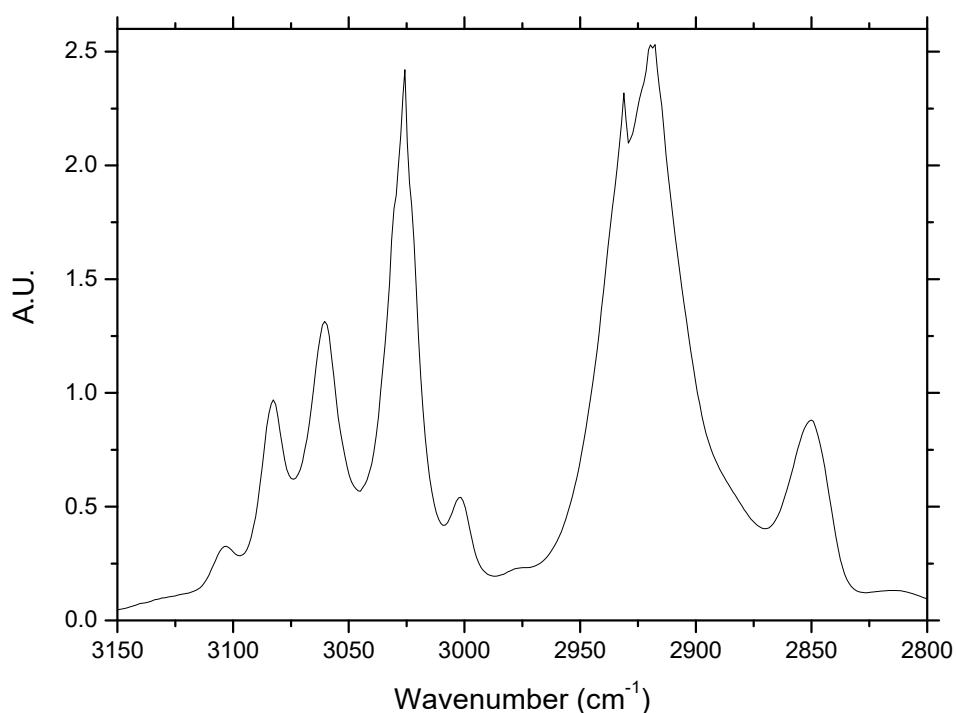


Figure 24: A standard fs-vSFG spectrum of a polystyrene film in air.

The surface of choice was sputtered gold, which creates a significant background spectrum (red line, see Figure 25) which requires normalisation [161].

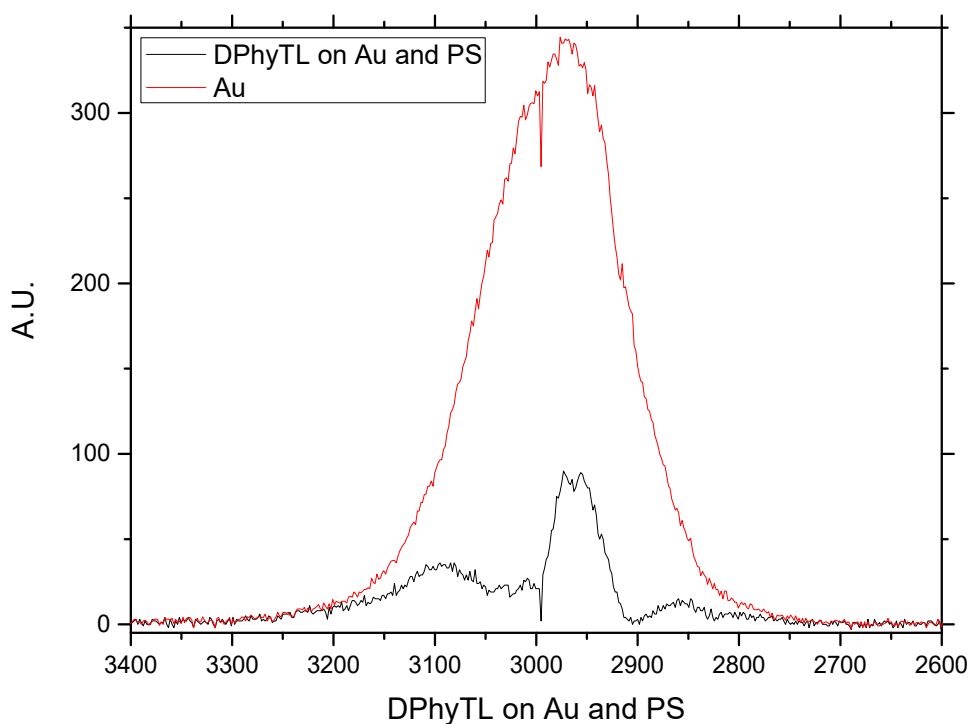


Figure 25: fs-vSFG spectra of DPhyTL with polystyrene on Au and a bare gold surface

Note: (Black) DPhyTL-coated gold with a polystyrene film in the beam-path before normalisation. (Red) A clean bare-gold spectrum (red).

After aligning the polystyrene spectrum to its relevant peaks, the gold background was adjusted to fit the sample, before the DPhyTL was normalised using the gold background; the outcome of this leaves peaks which are more well defined and accurate in representation.

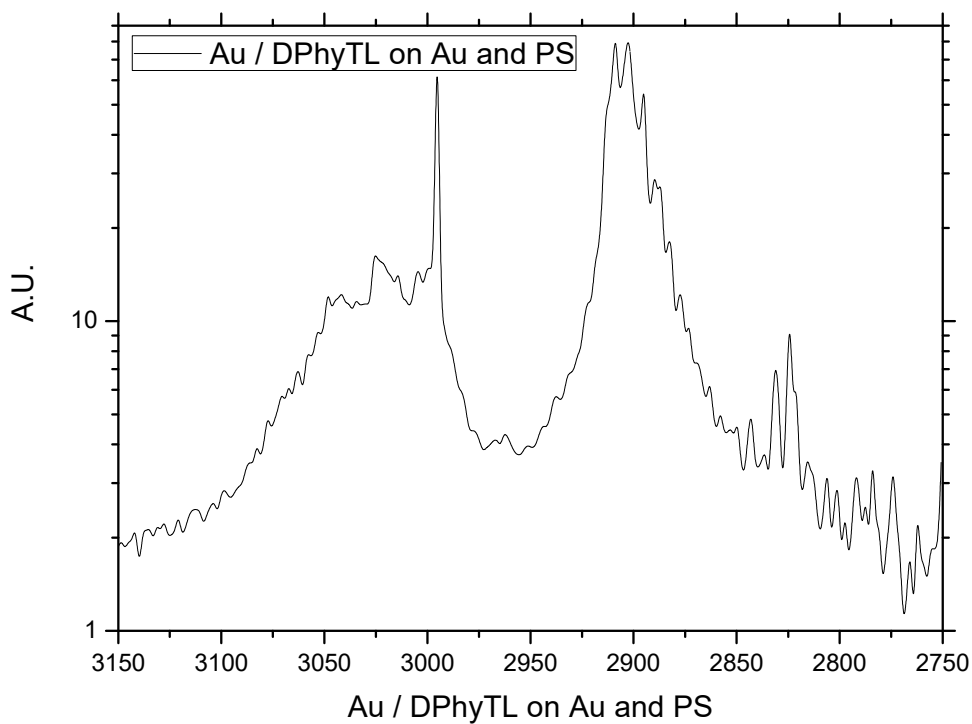


Figure 26: fs-vSFG spectrum of DPhyTL on Au with polystyrene after normalisation.

Note: This spectrum can be directly compared to Figure 25.

This process was repeated for all spectra which were used in the interpretation of fs-vSFG spectra regarding the tBLM. All data during testing was collected in replicate, typically collected twice.

3.5. Neutron Reflectometry

The NR technique involves specular reflection whereby the angle of the incident beam is equal to that of the reflected beam. The reflected beam angle is determined by the momentum transfer vector (q_z), stated in units \AA^{-1} , where the z-direction is orthogonal to the film and the amount a neutron is scattered depends on the neutron wavelength and its incident angle (Equation 16). By keeping the neutron wavelength the same, the scattering angles can be studied and presented as reflected intensity (relative to the incident beam) as a function of scattering vector (Figure 27) [186].

Equation 16: The ‘momentum transfer vector’ or ‘scattering vector’ equation.

Where λ is the neutron wavelength and θ is the neutron beam incident angle [168].

$$Q \equiv q_z = \frac{4\pi\sin(\theta)}{\lambda}$$

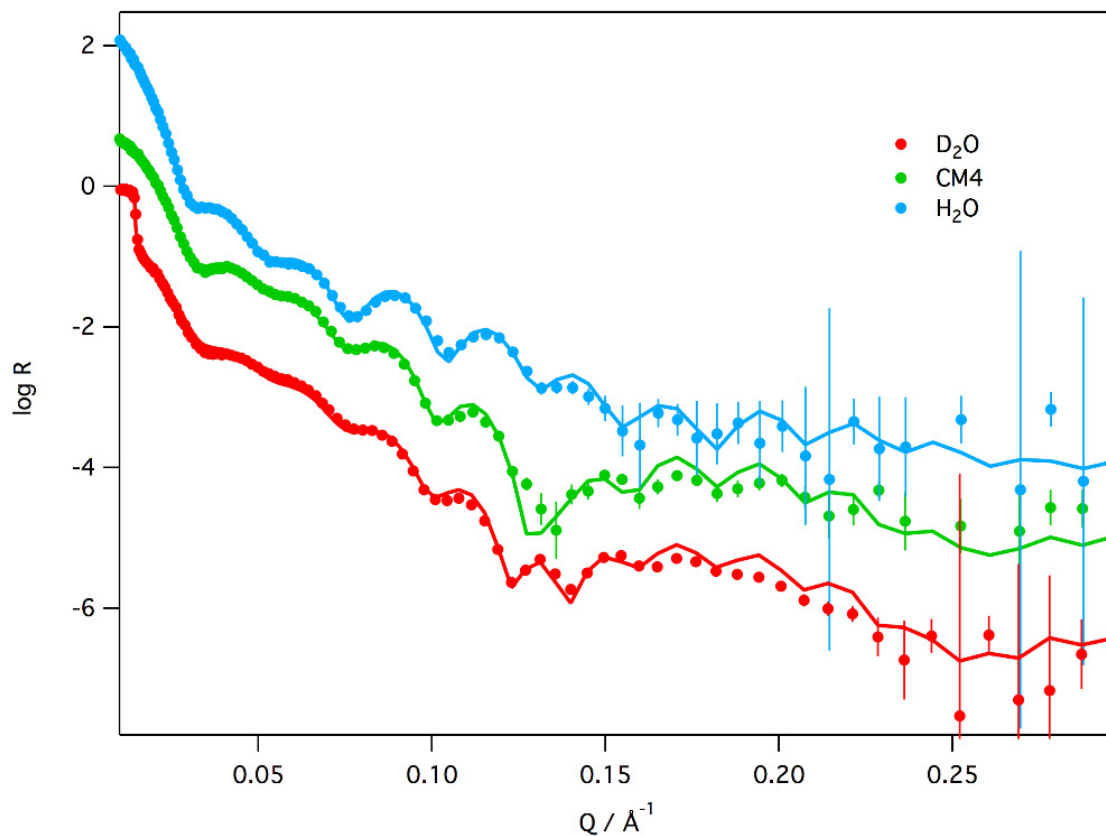


Figure 27: Example NR reflectivity curves of three different solvent ratios as a function of Q of a tBLM.

Note: Log R is the intensity and Q is the scattering vector.

The roughness of the surface directly affects the sharpness of the peaks (Equation 17).

The smoother, or flatter, the surface is, the sharper the peaks will be.

Equation 17: The ‘momentum transfer vector’

Where d is the sample’s general object size.

$$Q \equiv q_z = \frac{2\pi}{d}$$

Prior to starting the NR experiments, small-angle x-ray scattering was used to determine the thickness of the gold surface to aid modelling accuracy later. Once completed, NR measurements were taken. Before modelling the NR data, the background was subtracted and any detector inefficiency was corrected for before each diffraction peak was integrated.

The nSLD profile is the sum of the coherent neutron scattering lengths of all atoms in that layer divided by that layer in one-dimension (z-axis) as a function of film-depth [168]. The nSLD profile cannot be determined directly from the measured $|Q|^2$ values and instead needs a model to be applied. The model, which in the case of MOTOFIT, is a slab model and is described by Nelson [2006]. Applying the Abeles method, at least five parameters are fitted per layer of the film [168, 186, 187]. The neutron scattering length density (nSLD) profile used the following layers: silicon oxide, chromium, gold, DPhyTL tether region, DPhyTL inner leaflet, DPhyPC outer leaflet, and DPhyPC head groups. MOTOFIT was run using IGOR Pro (Wavemetrics, Lake Oswego, OR, USA) environment. The parameters used for fitting each layer include: the instrumental scale factor, the SLD, the sample background, the Gaussian roughness of the sub-phase thickness, and surface roughness [168]. Furthermore, MOTOFIT allows different contrasts to be combined to aid fitting. Overall, the data obtained provides structural information at high resolution (Figure 28) [188]. Note: for these experiments, three wafers were used to average the results.

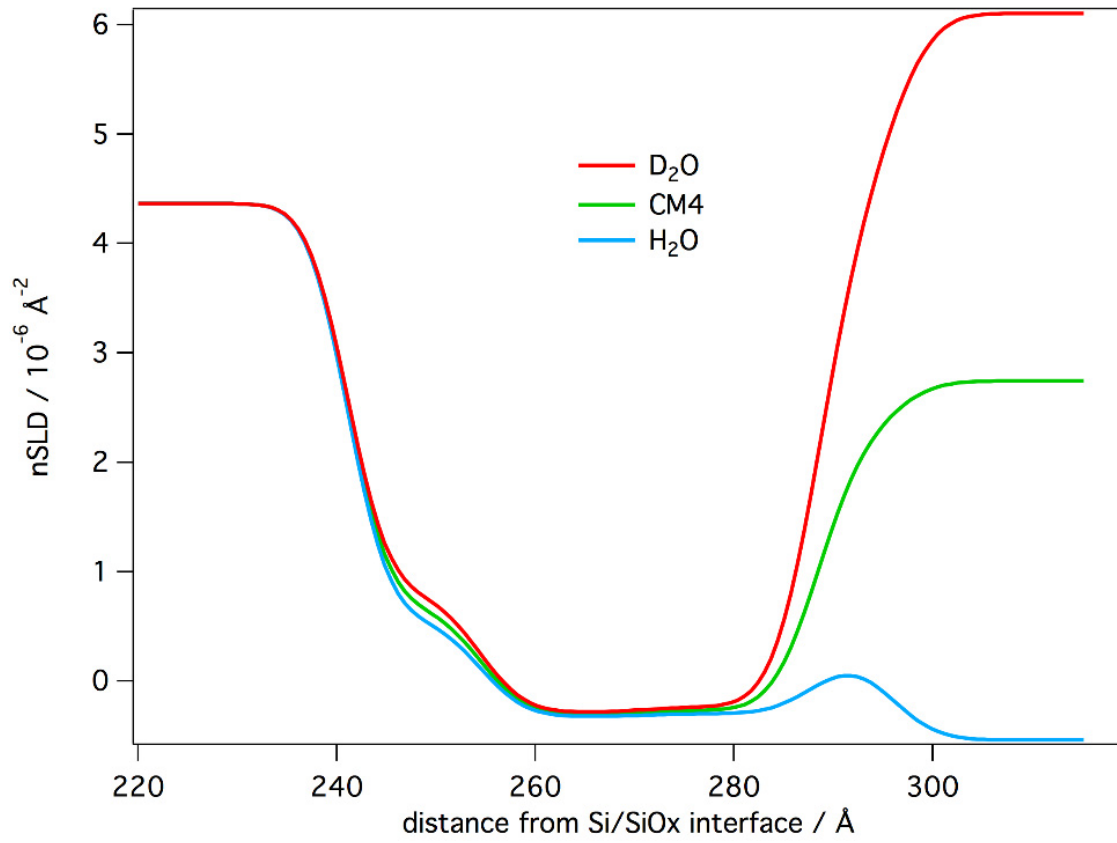


Figure 28: Example NR nSLD profile of each contrast solution while testing a tBLM.

4. Results: Ethanol and tethered membranes

4.1. Chapter Overview

In this chapter the effects of ethanol on the structure and function of a tBLM are studied in two parts.

First, EIS is used to study the effects of ethanol on the electrical properties of a DPhyTL-DPhyPC bilayer. Then, FTIR, NMR, CV, fs-vSFG, and NR are used to study structural changes to the same tBLM system. Prior to using fs-vSFG, FTIR and NMR are used to check the purity of the DPhyTL followed by FTIR which is used further to determine the peaks used for fs-vSFG studies. CV is used to check the DPhyTL monolayer packing density. fs-vSFG is then used to determine the effect of ethanol on the membrane. To complete the series of experiments, NR is used to detail the interactions and effects of ethanol on the tBLM at various concentrations.

Secondly, EIS is used to study whether the effects of ethanol on the membrane effect the performance of Valinomycin.

4.2. Introduction

60-70% of pharmaceutical drugs currently on the market target membrane proteins. Although many drugs interact with membrane-proteins, drug-membrane research is underrepresented.

To study the interactions of drugs with membranes, rather than using a complex drug which includes various side groups, ethanol was chosen as it only contains the ethyl and hydroxyl groups, limiting the possible interactions of the drug with the lipid bilayer membrane. Previous studies of ethanol completed in the lab used both bacterial and eukaryotic systems, however, both examples have limited specificity as cells host thousands of different lipids and molecular pathways which mitigate unwanted circumstances. On the other hand, model membranes studied in the lab mainly used atomic force microscopy, micro-pipetting, or electron paramagnetic resonance systems, all of which are unable to define electrical membrane properties and, furthermore in those cases, the membranes are not tested supporting pores, proteins, or peptides (Chapter 1.5.3). Computer simulations have also been used but include approximations or short time frames which limit their model's complexity or results. Current studies suggest that, depending on the concentration, ethanol interacts with the headgroup region of phospholipid membranes, traverses the membranes, and interacts with the solution underneath the membrane, and/or interacts with the alkyl tails of the lipids and effects membrane fluidity (1.5.3).

The concentrations of ethanol which will be studied in this thesis are well-above what is observed in the human body (Table 4). A Blood Alcohol Concentration (BAC) of 0.05, which in Australia is the legal driving limit of ethanol in the blood, is equivalent to approximately 0.06%_{v/v} while a BAC of 0.5 (or 0.64%_{v/v}) will typically cause the intoxicated human recipient

to lose consciousness [189]. This thesis begins at 1%_{v/v}, where only permanent electrical changes and no visible permanent physical changes are observed (with the techniques used); this is likely because the model system is robust and includes far fewer components than a living membrane.

Table 4: Blood Alcohol Concentration (BAC) in terms of concentration and %_{v/v}.

Green text-colour highlights the approximate ethanol concentration range which has been used within this thesis' experiments. Note: Equation: $BAC = g_{(ethanol)} / 100mL_{(blood)}$ [190].

BAC	Ethanol (g.L ⁻¹)	Ethanol (mL.L ⁻¹)	Experimental Sample Ethanol % _{v/v}
0.05	0.5	0.6337	0.064
0.5	5	6.337	0.64
1	10	12.67	1.3
5	50	63.37	6.4
10	100	126.7	13
25	250	316.9	32
50	500	633.7	63
78.9 (max)	789	1000	100

To investigate the interactions of ethanol either in or with a cellular membrane, a DPhyTL-DPhyPC tBLM tethered to gold was used. This tBLM uses a lipid which represents approximately 55-60% of all lipids in natural membranes and with its metallic substrate enabled a number of techniques to be used to study its electrical and physical properties [4, 21, 191]. To study the interactions of ethanol with the membrane in greater detail, several techniques were used. EIS was used to observe overall electrical changes to a tBLM, focusing on the effect of ethanol on the properties of a membrane as well as a peptide Valinomycin. SFG was used to determine the position of ethanol on the bilayer. Neutron Reflectometry was used to clarify and confirm both the EIS and SFG results.

4.3. Ethanol's Effects on a tBLM

4.3.1. EIS Analysis

Tethered membranes consisting of DPhyTL-DPhyPC were formed by being self-assembled on gold and completed using vesicle fusion. The surfaces were then exposed to various ethanol concentrations. The electrical properties of the membranes were monitored and later modelled. The tBLMs were modelled using the EEC shown in chapter 1.6.5.2 and the EEC values for each fit are shown in Table 5. Each case in Table 5 is a representation of the membrane after washing.

Several clear indicators suggest ethanol is interacting with the membrane. The most significant changes are found in the defect resistance (R_{def}), the change in impedance of the sub-membrane space (Z_{sub}), and the alpha value. Although there are changes to the membrane-Helmholtz capacitance (C_{mH}), the changes are within error and do not follow an obvious pattern and as such will not be discussed further.

Table 5: Effects of ethanol on fitted EEC values of a DPhyTL-DPhyPC bilayer.

Data is normalised for a surface area of 0.28 cm² and shown in Figure 48. The chi-squared value of each fit is appropriate (less than 0.0015) and the percentage error for all circuit elements, but one, is less than 10%. Note, in each case the same frequency parameters, f_{min} and f_{max} are used to limit non-physical error and improve comparisons, therefore the EEC values between the post-25%_{v/v} ethanol test in Table 5 and Table 9 differ slightly.

Sample	R_{def} (M Ω .cm ²)			C_{mH} (μ F.cm ²)			Z_{sub} (Ω .s ^{-α} .cm ²)			Alpha	χ^2
Bilayer with Valinomycin (NaCl)	2.80	±	0.19	0.715	±	0.020	0.668	±	0.057	0.58	0.00058
Bilayer after 1%(v/v) Ethanol (NaCl)	2.05	±	0.041	0.690	±	0.025	2.05	±	0.077	0.81	0.00087
Bilayer after 5%(v/v) Ethanol (NaCl)	0.782	±	0.0081	0.698	±	0.022	3.34	±	0.047	0.91	0.00050
Bilayer after 10%(v/v) Ethanol (NaCl)	0.384	±	0.0027	0.697	±	0.018	4.18	±	0.032	0.93	0.00032
Bilayer after 25%(v/v) Ethanol (NaCl)	0.463	±	0.0027	0.700	±	0.015	4.45	±	0.057	0.93	0.00023

Focusing on R_{def} , the resistance dropped by almost an order of magnitude throughout the length of the experiments. Using two sets of data, the second is shown in Appendix 6.6, Table 6 indicates that a significant change in R_{def} occurs at low concentrations (1-5%_{v/v}) and stabilises by 10%_{v/v} ethanol. These values were attained after multiple washing attempts, indicating significant and permanent electrical changes to the defect areas of the membrane.

Table 6: EEC R_{def} resistance at various concentrations of ethanol normalised to initial bilayer resistance.

All values are based on the R_{def} values of two identical experiments, second not shown.

Conditions	R_{def} as a %
Pre-ethanol	100
post 1%	71.2
post 5%	22.1
post 10%	11.0
post 25%	12.8

Addressing Z_{sub} in Table 5, the impedance increased seven-fold, however, this value must be studied in combination with the alpha value. The EEC alpha value was initially approximately 0.5 and after submerging the tBLM in both 1%_{v/v} and 5%_{v/v} ethanol solutions, the alpha value increased and stabilised at approximately 0.9. This change indicates that the sub-membrane space became increasingly capacitive (closer to 1) over the period of the experiments when initially the behaviour was resistive (closer to 0.5). It has been shown that such a low alpha value (0.5) is indicative of large defects and diffusion-controlled processes, however, as C_{mH} does not change during the experiments (and it is implied that as a capacitor its alpha value is 1), the membrane stays intact and instead the defects and sub-membrane space, by focusing on Z_{sub} , are affected [138].

Considering R_{def} decreases significantly, the capacitance of the membrane (C_{mH}) is stable, but both Z_{sub} and its alpha value increase significantly throughout the length of the experiments, it can be proposed that: 1) the organised sealing areas of the membrane as well as

the Helmholtz layer at the water-metal interface stay unchanged; 2) the defect areas of the membrane are affected, likely due to a change in packing density of the distal leaflet; and 3) the properties of the sub-membrane space, above the Helmholtz layer, change, with the water molecules potentially being replaced by a greater concentration of ions or ethanol molecules in the areas below and around the defect.

As the sub-membrane space is becoming increasingly capacitor-like and the impedance values of Z_{sub} are continuously increasing, as per Equation 18, either the dielectric permittivity (due to ion concentration) or the thickness of the sub-membrane space must be changing [81].

Equation 18: Fricke's application of dielectric values to membrane capacitance.

Note: $A = 1 \text{ cm}^2$, $\epsilon_0 = \text{permittivity of free space}$, ϵ or $\epsilon_m = 2.0\text{-}2.2$, and d or t_m are the bilayer's thickness [47].

$$C_m = \frac{A\epsilon_0\epsilon_m}{t_m}$$

It is likely that replacing the ions and/or water molecules below the membrane with ethanol could cause an increase in insulating capacity of the tether region. This change would also limit ions passing through the sub-membrane space due to the inclusion of a bulkier molecule. It is less likely that a thinning of the tether region is occurring considering that the tether is unable to shorten due to density and stearic hindrance.

4.3.2. FTIR, NMR, and CV analyses

4.3.2.1. FTIR

Figure 29 and Figure 30 outline the vibrations observed in the carbon-oxygen and carbon-hydrogen bonding regions of the IR spectra respectively; both spectra were collected together but have been shown as separate graphs. The deconvoluted peaks seen in both figures are based on Leitch et al. [2009]. Both figures' peak positions are found at their expected positions. In terms of peak strength, Figure 29 is similar to those published previously whereas Figure 30 includes a greater absorbance between 2900 cm^{-1} and 2800 cm^{-1} . No specific reason is given by the authors mentioned in the article beyond that of molecular orientation, stating that bulk DPhyTL exhibits a greater absorbance than an organised DPhyTL monolayer surface. Nevertheless, the CO and CH FTIR measurements indicate the bulk-DPhyTL is equivalent of what would be expected, with both the CH and CO spectra equating to those seen in Leitch et al. [2009] and to a lesser extent Naumann et al. [2003]. This data will not be discussed in any further depth except during fs-vSFG data interpretation later as the intended purpose is to observe whether the purifying process was successful and to observe the deconvoluted peaks.

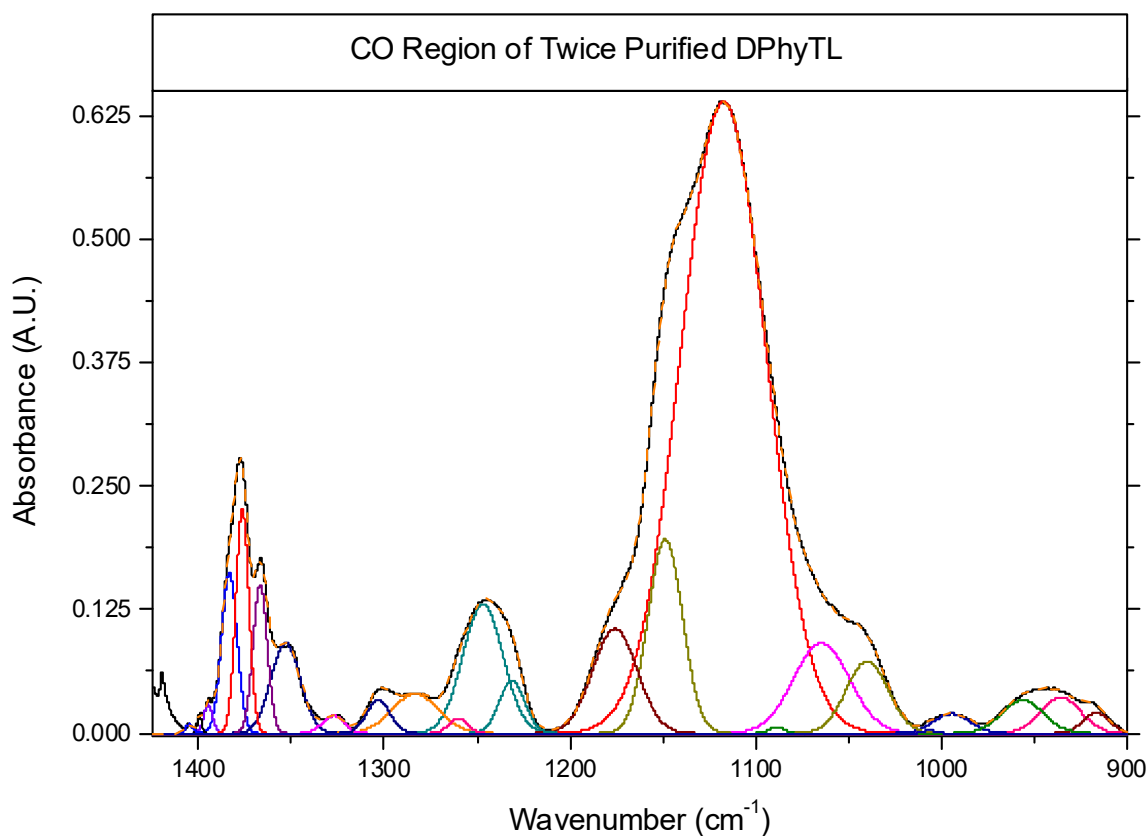


Figure 29: FTIR CO region spectrum of bulk DPhyTL.

Background and water has been removed from this spectrum. The thick black is that collected during FTIR measurements and the orange dotted line is the additive spectrum of all the deconvolutions, described in depth in Leitch et al. [2009] and Naumann et al. [2003]. Peak assignments from left to right: 1376 cm^{-1} , 1367 cm^{-1} , and 1352 cm^{-1} CH_2 gauche wag; 1327 cm^{-1} , 1300 cm^{-1} CH_2 trans wag; 1284 cm^{-1} CH_2 twist; 1244 cm^{-1} CH_2 twist; 1180 cm^{-1} , 1149 cm^{-1} , 1122 cm^{-1} , 1092 cm^{-1} , and 1073 cm^{-1} C-O, C-C stretch, CH_2 rock; 1043 cm^{-1} CO and C-C stretch as well as CH_2 rock; 994 cm^{-1} ; 960 cm^{-1} unknown; 941 cm^{-1} and 920 cm^{-1} CH_2 rock (gauche) and C-C stretch.

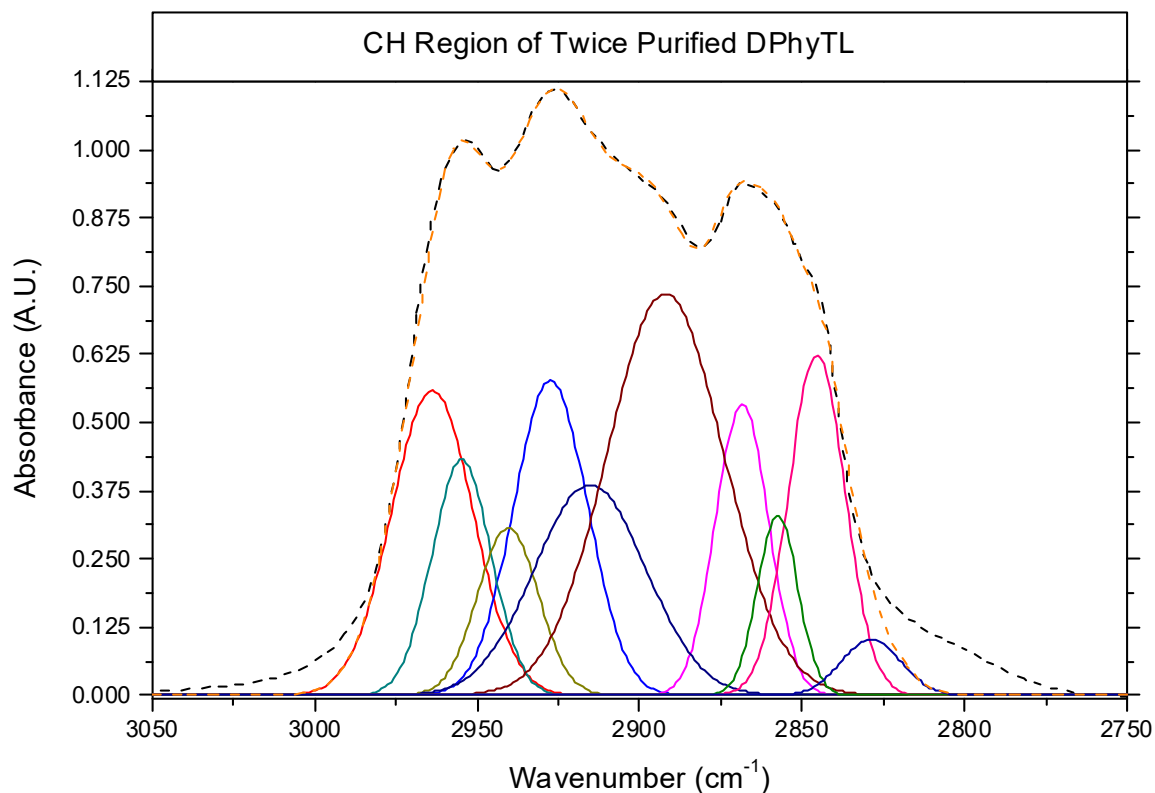


Figure 30: FTIR CH region spectrum of bulk DPhyTL.

Background and water has been removed from this spectrum. The thick black is that collected during FTIR measurements and the orange dotted line is the additive spectrum of all the deconvolutions, described in depth in Leitch et al. [2009]. Peak assignments from left to right: 2963 cm⁻¹ and 2951 cm⁻¹ $\nu_{as}(CH_3)$; 2939 cm⁻¹ $\nu_{as}(CH_2)$; 2926 cm⁻¹ $\delta_{FR}(CH_3)$; 2911 cm⁻¹ $\nu(CH)$; 2896 cm⁻¹ $\delta_{FR}(CH_2)$; 2868 cm⁻¹ $\nu_s(CH_3-m)$; 2856 cm⁻¹ $\nu_s(CH_2)$; and, 2845 cm⁻¹ $\nu_s(CH_3-t)$.

4.3.2.2. NMR

The NMR result of purified DPhyTL was compared to that collected by Breffa [2005]. The sample contained many similar features that were observed previously and as such no further analysis was needed. Furthermore, assigning each peak exemplified that the liquid was in fact bulk DPhyTL (Appendix Chapter 6.7). The NMR spectra of DPhyTL confirms the molecular structure and purity of the purified lipid (Figure 31).

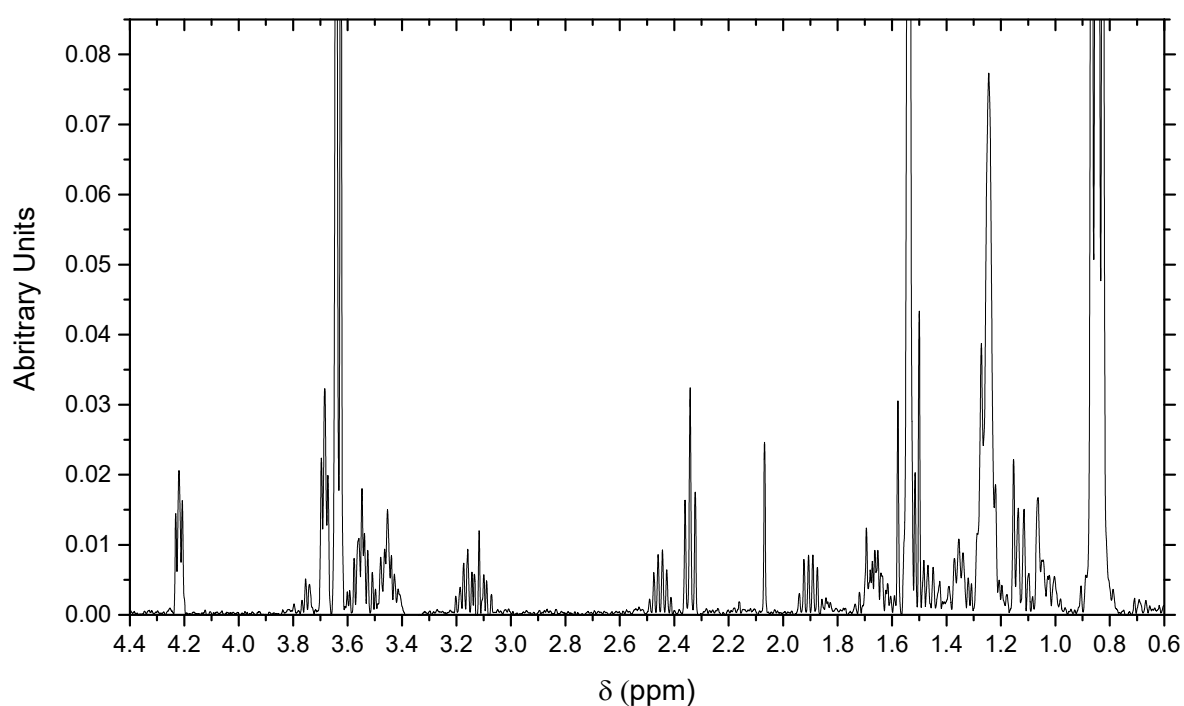


Figure 31: NMR (400MHz) spectrum of DPhyTL solution in chloroform-D.

For specific peak assignment using the method stated in 2.2.5 (Chapter 6.7).

4.3.2.3. Cyclic Voltammetry

Cyclic voltammetry was used to calculate the coverage of DPhyTL on a pure Au(111) surface to confirm the density of the monolayer. Collected cyclic Voltammograms are observed in Figure 32 and Figure 33, where Figure 32 is an example of a Voltammogram of an Au(111) surface before lipid monolayer attachment and Figure 33 is an example of Voltammogram of the DPhyTL from the same gold surface after monolayer formation.

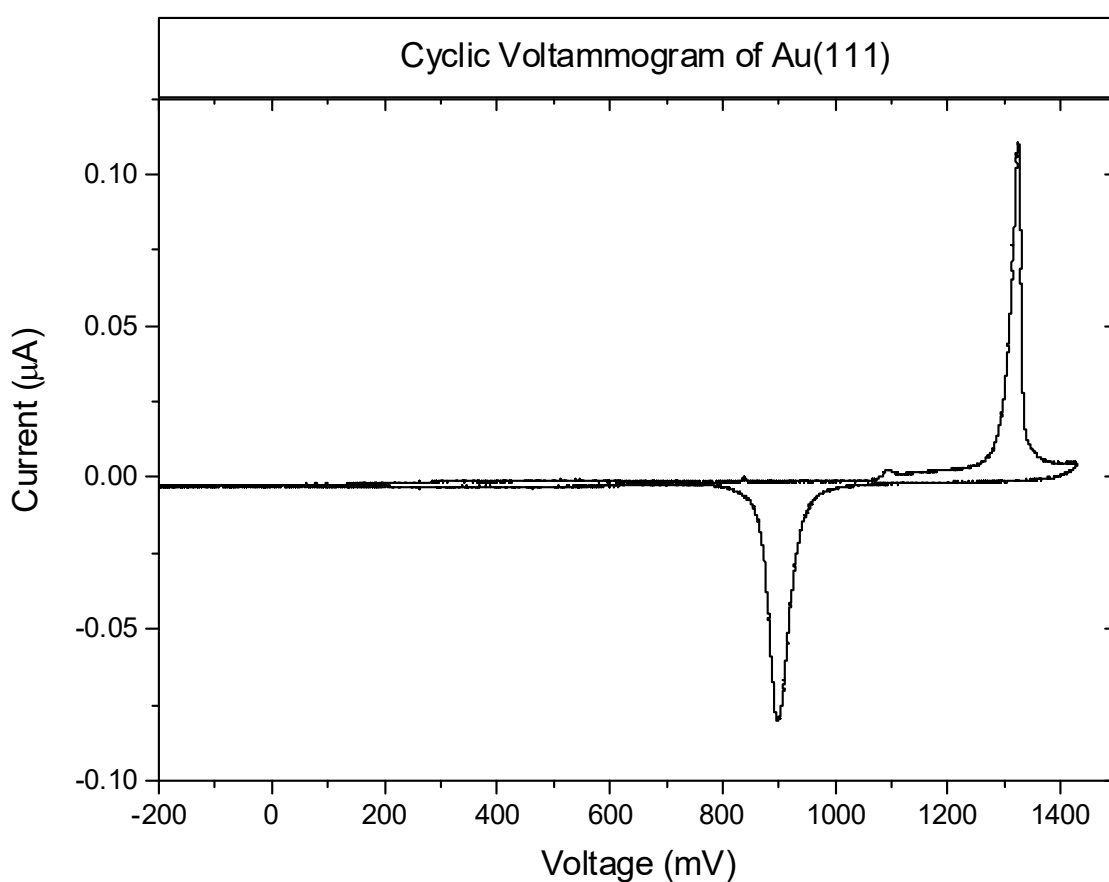


Figure 32: Cyclic Voltammogram of Au(111).

Observed is the Au(111) oxidation peak (1320 mV) and the following Au(111) reduction peak (920 mV). Solution: H_2SO_4 solution with N_2 bubbled through it.

Studying Figure 32, the tall peak at 1320 mV and shorter peak observed at 1100mV represent the oxidation of the Au(111) facet. As mentioned in 3.3.1 and 3.3.2, these peaks

represent the oxidation of gold, whereas the reductive peak, observed at 920 mV, represents the reduction of the gold-oxide surface. As no other peaks are observed which are commonly observed with other facets, it is clear that Au(111) is the predominant facet exposed to the solution [150]. The same surface was used to form a DPhyTL monolayer and tested a day later; observed in Figure 33.

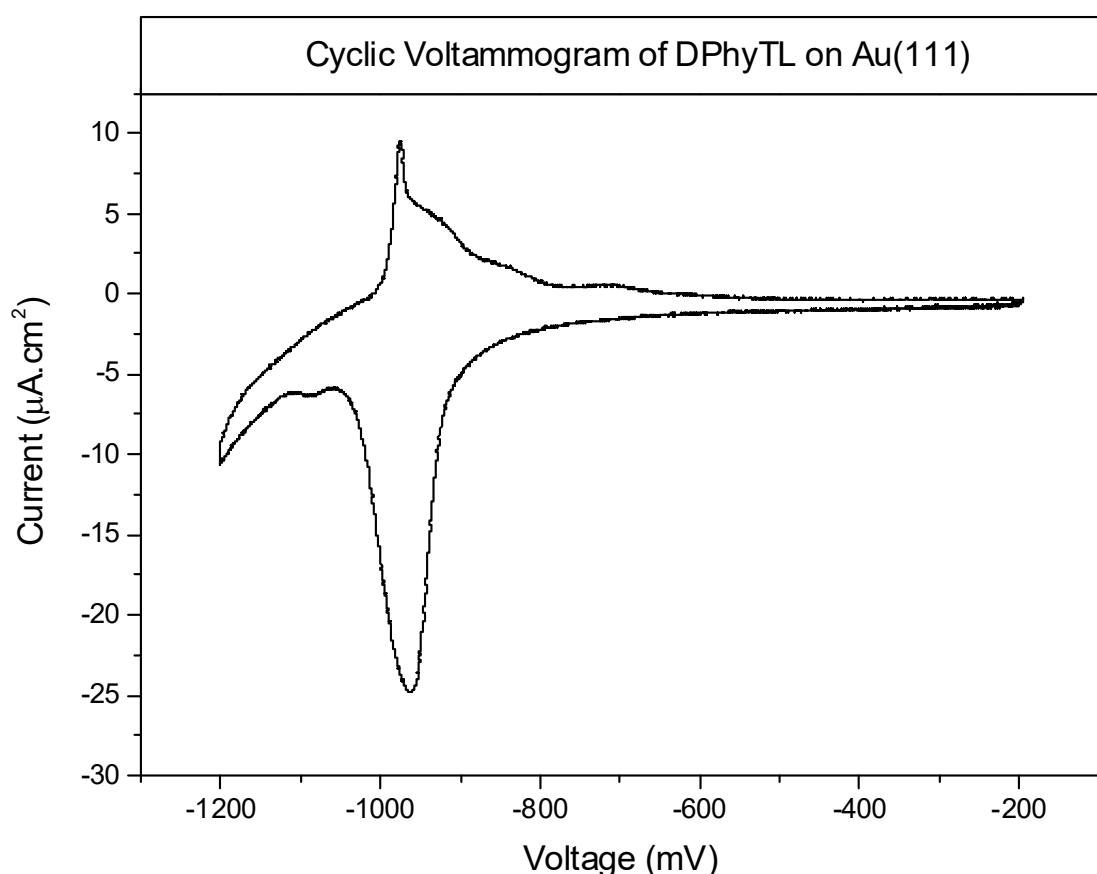


Figure 33: Cyclic Voltammogram of DPhyTL attached to Au(111).

Solution: 0.5 M KOH with N_2 bubbled through it. Electrode surface area approximately 0.0432 cm^2 .

Studying Figure 33, the reductive peaks observed at -950 mV and -1070 mV represent the desorption of a DPhyTL lipoic acid moiety from the Au(111) terraces and grooves between them respectively [62]. The relative size of each peak indicates that DPhyTL was mostly desorbed from the Au(111) terraces. Notably, there is a significant decrease in the most

negative region of the spectrum, indicative of dissolved oxygen in the system, however, as the scan is not repeated, the dissolved oxygen does not interfere with the desired result and is therefore not of importance.

The average coverage of DPhyTL on the Au(111) surface is based on 11 results, shown in Table 7.

Table 7: Coverage results of DPhyTL on Au(111) as per method 3.3.1 and 3.3.

The inaccuracy of the process is evident in the results and as such both the first desorption and repeat desorption (after annealing) are shown.

Sample	Round 1 (%)	Round 2 (%)
5	137	154.6
6	22.4	N/A
7	144	34.2
8	137.4	47.6
9	22.8	81.4
10	105.4	N/A
Average	94.8	80.45

Taking all of the coverage values into account, Table 7 indicates that the coverage of the surface, on average, is 94.8%. Looking at the table further indicates that the coverage results are highly erratic, spanning a large spectrum of values from 22.4% to 154%, without any observable pattern. As such, even with the use of high quality gold surfaces and applying the Adobe Photoshop CC method to limit the effect of noise (as per Chapter 3.3.3), these measurements were too variable to attain conclusive feedback. As such, it was concluded that DPhyTL was organising on the surface but the surface coverage values were not conclusive to determine whether the packing density would affect fs-vSFG.

4.3.3. fs-vSFG

By this point, EIS was able to determine that ethanol interacts with the defect areas of the membrane as well as the sub-membrane space while FTIR, NMR, and CV results collectively indicated that the tether molecule was pure and able to organise on a gold surface as expected. Fs-vSFG would now be used to study the formation of the monolayer, bilayer, and interaction of ethanol with the DPhyTL-DPhyPC bilayer.

To first observe a monolayer on the surface, the phytanyl tails were studied first. Using fs-vSFG, the terminal methyl cannot be observed, therefore, of the four methyls on each tail, the first, second, and third methyl, from the gold substrate, would be studied. According to Pohle et al. [2001], Leitch et al. [2009], and Quayum et al. [2002], the wavenumbers of specific interest are 2953 cm^{-1} and 2880 cm^{-1} , representing $\nu_{\text{as}}\text{CH}_3\text{-m}$ and $\nu_{\text{s}}\text{CH}_3\text{-m}$ respectively. For the chains to be able to be observed, the phytanyl chains would need to be pointed away from the substrate and organised in an imperfect crystal structure.

A major issue with the tBLM system is its use of gold. In general, vSFG observes a large background spectrum with gold, diminishing the signal to noise ratio of the phytanyl chains leaving standard vSFG unable to observe a signal. As such, fs-vSFG was required. Using fs-vSFG, the phytanyl region of the tBLM was observed (Figure 34). The symmetric and asymmetric $\text{CH}_3\text{-m}$ peaks were observed at 2953 and 2880 cm^{-1} . With the monolayer characterised in air, the next stage was to observe the tBLM in water.

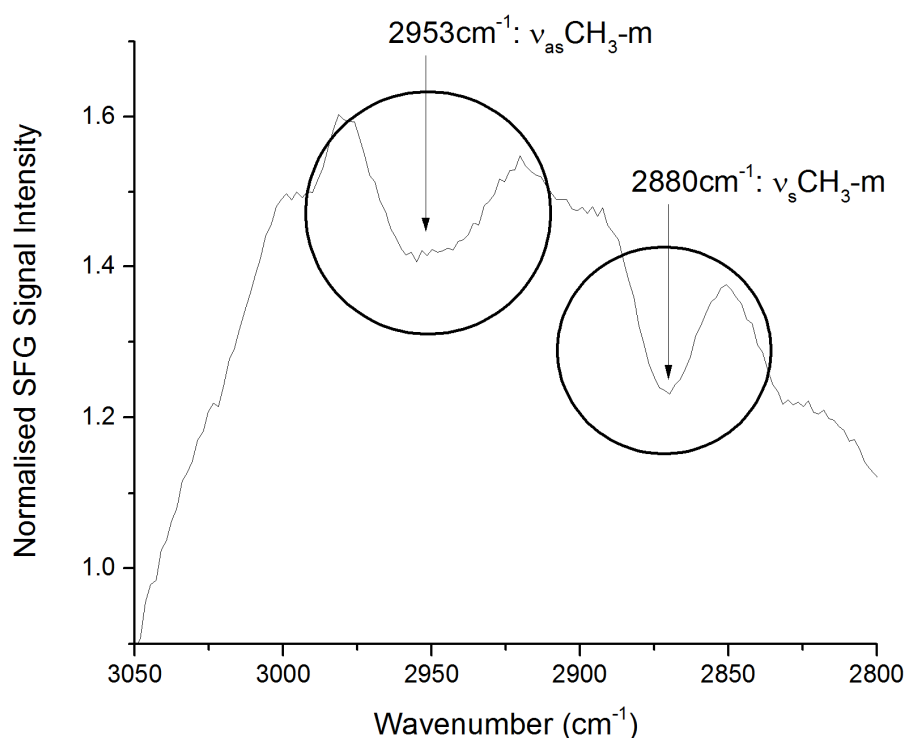


Figure 34: fs-vSFG spectrum of DPhyTL signal post normalisation in Argon.

DPhyTL surface is attached to a sputtered gold surface. Note: Experiments conducted at room temperature in Argon.

Before continuing further, the skew in Figure 34 and other fs-vSFG graphs requires discussion. The skew was caused, in part, by the alignment of the gold's background signal with any data collected during data processing. As mentioned in Chapter 3.4, polystyrene films were placed in-line with the samples to zero each sample, however, after aligning and normalising the spectra, skew was still evident. It was found that although the gold surface was formed on silicon, which was treated identically to the silicon used for TSG and NR, and the gold surface was sputtered at a low rate, the gold spectrum in various locations across the surface varied slightly. An average spectrum was collected, however, without collecting numerous samples, due to signal variation, some skew would still be incurred.

As a clear signal was obtainable from the SAM in argon, the DPhyTL SAM was subsequently tested in water. Testing the DPhyTL SAM in Milli-Q water obtained the same results as those in argon (Figure 35). The signals are partially red shifted from 2953 cm^{-1} to 2950 cm^{-1} for the $\nu_{\text{as}}\text{CH}_3\text{-m}$ bond and from 2880 cm^{-1} to 2800 cm^{-1} for the $\nu_{\text{as}}\text{CH}_3\text{-m}$ bond. Leitch et al. [2009] indicates that this effect is caused by hydration, though specifically discusses this in relation to the C-O-C stretching band of the tetraethylene glycol chain, based on Skoda et al. [2007].

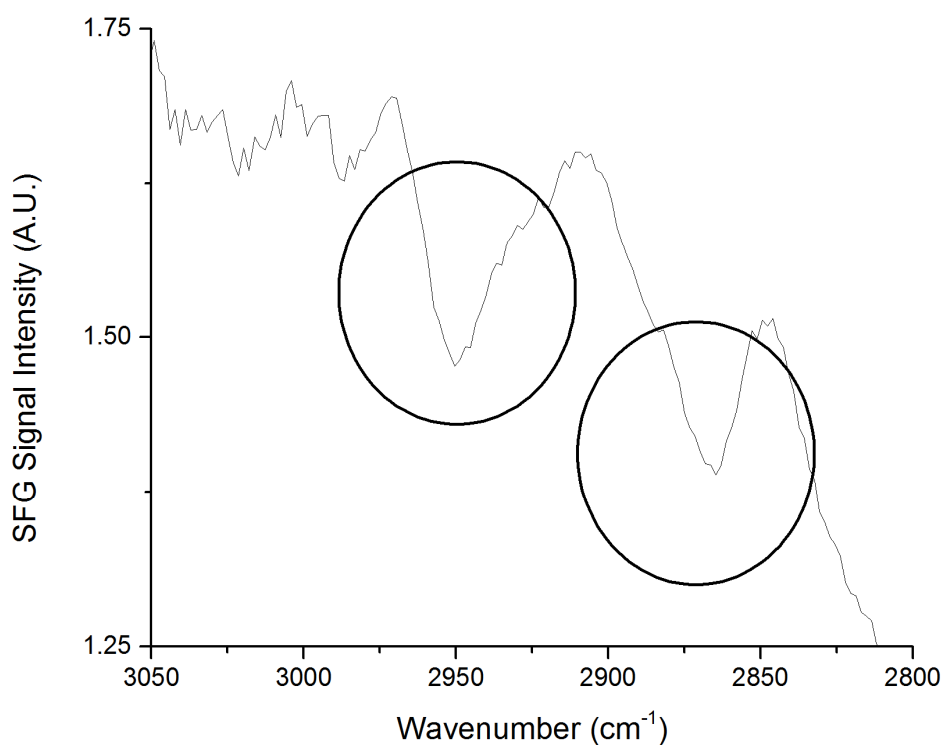


Figure 35: fs-vSFG spectrum of DPhyTL signal post normalisation in Milli-Q water.

DPhyTL surface is attached to sputtered gold surface. Note: Experiments conducted at room temperature in Milli-Q.

Following successful monolayer formation and observation under both Argon and Milli-Q conditions, solvent exchange was used to test the formation and observation of a DPhyTL-DPhyPC tBLM. The outcome is observed in Figure 36. The NIST database indicates expected dips at 3030 , 2920 , and possibly 2840 cm^{-1} [195]. Similarly, Figure 36 indicates peaks

at 3020, 2960, and 2875 cm^{-1} , which though significantly blue-shifted in two cases, are similar. According to Pohle et al. [2001], the only consistent band attributable to the choline region exists at 3030 cm^{-1} , which is the C-H bond of the nitrogen-bound methyl group. The same authors proceed to explain that several important peaks are observed between 2950 and 2800 cm^{-1} for DMPC which are not observed in cases such as acetylcholine, concluding that the other substituents effect the spectra significantly. Therefore, between the phosphocholine standard observed at NIST and the observations by Pohle et al. [2001], it was concluded that a tBLM formed by solvent exchange was observed by fs-vSFG.

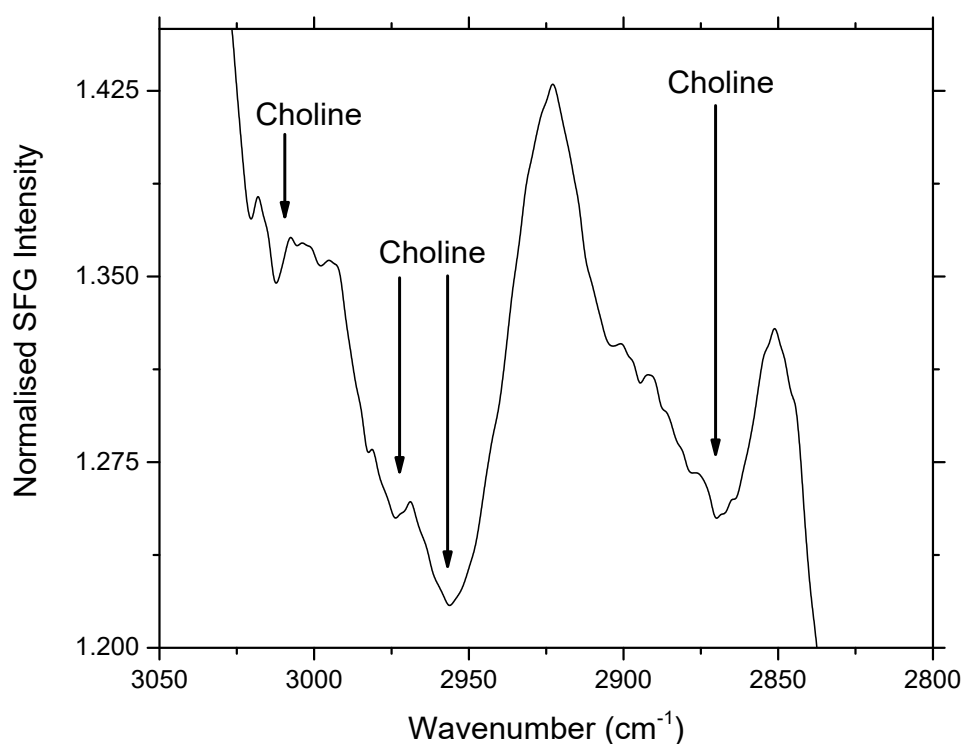


Figure 36: fs-vSFG spectrum of DPhyTL-DPhyPC Bilayer in Buffer Solution.

DPhyTL surface is attached to sputtered gold surface. DPhyPC was deposited using Solvent Exchange. Peak positions based on NIST standard IR spectrum of choline chloride as well as data collected by Pohle et al. [2001] and NIST [2016].

Studying Figure 37, the introduction of 25%_{v/v} ethanol for approximately 30 minutes and then sampling over a further 30 minutes changed the surface of the bilayer markedly. The peaks observed in Figure 36 no longer exist and only small peaks are evident afterward. NIST provides two gas-phase spectra which both present two key absorbance bands for ethanol: 2980 cm^{-1} and 2910 cm^{-1} , however, none of these peaks are clearly represented in Figure 37 [196]. If the ethanol peaks are in fact from ethanol, then that would also indicate that ethanol is found in the top-few nanometres of the membrane as fs-vSFG is surface sensitive. From this it was concluded that the ethanol changed the order or structure of the membrane markedly, possibly to a liquid disordered phase from a gel-phase, as the shape of the spectrum changed significantly with ethanol (Figure 36 and Figure 37). Further results regarding the interaction of ethanol with the membrane were not collected due to a lack of time to complete any further experiments.

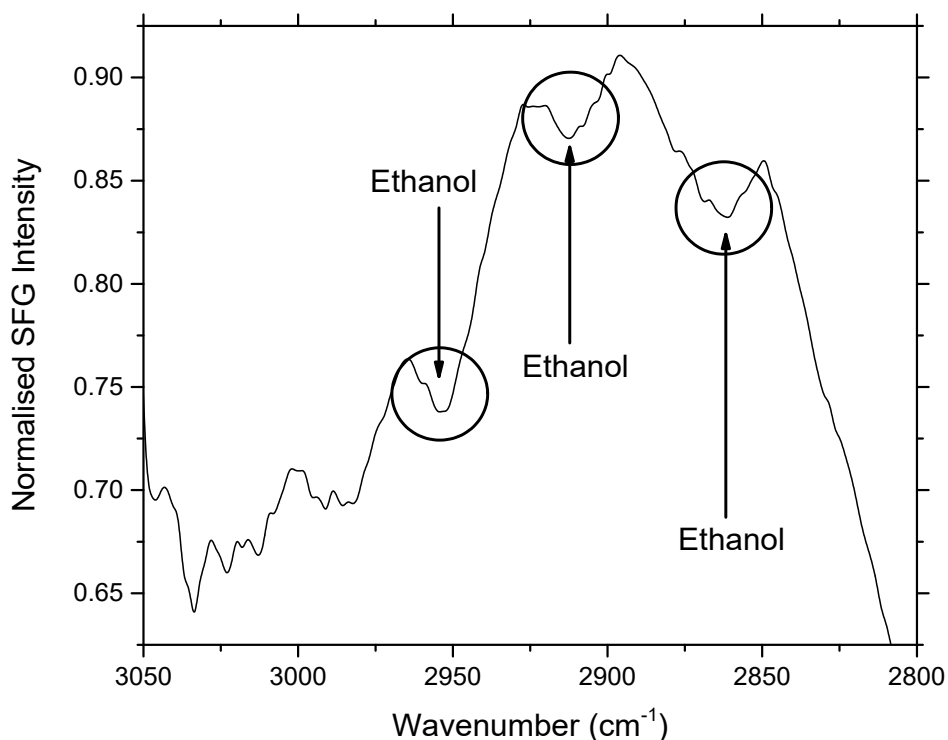


Figure 37: fs-vSFG spectrum of DPhyTL-DPhyPC Bilayer in 25%_{v/v} ethanol solution.

DPhyTL surface is attached to sputtered gold surface. DPhyPC was deposited using Solvent Exchange.

A key issue raised early on during experiments regarded laser ablation, suggesting that the power of the lasers on the DPhyTL monolayer would either ablate or damage the DPhyTL over extended periods of time. In this case, two one-minute scans were taken every 15 minutes over the period of 1.5 hours. Between each scan, the laser was blocked from passing through to the sample as to not illuminate the surface. Observing Figure 38, the peak was weak, however, over successive tests the signal's change is minor, ruling out any issues of laser ablation.

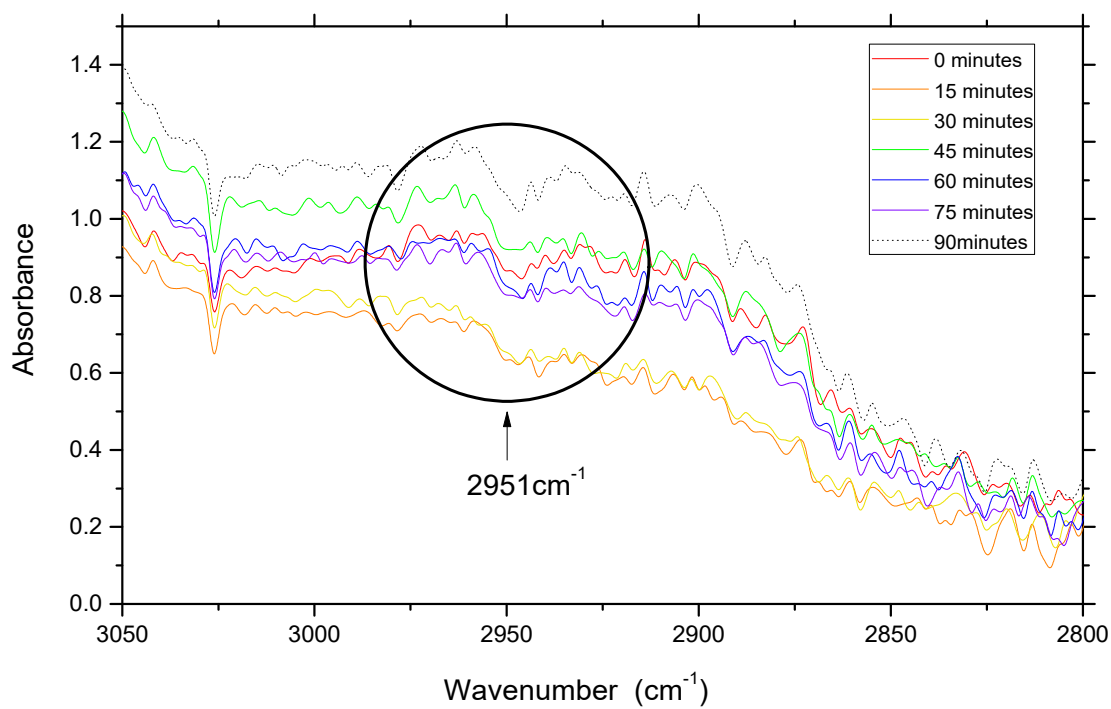


Figure 38: fs-vSFG spectrum of DPhyTL monolayer in Argon.

DPhyTL surface is attached to a sputtered gold surface. Note: Experiments conducted at room temperature in Argon.

4.3.4. Neutron Reflectometry

The fs-vSFG results were semi-conclusive regarding the effects of ethanol, therefore the final method of investigating the effects of ethanol on a DPhyTL-DPhyPC membrane was NR. Furthermore, where there was only time for one concentration of ethanol during fs-vSFG experiments, NR would be used to test three ethanol concentrations: 10; 25; and 50%_{v/v}.

Focusing first on 10%_{v/v} ethanol spectrum, the NR graphed in Figure 39 breaks the tBLM into six slabs: The gold substrate; tether region; inner leaflet; outer leaflet; head group region; and solvent. Due to the fact that d-EtOD has an nSLD of 6.1, any changes in the form of alcohol embedding in any area of the hydrogenated lipid membrane would be observed as a change in nSLD profile within each graph. The data in Figure 39 indicates that at low concentrations, ethanol mainly interacts with the upper leaflet of the membrane. It was observed that at 10%_{v/v} ethanol, the tBLM is mostly effected in two areas: the head-group region mostly followed by the tether region. In this case, full-recovery is observed which suggests that the effects of ethanol on the overall structure of the membrane are temporary.

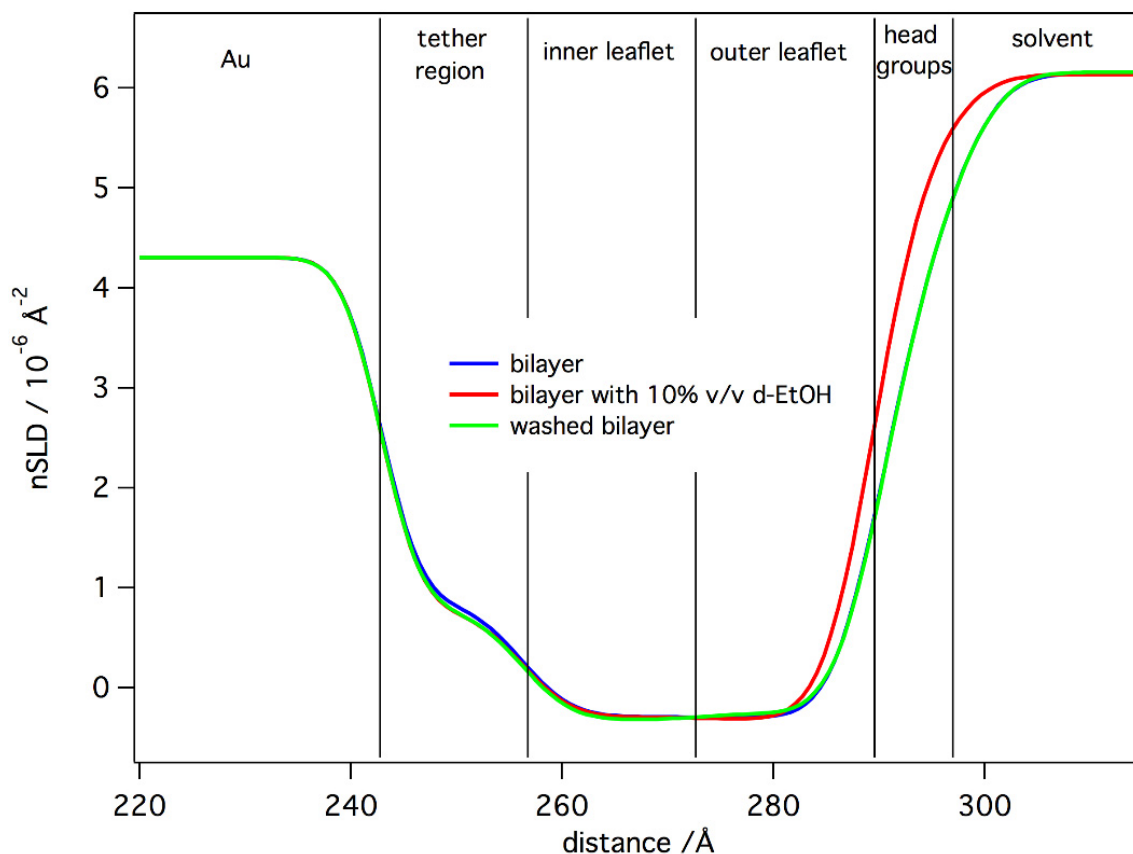


Figure 39: nSLD profile of a DPhyTL-DPhyPC tBLM before, during, and after 10%_{v/v} d-EtOD in D₂O.

After increasing the concentration of ethanol to 25%_{v/v}, Figure 40 indicates that ethanol interacts with both the distal leaflet and the tether region of the tBLM more significantly than at 10%_{v/v}. In this case, a greater concentration of ethanol is observed interacting with both regions. It should be noted that at 10%_{v/v}, where both regions fully recovered after washing, in this case, it can be questioned whether the headgroup mostly, if not fully, recovered. The difference in solvent nSLD during fitting is equivalent to the difference seen between the before-and-after results of the headgroup region, and as such the difference can be determined to be within the error of the experiment.

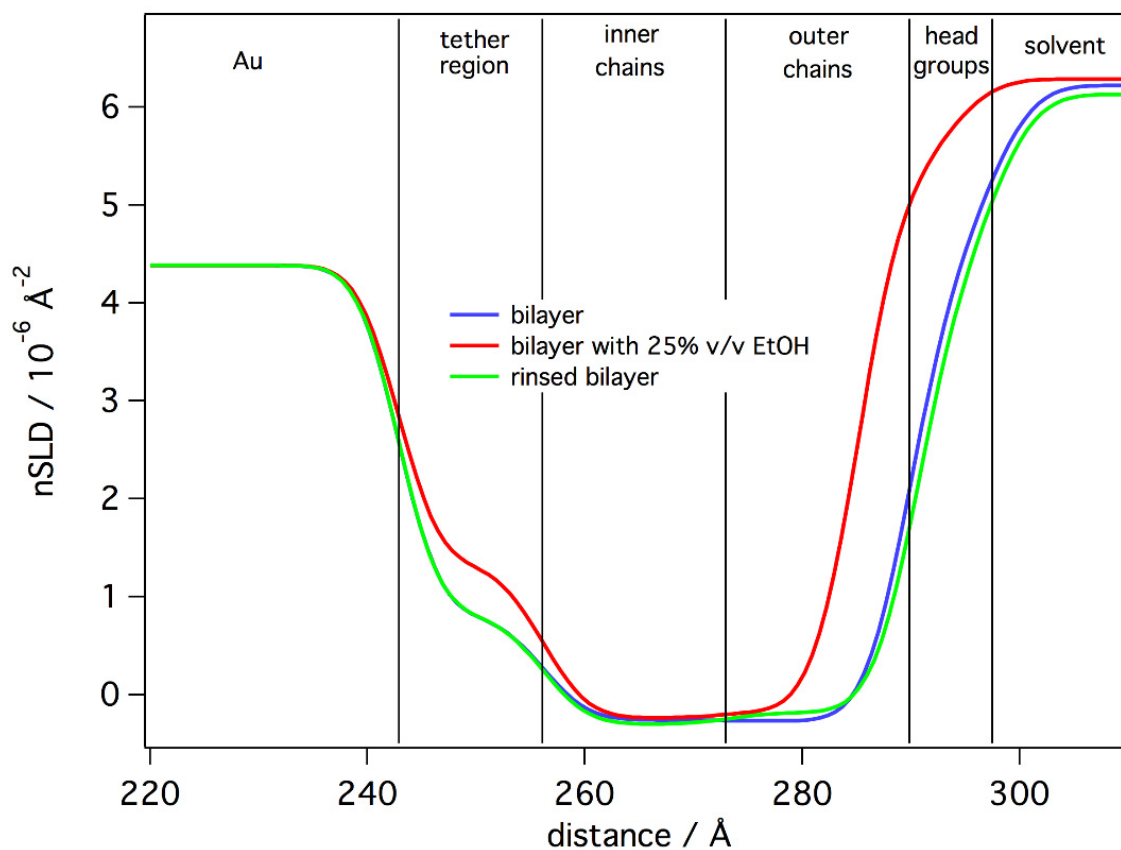


Figure 40: nSLD profile of a DPhyTL-DPhyPC tBLM before, during, and after 25%_{v/v} d-EtOD in D₂O.

Figure 41 exemplifies the tBLM changes observed by increasing the ethanol concentration to 50%_{v/v}; at this concentration, ethanol no longer interacts with specific areas of the membrane but instead interacts with all regions of the tBLM. It is likely that these changes can be explained in terms of solvation, whereby the ethanol first interacts with the defect areas of the membrane but then damages the distal leaflet before interacting with the tails of the proximal leaflet. Figure 41 indicates that the bilayer is left permanently damaged as it never recovers to its original state; as the nSLD profile is more-negative in all cases afterward. Overall, the lack of recovery would suggest that lipids have been washed away with rinsing.

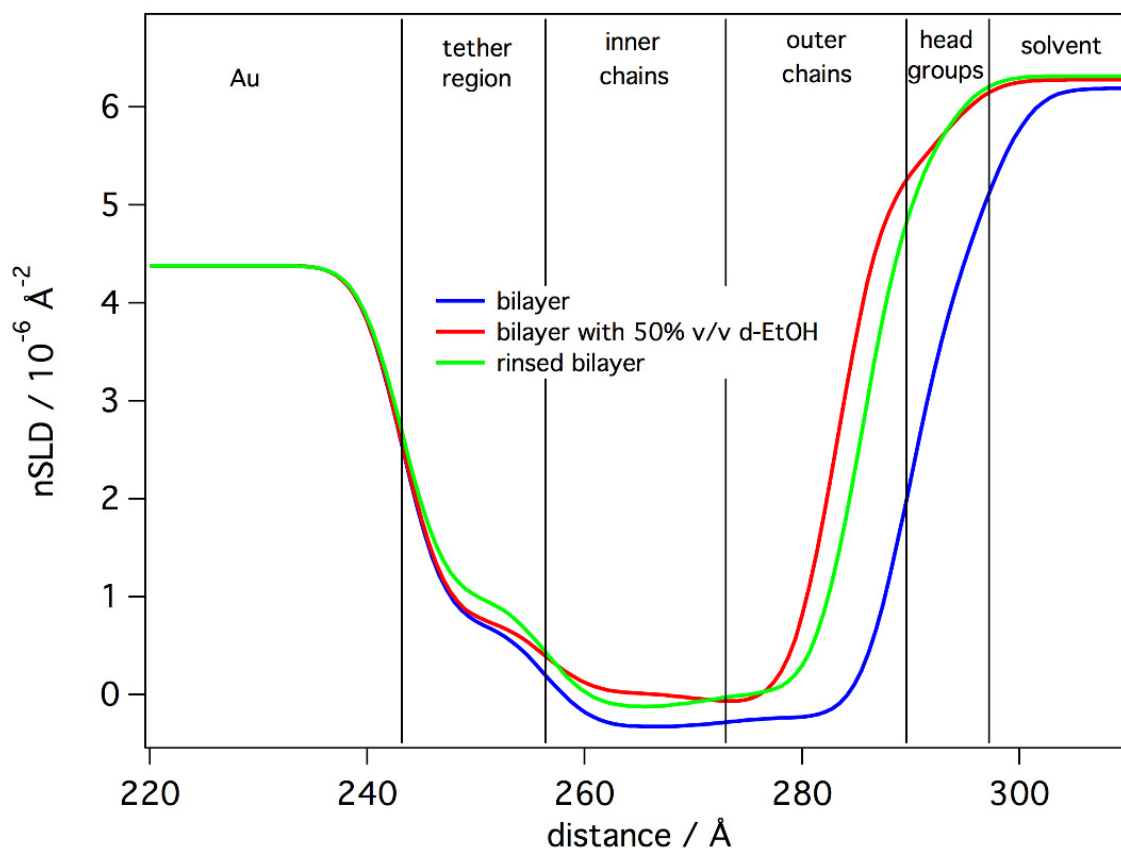


Figure 41: nSLD profile of a DPhyTL-DPhyPC tBLM before, during, and after 50%_{v/v} d-EtOD in D₂O.

Contrasting the EIS results against those collected by NR develops a clearer picture of the interaction of ethanol with the tBLM: EIS results indicate that the bilayer is affected by ethanol almost instantly (5 and 10%_{v/v}); as NR does not observe any specific changes with the membrane at 10%_{v/v} it can be hypothesised that ethanol is causing lipid rearrangement, however, it is more likely that ethanol is causing permanent changes within the defect areas which do not dominate the structure of the membrane and therefore are not observed by NR at the low concentration (10%_{v/v}); EIS observed that greater concentrations of ethanol, up to 25%_{v/v} were electronically permanent, however, the sealing areas of the membrane did not show any significant changes, in line with the NR results; higher concentrations of ethanol (50%_{v/v}) were unable to be studied by EIS, as is mentioned earlier, however, in EIS' absence

NR indicates that the membrane is permanently damaged. Overall, between the two methods, it is evident that ethanol interacts with the headgroup and tether region of the membrane, supporting previous studies.

Furthermore, although bilayers are an organised network of molecules, their headgroup region can be highly hydrated and saturated with polar molecules, causing the height-positions of molecules to vary and be broadly distributed [7]. As such, at any stage, lipids can be found to be dislodged from the membrane, causing local thinning of the hydrophobic core, water penetration, and thermal fluctuations, driving dynamic and transient rearrangements [7]. Ethanol, known to interact with PC headgroups, could be increasing this propensity, especially permanently at higher concentrations.

4.4. Ethanol's Effect on Valinomycin through the tBLM

Having determined the effects of ethanol on the tBLM experimentally, the action of ethanol on Valinomycin, through its effect on the membrane, was investigated. To study this, by having included Valinomycin at the beginning of the experiments, the change in R_{def} due to Valinomycin transport was studied after each successive ethanol concentration.

Table 8 indicates the action of Valinomycin is consistent at all ethanol concentrations, with the change in defect resistance, R_{def} , being approximately one or more orders of magnitude in all cases (before, during, and after ethanol). The variation in the change has no observable pattern across the ethanol concentrations. It should be noted that the error observed with certain values is significant, at 1%_{ov/v} change and 10% change, the errors of R_{def} are 53% and 89% respectively, however, the changes due to Valinomycin are still well outside of error. As the action of Valinomycin is observed in all cases, Valinomycin's transport is arguably left unaffected by the ethanol, either through direct interaction or through ethanol's effect on the membrane.

Focusing on the capacitance of the membrane-Helmholtz element, the action of Valinomycin indicates no repeating pattern. As such, the intact areas of the tBLM, as well as the Helmholtz layer, are relatively unchanged, as would be expected. On the other hand, the Z_{sub} impedance was found to increase by over 400% between sodium and potassium before any ethanol is included in the system and stabilising to 150% in all other cases but one, where it stays unchanged. It is suggested that this could be attributed to the equilibration of the membrane to potassium. After all ethanol conditions had been completed, a final test with Valinomycin indicated that the Z_{sub} changed dramatically, decreasing ten-fold (to 0.130), outside even the values observed during post-ethanol washes in Table 5.

Comparing the values of post-25%_{ov/v}-washes of both tables, there are significant differences which are apparent.

	R_{def} ($M\Omega.cm^2$)			C_{mli} ($\mu F.cm^2$)			Z_{sub} ($\Omega.s^a.cm^2$)			Alpha	χ^2
Table 5: Bilayer after 25%(v/v) Ethanol (NaCl)	0.463	±	0.0027	0.700	±	0.015	4.45	±	0.057	0.93	0.00023
Table 8: Bilayer after 25%(v/v) Ethanol (NaCl)	0.200*	±	N/A	0.699	±	0.0032	.130	±	.079	1*	N/A

The differences can be attributed to the f_{min} value used to model each experiment as the f_{min} value had to be limited (to higher frequencies) to fit the potassium peak, which was not the case when only focusing on the sodium solutions during the NaCl-ethanol solutions (which included lower f_{min} values). Furthermore, the error for this specific Z_{sub} value is significant ($\pm 60\%$), which can be attributed to the limited range of data and slightly to the held R_{def} as well as alpha values on auto-fitting for that specific experiment; as such, the significance of this specific value is diminished.

Table 8: Fitted ethanol-valinomycin data using a R_s -[C_{mH}/R_{def} - Z_{sub}] EEC.

Note: R_{def} is held constant post-25% ethanol-based on the fitting completed for the larger frequency-range and Z_{sub} -alpha is held constant at 1 as it otherwise crept to 1.2.

Sample	R_{def} (M Ω .cm ²)			ΔR_{def} (%)	C_{mH} (μ F.cm ²)			Z_{sub} (Ω .s ^{-α.cm²)}			Alpha	χ^2
Bilayer with Valinomycin (NaCl)	2.80	±	0.17		0.715	±	0.0020	0.668	±	0.057	0.58	0.000578
Bilayer with Valinomycin (KCl)	0.0284	±	0.0017	1.0%	0.782	±	0.0090	2.84	±	0.074	0.78	0.00391
Bilayer during 1%(v/v) Ethanol (NaCl)	1.42	±	0.10		0.684	±	0.0022	1.09	±	0.090	0.53	0.000635
Bilayer during 1%(v/v) Ethanol (KCl)	0.0188	±	0.010	1.3%	0.679	±	0.0082	1.74	±	0.034	0.49	0.00234
Bilayer during 5%(v/v) Ethanol (NaCl)	0.878	±	0.014		0.701	±	0.0024	3.10	±	0.073	0.87	0.000635
Bilayer during 5%(v/v) Ethanol (KCl)	0.0957	±	0.010	11%	0.725	±	0.015	2.97	±	0.12	0.74	0.0143
Bilayer during 10%(v/v) Ethanol (NaCl)	0.177	±	0.0043		0.720	±	0.0026	3.81	±	0.35	0.90	0.000433
Bilayer during 10%(v/v) Ethanol (KCl)	0.00156	±	0.0014	0.89%	0.691	±	0.027	5.64	±	0.19	0.52	0.00285
Bilayer during 25%(v/v) Ethanol (NaCl)	0.0146	±	0.00026		0.761	±	0.0025	6.44	±	0.87	0.85	0.000176
Bilayer during 25%(v/v) Ethanol (KCl)	0.00151	±	0.00014	10%	1.09	±	0.035	7.87	±	1.0	0.79	0.00407
Bilayer after Ethanol (NaCl)	0.200*	±	N/A		0.699	±	0.0032	.130	±	.079	1*	N/A
Bilayer after Ethanol (KCl)	0.000618	±	0.0000027	0.31%	0.701	±	0.0021	1.70	±	0.073	0.81	0.000121

Note: ($\Delta R_{def} = R_{def-conduction} / R_{def-non-conduction}$) and a * indicates that the value was controlled

To maintain the modelling method and understand the effect of limited and increasingly higher f_{\min} frequencies with successive ethanol concentrations or washes, the effect of limiting the modelling parameter f_{\min} , was investigated. Changing the frequency range indicated that the Z_{sub} values decreased with increasing f_{\min} values, as is exemplified in Table 9.

Table 9: Effect of f_{\min} on Z_{sub} of an R_s -[$C_{\text{mH}}/R_{\text{def}}-Z_{\text{sub}}$] EEC.

This table exemplifies the effect of three different fitting frequency ranges on Z_{sub} .

f_{\min} (Hz)	f_{\max} (Hz)	Z_{sub} ($\Omega \cdot \text{s}^{-\alpha} \cdot \text{cm}^2$)		
0.0305	4150	3.04	±	0.12
0.120	4150	2.70	±	0.082
0.737	4150	2.60	±	0.061

Focusing on Table 8, there is a pattern of generally increasing Z_{sub} values over the period of the experiments which is not observed as significantly in Table 5. As such, in part, the pattern of increasing Z_{sub} values over the period the successive Valinomycin experiments is attributable to the changing f_{\min} and not the effects of ethanol on Valinomycin. The alpha values indicate no consistent pattern specific to Valinomycin's conduction, especially when comparing multiple data sets; instead this factor plays a more important role when comparing the action of ethanol.

Before concluding, it should be noted that Valinomycin is used as an indicator of an active lipid bilayer matrix, however, due to its solubility in ethanol, one can argue it is potentially leached into the surrounding solution in the presence of ethanol. This theory is discounted by Valinomycin's continued ability to transport potassium ions at all ethanol concentrations (Table 8). Overall, Valinomycin's transport stays constant. The greatest change, due to ethanol, occurs within the sub-membrane space, however, between being able to be attributed to the changing f_{\min} modelling boundary value and the change due to ethanol, it can be concluded that ethanol's effect on Valinomycin is minimal while significant to the bilayer.

One can therefore hypothesise that ethanol does not affect the action of Valinomycin, instead directly acting on the membrane like the results observed in Table 5.

4.4.1. Qualitative observations of Bode plots during Valinomycin condition

During the potassium ion conditions of Figure 44, Figure 45, Figure 46, and especially Figure 47, it was also observed that the phase responses became increasingly tri-modal. AFM experiments of model membranes previously reported that model membranes become increasingly damaged with increasing concentrations of ethanol; specifically, after a thinning of the membrane, the model formed islands [118].

One can hazard that the tri-modal phase response in fact represents three types of surfaces: intact bilayer islands; defect areas at the islands edges and throughout the islands; and uncovered monolayers. Further information cannot be deduced from impedance data, as the quality of the interpretation is limited to the complexity of the EEC, which at this stage has no accurate physical basis. An exhaustive literature search of damaged surfaces tested by EIS is only evidenced by one paper, Valincius, Meškauskas, and Ivanauskas [2012], which indicates that the decrease in phase values of the higher frequency modes in the aforementioned figures, especially Figure 46 and Figure 47, is indicative of dense defects, in line with expectations of island formation. At a stretch, depending on the impedance of the unmasked areas, it is possible that the effect of the unmasked areas is only observable with EIS when the R_{def} resistance is low-enough due to the action of Valinomycin in already damaged areas. No EEC has been found to be able to mimic this outcome at this stage. The observations discussed here are tentative, however, the ethanol concentrations and suggested outcomes are in line with current literature which suggest that the effects of ethanol are significant beyond 10%_{v/v} (Chapter 1.5.3); thus this observation was worth mentioning.

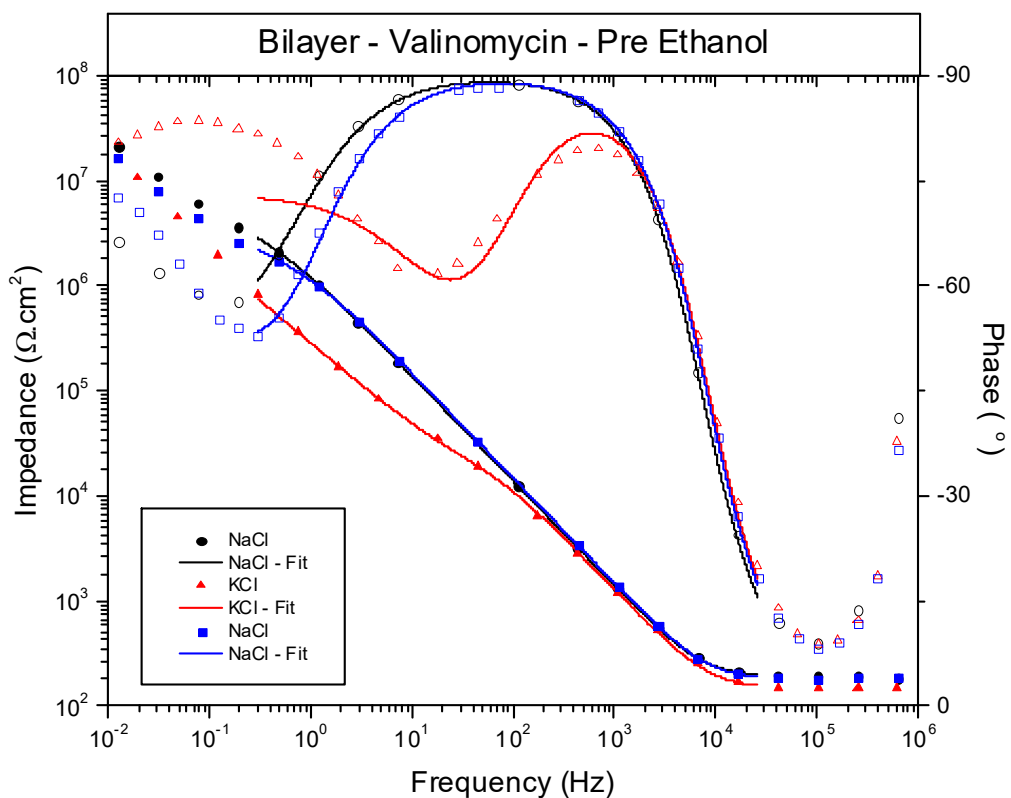


Figure 42: Bode plot, pre-ethanol, indicating the effect of Valinomycin in NaCl and KCl solution.

The data is fitted using an $R_s-[C_{mt}/R_{def}-Z_{sub}]$ EEC. Symbols represent data points where as the lines represent the fits. Closed symbols refer to the impedance trace whereas the open symbols refer to the phase trace.

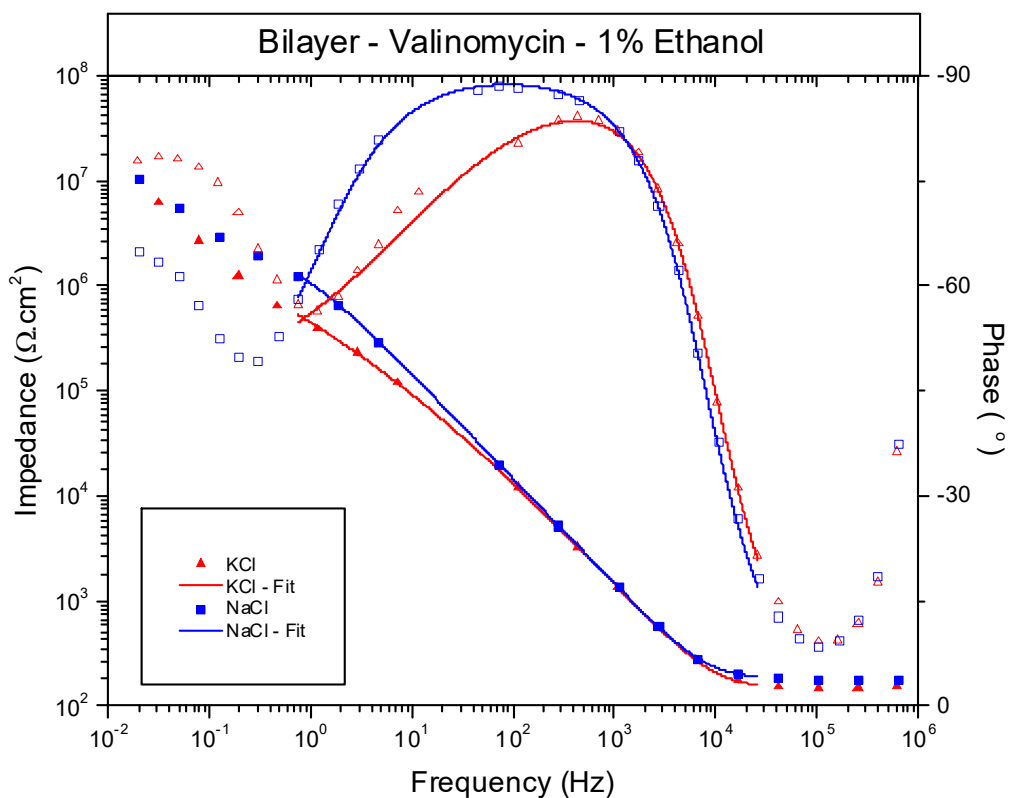


Figure 43: Bode plot indicating the effect of 1%_{v/v} ethanol on Valinomycin function.

The data is fitted using an $R_s-[C_{mt}/R_{def}-Z_{sub}]$ EEC. Symbols represent data points whereas the lines represent the fits. Closed symbols refer to the impedance trace whereas the open symbols refer to the phase trace. Note: The first NaCl run was corrupt and as such is not presented.

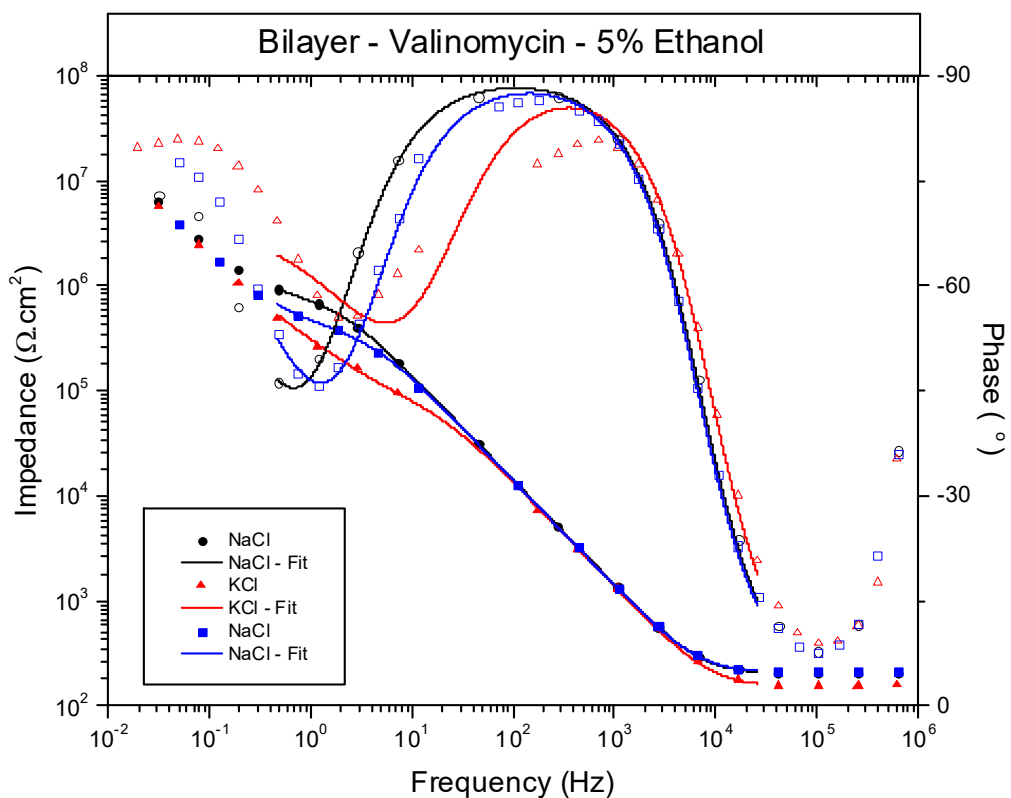


Figure 44: Bode plot indicating the effect of 5%_{v/v} ethanol on Valinomycin function.

The data is fitted using an $R_s-[C_{mt}/R_{def}-Z_{sub}]$ EEC. Symbols represent data points whereas the lines represent the fits. Closed symbols refer to the impedance trace whereas the open symbols refer to the phase trace.

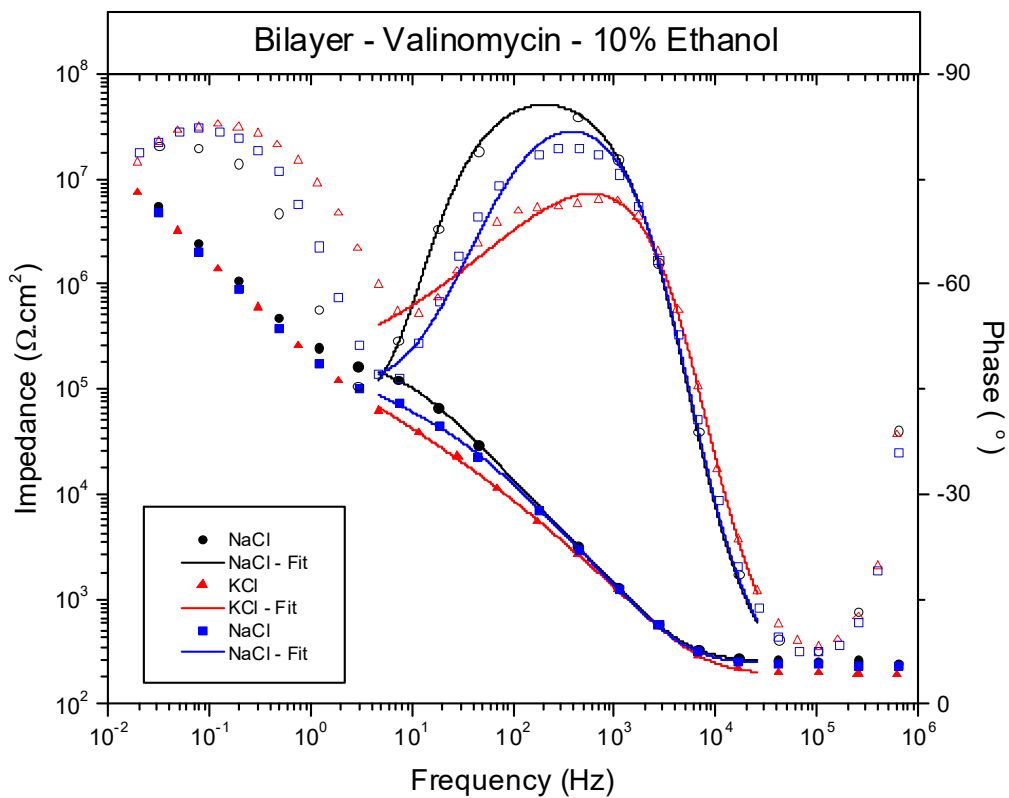


Figure 45: Bode plot indicating the effect of 10%_{v/v} ethanol on Valinomycin function.

The data is fitted using an $R_s-[C_{mt}/R_{def}-Z_{sub}]$ EEC. Symbols represent data points whereas the lines represent the fits. Closed symbols refer to the impedance trace whereas the open symbols refer to the phase trace.

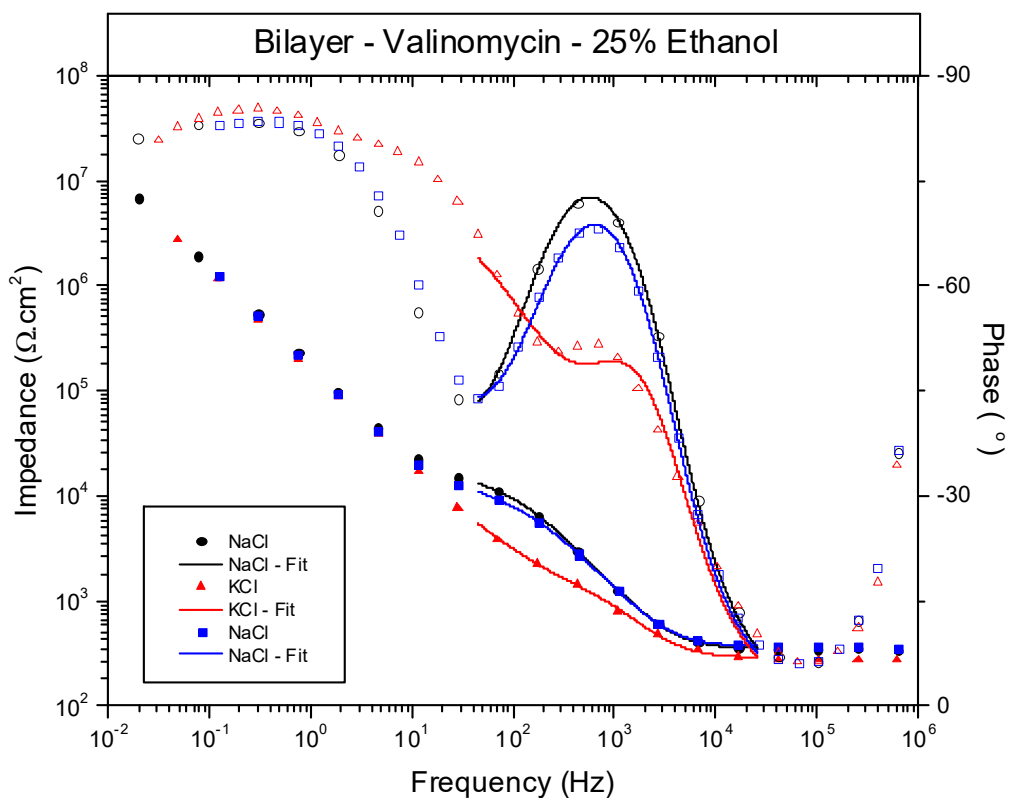


Figure 46: Bode plot indicating the effect of 25%_{v/v} ethanol on Valinomycin function.

The data is fitted using an $R_s-[C_{mt}/R_{def}-Z_{sub}]$ EEC. Symbols represent data points whereas the lines represent the fits. Closed symbols refer to the impedance trace whereas the open symbols refer to the phase trace.

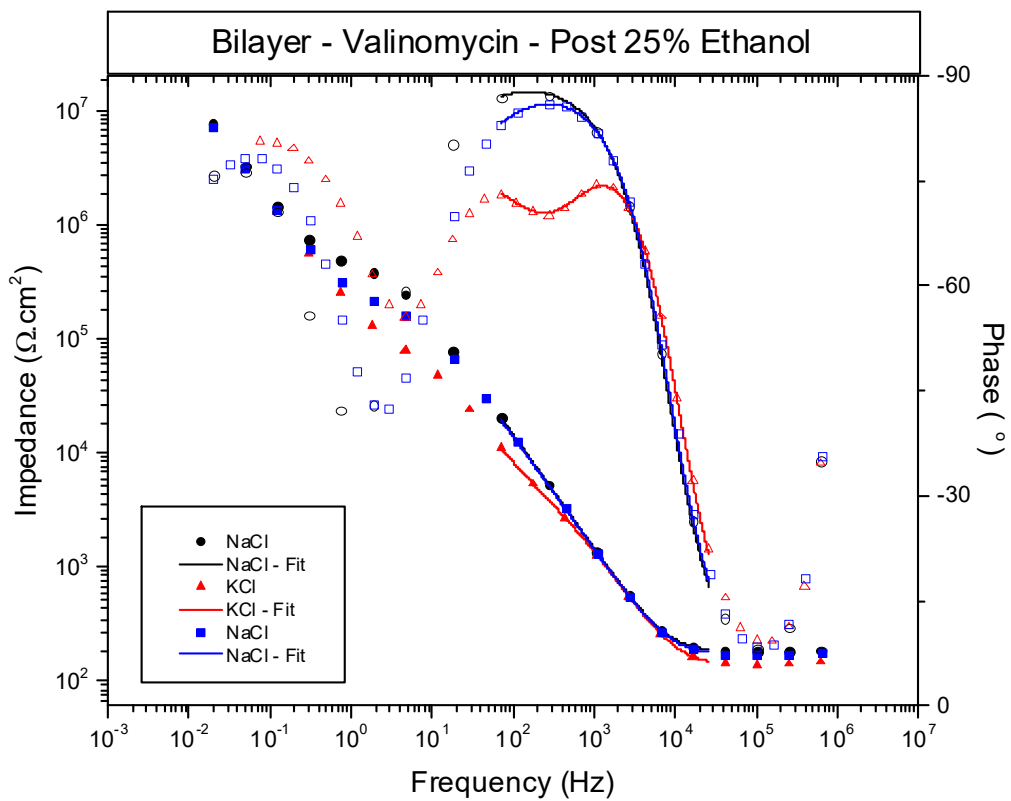


Figure 47: Bode plot indicating the effect increasing ethanol on Valinomycin function.

The data is fitted using an $R_s-[C_{mt}/R_{def}-Z_{sub}]$ EEC. Symbols represent data points where as the lines represent the fits. Closed symbols refer to the impedance trace whereas the open symbols refer to the phase trace.

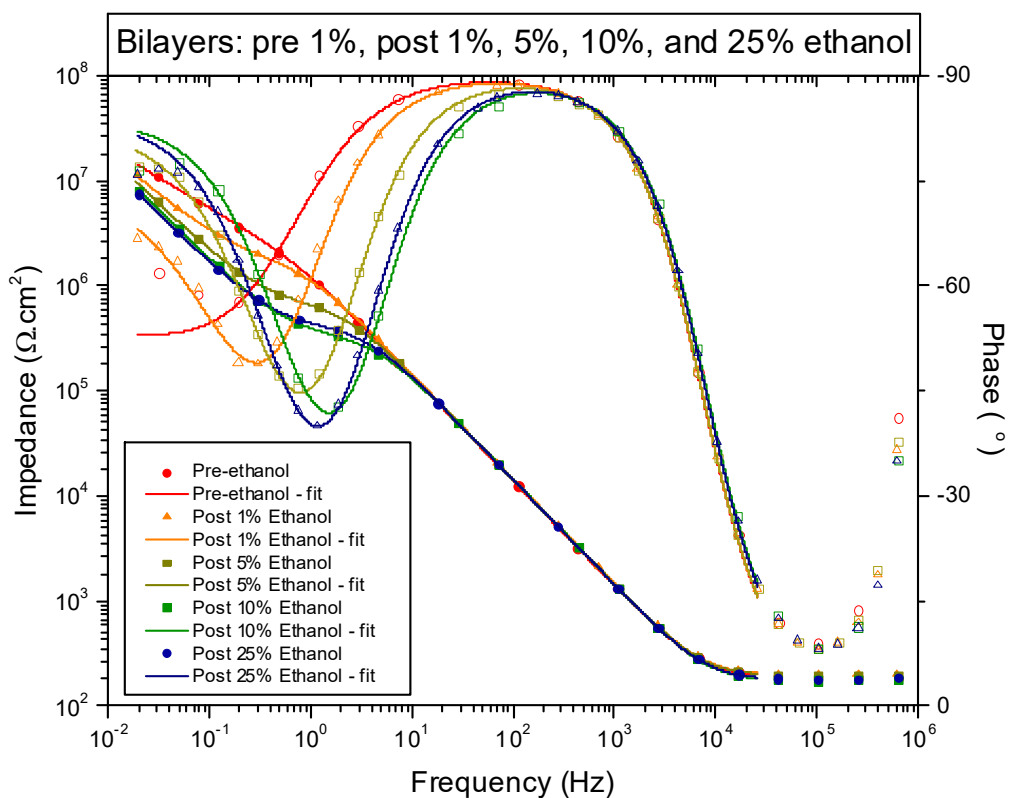


Figure 48: Bode plot presenting the effect of increasing ethanol concentrations on Valinomycin action.

All bode plots represent the tBLM in KCl solutions after rinsing the membrane to remove ethanol. The data is fitted using an $R_s-[C_{mt}/R_{def}-Z_{sub}]$ EEC. Symbols represent data points where as the lines represent the fits. Closed symbols refer to the impedance trace whereas the open symbols refer to the phase trace.

4.5. Conclusions

4.5.1. Ethanol

4.5.1.1. EIS

The impedance and phase responses of the bilayer change permanently due to ethanol. Two key changes were observed: there was a definite decrease in 1) low-frequency phase response and 2) impedance. These significant changes were observed in the EEC between 1 and 10%_{v/v} ethanol, after which there was a stabilisation of all EEC parameters up to 25%_{v/v}. 50% ethanol samples were also tested but an example was not fitted and is not presented as the membrane becomes destroyed. Studying the EEC closely, EIS experiments suggest that the ethanol interacted with the defect areas of the membrane while leaving the intact areas alone, causing: decreased defect-area resistance; increased sub-membrane impedance; and a change in sub-membrane property toward a capacitor more than a resistor. These suggestions are in line with current studies which indicate that, at low concentrations, ethanol interacts with membranes mainly with the headgroups, less with the tails, and creates islands, while at higher concentrations it changes the fluidity of the whole structure. The outcomes of the EIS studies are indicative of bilayer defect-area rearrangement at low concentrations and, at higher concentrations, partial solvation of defect areas and interactions with the sub-membrane space.

4.5.1.2. FTIR, NMR, and CV

FTIR successfully outlined the vibrations observed in the carbon-oxygen and carbon-hydrogen bonding regions of the bulk DPhyTL IR spectra respectively; both figures' peak positions were found at their expected positions. As such, the CO and CH FTIR measurements indicate the bulk-DPhyTL was relatively pure and a quick NMR study supported this conclusion. FTIR also successfully observed the peaks required to study DPhyTL monolayers during fs-vSFG. CV indicated that DPhyTL monolayers were formed on a surface, however,

using CV to determine the exact surface coverage was complicated due to the signal-to-noise ratio. The two reductive peaks expected in the Voltammograms were observed therefore qualitatively indicating the expected reduction of DPhyTL from the Au(111) surfaces.

4.5.1.3. fs-vSFG

Although it literature suggests that the DPhyTL monolayer is well-organised, too dense, and well-aligned to be observed, fs-vSFG successfully observed a DPhyTL monolayer under both Argon and Milli-Q conditions and a DPhyTL-DPhyPC bilayer under liquid conditions.

fs-vSFG was originally intended to define the position and orientation of ethanol molecules within the tBLM, potentially even defining the ratio of ethanol to lipid molecules. Instead, it was observed that the ethanol changed the order of the membrane markedly as the shape of the spectrum changed significantly, and it could be suggested that the ethanol interacted with the distal leaflet due to fs-vSFGs depth-limitations, however, further ethanol information, such as ethanol orientation, molar ratio, and exact positions, could not be determined. Furthermore, the time limitations meant that the ethanol results were only completed at one concentration and were difficult to interpret. As such, fs-vSFG was only partly successful, however, generally supportive of EIS and NR results.

4.5.1.4. NR

NR was successful in studying the interaction of ethanol with the bilayer. Using NR, it was observed that ethanol did not permanently affect or damage the membrane at 10 or 25%_{v/v}, however, only at a concentration of 50%_{v/v} was the effect was permanent. At all concentration ethanol interacted with both the headgroup and sub-membrane regions, which agrees with the impedance data. On the other hand, at 50%_{v/v}, ethanol visibly interacted with all areas of the membrane.

These conclusions are reasonable considering the free energy profiles of the DPhyPC bilayers [197]; the barrier for water is quite significant and although ethanol is less polar, it would still be limited in its ability to pass through the hydrophobic areas of the bilayer.

4.5.2. Valinomycin

Valinomycin was used for two key reasons: 1) to confirm that the membrane represented an active matrix and 2) to study the interaction of ethanol with the peptide through the membrane.

Prior to the inclusion of ethanol experiments, the peptide successfully transported potassium ions across the tBLM, as expected; indicating that all the changes observed above were applicable to a matrix which could be active and therefore applicable to more realistic studies than studies shown in the literature. After the inclusion and rinsing of each ethanol concentration, the action of the peptide was still observed and its transport was considered to be unaffected. It was expected that during ethanol testing one of two cases would occur, either the Valinomycin would be leached from the membrane or the Valinomycin would cease to act within the membrane as the ethanol concentrations increased. Neither occurred and the Valinomycin continued to transfer ions, changing the membrane defect resistances at expected ratios (R_{def} of KCl was $1/10^{\text{th}}$ that of R_{def} in NaCl). As such, the effects of ethanol are able to be attributed back to the effects of ethanol on the membrane.

In part, this interpretation is attributable to the use of this particular EEC, which separates intact membrane areas from the defects; Valinomycin would potentially have less of an effect in intact areas than it would in defect areas which are likely more exposed and less-dense.

4.5.3. In Summary

It was originally understood that ethanol, even at low concentrations, interacts first with the headgroup region of a DPhyPC-based bilayer and slowly solvates and permanently damages the membrane, however, the results of this study tell a more detailed story.

It can be concluded that at low concentrations (1-25%_{v/v}), ethanol rearranges the membrane and permanently effects it but in a non-damaging way. At higher concentrations (50%_{v/v}) the effect is severe, damaging, and permanent. This research supports and builds on current data, which states that ethanol prefers to interact with the more disordered areas first, by indicating that ethanol interacts initially with the headgroup region of DPhyPC before traversing the membrane and interacting with the sub-membrane space [118]. An effect of ethanol on the peptide directly was not observed. The changes to the membrane defect-resistance was observed only in terms of a change to the defect resistance due to increasing ethanol concentrations but not as a change in the peptide's performance, with it able to continue performing at expected changes in R_{def} ratios.

As such, ethanol interacts with the membrane. At low concentrations, it arguably causes rearrangement, and at higher concentrations, it causes permanent damage. At no point was it observed that ethanol's effect on the membrane changed the action of Valinomycin.

This work confirms the results observed in previous physical and theoretical studies and develops methods which can be used for future studies and helps develop an understanding for the way the simple anaesthetic, such as ethanol, interacts with a simple zwitterionic model membrane. This research brings the understanding of drug-membrane interactions one step closer toward improving future studies of drugs on model membranes.

4.6. Importance of Current Outcomes and Future Suggestions

4.6.1. Importance of this work

This work is useful for electrical and physical tBLM experiments as it informs: 1) the concentrations that ethanol effects the bilayers at; 2) to what degree the bilayers are effected by ethanol, at varying concentrations; 3) that a bilayer can be reorganised with little physical damage by ethanol (at low concentrations); and 4) that Valinomycin works in a tBLM membrane irrespective of the state of the membrane and level of ethanol in the surrounding solution. These are all outcomes which were not known prior to this work, to the extent that when I started this project I was worried that any concentration of ethanol would damage the membrane permanently and/or leach the Valinomycin from the membrane, limiting data which could be collected with respect to the tBLM.

4.6.2. Improvements

First, regarding EIS experiments, the EIS EEC data allowed for a number of inferences to be made regarding the state of the tBLM, however, theoretically modelling the system would allow the influences of ethanol to be supported by testing whether the outcomes of ethanol on the bilayer in fact lead to the changes observed with the EEC; this work would aid result interpretations by adding depth and understanding to the arguments, such as is observed with Kwak et al. [2010].

Second, extending this work with a more realistic model membrane by including cholesterol would bring this work one step closer toward mimicking natural systems. An AFM study indicates that low concentrations of cholesterol (2%_{mol}) enhance the effects of ethanol whereas high concentrations (20%_{mol}) limit interdigitation [199]. The cause of these effects is speculated to be that a small amount of cholesterol perturbs the gel-phase making it less

compact; the same author states that another sterol, ergosterol did not have the same effect [199]. It is hypothesised that cholesterol might increase the effect of ethanol at lower concentrations while aiding bilayer stability at higher concentrations.

Third, the current work is limited to ethanol, however, there are many other drugs on the market which are simple and could be studied to contrast their moieties. Initial experiments were completed on the ethanol metabolites acetaldehyde and ethyl acetate, however, few experiments were completed on the first drug and the second was found to be non-miscible in water and as such an alternative would need to be used; no data was presented on either in this thesis.

Fourth, the work completed with fs-vSFG was limited as experiments were completed at NIMS. At the time, all conditions and experiments needed to be determined and tested, and time was limited. The existing results indicate the feasibility of this method, which is promising and could be extended further. Therefore, regarding fs-vSFG, a similar process to that seen in NR would be applied, where by deuterated molecules would allow the effects of drugs, such as ethanol, to be defined to either the distal or proximal leaflet of the membrane. It has been shown that by deuterating one side of the bilayer, the signal strength and quality can increase significantly due to standard bilayers having high amounts of symmetry [160]. By deuterating one side of the bilayer the inversion symmetry is broken allowing for the bilayer's response to be significantly larger. Using this method, depth profiles can also be measured within bilayers using fs-vSFG. By controlling the isotopic asymmetry, stronger acyl peaks have been shown to appear from the terminal methyl groups of hydrogenated leaflets. As a sidenote, if fs-vSFG experiments were to be completed in future, chrome would be used between the silicon and the gold to improve structural performance, as a significant issue throughout the experiments was the peeling of gold.

5. Results: Borate transport using the barley Bot1 anion efflux transporter, HvBot1.

5.1. Chapter Overview

Note: This research project was completed in collaboration with the group of Professor M. Hrmova, The University of Adelaide. Barley Bot1 anion efflux transporter (HvBot1) protein preparation and characterisation was performed in Professor M. Hrmova's laboratory. All EIS tBLM measurements were performed at the Flinders University.

Prior to the start of this project, the protein structure of the HvBot1 transporter had been predicted and its cell-free synthesis had been successfully performed through co-translational incorporation into vesicles (by the team of Professor M. Hrmova's laboratory) [86]. At this point, a collaboration was created to extend this work, seeking to determine the physical structure and electrical properties of HvBot1 in a tethered membrane. After determining that cell-free synthesis would be tested in a Teflon-cell 'reactor', experiments were completed using a tBLM to test the membrane-protein's ability to transport anions at various borate concentrations (determined by pH) and the presence of additives (such as NaCl).

This data was published in 2016 [84]. The article concluded that HvBot1 was embedded into a DPhyTL-DPhyPC membrane using *in vitro* eukaryotic cell-free synthesis and that the protein was mediated via pH-dependent transport [84, 86]. The original interpretation used an R-RC-C EEC (Appendix 6.1). Given the developments in the EIS model-membrane field (Appendix 6.1 and 6.2), this chapter seeks to re-interpret the data in the context of a different EEC; the same EEC used in Chapter 4 (Figure 18), which is more applicable to the tBLM model system. Additionally, the outcomes of the previous and updated EECs will be compared focusing on the similarities and differences in their interpretations.

5.2. Introduction

Cells use membrane proteins to mediate the passage of reactants and products, allowing the traffic of ions and molecules between compartmentalised areas. The study of membrane proteins, especially in their natural environment, is limited due to their hydrophobic nature and often complex structural features [67].

The cell-free synthesis procedure is an alternative to cell-based expression, as it is quick and allows proteins to be formed without the need for cells [200]. Using cell-free synthesis, α -Hemolysin has previously been expressed into vesicles while aquaporin Z has been embedded into tBLMs and tested using a quartz crystal microbalance and surface plasmon resonance [200, 201].

In our experiments, we focused on the permeation function of a large membrane transporter from barley, termed anion efflux transporter HvBot1 [61]. HvBot1 was originally identified in barley, specifically in *Hordeum vulgare*, but its orthologues have been found in many other plant species [61]. HvBot1 forms a homo-trimeric protein, of which each monomer has a mass of approximately 70 kDa.

Supported membrane systems have been used for decades, studying membrane properties and pores, and protein transport. tBLMs are one form of SLB and are used due to their controlled composition, metallic substrate, tether region, and applicability to a variety of techniques to test membrane protein function. Suggestions indicate that rigidly bound spacer molecules are important to lift the membrane from the metallic substrate but can be detrimental to the inclusion of macro-molecular structures where the membrane-incorporated fraction exceeds approximately 1 kDa, assuming a 4 nm thick membrane and a lipid area of 1 nm² per lipid (DPhyTL has been shown to be between 0.6 and 0.9 nm²) [42, 202]. At tether densities of

approximately 10%, the mobile lipid patches are large enough to sustain molecular masses of 40 kDa, [42]. As such, the tBLM in this case is imperfectly matched to enable the HvBot1 cell-free synthesis, however, in common model membrane systems, apart from vesicles, no other model membrane includes a sub-membrane space of this kind or can be electrically studied. A space below the membrane allows for extra-membrane elements to have the freedom to fold or position correctly, which is important for HvBot1 (Appendix 6.9), while the electrical properties of the membrane allow for transport processes to be studied. It has been stated previously that pores, peptides, and proteins placed within a tBLM have approximately one-third of the activity typically found in a natural membrane, however, ether reservoir tethered membranes, such as DPhyTL used here, have been shown to have the higher activity than other tether types [40, 203].

5.3. EIS study of HvBot1 in tBLM membranes

Prior to starting the data analysis certain aspects, known to affect the data collected during EIS experiments, need to be mentioned; these include the depth that the displacement current can reach and the effect of bias potential on the Helmholtz layer. Theoretically, at frequencies below 1 Hz, the AC displacement current reaches throughout the full depth of the tBLM and is not diffused by the Helmholtz layer [141]. In this case, across all Bode plots (Figure 49 to Figure 54), the phase minima values always appear below 1 Hz, suggesting that the full depth of the bilayer has been sampled. Further, the Helmholtz capacitance affects the equivalent circuit most significantly with changing bias potentials. Considering that the bias potential was held at 0 mV across all experiments, its changing capacitance is not an issue and would be expected to be consistent throughout all experiments. Finally, a study by Tran et al. [2011] indicates that if EIS tests are completed with quantitative values being acquired above 10 kHz or the EEC values are below approximately 50 nF.cm⁻², the experiments require extra measures to be taken; neither of these occurred and no extra precautions were necessary.

5.3.1. Prior to HvBot1 incorporation

Before HvBot1 was embedded into the tBLM, each membrane was tested with Valinomycin for ion transport; this was a quick indicator which meant that only membranes with appropriate properties exerting Valinomycin conduction were used for HvBot1 incorporation and transport testing. During the process of Valinomycin testing, as each tBLM was formed, it was exposed to sodium ions. This was later identified to be a potential issue during ongoing studies by Professor Maria Hrmova's group. In the process, it was identified that the origin of HvBot1 transporter function is related to the presence of hydrated sodium (ever present in soils) in a particular location of the transporter; a mechanism Maria's group termed 'quantum tunnelling' (Chapter 6.9, Figure 63-C) [86]. Nagarajan et al. [2016] indicated

that sodium cations were a HvBot1 co-factor for conduction, with potassium and lithium cations exhibiting far lower permeation activity.

A part of the process of testing HvBot1 activity is to observe its lack of conductivity without sodium ions, the sodium ions used during membrane formation were replaced with potassium ions, however, they were retained for Valinomycin testing and after rinsing the concentration of sodium ions was unknown. As such, with the co-factor potentially present in small quantities, Valinomycin testing would need to be omitted.

Two key reasons suggested why it was unlikely that the sodium contamination, left over after rinsing, would have activated HvBot1 without extra sodium cations present. Firstly, repeated studies over an extended period of time found that HvBot1 was expressed and inserted into the membrane but was never active, except in one case. In these cases the protein was observed by SDS-Page experiments. Other bilayers which were tested during this time included the use of 400 nm POPC/POPE/POPG/POPS/Cholesterol vesicles and Asolectin vesicles (data not shown). Secondly, once the co-factor had been identified and a controlled concentration (5 mM) of sodium ions was present, HvBot1 conduction was observed (Figure 49 to Figure 54) [205]. Therefore, Valinomycin testing was retained prior to HvBot1 reconstitution and the inclusion of 5 mM NaCl enabled the transport testing of HvBot1 in DPhyTL-DPhyPC membranes.

Using the same EEC as in Chapter 4, the effect of Valinomycin and HvBot1 was modelled. In Table 10, the action of Valinomycin and HvBot1 is presented. The change in defect resistance, R_{def} , due to Valinomycin, was 0.53 orders in magnitude, which is lower than what is usually expected but still appreciable.

5.3.2. HvBot1 Testing and Discussion

After reconstitution of HvBot1, using a buffer solution with a lower pH and without sodium chloride, transport was non-existent, exhibiting a change in defect resistance of 0.1 and 0.02 orders of magnitude respectively. By including sodium ions, but at a low pH, a change in resistance of 0.12 orders of magnitude indicated that HvBot1 transported slowly. But, by including sodium ions and raising the pH of the buffer solution, the action of HvBot1 was evident. At both pH values of pH = 7.5 (borate concentration = 90 μ M) and pH = 9 (borate concentration = 1.8 mM) the decrease in resistance of the defect was 0.33 and 0.30 respectively (Figure 53 and Figure 54). This pattern could be repeated.

Within the data (Figure 53 and Figure 54), the change in defect resistance (of 0.33 and 0.30 respectively) is low. Three theories explain the HvBot1 action: (i) slow transport; (ii) mono-directional transport; and (iii) the lack of sodium cations in the sub-membrane space.

The first potential explanation for HvBot1 conduction is slower transport, however, it is difficult to compare expected differences in transport between Valinomycin and HvBot1 directly because the transport rates of Valinomycin are quoted in anions per second or by kinetics of association and dissociation, whereas the HvBot1 transport is quantified using the Michaelis-Menten equation [23, 86, 206, 207]. Further, the number of proteins or peptides per a given area is different due to a physical area they require. It should also be noted that the decreased diffusion of the sub-membrane space would slow down or limit rinsing of the membrane. As such, the slower transport of borate ions paired with a slow diffusion of the sub-membrane space could cause this decreased rinsing rates. Extended rinsing times were used, however, they did not affect the resistance of the defect.

Second, HvBot1 is a uniporter, and as such its action is mono-directional. Nagarajan et al. [2016] suggested that HvBot1 can embed in either configuration across a membrane, however, the large extra-membrane region, termed ‘sombbrero’ (6.9) protruding from the membrane, causes its preferential orientation. Because the tBLM’s sub-membrane space is approximately 1.1 nm deep, whereas the sombrero protrudes 1.7 nm from a membrane surface [68, 86], the protein would embed with the sombrero pointed toward the large reservoir or otherwise it would embed and denature. Alternatively, the uniport’s mono-directional transport would only cause the resistance of the defect to increase during borate-sodium inclusion, but would not allow adequate rinsing and recovery in resistance. Further this would explain the increase in capacitance due to a greater charge separated across the membrane. Additionally, although the sub-membrane space is tightly packed and difficult to polarise, with the increase in ion concentrations, it could potentially polarise more (See Appendix, Chapter 6.6).

The third potential cause affecting HvBot1 permeation is the lack of sodium ions below the membrane. As mentioned above, the residual amount of sodium cations left over after rinsing was not found to activate HvBot1. As such, the HvBot1 proteins embedded with the sombrero pointed into the sub-membrane space would likely be inactive due to the lack of sodium ions below the membrane, which are required for borate transport. As stated earlier, it is difficult to know how much credence can be given to EEC data when comparing the values using various pH values with or without NaCl being present, as these comparisons would be affected by changed frequency parameters to meet the needs of the spectra being collected. It should be noted that other anions were planned to be tested, however, time constraints led to only borate anions being tested.

Other membrane EEC elements had mixed patterns in their properties. Z_{sub} was found to have an inconsistent pattern while the alpha values consistently increased after HvBot1

reconstitution and stayed relatively constant throughout the length of the experiment (~ 0.88). This second parameter potentially suggested that the sub-membrane space became less like-a-resistor and more like-a-capacitor. C_{mH} did not change during HvBot1 conduction experiments, although, throughout the length of experiments C_{mH} generally increased, possibly due to the changing alpha value. In rudimentary terms, the increasing capacitance either indicated a thinning of the membrane or a break-down or increase in dielectric values (Equation 18).

Table 10: EEC values during HvBot1 experiments in a DPhyTL-DPhyPC membrane.

Sample	R_{def} ($M\Omega \cdot \text{cm}^2$)		ΔR_{def} (%)	C_{mH} ($\mu\text{F} \cdot \text{cm}^{-2}$)		Z_{sub} ($\Omega \cdot \text{s}^{-\alpha} \cdot \text{cm}^2$)		Alpha	χ^2
<i>Bilayer with Valinomycin (NaCl)</i>	4.10	± 0.248		0.700*	± N/A	0.504	± 0.0139	0.58*	.00598
<i>Bilayer with Valinomycin (KCl)</i>	2.16	± 0.0948	53%	0.720*	± N/A	1.16	± 0.271	0.78*	.00778
<i>Bilayer pre HvBot1, pH 6</i>	11.7	± 0.622		0.680*	± N/A	0.743	± 0.0599	0.86*	.0109
<i>Bilayer pre HvBot1 (+Borate), pH 6</i>	10.5	± 0.527	90%	0.690*	± N/A	1.11	± 0.108	0.86*	0.137
<i>Bilayer with HvBot1, pH 6</i>	1.20	± 0.0359		0.815	± 0.0035	1.04	± 0.217	0.85	.000898
<i>Bilayer with HvBot1 (+Borate), pH 6</i>	1.17	± 0.0340	98%	0.816	± 0.0034	1.02	± 0.202	0.86	.000900
<i>Bilayer with HvBot1, pH 6, NaCl</i>	0.926	± 0.0231		0.874	± 0.0033	1.04	± 0.0157	0.87	.000870
<i>Bilayer with HvBot1 (+Borate), pH 6, NaCl</i>	0.811	± 0.0222	88%	0.867	± 0.0037	1.03	± 0.0160	0.87	.00102
<i>Bilayer with HvBot, pH 7.5, NaCl</i>	0.687	± 0.0210		0.873	± 0.0048	1.28	± 0.0241	0.87	.00141
<i>Bilayer with HvBot1 (+Borate), pH 7.5, NaCl</i>	0.321	± 0.00908	47%	0.867	± 0.0050	1.37	± 0.0186	0.89	.00120
<i>Bilayer with HvBot1, pH 9, NaCl</i>	0.220	± 0.00682		0.914	± 0.0066	1.81	± 0.0275	0.88	.00176
<i>Bilayer with HvBot1 (+Borate), pH 9, NaCl</i>	0.108	± 0.00305	49%	0.926	± 0.0075	2.84	± 0.0286	0.89	.00171
Note: (ΔR_{def} (%) = $R_{\text{def-conduction}} / R_{\text{def-non-conduction}}$) and a * indicates that the value was controlled									

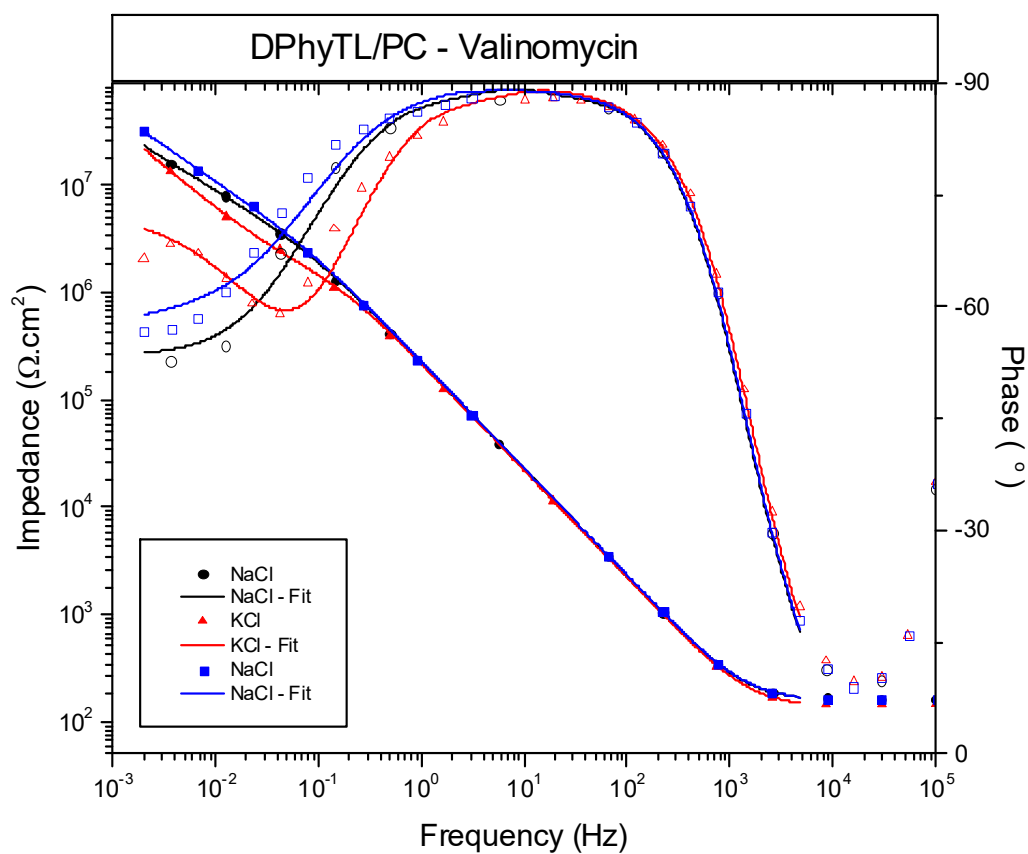


Figure 49: Bode plot of tBLM pre HvBot1 reconstitution, testing the bilayer matrix using Valinomycin.

Symbols represent data points where as the lines represent the fits. Closed symbols refer to the impedance trace whereas the open symbols refer to the phase trace.

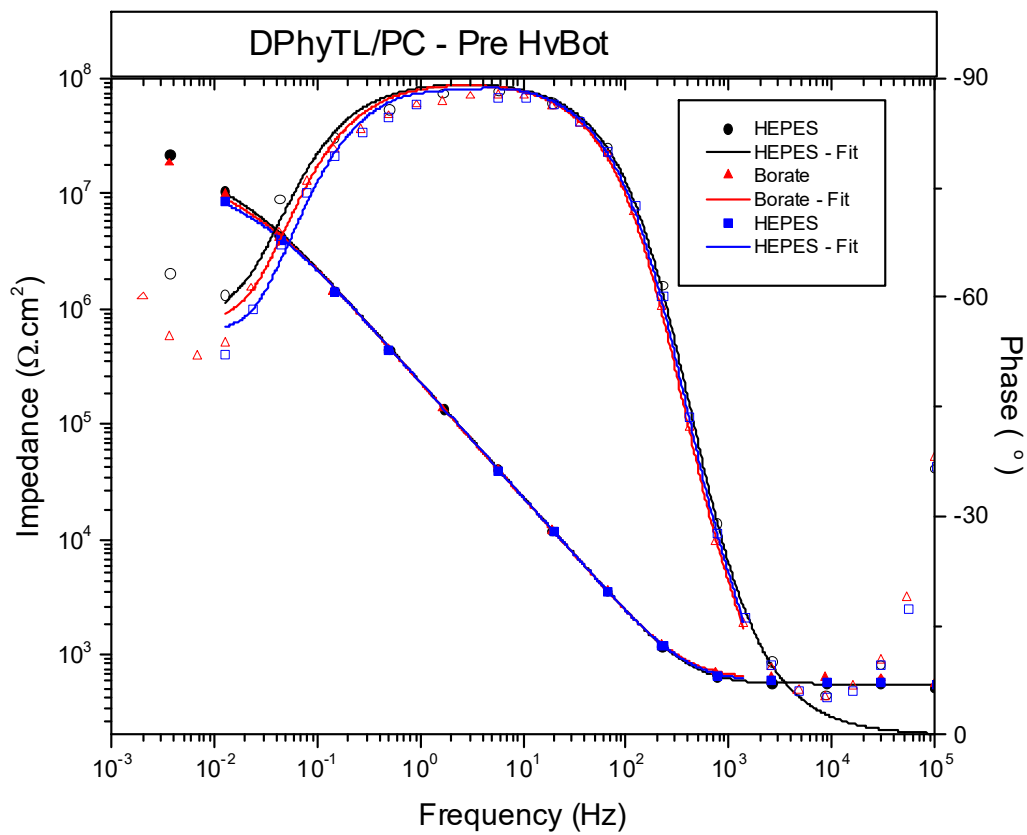


Figure 50: Bode plot of a tBLM testing borate anion conduction pre-HvBot1 reconstitution.

Symbols represent data points where as the lines represent the fits. Closed symbols refer to the impedance trace whereas the open symbols refer to the phase trace.

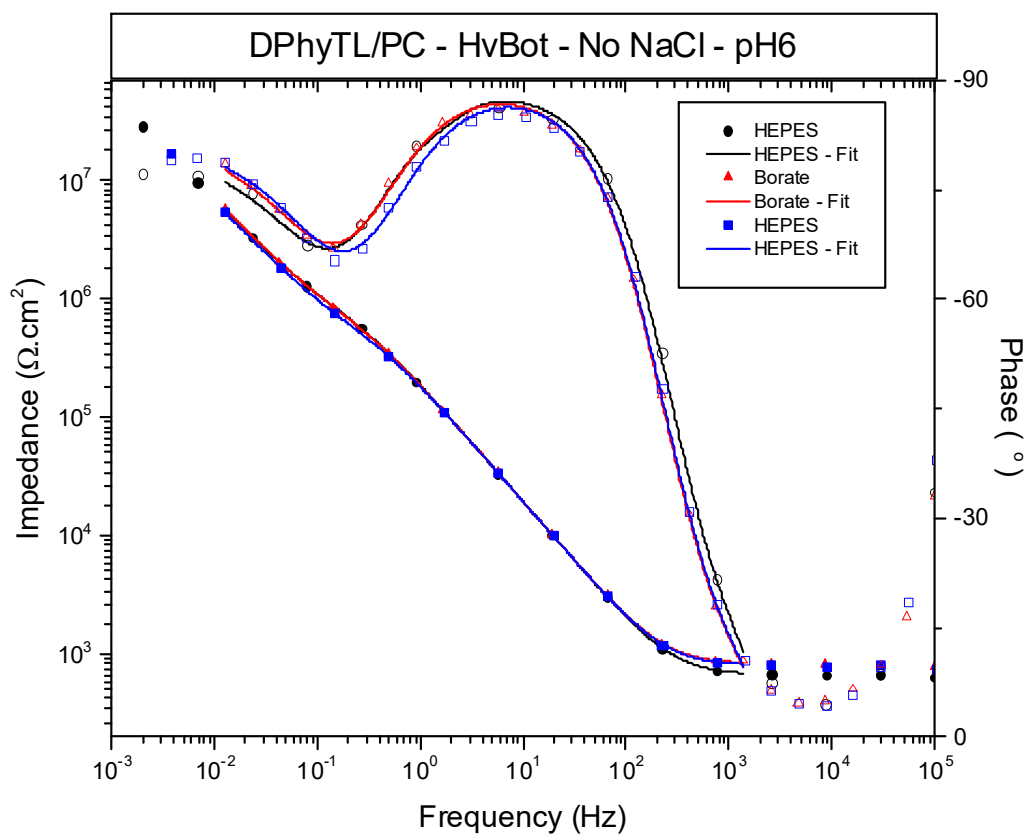


Figure 51: Bode plot of a tBLM pre HvBot1 reconstitution, prior to NaCl inclusion at pH 6.

Symbols represent data points where as the lines represent the fits. Closed symbols refer to the impedance trace whereas the open symbols refer to the phase trace.

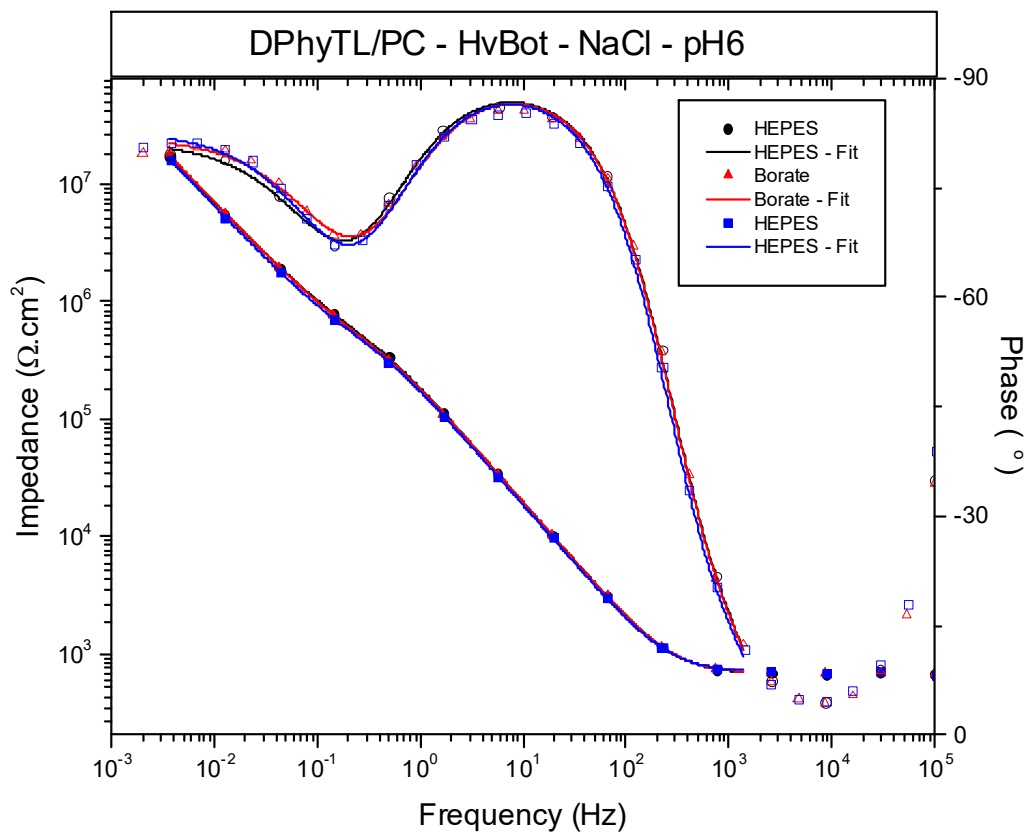


Figure 52: Bode plot of a tBLM pre HvBot1 reconstitution, including NaCl at pH 6.

Symbols represent data points whereas the lines represent the fits. Closed symbols refer to the impedance trace whereas the open symbols refer to the phase trace.

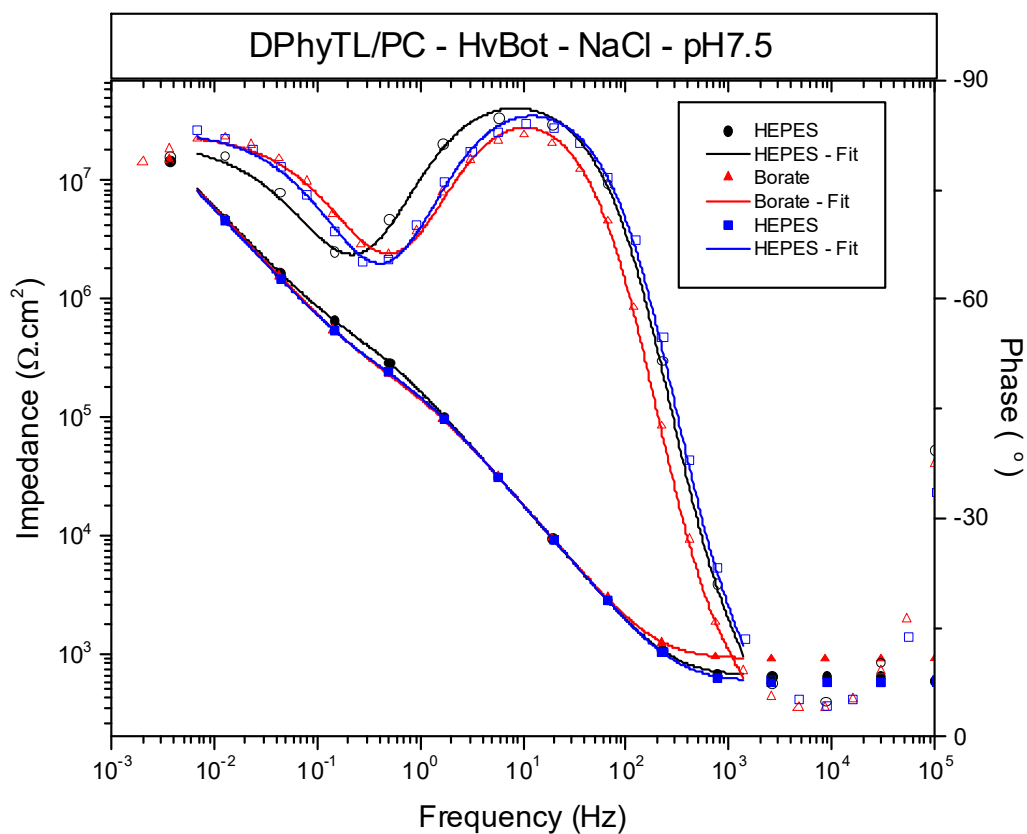


Figure 53: Bode plot of a tBLM pre HvBot1 reconstitution, including NaCl at pH 7.5.

Symbols represent data points where as the lines represent the fits. Closed symbols refer to the impedance trace whereas the open symbols refer to the phase trace.

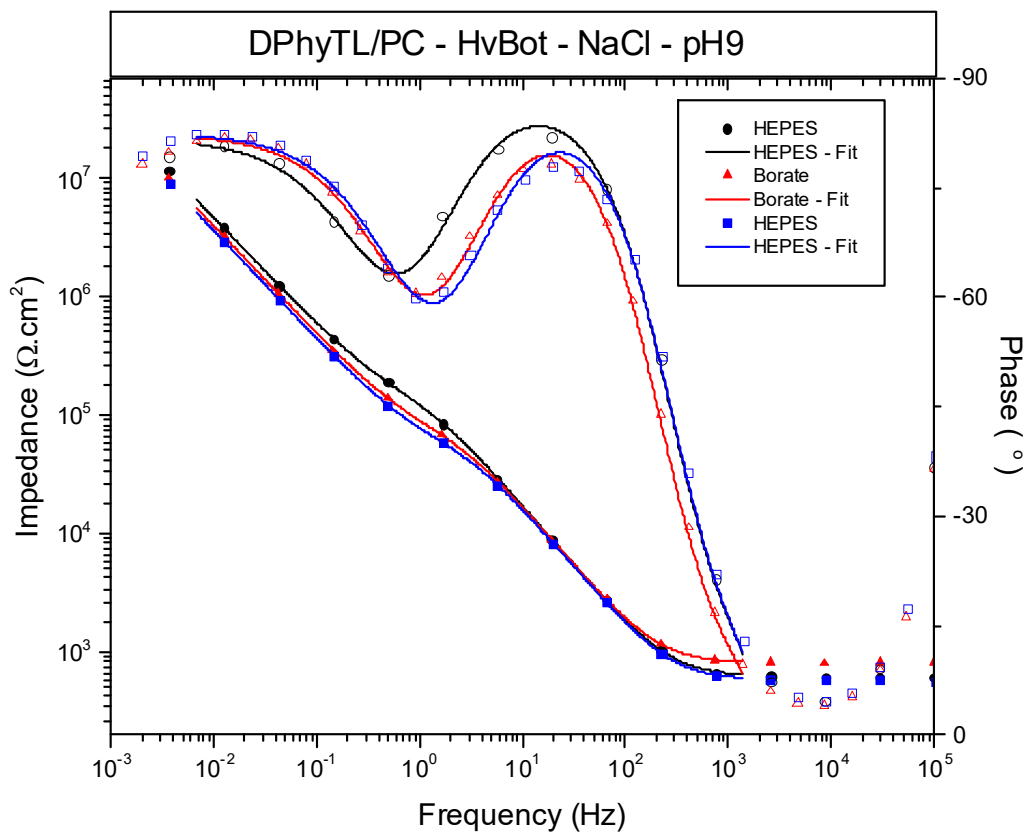


Figure 54: Bode plot of a tBLM pre HvBot1 reconstitution, including NaCl at pH 9.

Symbols represent data points where as the lines represent the fits. Closed symbols refer to the impedance trace whereas the open symbols refer to the phase trace.

5.4. Comparisons between previous and updated EIS EECs results

The key findings for each EEC followed a similar trend; the original EEC stated that the bilayer was unaffected by borate anions and the updated EEC suggests the same outcome.

Before introducing HvBot1, the defect resistance decreased by 10% (11.7 to 10.5 $M\Omega.cm^2$), possibly due to the inclusion of borate anions or the effect of controlled pH (Figure 50 and Table 10); these values are well-outside their respective errors, however, a larger chi-squared value was also attributable to the second, suggesting less credence should be given to this change in defect resistance. The capacitance of the membrane-Helmholtz layers did not change, suggesting that membrane continued to retain its structure during the change in buffer solutions. The impedance of the sub-membrane space almost doubled when borate ions were included (Table 10), however, an equivalent change in sub-membrane impedance was observed when potassium ions were first introduced to the system during Valinomycin testing, suggesting this was a case of equilibration of ions below the membrane. During these two buffer solutions, the Z_{sub} alpha value almost reached its end-value (Table 10: 0.86 out of 0.89), suggesting the sub-membrane space became more capacitor-like, persisting for the duration of the following experiments. Combining the C_{mH} , Z_{sub} , and alpha changes, the sub-membrane space changed only slightly in response to the washing steps (after rinsing or replacing potassium or sodium ions left-overs from the Valinomycin tests, with the HEPES buffer containing borate ions). One can deduce that the tBLM properties in the initial HEPES/bis-Tris-propane buffer without borate is similar to that of the HEPES wash after borate addition, as is observed using the previous EEC [84]. This particular aspect was not discussed in the original paper.

Regarding HvBot1, the initial investigation of the bilayer using the previous EEC model suggested that the change in membrane resistance is an indicator of conduction with membrane capacitance, as a measure of integrity. It was stated that a change in resistance during cell-free synthesis was witnessed through the electrical values; this indicated that a well-sealed bilayer was conserved [84]. With the updated EEC, the same effect is observed, whereby there is a significant decrease in defect resistance, $11.7 \text{ M}\Omega\cdot\text{cm}^2$ to $1.2 \text{ M}\Omega\cdot\text{cm}^2$, which is larger than the change recorded with the previous model ($14 \text{ M}\Omega\cdot\text{cm}^2$ to $3.7 \text{ M}\Omega\cdot\text{cm}^2$). On the other hand, the C_{mH} increased by 25%, the Z_{sub} changed insignificantly, and the alpha value held constant. The increase in capacitance was constant throughout the length of the experiment and its pattern of increase seemed to be unaffected by a cell-free synthesis procedure. As such, it can be suggested that the outcome of the new EEC is similar to that of the EEC used by Zieleniecki et al. [2016].

The final comparison is focused on the transport of borate anions by HvBot1. The initial interpretation of the bilayer indicated that the membrane resistance increased with the inclusion of borate anions in the presence of HvBot1. The initial interpretation similarly concluded that the addition of sodium ions at $\text{pH} = 6$ made no observable changes visible to EIS. It is suggested that this occurred because there were no borate ions present at this pH value, however, it is also possible that no transport was detected either because there was no transport or because the change in defect resistance was too small to measure. The most important issue at this point is that the defect resistance was far lower in the new EEC than the membrane resistance in the previous model ($1.2 \text{ M}\Omega\cdot\text{cm}^2$ as compared to $3.84 \text{ M}\Omega\cdot\text{cm}^2$). Furthermore, the C_{mH} was $0.815 \mu\text{F}\cdot\text{cm}^{-2}$ and Z_{sub} was $0.217 \Omega\cdot\text{s}^{-\alpha}\cdot\text{cm}^2$, in contrast to Zieleniecki et al. [2016] which states that the capacitance of the membrane is almost double that seen here (C_{mem} is $1.23 \mu\text{F}\cdot\text{cm}^{-2}$ and the spacer is $2.49 \mu\text{F}\cdot\text{cm}^{-2}$); these values are on the same order of magnitude and in fact both the Z_{sub} value of the new EEC and the C_{sub} value of the old EEC both increased throughout the

length of the experiment. The only significant difference between the two models at this point was found in the C_{mH} value of the new EEC, which increased unlike the C_{mem} value of the previous model which stayed relatively stable or decreases slightly (Table 10).

Increasing the concentration of borate anions (pH 7.5) both with the previous and updated EECs indicate that HvBot1 is transporting anions. The previous model indicated a decrease in resistance of 49%; a little larger than the updated EEC. Both EECs also suggested that no other properties of the membrane changed between non-conduction and conduction. Increasing the borate concentration further (pH 9) indicated no increase in transport, with the new EEC only showing a change in resistance of 47% where the previous EEC indicated a change of 60%. Both models therefore determined that the maximum transport rate of borate was reached at approximately pH 9.

These results demonstrate a similar pattern to the data published previously [84]. HvBot1 was found to be inactive until NaCl was included and a higher pH was reached. The latter parameter, pH, is related to the pK_a value of boric acid (9.24), meaning that a higher concentration of borate anions is present for transport to occur [86].

5.5. Conclusions

By using both EIS and electrophoretic techniques, such as SDS-PAGE, that HvBot1 was correctly synthesised and reconstituted into the membrane. EIS confirmed that the HvBot1 transport function was observed at pH 7.5 and pH 9, but not at pH 6. This work has shown that, even with dense tethering systems such as the DPhyTL-DPhyPC membrane, the tBLM is an appropriate system for testing the transport function of highly complex proteins such as HvBot1. Furthermore, although the updated EEC is more applicable physically, both EECs are applicable to analysing the surface and transport of a protein.

The DPhyTL-DPhyPC membrane contains $\leq 5\%_{v/v}$ water in the sub-membrane space, and as such the mobility of ions within such spaces is low. This is observed in both the previous as well as updated EEC. The small volume and limited mobility meant that the solution had decreased polarizability, and as such the decreased conductivity was expected [141]. More precise conclusions regarding the HvBot1 activity could be made with further data collection and analysis.

5.6. Importance of Current Outcomes and Future Suggestions

5.6.1. Importance of this work

This work is one of the few examples in literature where cell-free synthesis of a functional protein has been successfully completed with a tBLM. Prior to starting these experiments, it was unknown if the protein would be able to be reconstituted in the Teflon reactor and if the size of the protein would limit the protein entering the membrane and/or retain a functional structure. This work is vital considering the number of articles suggesting the density of the tethers and hydration of the sub-membrane space limits the use of realistic proteins. This work paves the way for studying other membrane-proteins and optimising the tether structure for specific proteins.

5.6.2. Future Work

First, the tBLM used in this case is known to have a dense sub-membrane space due to the tightly packed tether region and repulsion due to the confirmation of the tether (Chapter 1.3.2.4). A tBLM of a different chemical composition could possibly improve the performance of complex membrane proteins, e.g. that of HvBot1; suggestions in this case could include spacer molecules or altogether different tethers. Testing even one such less-dense tethered surface would determine whether the HvBot1 transport was limited due to the density of the sub-membrane space.

Second, by using held potentials prior to EIS experiments, the directionality of HvBot1 transport could be tested. EIS experiments which have used DC biases have indicated that the properties of the membrane do change at those potentials, however, in this case, a DC bias would be used prior to starting the experiment to flush anions either above or below the membrane; during the experiments the DC bias would be removed, i.e. set to 0V. This would

further confirm the mono-directionality, and in fact, could boost the transport of the protein if many ions are flushed onto its conducting side.

Third, pending successful results from the suggestions of the paragraphs prior, HvBot1's transport being increased would improve the detection of a change with more significant changes in R_{def} ; this would mean clearer changes in R_{def} which would allow for tests which require greater sensitivity. Examples of experiments with lesser transport would include ions such as phosphite, sulphate, chloride, and nitrate anions, thus confirming patch-clamp spectroscopy and voltage clamp electrophysiology results and quantitatively determining the viability for a possible borate-specific biosensor.

6. Appendices

6.1. EIS EECs without CPEs

6.1.1. Single RC-Meshes: (R(RC)C) and (R(RC))

Before introducing EECs with CPEs, first EECs without CPEs will be discussed.

Valincius, Meškauskas, and Ivanauskas [2012] state that, historically, all equivalent circuits can be combined into two categories: those of which are visually fitted to the data collected and those that use a rigorous mathematical approach. The same authors insist that the first method is appropriate for simple systems which are not doped with ion-transporters or attached to surfaces on one side, however, more complex systems, such as an ion-transporting doped bilayers which include various interactions, should be mathematically modelled where possible to be more applicable [138].

Black lipid membranes have generally been modelled using a series of RC meshes; a method which has long been considered translatable to tBLMs [138]. Though unlike black lipid membranes, tBLMs do not exhibit geometrical homogeneity, commonly have defects, the tether replaces a typical BLM's substrate-water interface with a substrate-tether-bilayer-water interface and their density is directly related to many parameters controlled during formation [138]. Pores, peptides, and proteins all further alter the structure and physical properties of the membrane asymmetrically between the distal and proximal sides [138]. The buffer solution above the membrane is infinite in depth considering the membrane's size, whereas the solution contained within the tether region is limited in volume and rate of transport. All of the aforementioned properties affect the features of the EIS immittance and should be taken into account [138]. It should be noted that a key difficulty with EECs is that, in some cases, they may exhibit an identical immittances, and as such are referred as identical circuits, ambiguous circuits, or degenerate circuits [208].

Historically, papers have interpreted bilayer data generally using R-RC or R-RC-C EECs (see Figure 55). Strictly speaking, these circuits combine the capacitive elements of the sub-membrane space and Helmholtz layer with those of the membrane, channels, or defects. Both EEC types have been capable and relatable in interpreting data with either similar or almost identical emittances, however, both the R-RC and R-RC-C EECs critically ignore defect non-polarisability within the sub-membrane space.

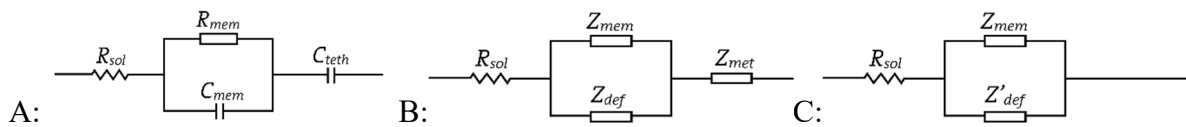


Figure 55: Common types of R-RC and R-RC-C meshes.

A is a common circuit used to model monolayers and in some cases membranes. B is an example of an equivalent circuit of an ideal membrane without defects, where Z_{def} does not affect Z_{mem} . C is an equivalent circuit of a non-ideal membrane.

Figure 55-A is a common EEC representation used on mono- and bi-layers as early as 2002-2003 [39, 136]. Schiller et al. [2003] used it to represent a complete DPhyTL-DPhyPC membrane before, during, and after Valinomycin conduction. In that case, the last capacitor in Figure 55-A, instead of representing a tether, represented the double layer adjacent to the gold [39].

Alternatively, Vockenroth et al. [2008] used a single parallel RC EEC when testing mono- and bi-layers and an RC-RC EEC when studying protein doping, where the second RC mesh represented the space charge [135]. Within the same paper the authors also demonstrated the relative properties between tBLM size, capacitance, and resistance [135]. In a second and third paper, Vockenroth et al. [2008] use R-RC-C EECs to test bilayer responses to different tethers as well as the incorporation of M2 ion channels [68, 130]. The EECs used in those cases

were the same as in Figure 55-A, however, the last capacitor represented both the spacer region and the gold interface [68].

Braunagel, Junghans, and Köper [2011] used Figure 55-A when testing ferrocene-Valinomycin on several different bilayers. In this case, Braunagel, Junghans, and Köper [2011], noted in conclusion that the model poorly mimicked the data once the peptide was incorporated, stating that the inhomogeneity of the surface as well as added peptide were significant sources of complexity.

Naumann et al. [2003] used DPhyTL-DPhyPC membranes to compare the quality of membranes formed on various types of TSG as well as polycrystalline gold. Curiously, Naumann et al. [2003] quoted that they used a circuit originally introduced by Cornell et al. [1997], R-RC-C, however, Cornell et al. use a RC-C EEC in that paper [79].

Atanasov et al. published two articles in quick succession on tethered membranes using silicon [29, 77]. The earlier article extends Figure 55-A to two RC meshes, representing the solution, membrane, and silicon oxide surfaces. In their later article, Figure 55-A was used to model Si-silanised and Au-thiolated surfaces and combined later with that of a twin-RC mesh equivalent circuit for a bilayer; thus, like with Valincius, Meškauskas, and Ivanauskas [2012], the values were not directly comparable.

Rose, and Jenkins [2007] combine both Figure 55-A and a simpler version of Figure 14, when studying DPPTE/EPC membranes. The ‘perfect’ membranes were modelled using an R-RC equivalent circuit while the ion conduction of Valinomycin was studied using the more complex circuit similar to Figure 14-B

Figure 55-A has also been used when modelling protein-tethered BLMs [69]. Giess et al. [2004] used a TSG surface with a bilayer consisting of immobilized His-tagged Cytochrome C Oxidase completed with DPhyPC. The R-RC-C circuit was used to observe electrolyte resistance, membrane resistance and capacitance, and capacitance of the interface [69]. In this case Giess et al. [2004] notes that the change in membrane properties was indicative of protein activation. The authors also note that the higher capacitance may have been caused by the increased dielectric of the highly prevalent proteins [69].

6.1.1.1. Deeper Theory

By extension, Figure 55-B is a more general but also more complex example of Figure 55-A, and Figure 55-C this step even further. In Figure 55-B there are three impedances present: the membrane; membrane-defects; and the metal-liquid interface. When no redox species are present, Z_{met} can be considered to be an ideal capacitor formed by the Helmholtz layer at high concentration [138]. However, as Valincius, Meškauskas, and Ivanauskas [2012] suggest, this is an ideal case and as such this model would suggest a uniform potential across the whole metal-tether-water interface, which realistically defects disrupt. In an ideal case the electrical potential vectors would be strictly perpendicular to the plane of the support, however when a defect appears, that is no longer the case. Depending on the size of the defect a range of electrical potential vectors are present. Before continuing, it is important to note that given a thick metallic support, the equipotential layer, previously described in Figure 55-B as the unaffected Helmholtz layer, is transferred into the metal, leaving two clear pathways for potential transfer, as seen in Figure 55-C and Figure 56 [138].

In Figure 55-C, Z'_{def} is in fact a combination of two different potential vectors, across the defect and across the sub-membrane space emanating from the defect. As such, in actual fact, in Figure 56, $Z'_{\text{def}} = Z_{\text{def}} + Z_{\text{sub}}$, and thus Z_{mem} retains its original definition [138].

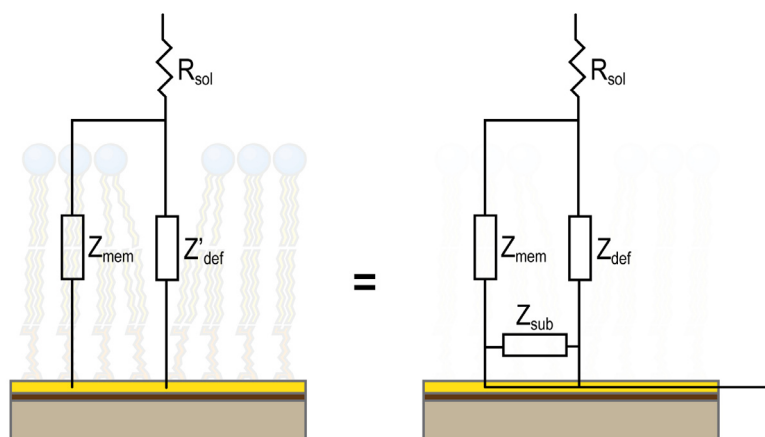


Figure 56: Schematic of a lipid bilayer membrane with a defect and the circuit applied to it.

based on Valincius, Meškauskas, and Ivanauskas [2012]. Left: simplified equivalent model circuit for interpreting tBLM properties. Right: A more defined version of the same circuit.

It is important to mention that the defect-induced electrical-field vectors' angles, as well as size, will strictly depend on the conductivity of the sub-membrane space as well as metal-reservoir interface [138]. In turn, this is strictly determined by the dielectric properties of the membrane, size of the defect, its geometry, and the conductivity of the sub-membrane space and Helmholtz layer [138]. Valincius, Meškauskas, and Ivanauskas [2012] state that by interpreting data collected, the sub-membrane electrolyte resistance, though difficult to gain information on, can be calculated, while the impedance of the Helmholtz layer cannot be determined.

Kirchhoff's loop and junction rules together state that if two circuit elements have a significantly different impedance, their overall impedance is controlled by the circuit element which has a higher impedance when they are in series and by the element with a lower impedance when in parallel [123]. From capacitive impedance, $Z = i/\omega C$, it should can be deduced that a low impedance element appearing at a higher frequency must mean that the capacity of the capacitor is smaller than that of one which has a high impedance at a low

frequency [123]. Previously, this led to relations between $R_{bilayer}$, R_m , and R_{ch} , where $R_{ch} < R_{bilayer}$ and as such $R_m \approx R_{ch}$ [47].

At such a time, the resistance of the various elements of a bilayer added in parallel ($\frac{1}{R_m} = \frac{1}{R_{bilayer}} + \frac{1}{R_{ch}} = \frac{R_{bilayer}R_{ch}}{R_{bilayer}+R_{ch}}$) [47]. For this reason, when the transporter or channel was active, the change in resistance was witnessed because R_m was a combination of the bilayer and channel, not discerning between the two [47]. This pattern continued through many papers, such as in chapters 6.1.2, 6.1.3, and 6.2. In general, many of the papers quoted use these slab systems to interpret biomimetic thio-lipid tethered membranes; consisting of a hydrophilic spacer, the bilayer, and the aqueous solution above the bilayer [123].

Differently to the previous articles, Ge et al. [2003] used an R-CRW circuit to interpret DNA bilayers form on top of tethered 2-amino ethanolthiol on gold; by using this circuit, Ge et al. [2003] were able to interpret the capacitance of the surfaces. The analysis itself was not complex, however, it broached on a concept that is seen later in Figure 55-C, focusing on the parts of the membrane frequency dependent and independent elements, but both with varying frequency dependencies.

6.1.2. Double RC-Meshes (R(RC)(RC)), (R(RC)(RC)C)

One of the more common equivalent circuits used to study model membranes uses the double RC mesh in series.

Atanasov et al. [2006] used this circuit in an R-RC-RC-C configuration to model various bilayers which used modified linkers depending on their surface requirements; TSG gold or Boron doped single crystal silicon (100). Atanasov et al. [2006]'s conclusion did not offer a clear distinction between elements of the model circuit however went on to make the

distinction that a monolayer of thiolated or silanised lipid only required an R-RC-C configuration whereas bilayers required a more complex R-RC-RC-C circuit. The author also stated that silane based tBLMs showed better electrical properties, even though thiol-based lipids had a higher membrane resistance.

Membrane resistance in the last case was attributed to membrane leakage, however, Lin et al. [2008] also presented data which used an R-RC-RC-C circuit to model doping effects on bilayers on n⁺-Si and n-Si (111). In Lin et al. [2008]'s case, the circuit represented different properties to Atanasov et al. [2006]. Unlike Atanasov et al. [2006], Lin et al. [2008]'s EEC modelled solution resistance, membrane resistance in parallel with membrane capacitance, followed by resistance to charge transfer with parallel with space charge and double layer capacitances combined into one capacitor, the resistance of the membrane is a combination: $1/R_{\text{mem}} = 1/R_{\text{bilayer}} + 1/R_{\text{channel}}$ [47]. Lin et al. [2008]'s conclusion was that the surfaces could be integrated with semiconductors, however that it was critical to determine what was occurring at the semiconductor-solution interface before introducing transmembrane proteins. According to Lin et al. [2008], membranes formed on highly-doped silicon were able to withstand a large variation in potential and were therefore incredibly applicable to electrical studies. Both cases are an example of interpreting anchor and tether wetting and physical parameters through membrane parameters, which has been superseded (Chapter 1.6.5.2).

Vockenroth et al. [2009] used a circuit such as Figure 57 to analyse a TSG supported DPhyTL-DPhyPC membrane in a case where monolayer resistance was low and the spacer charge was witnessed (spacer-charge capacitance and capacitance of the tether double layer).

Naumann et al. [2002] used a circuit similar to Figure 57 when studying thiolopeptides attached to gold surfaces, completing bilayers using phosphatidylcholine. In

that case, the first RC element represented higher frequencies and the second RC element represented lower frequencies [136]. Little is described about the EEC itself, however, it is used to study the changes in transport with and without activation [136]. It should be noted that this paper is one of the earliest of its kind, published in the year 2002 [136].

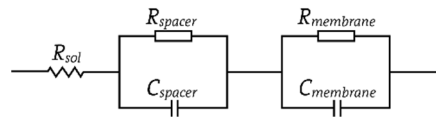


Figure 57: A type of R-RC-RC EEC

Note: Used by Vockenroth et al. [2009] to describe lower resistance DPhyTL-DPhyPC membranes.

6.1.3. Triple-RC meshes or greater

Triple RC meshes are less common. Becucci, and Guidelli [2014] used them when discussing the virtues of mercury supported DPhyTL-DPhyPC membranes in a recent review. Each element (Figure 58) was attributed and Becucci, and Guidelli [2014] continued on to show that Gramicidin decreases the resistance of the membrane by three orders of magnitude.

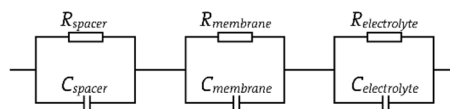


Figure 58: A type of triple RC mesh EEC.

Note: Becucci, and Guidelli [2014] use this particular model to study mercury supported membranes.

Becucci et al. [2008], based on the four RC mesh system, extended the series of RC elements to five RC meshes when studying DPhyTL-DPhyPC membranes formed on mercury. The five RC meshes represented, in order of slabs: the lipoic acid residue interacting with the mercury surface; the water electro-reduction taking place at the surface of the silver; the spacer; the membrane; and the aqueous solution [137]. Becucci et al. [2008] went on to state that a

comparison between five and three RC mesh models was only semi-quantitative, however, clarified that under certain conditions, EIS may have revealed many dielectric slabs expected in mercury supported tBLMs (Hg-tBLMs) [137]. Becucci, and Guidelli [2014] especially insisted that this was the case when Hg-tBLM mixtures formed gel phase micro-domains as well as lipid rafts.

Shamsi, and Coster [2011] used an R-[RC]₄ mesh system to analyse two different types of membranes on silicon formed from two types of peptides. Although not applicable to tethered membranes, the authors suggested that the meshes represented the electrolyte, ionic double layer, polar head region, hydrophobic region of the peptide, and hydrophobic region of the lipid.

6.1.4. Overall

Overall, Valincius, and Mickevicius [2015] have shown, in great detail, that no matter the model used, defining some of the parameters with a single element is futile [141]. According to best estimations, an infinite set of conventional elements is best, however, due to a limit, it is best to consider that at high frequencies the sub-membrane impedance becomes a CPE with exponent $\alpha \approx 0.5$, and in the low-frequency domain the response of a single defect is resistive while multiple defects are capacitive.

6.2. EECs with CPEs

Thus far within this review, CPE elements have been interpreted as capacitors where appropriate. However, the general consensus between data and model possibly hits the bullseye of the wrong target, but is a gap that is slowly closing (Chapter 6.1) [138]. Barsoukov, and Macdonald [2005] and Becucci et al. [2008] together agree that CPE elements were mentioned as early as 1932 however Cole and Cole modified the Debye expression for the complex dielectric constant and used it for the first time representing an element's time constant distribution. CPEs are one way to account for either the presence of inhomogeneity in the distribution of the transmission line or distortion of the relaxation times approximately a mean value. The time constants differ by up to two orders of magnitude, leading to non-uniform diffusion [125, 137]. The application of CPEs is not rigorous, with papers rarely demanding rigorous interpretations with included *ab initio* calculations, a point made clear by Valincius et al. (2011), Bertheir et al. (2001), and He et al. (2005) [138, 208, 210]. Specific articles which have applied an *ab initio* approach to membrane properties and defined important paradigm shifts from common methodologies focus on pore-modelling [41, 138]. Current *ab initio* experiments indicate that the standard series of parallel meshes struggle to mimic the realistic behaviour of membranes and that CPEs are important in modelling membranes correctly [138]. Macdonald et al. states that, historically, the real and imaginary expressions of the Debye relaxation relations remain consistent models for CPE -like effects since their introduction in the late 1920s [125]. To clarify, Macdonald states that by plotting both the real and imaginary expressions against normalised frequency the dielectric loss peak corresponds to the real admittance of AC impedance data and is commonly applied to solid-state relaxation processes, however this only applies for solid-state devices. In the case of tBLMs, AC impedance circuits can be used in place of those relations to model conductivity and space charge accumulation

within bilayers, even though their explanation through physical phenomena is quite different. The standard expression for a CPE element is empirically derived [125]. Unlike Equation 13, a more practical equation is presented forthwith.

Equation 19: Common forms of a CPE equations

Note: for further information, see Chapter 6.1 [138, 208].

$$Z_{\text{Capacitor}} = \frac{1}{C(j\omega)} = \frac{1}{Q^0(j\omega)^\alpha}, \alpha = 1$$

$$Z_{\text{CPE}} = \frac{1}{Q^0(j\omega)^\alpha} = A(j\omega)^{-\alpha}, A = \frac{1}{Q^0}$$

Q^0 and α are the incomplete capacitance of the element and the fractional exponential respectively. The units of A are defined as $\Omega \cdot s^{-\alpha}$ and as such Q^0 is the inverse ($\Omega^{-1} \cdot s^\alpha$). By extension, taking into account the impedance of a capacitor using Equation 12 and normalising the capacitance to the area, Q^0 's units can be converted to $\mu\text{F} \cdot s^{\alpha-1} \cdot \text{cm}^{-2}$ [125]. Therefore, when α is 1, the CPE element acts as a capacitor and when it is zero it acts like a resistor. Overall, Q^0 can be defined as either $\Omega^{-1} \cdot s^\alpha \cdot \text{cm}^{-2}$ or $\mu\text{F} \cdot s^{\alpha-1} \cdot \text{cm}^{-2}$. In this way, the units quoted throughout the thesis for the Z_{sub} are in $\Omega \cdot s^{-\alpha} \cdot \text{cm}^2$.

Models are applied routinely using programs such as WinSPICE [125]. A consequence of this equation is that a CPE compares a distribution of dielectric properties against the relaxation time of a surface being tested, $\varepsilon - \varepsilon_\infty = \frac{(\varepsilon_s - \varepsilon_\infty)}{[1 + (i\omega\tau_0)^{1-\alpha}]}$, where ε is the dielectric constant, ε_∞ is the high-frequency dielectric constant, ε_s is the static dielectric constant (at an infinitely long time), and τ_0 is the mean relaxation time for the system [125]; $\varepsilon_s - \varepsilon_\infty$ represents a fraction of the total dispersion of the dielectric constants.

Articles which mentioned Q_0 mainly focused on factors affecting: membrane formation [133, 211]; comparing membrane systems [36, 80, 212-214]; comparing phase separation due to molecular composition [11, 80], peptides and the proteins gramicidin and FSKRGY [80, 213, 215]; effects of drugs [214]; and patterning of membranes [134]. On the other hand, when Q_0 was used in greater detail the articles mainly focused on circuit distinguishability [208, 216], comparing tBLM properties with a Finite Element Analysis models [198], the effect of temperature and concentration on the transport of sodium ions by gramicidin on a self-assembled monolayer [217], and the application of a model circuit and its intricacies due to different monolayers [218]. When Q_0 is not the focus of an EIS-membrane article, but deep analyses have still been performed into either quantitative or physical representations of membranes, permittivity of membranes, potentials across membranes, ionic mobility studies, and issues relating to reference electrodes. Bridging articles between Q_0 and permittivity were specifically linking drug effects to membranes [214] or Q_0 and potential while studying the peptide Melittin [210].

By using permittivity, still using EIS data by applying a commonly used equation (see Appendix 1), specific interests included contrasting membrane types [210], the peptide action of Valinomycin [210], and studying vesicle-membrane circuits with far more elaborate model circuits [219].

6.3. Types of EIS plots

The Nyquist plot is an Argand diagram which compares impedance on the complex plane. The advantage of a Nyquist plot is that capacitive impedance is plotted against the real impedance, and can be used to separate RC meshes [126]. Each parallel RC mesh appears as a separate semicircle in the final plot, allowing both resistance and capacitance values to be extracted. The intercept with the x-axis is equal the double of the real impedance, while applying the equation $\omega_{\max}RC=1$ will allow you to extract the capacitance [126]. An alternative version of this plot is the admittance plot, plotting the real admittance ($1/Z'$) against the imaginary admittance ($1/Z''$) [130]. Again, RC elements are identified as semi-circles. However, in this case, the capacitance is equivalent to the intersection with the y-axis while resistors give a line that is parallel to the y-axis [130].

The Cole-Cole plot is an Argand diagram which compares dielectric on the complex plane. Each point on the Cole-Cole plot represents complex dielectric permittivity obtained at certain frequencies [220]. This specific plot is able to exemplify system resonances and relaxations [220]. Within membrane EIS, this type of plot is used to study the capacitances of a system.

The M^* plot plots the complex electric modulus against the complex impedance [126]. The equation representing this is $M^* = M'' = i\omega C_0 Z''$, where $C_0 = \epsilon_0 A/l$ [126]. This plot is most useful when grain-boundaries exist, as their response may dominate that of bulk regions [126]. According to Irvine, Sinclair, and West [1990], the higher frequency M'' peak represents the bulk region. Overall however, the Nyquist plot is best used to observe the most resistive elements in the sample whereas the modulus plot is used to observe the elements with the smallest capacitance. Z''_{\max} is equal to $R/2$ in the Nyquist plot, whereas $M'' = \epsilon_0/2C$ for the

modulus plot. As such, comparing the two spectra allows a samples homogeneity to be compared, with inhomogeneous samples looking significantly different between the two spectra [126].

6.4. Concerns regarding Cyclic Voltammetry

Current density, j , is stated as:

$$j = \frac{dQ}{dt} = \frac{dQ}{dE} \frac{dE}{dt} = Cv$$

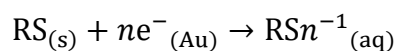
Where, in this case, Q is the capacitive charge density, v is the scan rate. It should be noted at this point that the current also includes a resistive contribution, as the resistance of a bilayer is not infinite, which imparts a slight tilt to the current trace [123]. When the current is reversed, the opposite offset with respect to the zero-current axis, with in identical angle to that seen before as the resistance is identical [123]. Under constant conditions, the vertical distance between the negative and positive voltages in the scan is equal to $2Cv$, or double the current density [123].

Reductive desorption traces the current against potential [154]. By integrating the reductive desorption peak from point of SAM adsorption to desorption, the total charge of the thiol desorption can be calculated [154].

$$\int_{E_a}^{E_d} \frac{i}{v} dE$$

, where v is the sweep rate [154].

The process of desorption can be show using the equation:



, where (s) , (Au) , and (aq) refer to the surface, bulk gold phase, and solution phase.

Coverage is calculated as follows:

$$\Gamma = \left| \frac{Q}{nF} \right|$$

Where F is Faraday's constant, n is the number of electrons in the process (which according to the author is on the order of 10^{15} for thiolates), and Q is charge [154]. All of this occurs in a cell which has a basic pH to limit hydrogen evolution [154].

A few key issues are important to consider. Firstly, in the first equation the integrand equals the differential capacity:

$$\frac{i}{\nu} = C$$

$$C_{thiol\ electrode} = C_{\infty} + \left(\frac{\partial \sigma_M}{\partial \Gamma} \right)_E \frac{d\Gamma}{dE}$$

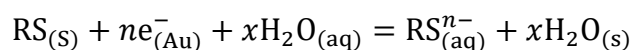
Where $\left(\frac{\partial \sigma_M}{\partial \Gamma} \right)_E = -lF$, C_{∞} is the capacitance at infinite frequency, and l is the formal charge number at a constant potential, also known as the electrosorption valency [154]. As such the integral of the voltametric current during cathodic desorption is:

$$Q = \int_{E_a}^{E_d} \frac{i}{\nu} dE = \int_{E_a}^{E_d} C_{\infty} dE - F \int_{\Gamma}^0 l d\Gamma$$

The double layer charging term, $\int_{E_a}^{E_d} C_{\infty} dE$, is never equivalent to zero, which means that reductive desorption is stated to lead to too tight packing densities and equivalently too small foot-prints, as stated by Schneider and Buttry almost 25 years ago [154]. Further, this is

a commonly neglected term. According to the same paper, efforts within the field have been made to deal with this issue, however the process have not been commonly introduced [154].

Secondly, $|l| \neq n$, and has been shown to be a partial charge number that is dependent on the electrode's potential [154]. The same authors continue to state that, as clarified by Schneider and Buttry, the charge number l does not need to be an integer, and like the reaction shown above, is also an over simplification, which more realistically is defined as a substitution reaction between a thiol and water from the bulk solution:



, with $|l|$ changing as a function of applied potential from 0 to n [154]. However, although the data in the same paper supports the equation above, it does not provide any evidence of partial charge transfer being a partial integer, within error [154]. In fact, Kunze et al. (2008) use three different methods to investigate DPhyTL reductive desorption: two electron transfer, partial charge transfer, and desorption without electron transfer [49]. The authors conclude that the electrosorption valency is described by the same expression regardless of the nature of the mechanism and that its magnitude cannot determine oxidation state [49]. The authors conclude by stating that the 'reductive desorption' of thiols does not have a strong physical basis and in fact is not a reduction reaction at all [49].

6.5. VSFG

6.5.1. Theory

vSFG works by aligning two lasers' pulses and having them overlap both spatially and temporally in a non-centrosymmetric medium [158, 163]. The signal intensity is determined by a combination of both lasers' incident electric fields, the interface's Fresnel factors associated with those fields, and the second-order susceptibility, as can be seen in the equations below [163].

$$\chi^{(2)} = \chi_{NR}^{(2)} + \chi_R^{(2)} = |A_{NR}|e^{i\varphi} + \sum_q \frac{|A_q|}{\omega_{IR} - \omega_q + i\Gamma_q}$$

$$\text{Note: } |A_q| \propto N \langle \beta^{(2)} \rangle \propto N \left\langle \frac{\partial \alpha}{\partial Q_q} \frac{\partial \mu}{\partial Q_q} \right\rangle$$

Where $\chi_{NR}^{(2)}$ and $\chi_R^{(2)}$ are the non-resonant background and resonant contributions, A_q , ω_q , and Γ_q are the oscillator strength, the resonance frequency, and the damping factor of the q^{th} vibrational mode respectively [160, 221]. $|A_{NR}|$ and φ represent the non resonant susceptibility and phase factor, also known as the difference between the phase of the non-resonant and resonant signals. $\langle \beta^2 \rangle$ is the hyperpolarisability of the molecule averaged over an orientational distribution and containing the dipole moment and the Raman tensor derivatives [163]. The SFG intensity is therefore proportional to the complex sum of the non-resonant frequency term and resonant term, which mainly originates from the substrate and ad-layer respectively [163]. Each time a photon, ω_{IR} , matches a specific vibrational mode of a molecule, ω_q , an increase in the resonant susceptibility term is observed [163]. As such, vSFG studies the intensity of all the vibrational modes and background signals which are proportional to the square of the sum of all of the terms [160].

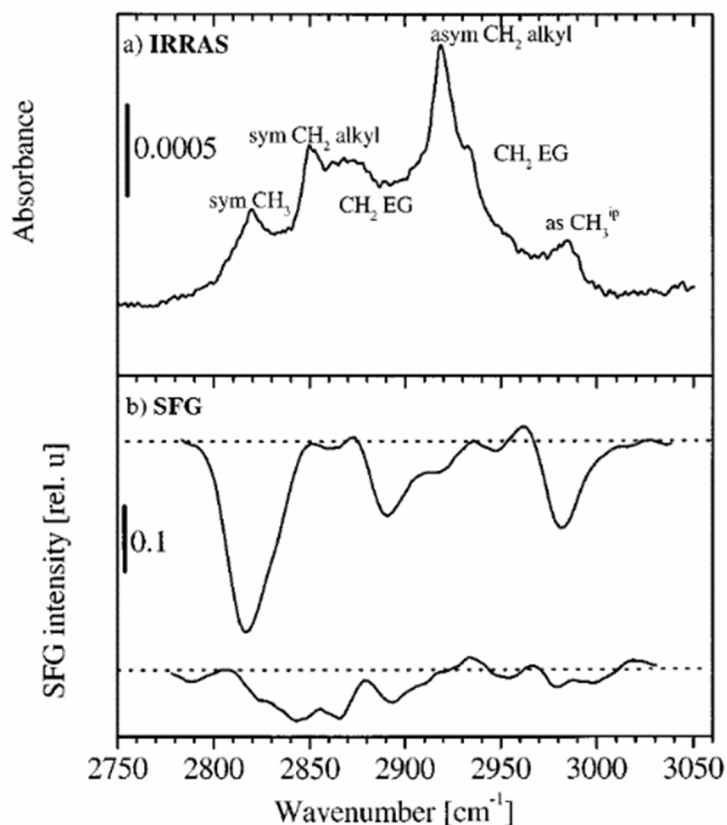
Less rigorously, vSFG studies the superposition of the non-resonant and resonant susceptibilities:

$$I_{SFG} \propto \left| \chi_{NR} + \sum_{n=2,3}^{\nu} \chi_{CH_n(\nu)}^{\nu} \right|^2 I_{vis} I_{IR}$$

Where χ_{NR} is the contribution from the substrate and the interaction of the thiol with the substrate, $\chi_{CH_n(\nu)}^{\nu}$ is an example of various CH groups' modes contributing to the overall resonant susceptibilities [60]. Where χ_{NR} is a constant, $\chi_{CH_n(\nu)}^{\nu}$ depends on two factors, the orientation of the molecular moieties as symbolised by the tilt angle, ν , and the molecule's symmetry, which is what specifically separates this technique from IR [60]. In the presence of centrosymmetric and amorphous structures the susceptibility, $\chi_{CH_n(\nu)}^{\nu}$, vanishes. Overall, this makes vSFG sensitive to changes in conformation, which when studying the changes due to ethanol are particularly useful [60].

6.5.2. Molecular orientation and interaction

The significant usefulness of SFG is its ability to not be affected by centrosymmetric or asymmetric alignments. For example Figure 59 is a comparison of a SAM of OG₃-OMe on gold between an Infra-Red Reflection Absorption Spectroscopy (IRRAS) and SFG spectrum in ambient atmosphere [60]. In the IR spectrum the methylene groups contribute irrespective of conformation and therefore dominate the signal, whereas by using SFG, the lack of CH₂ contributions suggests a predominantly centrosymmetric structure trans with gauche defects with aligned CH₃ groups of the alkane chains [60]. The gauche defects and aligned methyl groups define the signal.



Reprinted (adapted) with permission from Zolk, M., F. Eisert, J. Pipper, S. Herrwerth, W. Eck, M. Buck & M. Grunze, *Solvation of Oligo(ethylene glycol)-Terminated Self-Assembled Monolayers Studied by Vibrational Sum Frequency Spectroscopy*. *Langmuir*, 2000. 16(14): p. 5849-5852. Copyright 2000 American Chemical Society.

Figure 59: SAM of EG₃-OMe on gold. Reproduced from Zolk et al. [2000]

6.5.3. Types of polarisations

In another example, the relative intensities of the different vibrational models were considered with different polarisation configurations [163]. Orientation, in this case, was partly deduced by simulation [163]. There are 27 components of the macroscopic second-order susceptibility tensor, although only seven are non-vanishing. Furthermore, only four combinations of polarisations lead to non-linear activity: PPP, SSP, SPS, and PSS, and of these, only two are use on metallic substrates, PPP, and SSP, due to Fresnel's factors for infrared polarisation being too small [163]. Lis et al. (2009) goes into far more detail on this if needed [163]. As such, Zhang et al. (2013) state that a common method of analysis is as follows: s-polarised SFG, s-polarised visible laser, and a p-polaire IR laser (SSP setup) [180].

6.5.4. Effect of solvent

In the same way, the effect of solvent, and specifically water, on the SFG signal is seen as follows (Figure 60). The signal almost may be shifted based on the change to the orientation of the surface being tested. For example, when considering a dense maleimide surface, there is a high degree of order and orientational alignment of the maleimide SAM, common of other thiol-SAM substrates [161]. By disordering the surface beyond the SFG limit of orientational disorder, the signal decreases beyond recognition [161]. The remaining signals may be shifted slightly which indicates a change to the area, considering that amide I carbonyl stretch normally appears below 1700cm^{-1} in FTIR literature [161].

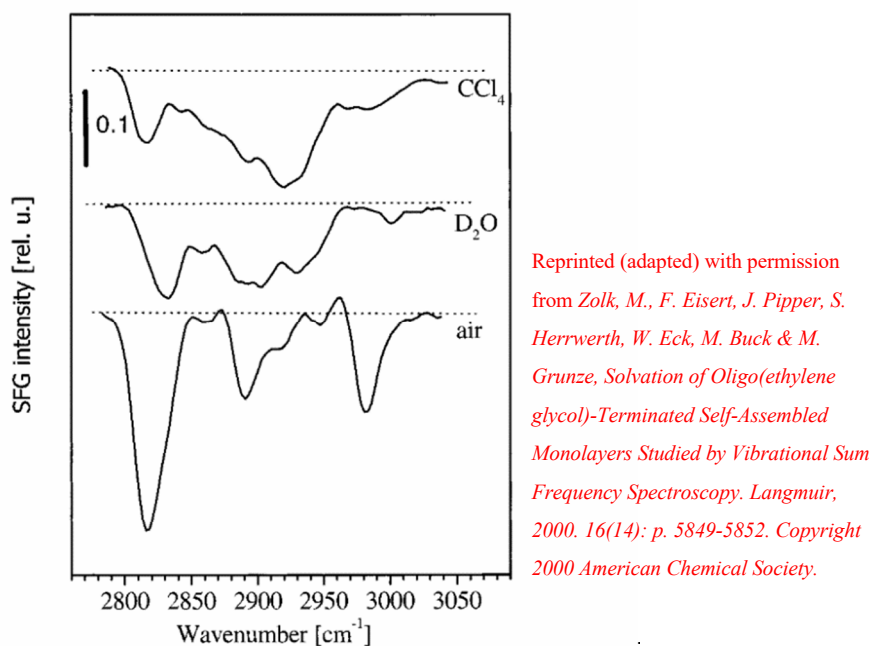


Figure 60: SFG spectrum of EG₃-OMe on gold in ambient atmosphere in CCl₄, D₂O, and air.

Reproduced from Zolk et al. [2000].

6.6. Ethanol Data

Sample	R_{def} ($M\Omega.cm^2$)			C_{mH} ($\mu F.cm^{-2}$)			Z_{sub} ($\Omega.s^{-\alpha}.cm^2$)			Alpha	χ^2
<i>Bilayer with Valinomycin (NaCl)</i>	17.0	±	N/A	0.194	±	0.0007	0.0291	±	0.001	0.38	0.00140
<i>Bilayer after 1%(v/v) Ethanol (NaCl)</i>	11.8	±	0.352	0.183	±	0.00090	0.305	±	0.013	0.78	0.00148
<i>Bilayer after 5%(v/v) Ethanol (NaCl)</i>	2.77	±	0.0403	0.187	±	0.00081	0.618	±	0.0089	0.89	0.000943
<i>Bilayer after 10%(v/v) Ethanol (NaCl)</i>	1.27	±	0.0173	0.188	±	0.00095	0.785	±	0.0088	0.91	0.00104
<i>Bilayer after 25%(v/v) Ethanol (NaCl)</i>	1.52	±	0.0294	0.191	±	0.00073	0.982	±	0.0021	0.89	0.000992

6.7. Assigned NMR Spectrum of DPhyTL

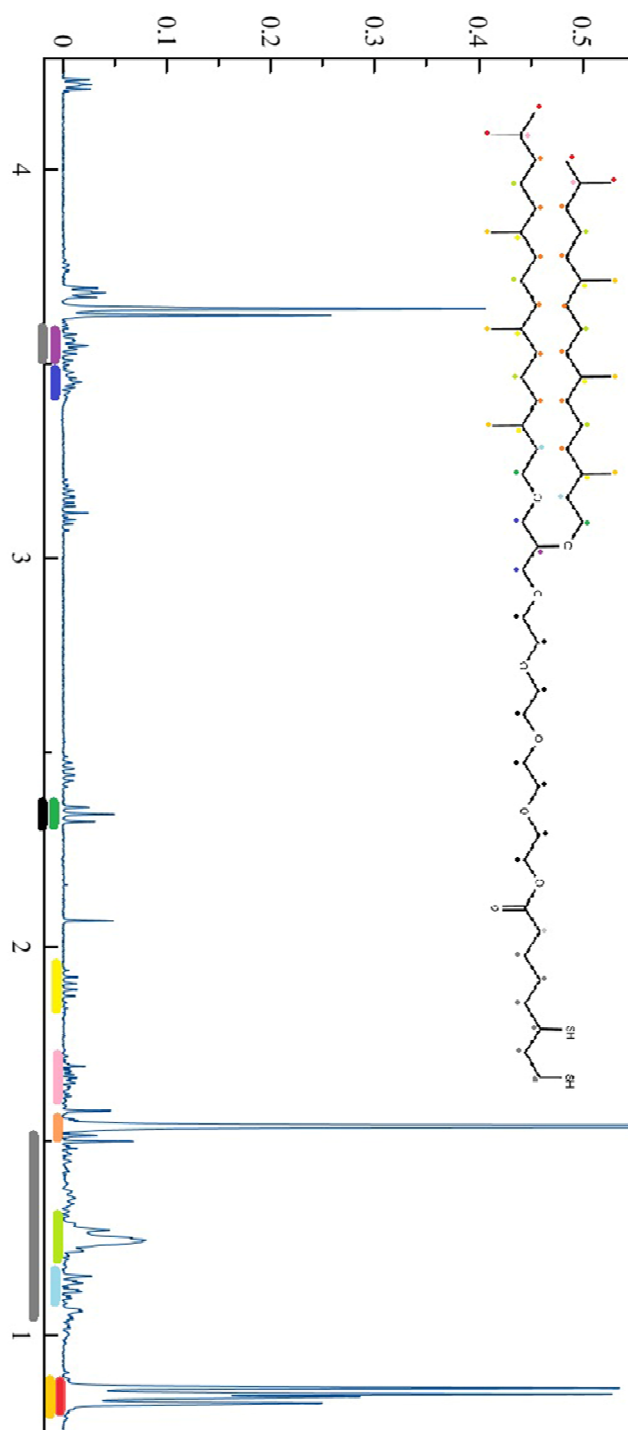


Figure 61: Assigned 400 MHz NMR Chloroform-D spectrum of DPhyTL

Coloured dots on the molecule can be translated to the positions of the peaks on the spectrum.

6.8. HvBot1 Information

Molecular dynamic studies evidenced that HvBot1 is naturally a trimeric protein due to the lowest surface energies between monomers in that conformation [86]. Due to the lack of any previous model, a structural framework was used to construct an in silico atomistic model of HvBot1 which included 574 residues. Using a crystal structure similar to a uracil/H⁺ symporter, which has been identified as a structural homolog. By predicting the disposition of secondary structural elements and boundaries of membrane α -helices using various tools. Overall it was predicted that the protein folded in a complex architecture which included α -helical folds which were independent to membrane and cytoplasmic areas. Importantly there were five short α -helices which formed an independent domain known as the ‘sombbrero’, protruding from the membrane by approximately 17 Å (Figure 63).

AFM results of bilayer testing on vesicles of DMPC indicated that although the protein’s features protrude at both ends, only the sombrero was witnessed in 66% of cases, with only protrusions of 17 Å observed and not ~9 - 10 Å in high-resolution scans ($\leq 1 \times 1 \mu\text{m}$; minimum pixel resolution of 512x512; vertical detection limit 1 Å). When the same scans were completed on the same vesicles using the same system, though without HvBot1 mRNA, features of any kind were only witnessed approximately 10% of the time on an otherwise smooth surface [86].

Nagarajan et al. [2016] tested the yield of HvBot1 protein during WP-CFS to both quantify the amount of protein produced as well as to test whether various surfactants would improve yield [86]. It was ascertained that there yield was high (0.16 mg.mL⁻¹) and that there was no need for surfactants due to the presence of soluble chaperones, native lipids in the

wheat-germ extract, and close-proximity of ribosomes; which is important to not disturb the membrane beyond protein insertion.

Prior to initial EIS-tBLM HvBot1 transport experiments, Wheat Germ Cell-Free Synthesis (WG-CFS) was analysed for full-length barley HvBot1 co-translational insertion into vesicles. Nagarajan et al. [2016] successfully tested the mRNA expression process in a number of vesicle types, specifically: POPC; POPE; DMPC; POPC:POPE:POPG:cholesterol, and Asolectin (Figure 62) using SDS-Page gel tests and Immunoblot assays; this process of checking for expression and insertion was used later to confirm HvBot1 WG-CFS into tBLMs post-EIS studies [86].

In terms of applicability for tBLM-EIS spectroscopy, Nagarajan et al. [2016] suggested that HvBot1 acted as an ion channel between -60 and +100 mV, ideal for further experiments [86]. Further, when a blocking ion was introduced (4,4'-diisothicyano-2,2'-stilbenedisulfonic acid) the HvBot1 current ceased. Using MD as well as patch-clamp studies, they indicated that the HvBot1 protein includes a binding site for sodium ions, which without the inclusion of 5mM NaCl in solution, inhibits the action of the protein [86]. Finally, evidenced that the HvBot1 conductance is nonspecific, conducting chlorides, phosphates, nitrates, and sulfates with conductance values of 7.8, 7.3, 6.2, and 5.9 pS respectively at a concentration of 25mM. None of the ions mentioned had a detectable currents between 0.5 and 10 mM, whereas borate did, suggesting monovalent tetrahydroxy borate is the preferred ion by HvBot1 [86]. Finally, the protein's action was bimodal, as indicated by both the monomer and oligomers function, however because EIS observes an average change to a surface, it was unlikely for mixture of oligomeric forms to cause a significant change in later tBLM-EIS studies unless a specific type of oligomer was encountered, which was unlikely.

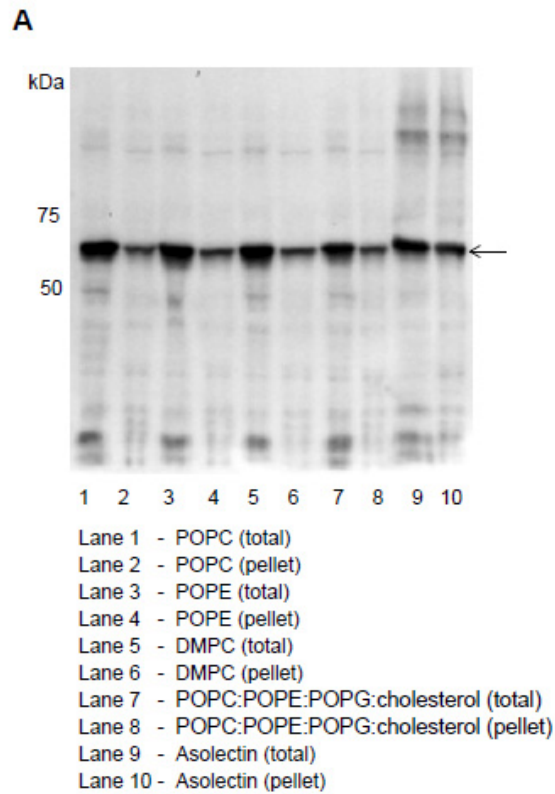


Figure 62: SDS-Page gel electrophoresis of HvBot1 into various types of liposomes

From left to right: POPC, POPE, DMPC, POPC:POPE:POPG:cholesterol=6:3:1:0.1 and asolectin. Control tests without HvBot1 mRNA indicated that no protein was expressed (not shown here). Reproduced from Nagarajan et al. [2016]

6.9. HvBot1 Structure

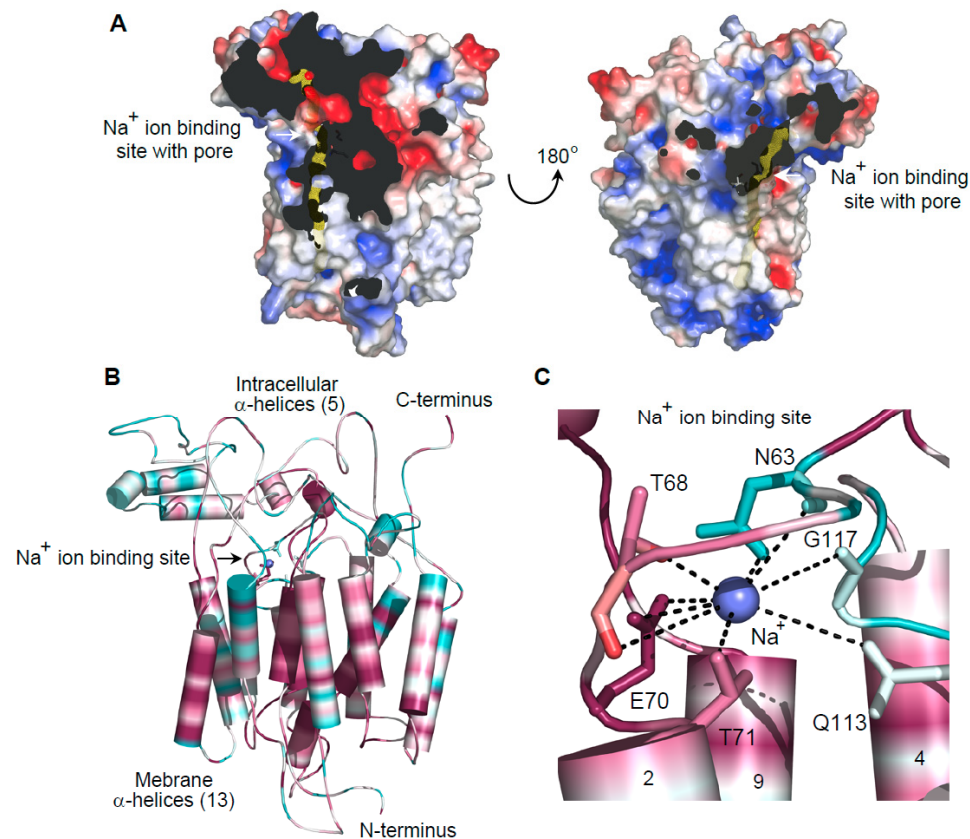


Figure 63: Modelled structure of HvBot1.

(A) Surface morphology of HvBot1 as coded by electrostatic potentials. There are two orientations: left panels is the front side; right panel is the back side. The views are rotated about 180° about the horizontal axis from each other. Blue areas denote electro-positive zones and red areas denote electro-negative zones, with a range of $\pm 3 kTe^{-1}$. The protein has been sectioned in both panels (black cut-away) indicating the position of the pore with relation to the Na⁺ ion binding site. (B) Conservation for the modelled HvBot1 structure. (C) The Na⁺ ion binding site of the six amino acid residues. Reproduced from Nagarajan et al. [2016].

Simulations were completed on HvBot1 in a DOPC lipid bilayer environment. It was observed that an Na⁺ binding site consisted of six residues which participated in a nonahedral co-ordination of Na⁺ [86]. Further calculations of the surface electrostatic properties concluded that the higher density of electronegative charges existed near the Na⁺ binding site, with a lower density of charges observed in the membrane embedded regions. Due to HvBot1 commonly

forming di- and tri-mers, quaternary structures of HvBot1 were predicted using geometry-based docking and searches for complementary interfaces between neighbouring promoters (Figure 64). The predicted trimer used here on in is the most compact with the lower interface atomic contact energy configuration. It is predicted that this is the configuration used *in planta* and that mono-, di-, and the tri-meric forms are in equilibrium.

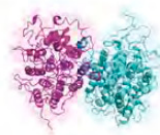

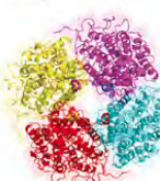


Multimeric form of Bot1	Interface atomic contact energy (kcal/mol)	Spatial arrangement
Dimer	-781	
Trimer	-1,152	
Tetramer	-816	
Pentamer	-450	
Hexamer	-757	

Figure 64: Various spatial arrangements of the multimeric forms of HvBot1.

as organised using interfacial atomic contact energies with Symmdock. Individual promoters in the cartoons and surface representations are colour coded. Images created in PyMOL. Reproduced from Nagarajan et al. [2016].

7. References

1. Light, D.W. & J.R. Lexchin, *Pharmaceutical research and development: what do we get for all that money?* BMJ : British Medical Journal, 2012. **345**.
2. Josic, D., J.G. Clifton, S. Kovac & D.C. Hixson, *Membrane proteins as diagnostic biomarkers and targets for new therapies*. Current opinion in molecular therapeutics, 2008. **10**(2): p. 116-123.
3. Lindsay, M.A., *Target discovery*. Nature Reviews Drug Discovery, 2003. **2**(10): p. 831-838.
4. Holthuis, J.C. & A.K. Menon, *Lipid landscapes and pipelines in membrane homeostasis*. Nature, 2014. **510**(7503): p. 48-57.
5. Alberts, B., A. Johnson & J. Lewis, *Cell Junctions, Cell Adhesion, and the Extracellular Matrix*, in *Molecular Biology of the Cell*. 2002, Garland Science: New York.
6. van Meer, G., D.R. Voelker & G.W. Feigenson, *Membrane lipids: where they are and how they behave*. Nat Rev Mol Cell Biol, 2008. **9**(2): p. 112-24.
7. Fuertes, G., D. Giménez, S. Esteban-Martín, O.L. Sánchez-Muñoz & J. Salgado, *A lipocentric view of peptide-induced pores*. European Biophysics Journal : EBJ, 2011. **40**(4): p. 399-415.
8. Huffer, S., M.E. Clark, J.C. Ning, H.W. Blanch & D.S. Clark, *Role of alcohols in growth, lipid composition, and membrane fluidity of yeasts, bacteria, and archaea*. Applied and Environmental Microbiology, 2011. **77**(18): p. 6400-6408.
9. Sud, M., E. Fahy, D. Cotter, A. Brown, E.A. Dennis, C.K. Glass, A.H. Merrill, Jr., R.C. Murphy, C.R. Raetz, D.W. Russell & S. Subramaniam, *LMSD: LIPID MAPS structure database*. Nucleic Acids Res, 2007. **35**(Database issue): p. D527-32.
10. Tanford, C., *The hydrophobic effect: Formation of micelles and biological membranes*. 1980, New York: Wiley-Interscience.
11. Jeuken, L.J., *AFM study on the electric-field effects on supported bilayer lipid membranes*. Biophysical Journal, 2008. **94**(12): p. 4711-4717.
12. Corvalán, N.A., J.M. Kembro, P.D. Clop & M.A. Perillo, *Cholesterol favors the emergence of a long-range autocorrelated fluctuation pattern in voltage-induced ionic currents through lipid bilayers*. Biochim Biophys Acta, 2013. **1828**(8): p. 1754-1764.
13. Tenchov, B., *On the reversibility of the phase transitions in lipid-water systems*. Chemistry and Physics of Lipids, 1991. **57**(2-3): p. 165-177.
14. Giocondi, M.-C.C., D. Yamamoto, E. Lesniewska, P.-E.E. Milhiet, T. Ando & C. Le Grimellec, *Surface topography of membrane domains*. Biochimica et biophysica acta, 2010. **1798**(4): p. 703-718.
15. Pike, L.J., *Lipid rafts: bringing order to chaos*. Journal of Lipid Research, 2003. **44**(4): p. 655-667.

16. Schreier, S., S.V.P. Malheiros & E. de Paula, *Surface active drugs: self-association and interaction with membranes and surfactants. Physicochemical and biological aspects*. Biochim Biophys Acta, 2000. **1508**(1-2): p. 210-34.
17. Pollard, T.D., W.C. Earnshaw & J. Lippincott-Schwartz, *Cell biology*. 2007: Elsevier Health Sciences.
18. McMullen, T.P.W., R.N.A.H. Lewis & R.N. McElhaney, *Cholesterol–phospholipid interactions, the liquid-ordered phase and lipid rafts in model and biological membranes*. Current Opinion in Colloid & Interface Science, 2004. **8**(6): p. 459-468.
19. Lee, A.G., *Biological membranes: the importance of molecular detail*. Trends in Biochemical Sciences, 2011. **36**(9): p. 493-500.
20. Gorter, E. & F. Grendel, *On Bimolecular Layers of Lipoids on the Chromocytes of the Blood*. The Journal of Experimental Medicine, 1925. **41**(4): p. 439-443.
21. Peetla, C., A. Stine & V. Labhasetwar, *Biophysical interactions with model lipid membranes: applications in drug discovery and drug delivery*. Molecular Pharmaceutics, 2009. **6**(5): p. 1264-76.
22. Farsad, K. & P. De Camilli, *Mechanisms of membrane deformation*. Current opinion in cell biology, 2003. **15**(4): p. 372-81.
23. Naumowicz, M., J. Kotynska, A. Petelska & Z. Figaszewski, *Impedance analysis of phosphatidylcholine membranes modified with valinomycin*. European Biophysics Journal, 2006. **35**(3): p. 239-246.
24. Fabre, R.M. & D.R. Talham, *Stable supported lipid bilayers on zirconium phosphonate surfaces*. Langmuir, 2009. **25**(21): p. 12644-12652.
25. Vogel, N., J. Zieleniecki & I. Köper, *As flat as it gets: ultrasoother surfaces from template-stripping procedures*. Nanoscale, 2012. **4**(13): p. 3820-3832.
26. Junghans, A., C. Champagne, P. Cayot, C. Loupiac & I. Köper, *Probing protein-membrane interactions using solid supported membranes*. Langmuir, 2011. **27**(6): p. 2709-2716.
27. Sackmann, E., *Supported membranes: scientific and practical applications*. Science, 1996. **271**(5245): p. 43-48.
28. Suzuki, H. & S. Takeuchi, *Microtechnologies for membrane protein studies*. Analytical and Bioanalytical Chemistry, 2008. **391**(8): p. 2695-2702.
29. Atanasov, V., P.P. Atanasova, I.K. Vockenroth, N. Knorr & I. Köper, *A molecular toolkit for highly insulating tethered bilayer lipid membranes on various substrates*. Bioconjugate chemistry, 2006. **17**(3): p. 631-637.
30. Braunagel, J., A. Junghans & I. Köper, *Membrane-Based Sensing Approaches*. Australian Journal of Chemistry, 2011. **64**(1): p. 54-61.

31. Bergveld, P., *Development of an Ion-Sensitive Solid-State Device for Neurophysiological Measurements*. IEEE Transactions on Bio-medical Engineering, 1970. **17**: p. 2.
32. Cornell, B.A., V.L. Braach-Maksvytis, L.G. King, P.D. Osman, B. Raguse, L. Wieczorek & R.J. Pace, *A biosensor that uses ion-channel switches*. Nature, 1997. **387**(6633): p. 580-3.
33. Rolando, G. & B. Lucia, *Ion transport across biomembranes and model membranes*. Journal of Solid State Electrochemistry, 2011. **15**(7-8): p. 1459-1470.
34. Cornell, B.A., G. Krishna, P.D. Osman, R.D. Pace & L. Wieczorek, *Tethered-bilayer lipid membranes as a support for membrane-active peptides*. Biochemical Society Transactions, 2001. **29**(4): p. 613-617.
35. Tien, H.T. & A. Ottova, *The bilayer Lipid membrane BLM under electrical fields*. IEEE Transactions on Dielectrics and Electrical Insulation, 2003. **10**(5): p. 717-727.
36. McGillivray, D.J., G. Valincius, D.J. Vanderah, W. Febo-Ayala, J.T. Woodward, F. Heinrich, J.J. Kasianowicz & M. Losche, *Molecular-scale structural and functional characterization of sparsely tethered bilayer lipid membranes*. Biointerphases, 2007. **2**(1): p. 21-33.
37. Vockenroth, I.K., C. Ohm, J.W.F. Robertson, D.J. McGillivray, M. Lösche & I. Köper, *Stable insulating tethered bilayer lipid membranes*. Biointerphases, 2008. **3**(2).
38. Lipkowski, J., *Building biomimetic membrane at a gold electrode surface*. Physical Chemistry Chemical Physics, 2010. **12**(42): p. 13874-13887.
39. Schiller, S.M., R. Naumann, K. Lovejoy, H. Kunz & W. Knoll, *Archaea Analogue Thiolipids for Tethered Bilayer Lipid Membranes on Ultrasoother Gold Surfaces*. Angewandte Chemie International Edition, 2003. **42**(2): p. 208-211.
40. Becucci, L., M. D'Amico, S. Cinotti, S. Daniele & R. Guidelli, *Tethered bilayer lipid micromembranes for single-channel recording: the role of adsorbed and partially fused lipid vesicles*. Physical Chemistry Chemical Physics: PCCP, 2011. **13**(29): p. 13341-13348.
41. Rose, L. & A.T. Jenkins, *The effect of the ionophore valinomycin on biomimetic solid supported lipid DPPE/EPC membranes*. Bioelectrochemistry, 2007. **70**(2): p. 387-393.
42. Cranfield, C.G., B.A. Cornell, S.L. Grage, P. Duckworth, S. Carne, A.S. Ulrich & B. Martinac, *Transient Potential Gradients and Impedance Measures of Tethered Bilayer Lipid Membranes: Pore-Forming Peptide Insertion and the Effect of Electroporation*. Biophysical Journal, 2014. **106**(1): p. 182-189.
43. Willey, T.M., A.L. Vance, T. van Buuren, C. Bostedt, L.J. Terminello & C.S. Fadley, *Rapid degradation of alkanethiol-based self-assembled monolayers on gold in ambient laboratory conditions*. Surface Science, 2005. **576**(1-3): p. 188-196.
44. Sackmann, E. & M. Tanaka, *Supported membranes on soft polymer cushions: fabrication, characterization and applications*. Trends in Biotechnology, 2000. **18**(2): p. 58-64.

45. Davis, F. & S.P. Higson, *Structured thin films as functional components within biosensors*. Biosensors and Bioelectronics, 2005. **21**(1): p. 1-20.
46. Jeuken, L.J.C., N.N. Daskalakis, X. Han, K. Sheikh, A. Erbe, R.J. Bushby & S.D. Evans, *Phase separation in mixed self-assembled monolayers and its effect on biomimetic membranes*. Sensors and Actuators B: Chemical, 2007. **124**(2): p. 501-509.
47. Lin, J., M. Merzlyakov, K. Hristova & P.C. Searson, *Impedance spectroscopy of bilayer membranes on single crystal silicon*. Biointerphases, 2008. **3**(2).
48. Sovago, M., E. Vartiainen & M. Bonn, *Observation of buried water molecules in phospholipid membranes by surface sum-frequency generation spectroscopy*. The Journal of Chemical Physics, 2009. **131**(16): p. 161107.
49. Kunze, J., J. Leitch, A.L. Schwan, R.J. Faragher, R. Naumann, S. Schiller, W. Knoll, J.R. Dutcher & J. Lipkowski, *New method to measure packing densities of self-assembled thiolipid monolayers*. Langmuir, 2006. **22**(12): p. 5509-5519.
50. Saliba, N., D.H. Parker & B.E. Koel, *Adsorption of oxygen on Au (111) by exposure to ozone*. Adsorption of oxygen on Au (111) by exposure to ozone, 1998.
51. Martin, H., C. Vericat, G. Andreasen, A. Hernández Creus, M.E. Vela & R.C. Salvarezza, *The Kinetics of the $(\sqrt{3}\times\sqrt{3})R30^\circ$ Sulfur Lattice Stripping from Au(111): Competitive Desorption–Hole Nucleation and Growth Model*. Langmuir, 2001. **17**(8): p. 2334-2339.
52. Ron, H., S. Matlis & I. Rubinstein, *Self-Assembled Monolayers on Oxidized Metals. 2. Gold Surface Oxidative Pretreatment, Monolayer Properties, and Depression Formation*. Langmuir, 1998. **14**(5): p. 1116-1121.
53. Leitch, J., J. Kunze, J.D. Goddard, A.L. Schwan, R.J. Faragher, R. Naumann, W. Knoll, J.R. Dutcher & J. Lipkowski, *In Situ PM-IRRAS Studies of an Archaea Analogue Thiolipid Assembled on a Au(111) Electrode Surface*. Langmuir, 2009. **25**(17): p. 10354-10363.
54. Zhu, L., D. Gregurec & I. Reviakine, *Nanoscale Departures: Excess Lipid Leaving the Surface during Supported Lipid Bilayer Formation*. Langmuir, 2013. **29**(49): p. 15283-15292.
55. Woodward, J.T., M.L. Walker, C.W. Meuse, D.J. Vanderah, G. Poirier & A.L. Plant, *Effect of an Oxidized Gold Substrate on Alkanethiol Self-Assembly*. Langmuir, 2000. **16**(12): p. 5347-5353.
56. Worley, C.G. & R.W. Linton, *Removing sulfur from gold using ultraviolet/ozone cleaning*. Removing sulfur from gold using ultraviolet/ozone cleaning, 1995. **13**(4): p. 2281-2284.
57. Kohli, P., K.K. Taylor, J.J. Harris & G.J. Blanchard, *Assembly of Covalently-Coupled Disulfide Multilayers on Gold*. Journal of the American Chemical Society, 1998. **120**(46): p. 11962-11968.

58. Fischer, L.M., M. Tenje, A.R. Heiskanen, N. Masuda, J. Castillo, A. Bentien, J. Émneus, M.H. Jakobsen & A. Boisen, *Gold cleaning methods for electrochemical detection applications*. *Microelectronic Engineering*, 2009. **86**(4-6): p. 1282-1285.
59. Myung, M.S., S. Kiwhan, G.K. Chang, S.L. Sun & K. Yunsoo, *Self-Assembled Monolayers of Alkanethiols on Oxidized Copper Surfaces*. *The Journal of Physical Chemistry B*, 2000. **104**.
60. Zolk, M., F. Eisert, J. Pipper, S. Herrwerth, W. Eck, M. Buck & M. Grunze, *Solvation of Oligo(ethylene glycol)-Terminated Self-Assembled Monolayers Studied by Vibrational Sum Frequency Spectroscopy*. *Langmuir*, 2000. **16**(14): p. 5849-5852.
61. Marsh, D., *Thermodynamics of phospholipid self-assembly*. *Biophysical journal*, 2012. **102**(5): p. 1079-1087.
62. Naumann, R., S.M. Schiller, F. Giess, B. Grohe, K.B. Hartman, I. Kärcher, I. Köper, J. Lübben, K. Vasilev & W. Knoll, *Tethered Lipid Bilayers on Ultraflat Gold Surfaces*. *Langmuir*, 2003. **19**(13): p. 5435-5443.
63. Jaikishan, S., A. Björkbom & J.P. Slotte, *Phosphatidyl alcohols: effect of head group size on domain forming properties and interactions with sterols*. *Biochimica et Biophysica Acta (BBA)-Biomembranes*, 2010. **1798**(8): p. 1615-1622.
64. Moss, R.A. & T. Fujita, *Dynamics of liposomes constructed from phytanyl lipids*. *Tetrahedron letters*, 1990. **31**(52): p. 7559-7562.
65. Roux, B., S. Berneche, B. Egwolf, B. Lev, S.Y. Noskov, C.N. Rowley & H. Yu, *Ion selectivity in channels and transporters*. *J Gen Physiol*, 2011. **137**(5): p. 415-426.
66. Goldshlegger, R., S.J. Karlish, A. Rephaeli & W.D. Stein, *The effect of membrane potential on the mammalian sodium-potassium pump reconstituted into phospholipid vesicles*. *The Journal of Physiology*, 1987. **387**: p. 331-355.
67. McGillivray, D.J., G. Valincius, F. Heinrich, J.W. Robertson, D.J. Vanderah, W. Febo-Ayala, I. Ignatjev, M. Lösche & J.J. Kasianowicz, *Structure of functional Staphylococcus aureus alpha-hemolysin channels in tethered bilayer lipid membranes*. *Biophysical Journal*, 2009. **96**(4): p. 1547-1553.
68. Vockenroth, I.K., P.P. Atanasova, J.R. Long, T.A.A. Jenkins, W. Knoll & I. Köper, *Functional incorporation of the pore forming segment of AChR M2 into tethered bilayer lipid membranes*. *Biochimica et Biophysica Acta (BBA) - Biomembranes*, 2007. **1768**(5): p. 1114-1120.
69. Giess, F., M.G. Friedrich, J. Heberle, R.L. Naumann & W. Knoll, *The protein-tethered lipid bilayer: A novel mimic of the biological membrane*. *Biophysical Journal*, 2004. **87**(5): p. 3213-3220.
70. Lee, M.T., F.Y. Chen & H.W. Huang, *Energetics of pore formation induced by membrane active peptides*. *Biochemistry*, 2004. **43**(12): p. 3590-3599.

71. Bruno, M.J., R. Rusinova, N.J. Gleason, R.E. Koeppe & O.S. Andersen, *Interactions of drugs and amphiphiles with membranes: modulation of lipid bilayer elastic properties by changes in acyl chain unsaturation and protonation*. Faraday Discussions, 2013. **161**: p. 461.
72. Marrone, T.J. & K.M. Merz, *Molecular Recognition of K⁺ and Na⁺ by Valinomycin in Methanol*. Journal of the American Chemical Society, 1995. **117**(2): p. 779-791.
73. Vockenroth, I.K., P.P. Atanasova, W. Knoll, I. Koper, A. Toby & A. Jenkins. *Functional tethered bilayer membranes as a biosensor platform*. in *IEEE Sensors, 2005*. 2005. IEEE.
74. Navrátil, T., I. Šestáková, K. Štulík & V. Mareček, *Electrochemical Measurements on Supported Phospholipid Bilayers: Preparation, Properties and Ion Transport Using Incorporated Ionophores*. Electroanalysis, 2010. **22**(17-18): p. 2043-2050.
75. Keplinger, C., I. Höfer & C. Steinem, *Impedance analysis of valinomycin activity in nano-BLMs*. Chemistry and Physics of Lipids, 2009. **160**(2): p. 109-113.
76. Becucci, L., M.R. Moncelli & R. Guidelli, *Ion carriers and channels in metal-supported lipid bilayers as probes of transmembrane and dipole potentials*. Langmuir, 2003. **19**(8): p. 3386-3392.
77. Atanasov, V., N. Knorr, R.S. Duran, S. Ingebrandt, A. Offenhäusser, W. Knoll & I. Köper, *Membrane on a Chip: A Functional Tethered Lipid Bilayer Membrane on Silicon Oxide Surfaces*. Biophysical Journal, 2005. **89**(3): p. 1780-1788.
78. Kunz, W., M.-C. Bellissent-Fune & P. Calmettes, *Structure of water and ionic hydration*, in *Bioelectrochemistry: General Introduction*, S.R. Caplan, I.R. Miller, and G. Milazzo, Editors. 1995, Birkhäuser Basel: Basel. p. 132-210.
79. Cornell, B., V. Braach-Maksvytis, L. King, P. Osman, B. Raguse, L. Wieczorek & R. Pace, *A biosensor that uses ion-channel switches*. Nature London, 1997: p. 580-582.
80. Kendall, J.K.R., B.R.G. Johnson, P.H. Symonds, G. Imperato, R.J. Bushby, J.D. Gwyer, C. van Berkel, S.D. Evans & L.J.C. Jeuken, *Effect of the Structure of Cholesterol-Based Tethered Bilayer Lipid Membranes on Ionophore Activity*. ChemPhysChem, 2010. **11**(10): p. 2191-2198.
81. Raguse, B., V. Braach-Maksvytis, B.A. Cornell, L.G. King, P.D.J. Osman, R.J. Pace & L. Wieczorek, *Tethered Lipid Bilayer Membranes: Formation and Ionic Reservoir Characterization*. Langmuir, 1998. **14**(3): p. 648-659.
82. Cafiso, D.S. & W.L. Hubbell, *Estimation of transmembrane potentials from phase equilibria of hydrophobic paramagnetic ions*. Biochemistry, 1978. **17**(1): p. 187-95.
83. Eisenman, G., S. Krasne & S. Ciani, *The Kinetic and Equilibrium Components of Selective Ionic Permeability Mediated by Nactinand Valinomycin-type Carriers Having Systematically Varied Degrees of Methylation*. Annals of the New York Academy of Sciences, 1975. **264**(1): p. 34-60.

84. Zieleniecki, J.L., Y. Nagarajan, S. Waters, J. Rongala, V. Thompson, M. Hrmova & I. per, *Cell-Free Synthesis of a Functional Membrane Transporter into a Tethered Bilayer Lipid Membrane*. *Langmuir*, 2016. **32**(10): p. 2445-2449.
85. Demarche, S., K. Sugihara, T. Zambelli, L. Tiefenauer & J. Vörös, *Techniques for recording reconstituted ion channels*. *Analyst*, 2011. **136**(6): p. 1077-1089.
86. Nagarajan, Y., J. Rongala, S. Luang, A. Singh, N. Shadiac, J. Hayes, T. Sutton, M. Gilliam, S.D. Tyerman, G. McPhee, N.H. Voelcker, H.D.T. Mertens, N.M. Kirby, J.-G. Lee, Y.G. Yingling & M. Hrmova, *A Barley Efflux Transporter Operates in a Na⁺-Dependent Manner, as Revealed by a Multidisciplinary Platform*. *The Plant Cell*, 2016. **28**: p. 202-218.
87. Ratti, E. & D. Trist, *Continuing evolution of the drug discovery process in the pharmaceutical industry*. *Pure and Applied Chemistry*, 2001. **73**(1): p. 67-75.
88. Coskun, Ü. & K. Simons, *Cell Membranes: The Lipid Perspective*. *Structure*, 2011. **19**(11): p. 1543-1548.
89. Smith, D., P. Artursson, A. Avdeef, L. Di, G.F. Ecker, B. Faller, J.B. Houston, M. Kansy, E.H. Kerns, S.D. Krämer, H. Lennernäs, H. van de Waterbeemd, K. Sugano & B. Testa, *Passive lipoidal diffusion and carrier-mediated cell uptake are both important mechanisms of membrane permeation in drug disposition*. *Molecular Pharmaceutics*, 2014. **11**(6): p. 1727-1738.
90. Ghosh, A., D.O. Scott & T.S. Maurer, *Towards a unified model of passive drug permeation I: Origins of the unstirred water layer with applications to ionic permeation*. *European Journal of Pharmaceutical Sciences*, 2014. **52**: p. 109-124.
91. Meyer, H., *Zur Theorie der Alkoholnarkose*. *Archiv für experimentelle Pathologie und Pharmakologie*, 1899. **42**(2-4): p. 109-118.
92. Roth, S. & P. Seeman, *The membrane concentrations of neutral and positive anesthetics (alcohols, chlorpromazine, morphine) fit the meyer-overton rule of anesthesia; negative narcotics do not*. *Biochimica et Biophysica Acta (BBA)-Biomembranes*, 1972. **255**(1): p. 207-219.
93. Bangham, A.D., M.M. Standish & J.C. Watkins, *Diffusion of univalent ions across the lamellae of swollen phospholipids*. *Journal of Molecular Biology*, 1965. **13**(1): p. 238-252.
94. Papahadjopoulos, D. & J.C. Watkins, *Phospholipid model membranes. II. Permeability properties of hydrated liquid crystals*. *Biochim Biophys Acta*, 1967. **135**(4): p. 639-652.
95. Bangham, A.D., M.M. Standish & G. Weissmann, *The action of steroids and streptolysin S on the permeability of phospholipid structures to cations*. *Journal of Molecular Biology*, 1965. **13**(1): p. 253-259.
96. Kraayenhof, R., G.J. Sterk, H.W.W.F. Sang, K. Krab & R.M. Epand, *Monovalent cations differentially affect membrane surface properties and membrane curvature, as revealed by fluorescent probes and dynamic light scattering*. *Biochimica et Biophysica Acta (BBA)-Biomembranes*, 1996. **1282**(2): p. 293-302.

97. Franks, F., *Water a comprehensive treatise: volume 4: aqueous solutions of amphiphiles and macromolecules*. 2013, New York: Springer Science & Business Media.
98. Conway, B.E., *Ionic hydration in chemistry and biophysics*. 1981, Amsterdam; New York: Elsevier Scientific Pub. Co.
99. Antonov, V.F., A.A. Anosov, V.P. Norik & E. Smirnova, *A soft poration of planar bilayer lipid membranes from dipalmitoylphosphatidylcholine at the temperature of the phase transition from the liquid crystalline to the gel state*. *Biofizika*, 2005. **50**(5): p. 867-877.
100. Seeman, P., *The membrane actions of anesthetics and tranquilizers*. *Pharmacological Reviews*, 1972. **24**(1): p. 583-655.
101. Kyrikou, I., S.K. Hadjikakou & D. Kovala-Demertzi, *Effects of non-steroid anti-inflammatory drugs in membrane bilayers*. *Chemistry and Physics of Lipids*, 2004. **132**(2): p. 157-169.
102. Victoria, V., M. Philippe, P. Tanja & B. Isak, *Alamethicin influence on the membrane bending elasticity*. *European Biophysics Journal*, 2006. **35**(3): p. 281-286.
103. Duwe, H.P., J. Kaes & E. Sackmann, *Bending elastic moduli of lipid bilayers : modulation by solutes*. *Journal of Physics*, 1990. **51**(10): p. 945-961.
104. Yong, Z. & M.R. Robert, *Effect of Salicylate on the Elasticity, Bending Stiffness, and Strength of SOPC Membranes*. *Biophysical Journal*, 2005. **89**(3): p. 1789-1801.
105. Evans, E., W. Rawicz & A. Hofmann, *Bile acids in gastroenterology: basic and clinical advances*. 1995: Kluwer Academic Publishers Lancaster, UK. 59-68.
106. Zhelev, D.V., *Material Property Characteristics for Lipid Bilayers Containing Lysolipid*. *Biophysical Journal*, 1998. **75**(1): p. 321-330.
107. Ly, H.V. & M.L. Longo, *The Influence of Short-Chain Alcohols on Interfacial Tension, Mechanical Properties, Area/Molecule, and Permeability of Fluid Lipid Bilayers*. *Biophysical Journal*, 2004. **87**(2): p. 1013-1033.
108. Thomas, J.A., J.L. Stringer, A.W. Cuthbert, F.E. Bloom, H.P. Rang & I.S. Snyder. *Drug (Chemical Agent)*. 2013; Available from: <http://www.britannica.com/EBchecked/topic/171942/drug>.
109. Imming, P., C. Sinning & A. Meyer, *Drugs, their targets and the nature and number of drug targets*. *Nature reviews Drug discovery*, 2006. **5**(10): p. 821-834.
110. Kumari, P., A. Nath & R. Chaube, *Identification of human drug targets using machine-learning algorithms*. *Computers in Biology and Medicine*, 2015. **56**: p. 175-181.
111. Overington, J.P., B. Al-Lazikani & A.L. Hopkins, *How many drug targets are there?* *Nature Reviews Drug Discovery*, 2006. **5**(12): p. 993-996.

112. Rajendran, L., V. Udayar & Z.V. Goodger, *Lipid-anchored drugs for delivery into subcellular compartments*. Trends in Pharmacological Sciences, 2012. **33**(4): p. 215-222.
113. Williams, A.C. & B.W. Barry, *Penetration enhancers*. Advanced Drug Delivery Reviews, 2012. **64**: p. 128-137.
114. Notman, R. & J. Anwar, *Breaching the skin barrier - Insights from molecular simulation of model membranes*. Advanced Drug Delivery Reviews, 2013. **65**(2): p. 237-250.
115. Patra, M., E. Salonen, E. Terama, I. Vattulainen, R. Faller, B.W. Lee, J. Holopainen & M. Karttunen, *Under the Influence of Alcohol: The Effect of Ethanol and Methanol on Lipid Bilayers*. Biophysical Journal, 2006. **90**(4): p. 1121-1135.
116. Griepernau, B., S. Leis, M.F. Schneider, M. Sikor, D. Steppich & R.A. Böckmann, *1-Alkanols and membranes: A story of attraction*. Biochimica et Biophysica Acta (BBA) - Biomembranes, 2007. **1768**(11): p. 2899-2913.
117. Stetter, F.W. & T. Hugel, *The nanomechanical properties of lipid membranes are significantly influenced by the presence of ethanol*. Biophysical journal, 2013. **104**(5): p. 1049-1055.
118. Marquês, J.T., A.S. Viana & R. Almeida, *Ethanol effects on binary and ternary supported lipid bilayers with gel/fluid domains and lipid rafts*. Biochimica et Biophysica Acta (BBA) - Biomembranes, 2011. **1808**(1): p. 405-414.
119. Ly, H.V., D.E. Block & M.L. Longo, *Interfacial Tension Effect of Ethanol on Lipid Bilayer Rigidity, Stability, and Area/Molecule: A Micropipet Aspiration Approach*. Langmuir, 2002. **18**(23): p. 8988-8995.
120. Ingram, L.O., *Ethanol Tolerance in Bacteria*. Critical Reviews in Biotechnology, 1989. **9**(4): p. 305-319.
121. Silveira, G.M., E.A. Golovina, F.A. Hoekstra, F.M. Rombouts & T. Abee, *Membrane fluidity adjustments in ethanol-stressed Oenococcus oeni cells*. Applied and environmental microbiology, 2003. **69**(10): p. 5826-5832.
122. Wang, X., M.M. Shindel, S.-W. Wang & R. Ragan, *A Facile Approach for Assembling Lipid Bilayer Membranes on Template-Stripped Gold*. Langmuir, 2010. **26**(23): p. 18239-18245.
123. Becucci, L. & R. Guidelli, *Mercury-supported biomimetic membranes for the investigation of antimicrobial peptides*. Pharmaceuticals (Basel, Switzerland), 2014. **7**(2): p. 136-168.
124. Subczynski, W.K., J. Widomska & J.B. Feix, *Physical properties of lipid bilayers from EPR spin labeling and their influence on chemical reactions in a membrane environment*. Free Radical Biology and Medicine, 2009. **46**(6): p. 707-718.
125. Barsoukov, E. & J.R. Macdonald, *Impedance spectroscopy: theory, experiment, and applications*. 2nd ed. 2005: John Wiley & Sons.

126. Irvine, J.T.S., D.C. Sinclair & A.R. West, *Electroceramics: Characterization by Impedance Spectroscopy*. Advanced Materials, 1990. **2**(3): p. 132-138.
127. Vockenroth, I.K., C. Rossi, M.R. Shah & I. Koper, *Formation of tethered bilayer lipid membranes probed by various surface sensitive techniques*. Biointerphases, 2009. **4**(2): p. 19-26.
128. Ge, C., J. Liao, W. Yu & N. Gu, *Electric potential control of DNA immobilization on gold electrode*. Biosensors and Bioelectronics, 2003. **18**(1): p. 53-58.
129. Naumowicz, M., A.D. Petelska & Z.A. Figaszewski, *Impedance Analysis of Complex Formation Equilibria in Phosphatidylcholine Bilayers Containing Decanoic Acid or Decylamine*. Cell Biochemistry and Biophysics, 2011. **61**(1): p. 145-155.
130. Vockenroth, I.K., P.P. Atanasova, A.T. Jenkins & I. Koper, *Incorporation of alpha-hemolysin in different tethered bilayer lipid membrane architectures*. Langmuir, 2008. **24**(2): p. 496-502.
131. Han, X., A.S. Achalkumar, R.J. Bushby & S.D. Evans, *A Cholesterol-Based Tether for Creating Photopatterned Lipid Membrane Arrays on both a Silica and Gold Surface*. Chemistry – A European Journal, 2009. **15**(26): p. 6363-6370.
132. Kohli, N., B.L. Hassler, L. Parthasarathy, R.J. Richardson, R.Y. Ofoli, R.M. Worden & I. Lee, *Tethered Lipid Bilayers on Electrolessly Deposited Gold for Bioelectronic Applications*. Biomacromolecules, 2006. **7**(12): p. 3327-3335.
133. Sahalov, H., B. O'Brien, K.J. Stebe, K. Hristova & P.C. Searson, *Influence of applied potential on the impedance of alkanethiol SAMs*. Langmuir, 2007. **23**(19): p. 9681-9685.
134. Han, X., K. Critchley, L. Zhang, S.N. Pradeep, R.J. Bushby & S.D. Evans, *A novel method to fabricate patterned bilayer lipid membranes*. Langmuir, 2007. **23**(3): p. 1354-1358.
135. Vockenroth, I.K., D. Fine, A. Dodabalapur, A.T.A. Jenkins & I. Köper, *Tethered bilayer lipid membranes with giga-ohm resistances*. Electrochemistry Communications, 2008. **10**(2): p. 323-328.
136. Naumann, R., T. Baumgart, P. Gräber, A. Jonczyk, A. Offenhäusser & W. Knoll, *Proton transport through a peptide-tethered bilayer lipid membrane by the H⁺-ATP synthase from chloroplasts measured by impedance spectroscopy*. Biosensors and Bioelectronics, 2002. **17**(1-2): p. 25-34.
137. Becucci, L., M. Innocenti, E. Salviotti, A. Rindi, I. Pasquini, M. Vassalli, M.L. Foresti & R. Guidelli, *Potassium ion transport by gramicidin and valinomycin across a Ag(111)-supported tethered bilayer lipid membrane*. Electrochimica Acta, 2008. **53**(22): p. 6372-6379.
138. Valincius, G., T. Meškauskas & F. Ivanauskas, *Electrochemical Impedance Spectroscopy of Tethered Bilayer Membranes*. Langmuir, 2012. **28**(1): p. 977-990.
139. Krishna, G., J. Schulte, B.A. Cornell, R.J. Pace & P.D. Osman, *Tethered bilayer membranes containing ionic reservoirs: selectivity and conductance*. Langmuir, 2003. **19**(6): p. 2294-2305.

140. Olofsson, L., M. Edvardsson, P. Delsing & B. Kasemo, *Vesicle and bi-layer kinetics at surfaces measured by electrical transmission*. Sensors and Actuators B: Chemical, 2004. **97**(2-3): p. 313-318.
141. Valincius, G. & M. Mickevicius, *Chapter Two - Tethered Phospholipid Bilayer Membranes: An Interpretation of the Electrochemical Impedance Response*, in *Advances in Planar Lipid Bilayers and Liposomes*, C.V.K. Aleš Iglíč and R. Michael, Editors. 2015, Academic Press. p. 27-61.
142. Scott, J.L., C.A. Musselman, E. Adu-Gyamfi, T.G. Kutateladze & R.V. Stahelin, *Emerging methodologies to investigate lipid-protein interactions*. Integrative Biology, 2012. **4**(3): p. 247-58.
143. Wolkers, W.F., H. Oldenhof & B. Glasmacher, *Dehydrating phospholipid vesicles measured in real-time using ATR Fourier transform infrared spectroscopy*. Cryobiology, 2010. **61**(1): p. 108-114.
144. Lewis, R.N. & R.N. McElhaney, *Membrane lipid phase transitions and phase organization studied by Fourier transform infrared spectroscopy*. Biochimica et Biophysica Acta (BBA), 2013. **1828**(10): p. 2347-2358.
145. Pohle, W., D.R. Gauger, H. Fritzsche, B. Rattay, C. Selle, H. Binder & H. Böhlig, *FTIR-spectroscopic characterization of phosphocholine-headgroup model compounds*. Journal of molecular structure, 2001. **563**: p. 463-467.
146. Laredo, T., J.R. Dutcher & J. Lipkowski, *Electric Field Driven Changes of a Gramicidin Containing Lipid Bilayer Supported on a Au(111) Surface*. Langmuir, 2011. **27**(16): p. 10072-87.
147. Zhumaev, U., A.V. Rudnev, J.-F. Li, A. Kuzume, T.-H. Vu & T. Wandlowski, *Electro-oxidation of Au (111) in contact with aqueous electrolytes: New insight from in situ vibration spectroscopy*. Electrochimica Acta, 2013. **112**: p. 853-863.
148. García-Raya, D., R. Madueño, M. Blázquez & T. Pineda, *Formation of 1,8-Octanedithiol Mono- and Bilayers under Electrochemical Control*. The Journal of Physical Chemistry C, 2010. **114**(8): p. 3568-3574.
149. Diaz-Morales, O., F. Calle-Vallejo, C. de Munck & M.T. Koper, *Electrochemical water splitting by gold: evidence for an oxide decomposition mechanism*. Chemical Science, 2013. **4**(6): p. 2334-2343.
150. Hamelin, A., *Cyclic voltammetry at gold single-crystal surfaces. Part 1. Behaviour at low-index faces*. Journal of Electroanalytical Chemistry, 1996. **407**(1-2): p. 1-11.
151. Delgado, J.M., J.M. Orts, J.M. Pérez & A. Rodes, *Sputtered thin-film gold electrodes for in situ ATR-SEIRAS and SERS studies*. Journal of Electroanalytical Chemistry, 2008. **617**(2): p. 130-140.
152. Uosaki, K., Y. Shen & T. Kondo, *Preparation of a highly ordered Au (111) phase on a polycrystalline gold substrate by vacuum deposition and its characterization by XRD, GISXRD*,

- STM/AFM, and electrochemical measurements.* The Journal of physical chemistry, 1995. **99**(38): p. 14117-14122.
153. Sumi, T. & K. Uosaki, *Electrochemical Oxidative Formation and Reductive Desorption of a Self-Assembled Monolayer of Decanethiol on a Au(111) Surface in KOH Ethanol Solution.* The Journal of Physical Chemistry B, 2004. **108**(20): p. 6422-6428.
 154. Laredo, T., J. Leitch, M. Chen, I.J. Burgess, J.R. Dutcher & J. Lipkowski, *Measurement of the charge number per adsorbed molecule and packing densities of self-assembled long-chain monolayers of thiols.* Langmuir, 2007. **23**(11): p. 6205-11.
 155. Weisshaar, D.E., M.M. Walczak & M.D. Porter, *Electrochemically induced transformations of monolayers formed by self-assembly of mercaptoethanol at gold.* Langmuir, 1993. **9**(1): p. 323-329.
 156. Raya, D., R. Madueno, M. Blázquez & T. Pineda, *Formation of a 1, 8-Octanedithiol Self-Assembled Monolayer on Au (111) Prepared in a Lyotropic Liquid-Crystalline Medium.* Langmuir, 2010. **26**(14): p. 11790-11796.
 157. Jian, Z.Y., T.Y. Chang, Y.C. Yang, W.P. Dow & S.L. Yau, *3-Mercapto-1-propanesulfonic acid and Bis (3-sulfopropyl) Disulfide Adsorbed on Au (111): In Situ Scanning Tunneling Microscopy and Electrochemical Studies.* Langmuir, 2008. **25**(1): p. 179-184.
 158. Anglin, T.C., Z. Sohrabpour & A.M. Massari, *Nonlinear Spectroscopic Markers of Structural Change during Charge Accumulation in Organic Field-Effect Transistors.* The Journal of Physical Chemistry C, 2011. **115**(41): p. 20258-20266.
 159. Ye, S., K.T. Nguyen, S.V.L. Clair & Z. Chen, *In situ molecular level studies on membrane related peptides and proteins in real time using sum frequency generation vibrational spectroscopy.* Journal of Structural Biology, 2009. **168**(1): p. 61-77.
 160. Chen, X. & Z. Chen, *SFG studies on interactions between antimicrobial peptides and supported lipid bilayers.* Biochimica et Biophysica Acta 2006. **1758**(9): p. 1257-73.
 161. Yatawara, A.K., G. Tiruchinapally, A.N. Bordenyuk, P.R. Andreana & A.V. Benderskii, *Carbohydrate surface attachment characterized by sum frequency generation spectroscopy.* Langmuir, 2009. **25**(4): p. 1901-1904.
 162. Sung, J., K. Park & D. Kim, *Surfaces of alcohol-water mixtures studied by sum-frequency generation vibrational spectroscopy.* The Journal of Physical Chemistry B, 2005. **109**(39): p. 18507-14.
 163. Lis, D., A. Peremans, Y. Sartenaer, Y. Caudano, A.A. Mani, L. Dreesen, P.A. Thiry, J. Guthmuller, B.t. Champagne & F. Cecchet, *Self-Assembled Film Organization in Fast Microcontact Printing Investigated by Sum Frequency Generation Spectroscopy.* The Journal of Physical Chemistry C, 2009. **113**(22): p. 9857-9864.
 164. Gan, W., Z. Zhang, R.-r. Feng & H.-f. Wang, *Identification of overlapping features in the sum frequency generation vibrational spectra of air/ethanol interface.* Chemical Physics Letters, 2006. **423**(4-6): p. 261-265.

165. Busson, B. & A. Tadjeddine, *Non-uniqueness of parameters extracted from resonant second-order nonlinear optical spectroscopies*. The Journal of Physical Chemistry C, 2009. **113**(52): p. 21895-21902.
166. Stępniewski, M., A. Bunker, M. Pasenkiewicz-Gierula, M. Karttunen & T. Róg, *Effects of the Lipid Bilayer Phase State on the Water Membrane Interface*. The Journal of Physical Chemistry B, 2010. **114**(36): p. 11784-11792.
167. Knobloch, J.J., A.R. Nelson, I. Köper, M. James & D.J. McGillivray, *Oxidative Damage to Biomimetic Membrane Systems: In Situ Fe(II)/Ascorbate Initiated Oxidation and Incorporation of Synthetic Oxidized Phospholipids*. Langmuir, 2015. **31**(46): p. 12679-12687.
168. Krueger, S., *Neutron reflection from interfaces with biological and biomimetic materials*. Current Opinion in Colloid & Interface Science, 2001. **6**(2): p. 111-117.
169. Giovanna, F.-C., *Neutron reflectivity at the solid/liquid interface: examples of applications in biophysics*. Journal of Physics: Condensed Matter, 2001. **13**(21): p. 4973.
170. James, M., A. Nelson, S.A. Holt, T. Saerbeck, W.A. Hamilton & F. Klose, *The multipurpose time-of-flight neutron reflectometer "Platypus" at Australia's OPAL reactor*. Nuclear Instruments and Methods in Physics Research Section A: Accelerators, Spectrometers, Detectors and Associated Equipment, 2011. **632**(1): p. 112-123.
171. Junghans, A. & I. Köper, *Structural analysis of tethered bilayer lipid membranes*. Langmuir: the ACS journal of surfaces and colloids, 2010. **26**(13): p. 11035-11040.
172. Li, L.B., I. Vorobyov & T.W. Allen, *The role of membrane thickness in charged protein-lipid interactions*. Biochimica et biophysica acta, 2012. **1818**(2): p. 135-145.
173. Pencer, J., M.P. Nieh, T.A. Harroun, S. Krueger, C. Adams & J. Katsaras, *Bilayer thickness and thermal response of dimyristoylphosphatidylcholine unilamellar vesicles containing cholesterol, ergosterol and lanosterol: A small-angle neutron scattering study*. Biochimica et Biophysica Acta (BBA) - Biomembranes, 2005. **1720**(1-2): p. 84-91.
174. Arsov, Z. & L. Quaroni, *Direct interaction between cholesterol and phosphatidylcholines in hydrated membranes revealed by ATR-FTIR spectroscopy*. Chemistry and Physics of Lipids, 2007. **150**(1): p. 35-48.
175. Yamada, R., H. Wano & K. Uosaki, *Effect of Temperature on Structure of the Self-Assembled Monolayer of Decanethiol on Au(111) Surface*. Langmuir, 2000. **16**(13): p. 5523-5525.
176. Clavilier, J., R. Faure, G. Guinet & R. Durand, *Preparation of monocrystalline Pt microelectrodes and electrochemical study of the plane surfaces cut in the direction of the {111} and {110} planes*. Journal of Electroanalytical Chemistry and Interfacial Electrochemistry, 1979. **107**(1): p. 205-209.
177. Darwish, N.A., P.K. Eggers, W. Yang, M.N. Paddon-Row & J.J. Gooding. *Step by step fabrication and characterization of Au (111) exposed single crystals*. in *Nanoscience and Nanotechnology (ICONN), 2010 International Conference on*. 2010. IEEE.

178. Dorvel, B.R., H.M. Keizer, D. Fine, J. Vuorinen, A. Dodabalapur & R.S. Duran, *Formation of tethered bilayer lipid membranes on gold surfaces: QCM-Z and AFM study*. *Langmuir*, 2007. **23**(13): p. 7344-7355.
179. Bard, A.J. & M. Stratmann, *Encyclopedia of Electrochemistry, Modified Electrodes; Volume 10*. 2003: Wiley-VCh.
180. Zhang, Y., H. Noguchi, S. Ye & K. Uosaki, *Structure of adsorbed molecular layer on fused quartz surface determined sequentially in sodium stearate solution, dry Ar, pure water, and dry Ar by sum frequency generation spectroscopy*. *Surface Science*, 2013. **607**: p. 92-96.
181. Wang, J., C. Chen, S.M. Buck & Z. Chen, *Molecular Chemical Structure on Poly(methyl methacrylate) (PMMA) Surface Studied by Sum Frequency Generation (SFG) Vibrational Spectroscopy*. *The Journal of Physical Chemistry B*, 2001. **105**(48): p. 12118-12125.
182. Robertson, J.W.F., M.G. Friedrich, A. Kibrom, W. Knoll, R.L.C. Naumann & D. Walz, *Modeling Ion Transport in Tethered Bilayer Lipid Membranes. I. Passive Ion Permeation*. *The Journal of Physical Chemistry B*, 2008. **112**(34): p. 10475-10482.
183. Cui, X. & D.C. Martin, *Electrochemical deposition and characterization of poly(3,4-ethylenedioxythiophene) on neural microelectrode arrays*. *Sensors and Actuators B: Chemical*, 2003. **89**(1-2): p. 92-102.
184. Naumowicz, M. & Z.A. Figaszewski, *Impedance Spectroscopic Investigation of the Bilayer Lipid Membranes Formed from the Phosphatidylserine-Ceramide Mixture*. *Journal of Membrane Biology*, 2009. **227**(2): p. 67-75.
185. Uosaki, K., *Formation and novel functions of self-assembled monolayers of thiol derivatives*. *Electrochemistry*, 1999. **67**(12): p. 1105-1113.
186. Majkrzak, C.F., N.F. Berk, S. Krueger, J.A. Dura, M. Tarek, D. Tobias, V. Silin, C.W. Meuse, J. Woodward & A.L. Plant, *First-Principles Determination of Hybrid Bilayer Membrane Structure by Phase-Sensitive Neutron Reflectometry*. *Biophysical Journal*, 2000. **79**(6): p. 3330-3340.
187. Nelson, A., *Co-refinement of multiple-contrast neutron/X-ray reflectivity data using MOTOFIT*. *Journal of Applied Crystallography*, 2006. **39**(2): p. 273-276.
188. Junghans, A., E.B. Watkins, R.D. Barker, S. Singh, M.J. Waltman, H.L. Smith, L. Pocivavsek & J. Majewski, *Analysis of biosurfaces by neutron reflectometry: From simple to complex interfaces*. *Biointerphases*, 2015. **10**(1): p. 019014.
189. Gregory, P. *Female driver blows 14 times Aussie blood-alcohol limit*. World 2009 [cited 2017 11/February]; Available from: <http://www.smh.com.au/world/female-driver-blows-14-times-aussie-bloodalcohol-limit-20091231-lkkm.html>.
190. No Author. *Drug Alcohol Concentration*. 2016 [cited 2016 2016/07/10]; Available from: <http://www.druginfo.adf.org.au/topics/bac>.

191. Kurniawan, J. & T.L. Kuhl, *Characterization of Solid Supported Dipalmitoylphosphatidylcholine Membranes Containing Cholesterol*. Langmuir, 2015. **31**(8): p. 2527-2732.
192. Breffa, C., *New synthetic strategies to tethered bilayer lipid membranes*, in *Fachbereich Chemie und Pharmazie*. 2005, Johannes Gutenberg-Universität: Mainz, Germany. p. 115.
193. Quayum, M.E., T. Kondo, S. Nihonyanagi, D. Miyamoto & K. Uosaki, *Formation of organic monolayer on a hydrogen terminated Si (111) surface via silicon-carbon bond monitored by ATR FT-IR and SFG spectroscopy: Effect of orientational order on the reaction rate*. Chemistry letters, 2002. **31**(2): p. 208-209.
194. Skoda, M.W., R.M. Jacobs, J. Willis & F. Schreiber, *Hydration of oligo (ethylene glycol) self-assembled monolayers studied using polarization modulation infrared spectroscopy*. Langmuir, 2007. **23**(3): p. 970-974.
195. NIST, *Choline Chloride: Infrared Spectrum*. 2016, United States Secretary of Commerce: U.S.A.
196. NIST, *Ethanol Gas Phase Spectrum: Infrared Spectrum*. 2016, United States Secretary of Commerce: U.S.A.
197. Shinoda, W., N. Namiki & S. Okazaki, *Molecular dynamics study of a lipid bilayer: convergence, structure, and long-time dynamics*. The Journal of chemical physics, 1997. **106**(13): p. 5731-5743.
198. Kwak, K.J., G. Valincius, W.C. Liao, X. Hu, X. Wen, A. Lee, B. Yu, D.J. Vanderah, W. Lu & L.J. Lee, *Formation and finite element analysis of tethered bilayer lipid structures*. Langmuir, 2010. **26**(23): p. 18199-18208.
199. Marquês, J.T., A.S. Viana & R.F.M. De Almeida, *Ethanol effects on binary and ternary supported lipid bilayers with gel/fluid domains and lipid rafts*. Biochimica et Biophysica Acta (BBA) - Biomembranes, 2011. **1808**(1): p. 405-414.
200. Coutable, A., C. Thibault, J. Chalmeau, J.M. Francois, C. Vieu, V. Noireaux & E. Trevisiol, *Preparation of tethered-lipid bilayers on gold surfaces for the incorporation of integral membrane proteins synthesized by cell-free expression*. Langmuir, 2014. **30**(11): p. 3132-3141.
201. Noireaux, V. & A. Libchaber, *A vesicle bioreactor as a step toward an artificial cell assembly*. Proc Natl Acad Sci U S A, 2004. **101**(51): p. 17669-74.
202. Glazier, S.A., D.J. Vanderah, A.L. Plant, H. Bayley, G. Valincius & J.J. Kasianowicz, *Reconstitution of the Pore-Forming Toxin α -Hemolysin in Phospholipid/18-Octadecyl-1-thiahexa(ethylene oxide) and Phospholipid/n-Octadecanethiol Supported Bilayer Membranes*. Langmuir, 2000. **16**(26): p. 10428-10435.
203. Separovic, F. & B.A. Cornell, *Gated ion channel-based biosensor device*, in *Biological Membrane Ion Channels*. 2007, Springer. p. 595-621.

204. Tran, A.-T., F. Huet, K. Ngo & P. Rousseau, *Artefacts in electrochemical impedance measurement in electrolytic solutions due to the reference electrode*. *Electrochimica Acta*, 2011. **56**(23): p. 8034-8039.
205. Shadiac, N., Y. Nagarajan, S. Waters & M. Hrmova, *Close allies in membrane protein research: Cell-free synthesis and nanotechnology*. *Molecular membrane biology*, 2013. **30**(3): p. 229-245.
206. Metzler, D.E., *Biochemistry: the chemical reactions of living cells*. 2 ed. 2003: Academic Press.
207. Naumann, R., D. Walz, S.M. Schiller & W. Knoll, *Kinetics of valinomycin-mediated K⁺ ion transport through tethered bilayer lipid membranes*. *Journal of Electroanalytical Chemistry*, 2003.
208. Berthier, F., J.P. Diard & R. Michel, *Distinguishability of equivalent circuits containing CPEs: Part I. Theoretical part*. *Journal of Electroanalytical Chemistry*, 2001. **510**(1–2): p. 1-11.
209. Shamsi, F. & H.G. Coster, *Mimicking cell membrane-like structures on alkylated silicon surfaces by peptide amphiphiles*. *Materials Chemistry and Physics*, 2011. **130**(3): p. 1162-1168.
210. He, L., J.W.F. Robertson, J. Li, I. Kärcher, S.M. Schiller, W. Knoll & R. Naumann, *Tethered Bilayer Lipid Membranes Based on Monolayers of Thiolipids Mixed with a Complementary Dilution Molecule. 1. Incorporation of Channel Peptides*. *Langmuir*, 2005. **21**(25): p. 11666-11672.
211. Basit, H., A. Heyden, C. Gondran, B. Nysten, P. Dumy & P. Labbé, *Tethered Bilayer Lipid Membranes on Mixed Self-Assembled Monolayers of a Novel Anchoring Thiol: Impact of the Anchoring Thiol Density on Bilayer Formation*. *Langmuir*, 2011. **27**(23): p. 14317-14328.
212. Abdelghani, A., C. Jacquin, M. Huber, R. Deutschmann & E. Sackmann, *Supported lipid membrane on semiconductor electrode*. *Materials Chemistry and Physics*, 2001. **70**(2): p. 187-190.
213. Briand, E., M. Zäch, S. Svedhem, B. Kasemo & S. Petronis, *Combined QCM-D and EIS study of supported lipid bilayer formation and interaction with pore-forming peptides*. *Analyst*, 2010. **135**(2): p. 343-350.
214. Mertins, O., P. Messina, E. Labbé, V. Vivier, S. Arbault, F. Lemaître, O. Buriez & C. Amatore, *Electrochemical analysis of the interactions and reactivity of ferrocene-based drugs with a lipid environment: A qualitative overview*. *Inorganica Chimica Acta*, 2011. **374**(1): p. 59-68.
215. Chang, W.K., W.C. Wimley, P.C. Searson, K. Hristova & M. Merzlyakov, *Characterization of antimicrobial peptide activity by electrochemical impedance spectroscopy*. *Biochim Biophys Acta*. 2008, 2008. **1778**(10): p. 2430-6.
216. Wiegand, G., N. Arribas-Layton, H. Hillebrandt, E. Sackmann & P. Wagner, *Electrical Properties of Supported Lipid Bilayer Membranes*. *The Journal of Physical Chemistry B*, 2002. **106**(16): p. 4245-4254.

217. Gervasi, C.A. & A.E. Vallejo, *Sodium ion transport through gramicidin-doped bilayers. Influences of temperature and ionic concentration*. *Electrochimica Acta*, 2002. **47**(13–14): p. 2259-2264.
218. Janek, R.P., W.R. Fawcett & A. Ulman, *Impedance Spectroscopy of Self-Assembled Monolayers on Au(111): Sodium Ferrocyanide Charge Transfer at Modified Electrodes*. *Langmuir*, 1998. **14**(11): p. 3011-3018.
219. Bai, S.-J. & F.B. Prinz, *In vivo electrochemical impedance measurement on single cell membrane*. *Microelectronic Engineering*, 2011. **88**(10): p. 3094-3100.
220. Haase, W. & S. Wróbel, *Relaxation phenomena: liquid crystals, magnetic systems, polymers, high-Tc superconductors, metallic glasses*. 2013: Springer Science & Business Media.
221. Joonyeong, K., K. Gibum & S.C. Paul, *Investigations of Water Structure at the Solid/Liquid Interface in the Presence of Supported Lipid Bilayers by Vibrational Sum Frequency Spectroscopy*. *Langmuir*, 2001. **17**(23): p. 7255-7260.